A SEARCH FOR EXTRA-SOLAR PLANETARY TRANSITS IN THE FIELD OF OPEN CLUSTER NGC 6819

Rachel Street

A Thesis Submitted for the Degree of PhD
at the
University of St Andrews

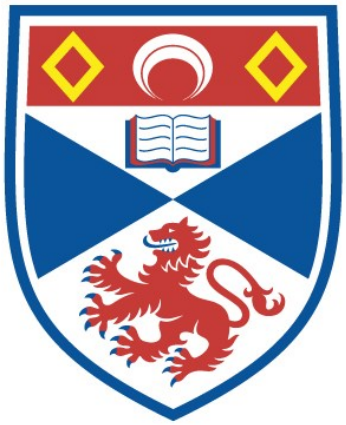

2002

THE UNIVERSITY OF ST. ANDREWS

A Search for Extra-Solar Planetary Transits in the Field of Open Cluster NGC 6819

Rachel Street

Submitted for the degree of Ph.D.

January 2002

DECLARATION

I, Rachel Amanda Street, hereby certify that this thesis, which is approximately 50000 words in length, has been written by me, that it is the record of work carried out by me and that it has not been submitted in any previous application for a higher degree.

Date. 7th. May. 2002 Signature of candidate.

I was admitted as a research student in October 1998 and as a candidate for the degree of Ph.D. in October 1998; the higher study for which this is a record was carried out in the University of St. Andrews between 1998 and 2002.

Date. 7th. May. 2002 Signature of candidate

I hereby certify that the candidate has fulfilled the conditions of the Resolution and Regulations appropriate for the degree of Ph.D. in the University of St. Andrews and that the candidate is qualified to submit this thesis in application for that degree.

Date..... Signature of supervisor.....

In submitting this thesis to the University of St. Andrews I understand that I am giving permission for it to be made available for use in accordance with the regulations of the University Library for the time being in force, subject to any copyright vested in the work not being affected thereby. I also understand that the title and abstract will be published, and that a copy of the work may be made and supplied to any *bona fide* library or research worker.

Date. 7th May 2002 Signature of candidate.

THE UNIVERSITY OF ST. ANDREWS

A Search for Extra-Solar Planetary Transits in the Field of Open Cluster NGC 6819

Submitted for the degree of Ph.D.

January 2002

Rachel Street

ABSTRACT

The technique of searching for extra-solar planetary transits is investigated. This technique, which relies on detecting the brief, shallow eclipses caused by planets passing across the line of sight to the primary star, requires high-precision time-series photometry of large numbers of stars in order to detect these statistically rare events.

Observations of $\sim$ 18000 stars in the field including the intermediate-age open cluster NGC 6819 are presented. This target field constrasts with the stellar environment surveyed by the radial velocity technique, which concentrates on the Solar neighbourhood.

I present the data-reduction techniques used to obtain high-precision photometry in a semi-automated fashion for tens of thousands of stars at a time, together with an algorithm designed to search the resulting lightcurves for the transit signatures of hot Jupiter type planets. I describe simulations designed to test the detection efficiency of this algorithm and, for comparison, predict the number of transits expected from this data, assuming that hot Jupiter planets similar to HD 209458 are as common in the field of NGC 6819 as they are in the Solar neighbourhood.

While no planetary transits have yet been identified, the detection of several very low amplitude eclipses by stellar companions demonstrates the effectiveness of the method. This study also indicates that stellar activity and particuarly blending are significant causes of false detections.

A useful additional consequence of studying this time-series photometry is the census it provides of some of the variable stars in the field. I report on the discovery of a variety of newly-discovered variables, including Algol-type detached eclipsing binaries which are likely to consist of M-dwarf stars. Further study of these stars is strongly recommended in order to help constrain models of stellar structure at the very low mass end.

I conclude with a summary of this work in the context of other efforts being made in this field and recommend promising avenues of further study.

ACKNOWLEDGEMENTS

There are a number of people without whom I would not have been able to fulfil my greatest ambition and become an astronomer, and I would like to thank them here.

Firstly, I would like to thank my family and particularly my parents for their unwavering support, material and emotional, right from the begining. Their tolerance and patience especially in times of stress is and has always been an inspiration. Without their commitment I would not have made it as far as a Ph.D. I also appreciate my Father's efforts in proof-reading this thesis in three days flat!

I would also like to thank my supervisor, Keith Horne, for his help, support and patience during the course of this work. I am very grateful to him, to Andrew Collier Cameron, Ron Hilditch, Alan Penny and many others for sparing a great deal of time and effort explaining and answering my questions, often many times over. My thanks go to Jasonjot Kalirai for generously sharing his colour data on the NGC 6819 field. I am especially grateful for the travel opportunities to various conferences and observing trips, which allowed me to visit places I never dreamed of going to. In particular I would like to thank Tsevi Mazeh and the Astronomy group at Tel Aviv University and Wise Observatory who made it possible for me to observe there and who looked after me during my stay. I would also like to thank my collaborators in this project; Neda Safizadeh, David Mitchell, Andreas Quirrenbach, Jeff Cooke, David James and Yiannis Tsapras for gathering the data which made it possible and for their efforts and many insights into tackling this challenging task.

None of the work in this thesis would have been possible without seriously powerful computers and I would like to thank Roger Stapleton and Tim Lister who maintain the computer systems at St. Andrews. It is a thankless task which no-one ever notices until the computers go wrong, whereupon they complain. I would like to thank them for their efforts and their assistance during my many computer crises.

I would like to thank Maria McNamara for friendship and support through some difficult times.

Finally I would like to thank Tim Lister. Tim contributes so much practical help and advice towards my work on a daily basis it is difficult to imagine how I could have

completed it without him. On a personal level he has made my stay at St. Andrews the happiest years of my life and has been a tower of strength when the going got tough. I cannot thank him enough for his love, support and generous kindness, and I dedicate this work to him and to my parents.

"While I'm still confused and uncertain, it's on a much higher plane, d'you see, and at least I know I'm bewildered about the really fundamental and important facts of the universe." Treatle nodded. "I hadn't looked at it like that," he said, "But you're absolutely right. He's really pushed back the boundaries of ignorance."

Scientists at work (Terry Pratchett, *"Equal Rites"*)

CONTENTS

LIST OF FIGURES

LIST OF TABLES

CHAPTER 1

Introduction

1.1 Introduction

The stirring concept of the plurality of worlds, and the prevalence of life beyond the Earth, is an ancient and persistent one.

It found its first formal expression in the Greek philosophy of atomism in the 4^{th} and 5^{th} centuries B. C., espoused by Leucippus, Democritus and Epicurus (Dick 1998) among others. The latter postulated an infinite number of atoms, resulting in an infinite number of worlds. This worldview was taken for granted until the Earth-centred theories of Aristotle, which dictated the uniqueness of Earth, came to dominate western popular and religious opinion. Following the intense suppression of astronomical enquiry in the Middle Ages it would be more than one thousand years before the concept of worlds existing beyond our Solar System could be openly resurrected. When it finally emerged, in the 16^{th} and 17^{th} centuries, it was with advocates of the calibre of Descartes (1644) and Huygens (1698).

In modern times, the idea that planets should be a common feature of stellar systems has gained widespread support amongst scientists and the general public alike. Although conclusive proof of their existence has only come in the last decade, the modern history of planet hunting spans nearly sixty years.

Intricately involved in this history is that of the search for "brown dwarfs", the so-called failed stars at the very lowest end of the stellar mass function. This is necessarily the case as in many respects these objects have similar characteristics to planets – they do not produce energy by nuclear burning and so only "shine" in the infra-red from the

residual heat from their formation. They can also be expected as stellar companions and so are detectable using the same techniques. Furthermore, a meaningful threshold below which an object ceases to be a brown dwarf and becomes a planet has yet to be firmly established, so many of the objects mentioned here as planets may yet be brown dwarfs. I will adopt the threshold of ~ 10 M_{jup} for the maximum mass of a planet, recommended by Marcy et al. (2001b) and others, this being slightly below the deuterium burning limit ($\sim 12M_{jup}$, Burrows et al. (1998)).

In the following sections therefore, I briefly review the important advances made in these fields to date, both observational and theoretical, in order to 'set the stage' for the work that follows. For a more complete discussion of the history of these topics, I recommend two excellent books: Boss (1998) and Dick (1998). This leads naturally into a discussion of the planets/brown dwarfs found to date, their properties and those of their parent stars. I then move on to discuss the various techniques employed in the search and their various strengths and weaknesses to illustrate the usefulness of the transit technique used here in relation to other search methods.

1.2 A Brief History of Planet Searches

The first extra-solar planet (hereafter ESP) searches, mounted in the 1940's, looked for the astrometric signatures of planets causing their stars to 'wobble' slightly in the sky (see Section 1.5 for details of this technique). Reuyl & Holmberg (1943) have the distinction of being the first to claim a detection of a planet ten times the mass of Jupiter orbiting 70 Ophiuchi. Their discovery was quickly refuted by Strand, however, who also announced his own discovery of a planet around 61 Cygni (Strand 1943) using the same technique. These papers began a 50-year saga of claims and counter-claims for both planet and brown dwarf detections, all of which would be eventually discounted. The lack of extra-solar planets did not, however, prevent theorists debating the origins of planets; they simply had only the Solar System to explain.

The first truly scientific theory of planet formation originated with Pierre Simon de Laplace (de Laplace 1784) and the philosopher Immanuel Kant (Kant 1798). They postulated that the Solar System formed from a gaseous nebula into a single disc rotating about the nascent Sun, and from there split into rings similar to those of Saturn, which

coalesced into planets. While rather lacking in detail by today's standards, this was a real breakthrough. It went virtually unchallenged until the early 1900's, when Moulton (1900) argued that conservation of angular momentum would result in the star at the centre of the disc rotating far more rapidly than the Sun actually does. Together with Chamberlain, Moulton (1905) suggested instead that the planets were formed from a filament of material pulled from the Sun by a passing star. This was later refuted by Russell (1935), who found that the filaments would dissipate too quickly to form planets.

In this theoretical vacuum, von Weizsacker (1944) proposed a modified version of Kant and Laplace's nebula theory: the nebula was comprised of hydrogen and helium with a lesser fraction of heavy elements. The evaporating H_2 and He then carried away angular momentum, sparing the Sun from overly fast rotation. But while the nebula theory was widely adopted, it still lacked in detail, and theorists began to address the problem of creating planets from a rotating disc of gas and dust.

The first suggestion, put forward by Edgeworth (1949), continues to be widely debated today; the gravitational instability model. In this model, Edgeworth suggested that once the material had formed into rings about the Sun, it would consist of small lumps dubbed 'planetesimals'. If these rings were dense enough and cool enough, the planetesimals would begin to join together into gradually larger and eventually planet-sized bodies, pulled together by their own gravity. In regard to this model, Weidenschilling (1976) pointed out that the slower orbiting nebula gas might cause sufficient gas pressure to keep the dust in suspension, so that it never formed a thin central disc and so never reached sufficiently high densities for gravitational instability. Later models including viscosity overcame this objection (Cameron 1978), but the model still could not explain why the cores of the giant planets of the Solar System were apparently all the same size ($\sim 10\ M_E$).

One of the most important works on the subject was published in 1969 by Safronov and Schmidt (Safronov 1969); describing what has become known as the core accretion model. Safronov and Schmidt suggested that the dust in the Solar disc would form a thin disc in the centre of the gaseous disc under its own gravity, thereby increasing the dust density and leading to collisions in which the particles increase in size. This, they calculated, would produce roughly marble-sized objects in $\sim$ 1000 years. After this, the dust disc would be subject to gravitational instability, leading to the planetesimals becoming

asteroid-sized in only a few decades, while any objects greater than 10 miles across would self-gravitate and grow even faster. In this way, Safronov and Schmidt thought that Earth could have formed within $\sim$ 100 Myrs. In order to explain the gas giant planets, a planetesimal simply had to grow a little larger – to ~ 2 M_E – after which it would gravitationally attract gas as well as dust, thus acquiring an atmosphere, until the surrounding nebula ran out of gas. This theory explains why the giant planet cores of our Solar System are all similar in size. Mizuno (1980) showed that once a body reaches ~ 10 M_E it will attract a gaseous envelope. The one great drawback to this theory was the timescale it required to form the outer ice giants, Neptune and Uranus: $\sim$ 100 billion years, due to the expected lower density of dust in the outer reaches of the system. Similar formation scenarios were later independently put forward by Goldreich & Ward (1973), and by Cameron (1973).

These two models, the core accretion model and the gravitational instability model, have remained valid upto the present day, and the details continue to be hotly debated.

In 1980, Goldreich & Tremaine (1980) made an amazing suggestion – their models implied that a Jupiter-mass planet should spiral in or out of the system within 10,000 years, as its orbit would be physically altered by gravitational interaction with the disc. This concept would become central to planetary formation theories, but not until the first extra-solar examples were discovered.

In the event, the first hard evidence for extra-solar planet formation came from those stars which were thought to be the most well understood - the Infra-Red Astronomical Satellite (IRAS) discovered 'infra-red excesses' around some of the stars used in calibration, most famously Vega (Harvey, Wilking & Joy 1984). While many explanations were initially put forward, almost all were discounted, and the most likely explanation was found to be a disc of dust surrounding the stars, just as theory predicted. This was spectacularly confirmed by Smith & Terrile (1984), who used a coronagraph to image the immediate surrounds of β Pictoris and found a disc of radius $\sim$ 400 AU.

So after years of of pure theory, at last there was hard, undisputed evidence of pre-planetary discs. But where were the planets? Then came another observational breakthrough: Latham et al. (1989) discovered that HD 114762 displays radial velocity variations (see Section 1.5) as if it were accompanied by a planet in an 84-day period. This technique cannot ascertain the mass of the companion exactly, but a minimum possible mass, $M. \sin i$, of ~ 11 M_{jup} indicated the discovery of a likely brown dwarf. Several

similar claims were made on the heels of this discovery.

In 1991 Duquennoy and Mayor published 13 years' worth of radial velocity measurements of nearby solar-type stars (Duquennoy, Mayor & Halbwachs 1991 and Duquennoy & Mayor 1991). They found that single stars were rare, $\frac{2}{3}^{rd}$ of the sample having at least one companion, all of which were found to have elliptical orbits (unlike the planets of the Solar System) unless they were close enough to the primary star to have had their orbits tidally circularised. Significantly, 8 percent of Solar-type stars were found to have brown dwarf companions with masses in the range $M \sim 10 - 100$ M_{jup}. These were also found to have mostly elliptical orbits, which was thought to indicate a stellar origin.

But despite 50 years of effort, and a number of false starts, no conclusive evidence of extra-solar planets had been found by the early 1990's.

Then came a surprise from an unexpected quarter. Wolszczan & Frail (1992) identified very slight ($\pm$15 picosecond) but cyclic variations in the arrival times of the light pulses from pulsar PSR B1257+12. The precision of these measurements allowed them to distinguish the Keplarian orbital motions of *two* (and later more) separate Earth-mass planets orbiting the pulsar. The confirmation of these planets existing in such a hostile environment flew in the face of all the conventional theories of the time, yet it was the first planetary detection to be confirmed. More surprises were in store. The following year, Stauffer et al. (1994) announced the discovery of free-floating brown dwarfs in the Taurus molecular cloud. One of these objects was later found to have lithium present in its atmosphere, suggesting that the object had not experienced nuclear burning. This evidence further enhanced the idea that brown dwarfs are formed by the same process as stars, but never gain sufficient mass to sustain nuclear burning.

Then, at last, came the landmark discovery. Mayor & Queloz (1995) announced the detection of the first extra-solar planet orbiting a Sun-like star. This planet, its presence revealed by variations in the radial velocity measurements of its primary star 51 Pegasi, was found to have a mass $0.47/\sin i$ times that of Jupiter, but orbiting at a distance of only hundreths of an AU from its star. Burrows et al. (2000) predicted that a planet of this size must be a gas giant (as opposed to a 'supermassive' terrestrial planet). Such a massive gaseous planet at this tiny separation, which has caused all similar planets to be dubbed 'hot Jupiters', was unexplainable by all contemporary planetary formation theories. Boss (1995) had already showed that the disc was not cool enough for gas giants to form closer

than 4 AU from its star, and so this discovery triggered the revival of the orbital migration theory.

Mayor et al. were not the only group using the radial velocity technique to look for planets. Spurred on by their announcement, Marcy and Butler were quick to analyse their own data and produce more planet and brown dwarf candidates (Marcy & Butler 1996 and Butler & Marcy 1996). A number of groups have followed these examples, and many more planet detections followed on the heels of these discoveries, the radial velocity technique proving to be by far the most prolific at producing planetary detections to date. These exciting discoveries have opened an entirely new field of research, and re-written all the theories of star and planet formation.

The characteristics of all the extra-solar planets found to date (October 2001) are tabularised in Appendix A, Table A.1, and those of their host stars in Table A.2. I will return to an indepth discussion of their overall characteristics in Section 1.3, but the series of discoveries begining in 1995 have been punctuated with a number of examples, which have made particular contributions to our understanding of planetary formation, and which are worth highlighting here.

- Planets found in multiple star systems.

  Cochran et al. (1997) announced the discovery of the first extra-solar planet orbiting a member of a multiple star. The wide separation G-dwarf binary components 16 Cyg A and B are both very similar to the Sun, while the third component is a distant M-dwarf. The planetary companion to 16 Cyg B was found to have an $M.\sin i = 1.5$ M_{jup} and an orbital eccentricity of 0.634. At the time of discovery this was the lowest mass object to have such a high eccentricity, causing much speculation as to how much of an influence the other stellar components had had on the planet's orbital evolution. Interestingly, the planet with the highest *currently* known eccentricity, HD 80606b (e = 0.927) is also a member of a wide binary, but it is not yet clear whether this is the cause of the extreme eccentricity of the planet. For more details, see Naef et al. (2001a) and Section 1.4.

- Multiple planetary systems found.

  Until 1999, all the known extra-solar planets were singletons – only one planet was found per star contrary to the evidence of our Solar System and to theoretical predic-

tions, which held (and still hold) that multiple-planet systems are much more likely to form. The first $0.68/\sin i$ M_{jup} planet around υ Andromedae was announced by Butler et al. (1997). Then Butler et al. (1999) revealed evidence of two more planets, making this the first system other than our own where multiple planets were found. This immediately raised the issue of dynamical stability, and planet–planet interactions. By the Hill stability criterion, the system is stable unless $\sin i < 0.2$ – and the authors note that this is ruled out by Hipparcos astrometry. Numerical simulations then and since (see for example, Rivera & Lissauer 2000 and Jiang & Ip 2001) have indicated that the system is stable, but that planet–planet interactions stimulate oscillation in the eccentricities of the outer two planets; the innermost planet is considerably separated from the others and is not significantly involved.

- The first planetary transits observed.

The end of 1999 saw the dramatic discovery of the first extra-solar planetary transits. The hot Jupiter-type planet orbiting HD 209458 with a period of around 3.5 days was discovered by radial velocity measurements by Marcy and Butler's group. Once the orbit was sufficiently well established, Gregory Henry began photometric observations, and in Henry et al. (2000), published both the radial velocity results and photometric evidence of a partial transit event. *In the same volume*, Charbonneau et al. (2000) also published photometry of two full transit events, observed prior to the photometry of Henry. This photometry, combined with the radial velocity data, allowed Charbonneau et al. (2000) to perform a theoretical fit and for the first time derived the *true* mass of a planet to be 0.63 that of Jupiter, but with a radius of 1.27 R_{jup}. This was the final proof that the low-mass companions discovered by the radial velocity technique were indeed of planetary mass. It also revealed far more about this planet than was available for any other; the radius, and hence the density, specific gravity and not least, the orbital inclination. These data implied that the planet was a true gas giant (Burrows et al. 2000). Theory predicts that the higher radius is due not to the heat from the star causing the planet to expand, but rather retarding the usual contraction of the planet as it gradually loses its internal heat from its formation. This in turn put limits on how quickly the planet must have migrated (if that was how it formed) from outside the ice condensate limit to its present location. Furthermore, its has also been shown (Guillot et al. 1996) that the planet is stable against evaporation despite its proximity to HD 209458.

This discovery sparked off a huge flurry of observational effort. Söderhjelm (1999), Castellano et al. (2000) and Robichon & Arenou (2000) all analysed HIPPARCOS observations of HD 209458 and produced a significantly improved ephemeris, though the photometry of the 5 observed events was too poor to provide any more details. Ground-based observations by Jha et al. (2000) and Deeg, Garrido & Claret (2001) were made in multiple bandpasses: BVRIZ and Strömgren u,v,b,y respectively. With the observations of Jha et al. it was possible to break the ambiguity in the planetary radius caused by the orbital inclination (see Section 2) and determine that the planetary albedo is low. Deeg et al. were able to produce the a colour sequence of accurate limb-darkening coefficients for a single primary star.

Similarly multicolour observations by Brown et al. (2001) using the *Hubble Space Telescope* resulted in extraordinarily precise photometry, from which the planetary parameters and stellar limb-darkening were determined with unprecedented accuracy, and even put limits on the possibilities of satellites and planetary rings. Transits have been detected in spectroscopic observations, by Queloz et al. (2000a). The change in the line profiles in the stellar spectrum revealed that the planet orbits in the same direction as the star, and most likely in the equatorial plane of the star, which supports the migration scenario for this planet. Attempts have even been made to detect the 'exosphere' of HD 209458b (for example, Moutou et al. (2001)). This is the theoretically-predicted extended gaseous envelope around the planet caused by its proximity to the star. While this remains undetected, upper limits close to the theoretical predictions were possible.

- The first planet detected in an Earth-like orbit.

  By 2001 however, no Solar System analogues had been found. With the sole exception of ι Hor, all the planetary candidates outside the tidal circularisation radius were found to have large eccentricities, and many systems had Jupiter-mass planets in orbits well inside that of Mercury around the Sun. In particular, no planets were known with Earth-type orbits; planets with separations around 1 AU were all non-circular, and would pass out of their star's habitable zone in the course of one planetary year.

  Then recently, Butler et al. (2001b) announced the discovery of a planet with a 1.18 AU separation from HD 27442 with a measured eccentricity of only 0.058,

comparable with the Earth's 0.0167. Mayor's group have also recently announced[1] the discovery of a giant planet around HD 28185 in an orbit even more similar to Earth's, with a separation of almost exactly 1 AU, a period of 385 days and an eccentricity of 0.06. This planet orbits a G5-type star and is therefore constantly within its star's habitable zone. This leads to the exciting possibility of habitability; while the planet itself is a gas giant and an unlikely abode for life, there is always a chance of habitable moons (Williams, Kasting & Wade 1997).

Recently, Fischer et al. announced[2] the discovery of a second planet in the 47 UMa system. The orbits of this pair of planets, both of low eccentricity with radii of 2.09 and 3.73 AU, resemble those of Jupiter and Saturn. While any Earth-mass planets in closer, perhaps habitable-zone orbits cannot yet be detected, having massive planets at radii of a few AU is thought to spare the inner system much of the meteoritic bombardment immediately after planetary formation. This greatly increases the chances for developing life.

These developments are also a challenge for planetary formation mechanisms. With a number of examples of planets in circular orbits outside the tidal circularisation radius, it looks increasingly likely that any formation theory will have to explain both high- *and* low-eccentricity systems as natural products, or else explain why these stars plus Solar System planets are flukes.

- Possible evidence of planets engulfed by their star.

While theories of planetary migration are often discussed, it is not at all clear whether the planets follow the migration all the way through and are engulfed by the star, or else are stopped in their tracks some short distance away. Some evidence for the former hypothesis was recently put forward by Israelian et al. (2001), which reports the discovery of ^{6}Li in the atmosphere of the Solar-type star HD 82943. It is commonly expected that lithium is destroyed by the early stellar evolution, so the authors interpret its presence as having been acquired from engulfed planetary material. This hypothesis has found some support in the measured difference in lithium abundance between 16 Cyg A and B (Deliyannis et al. 2000), but these authors note that the expected accompanying enhancement in beryllium was not seen, arguing against this hypothesis. None of the authors had sufficient data to

[1]ESO Press Release 07/01

[2]http://www.berkeley.edu/news/index.html

confirm or rule out the engulfment hypothesis.

A coherent understanding of planetary systems in general, including our own, will only be achieved by exploring a wide range of stellar environments and types to provide and characterise a large sample of planets. From this database, meaningful analysis may be made to constrain theories of formation, as our detection techniques strive towards smaller masses at great radial separations from their stars.

1.3 Characteristics of Known Exoplanetary Systems

At time of writing, around 60 companions to Solar-type stars have been found with $M. \sin i \leq 10\,\mathrm{M}_{jup}$, and many people are now directing their efforts into determining the global properties of this group of objects, and the impact of these inferences on planetary and stellar formation theories. A recent review of this work was written by Perryman (2000), and I discuss the main results below.

1.3.1 The Mass Distribution

Any effort to determine the mass distribution of very-low-mass stellar companions is clearly hindered primarily by the $\sin i$ ambiguity affecting the vast majority of the mass estimates. As this represents a lower limit on the mass of the object, we cannot be sure that a given object is of planetary mass, and the situation is even more uncertain for the brown dwarfs, some of which are expected to have masses above the hydrogen burning ignition limit of $0.08\,\mathrm{M}_{\odot}$. The only exception is the one known transiting system, HD 209458, where the inclination i has been determined, and hence the true mass. Furthermore, due to the limited time for which the radial velocity surveys have been running, the detection of companions is restricted to those orbiting fairly close ($a < 2$ AU) to their stars (Butler et al. 2001a). Companions in longer-period orbits have not yet travelled sufficiently far around their star to produce a detectable signal. Nevertheless, a sufficient sample of objects now exists that various statistical techniques can be reliably applied to overcome this problem.

For reference, the $M. \sin i$ values for the planets given in Appendix A, Table A.1 are plotted in histogram and cumulative histogram forms in Figures 1.1 and 1.2. The plots

in Figure 1.1 include all the very-low-mass companions found around Solar-type stars by the radial velocity surveys, making no distinctions between brown dwarfs and planetary objects. Those in Figure 1.2 show the finer detail of the distribution at planetary masses. These figures do not include objects of highly uncertain mass or those objects found around pulsars or free-floating in open clusters.

The mass distribution of companions rises at low masses, down to about $M_p \approx 1\,M_{jup}$, where the sensitivity of the radial velocity technique begins to wane (Butler et al. 2001a). This implies that the distribution could rise even further at low masses once our techniques can probe this regime. The most striking aspect of these figures is the relative paucity of stellar companions with masses between $10 - 100\,M_{jup}$ orbiting close ($a < 2$AU) to their parent stars: the so-called "Brown Dwarf Desert". Any such companions ought to be easily detected by the current surveys.

Recently, a number of authors have attempted to derive the true mass distribution using a range of statistical approaches; see for example Mazeh, Goldberg & Latham (1998), Jorissen, Mayor & Udry (2001), Zucker & Mazeh (2001), and Tabachnik & Tremaine (2001). These works all agree with the existence of the Brown Dwarf Desert, concurring with Marcy & Butler (1998) and Halbwachs et al. (2000).

However, the theory is not universally accepted. Heacox (1999) and Stepinski & Black (2000) have criticised the emphasis placed on the mass distribution histograms like those in Figures 1.1 and 1.2. Stepinski & Black (2000) remark that for small sample sizes where there is reason to believe that the probability distribution function (or PDF) is skewed, histograms are unrepresentative of the true distribution. For this reason, both sets of authors attempt to infer the parameters of the true PDF from the empirical *cumulative* distribution function (CDF). Heacox (1999) do note a "change in trend" in the mass CDF occuring around $10\,M_{jup}$, but find that a function which ignores this structure fits the data sufficiently well that "no more structured fit is justified by the data". Stepinski & Black (2000) concur, finding that a single-object model with a continuous mass distribution fits the available data just as well as a model comprising two separate populations of planets and brown dwarfs. It appears that the number of very-low-mass stellar companions is insufficient to distinguish between these models and many more discoveries are required before any concrete conclusions can be drawn.

Gizis et al. (2001) have recently contributed an interesting perspective to this

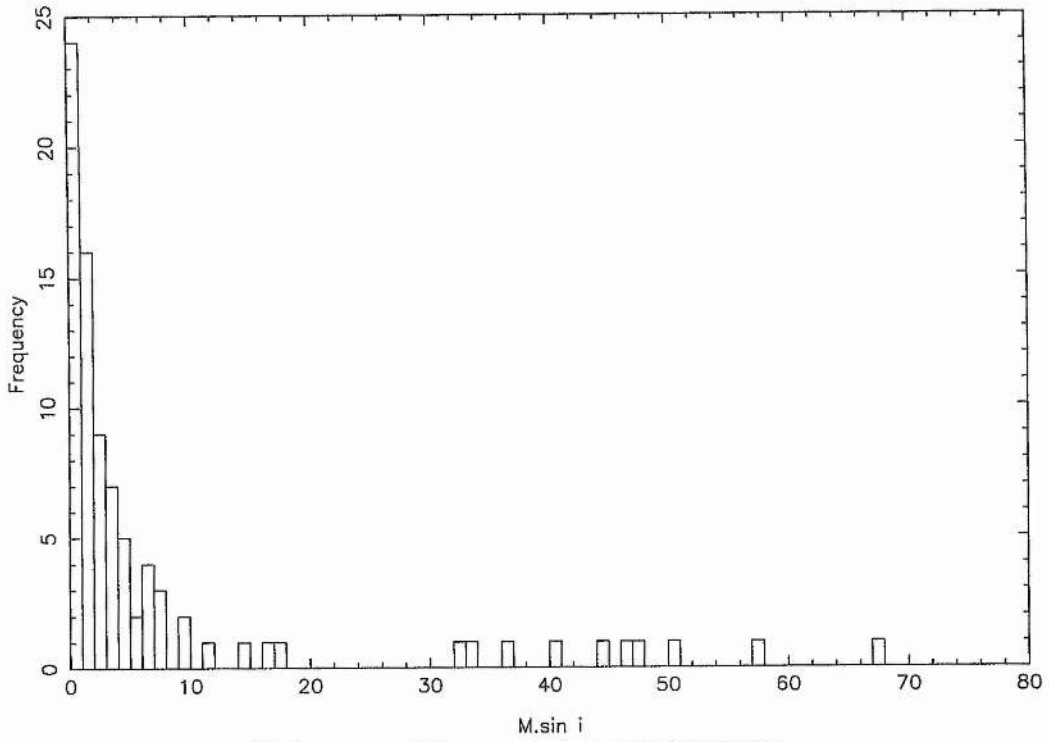

(a) Low-mass stellar companions mass distribution

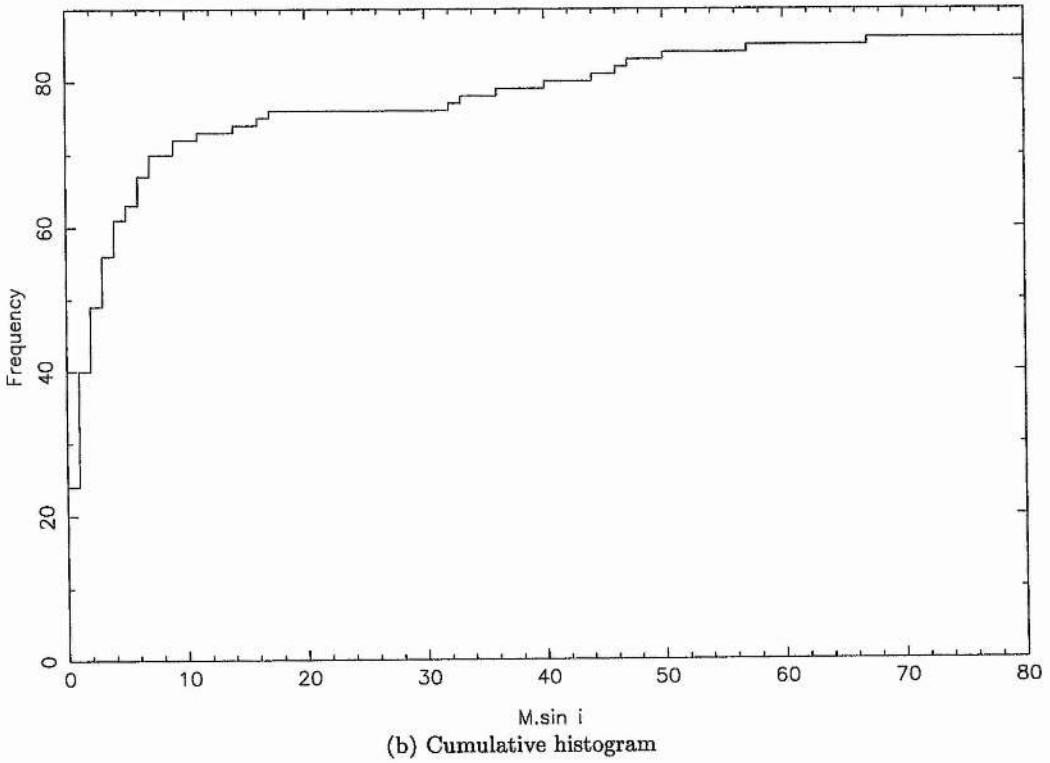

(b) Cumulative histogram

Figure 1.1: Histograms of the $M.\sin i$ values for the very-low-mass companions found around Solar-type stars to date

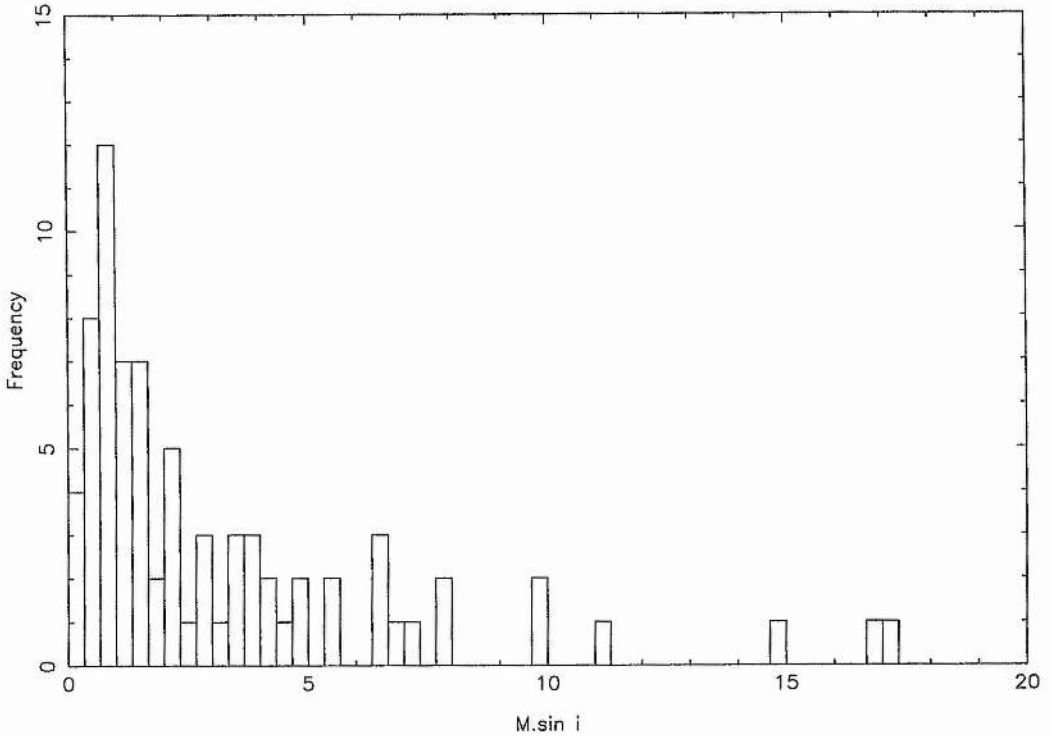

(a) Exoplanet mass distribution

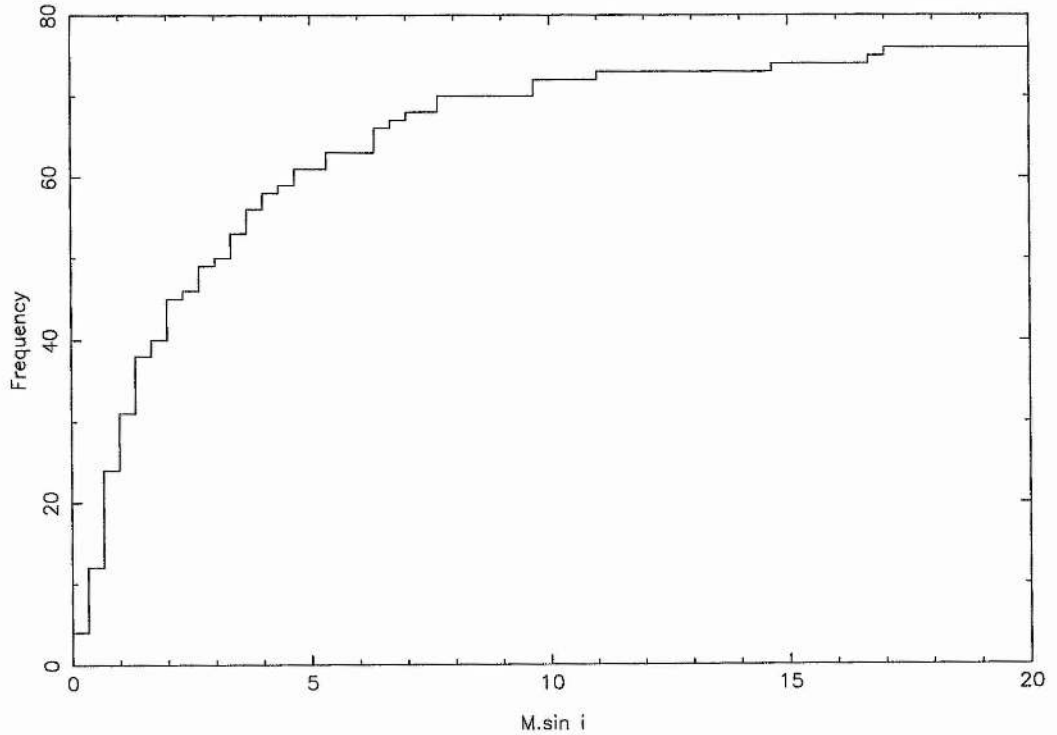

(b) Cumulative histogram

Figure 1.2: Histograms of the $M.\sin i$ values for the planetary mass companions found around Solar-type stars to date.

debate. They use 2MASS data to estimate the frequency of brown dwarfs companions at large ($a > 1000$ AU) separations, and find that they are not unusually rare in this regime. This work should be considered preliminary, being based on an extremely small set of example systems. Nevertheless, the authors further suggest that brown dwarf companion frequency could be a function of both separation and primary star mass, as the known examples of brown dwarf companions all orbit relatively massive companions.

1.3.2 Comparision of the Orbital Elements of Low-Mass Companions

Figure 1.3 illustrates the bias of the radial velocity technique towards small semi-major-axis orbits, a present restriction due to the relative youth of the high-precision surveys. Butler et al. (2001a) state that the discovery of planets at 5 AU (similar to that of Jupiter) are still a decade in the future. However, they further note that this sampling effect does not explain why there are apparently more planets within ~ 0.2 AU than between 0.2 – 0.6 AU, as any Jupiter-mass planets within this region would be apparent with less than the ~ 3 years radial velocity data currently available.

A number of authors, including Butler et al. (2001a) and Stepinski & Black (2000), have found a strong correlation between orbital period/semi-major axis and eccentricity. Figures 1.4(a) and 1.4(b) show these two distributions for comparison. Low-mass companions with periods greater than about 10 days seem to show high eccentricities. Stepinski & Black (2000) have shown that this is not a detection-threshold issue but a genuine property of the systems currently known. However, a number of systems have recently been discovered with circular orbits reminiscent of the Solar System (see Section 1.2). Whether a greater sample of objects will prove that circular orbits such as those in Solar System are common has yet to be seen.

It is also clear from Figure 1.4 that virtually all companions with separations less than ~ 0.1 AU have orbits close to circular. This is generally agreed to be due to tidal interactions with the parent star (Perryman 2000).

1.3.3 Comparision of Populations: Low-Mass Companions and Stellar Binaries

Heacox (1999), Stepinski & Black (2000) and Stepinski & Black (2001) performed comparisons of the orbital properties of low-mass companions with those of stellar binaries of

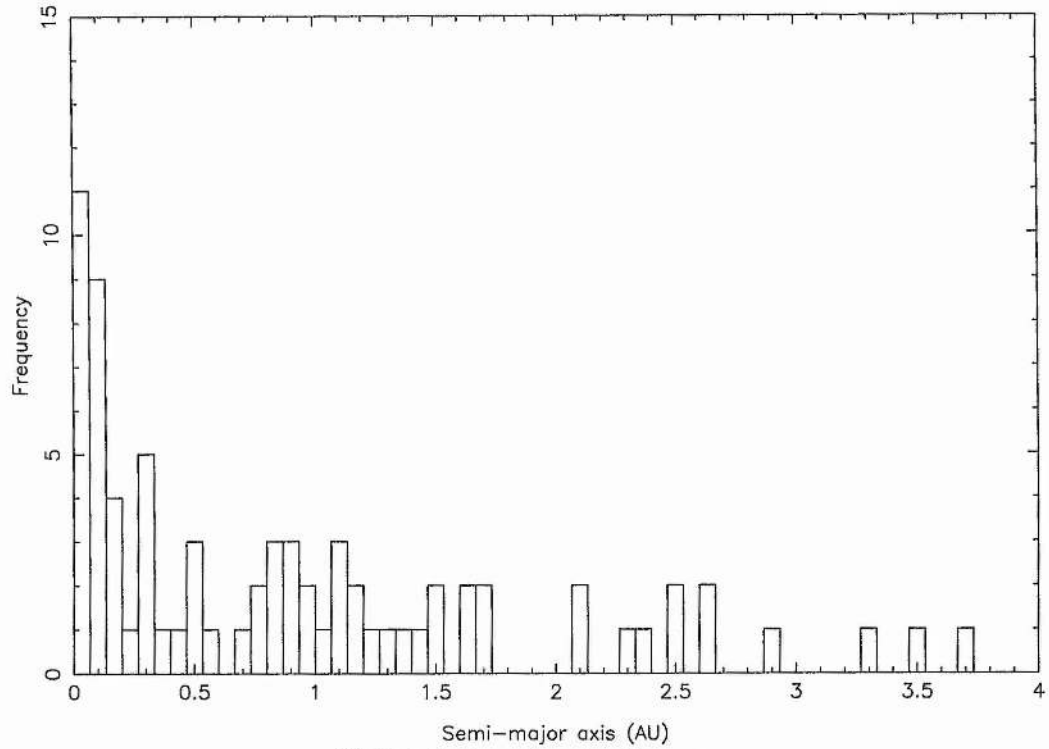

(a) Distribution of semi-major axes

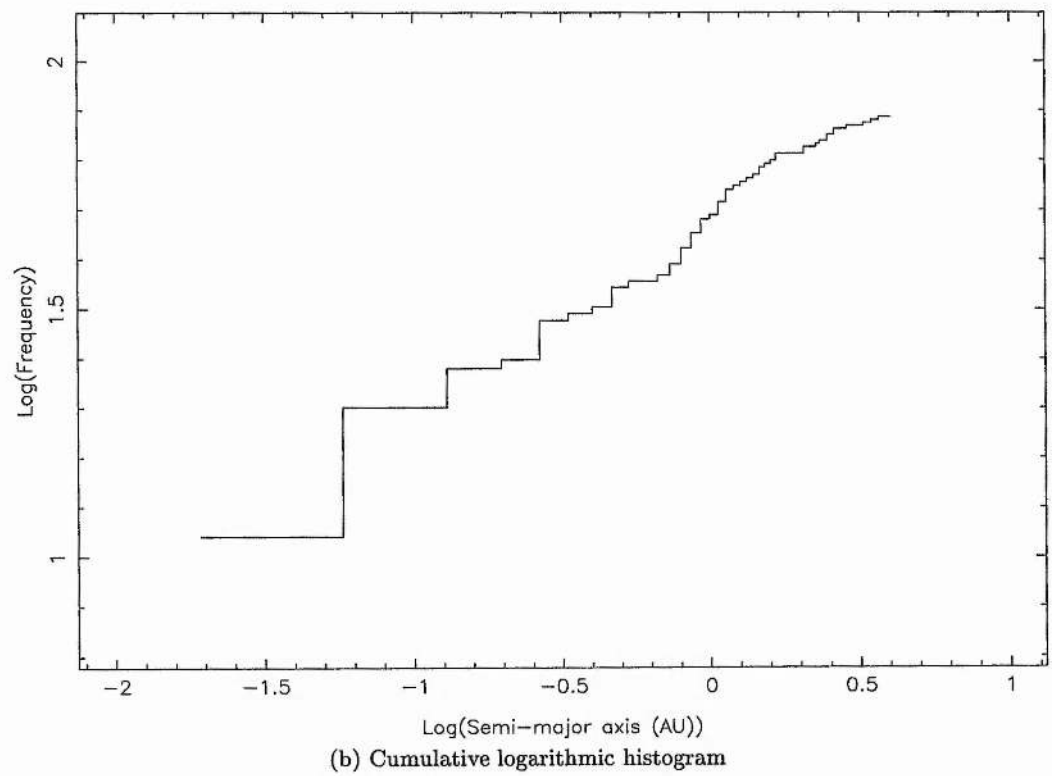

(b) Cumulative logarithmic histogram

Figure 1.3: Histograms of the distribution of the orbital semi-major axis of the very-low-mass companions found around Solar-type stars to date.

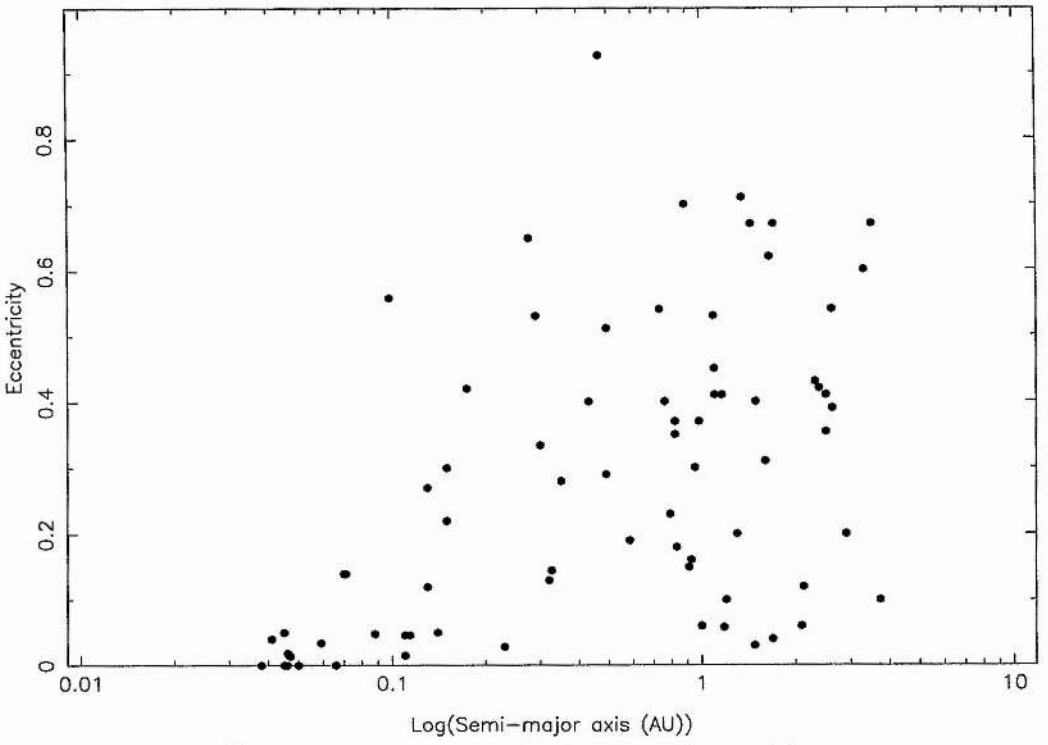

(a) Correlation between semi-major axis and eccentricity

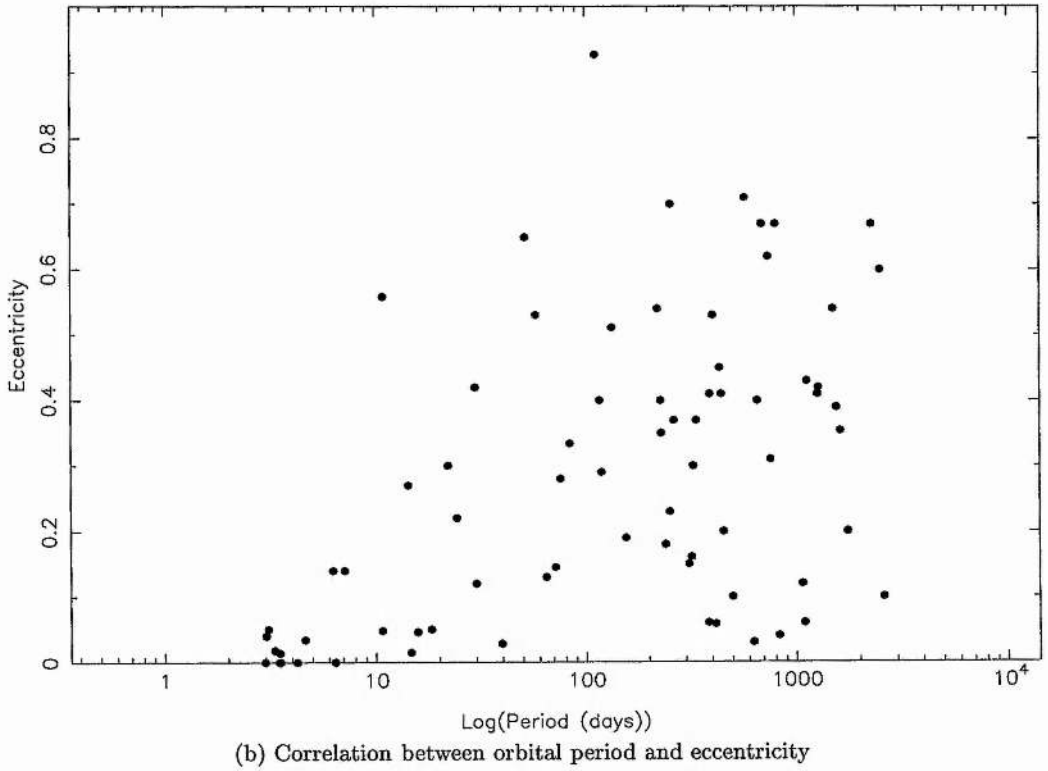

(b) Correlation between orbital period and eccentricity

Figure 1.4: Plots illustrating the correlation between period, semi-major axis and eccentricity in low-mass stellar companions.

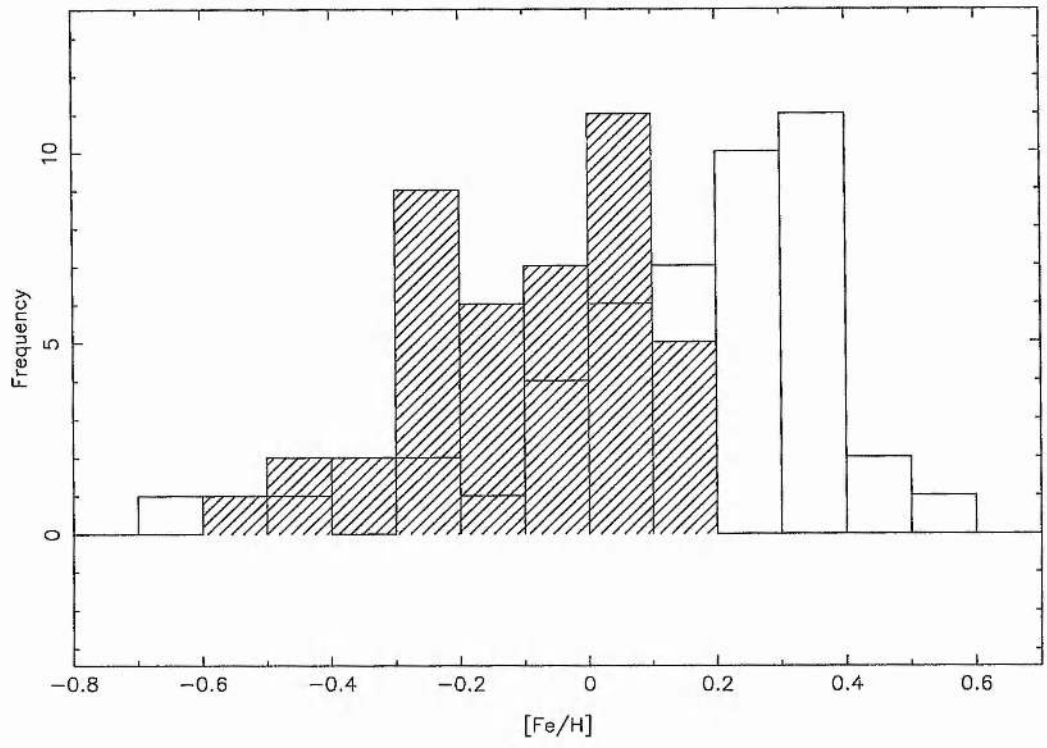

Figure 1.5: Histograms of the distributions of the metallicities of stars bearing 'hot Jupiter' type planets (clear) and stars without planets (hatched). Samples taken from Santos, Israelian & Mayor (2001).

similar spectral types and orbital scales. They found that for both populations, the orbital periods, semi-major axes, angular momenta (L) and binding energies (U) all follow an $f(x) \propto x^{-1}$ distribution (where $x = P$, a, L and U), while the eccentricities follow an $f(e) \propto e^{-0.5}$ distribution. They conclude that the two populations are statistically indistinguishable, showing no correlations of any orbital parameter with companion mass.

1.3.4 Properties of the Parent Stars

Table A.2 in Appendix A details the properties of the stellar hosts of the planets and brown dwarfs listed in Table A.1. A number of studies have attempted to identify some unusual characteristic which might distinguish planet-hosting stars from their single neighbours, and thus give a clue to the formation of the planets.

One correlation has gradually become apparent. Several studies, notably Gonzalez et al. (2001), and Santos, Israelian & Mayor (2001), have found that the metallicities of stars with 'hot Jupiter' type planets are significantly higher than a similar sample of

stars without planets. Santos, Israelian & Mayor (2001) recently clinched the issue: the authors compared a volume-limited sample of stars with planets found by the CORALIE survey with a sample of similar dwarf stars found by CORALIE to have constant radial velocity amplitude to within errors. Figure 1.5 shows the metallicity distributions for the two populations analysed by Santos, Israelian & Mayor (2001). They measure the mean metallicity of field stars to be -0.10 $\pm$ 0.18 while that of the planet-bearing stars was found to be +0.15 $\pm$ 0.23, where the errors represent the RMS scatter in the distributions. It was also determined that the metallicity index of the parent star has no correlation with the planetary orbital parameters. Laughlin (2000) and Murray & Chaboyer (2001) both note possible evidence for a metallicity increase with stellar mass for planet-bearing stars. This is currently contested by Santos, Israelian & Mayor (2001) (see Section 1.4.2).

1.4 Planet Formation

So what light do these discoveries shed on how planets formed? I will leave pulsar planets out of this discussion, as it is generally thought that they form by an entirely separate mechanism after the supernova (see Podsiadlowski (1995) for a review of the most likely scenarios). The details of the process(es) by which planets form around Solar-type stars are still hotly debated but are thought to fall into the following broad phases.

1.4.1 The Modern Paradigm

- The Collapsing Nebula Phase

  All modern theories begin with a cloud of gas and dust, though the exact proportions vary from model to model. A region of the cloud with a slight overdensity (caused by a shockwave for instance) can result in the gravity of the mass overcoming the thermal pressure of the region, triggering a collapse. A rotating cloud will collapse to form a flattened system due to angular momentum, which undergoes fragmentation to form many protostars, often in binary or multiple systems (Boss 1986).

- The Formation of the Protostar and the Solar Nebula Phase

  The cloud material not immediately taken up by the formation of the star will form a thin disc rotating around it. The radius of this disc is of the order of 100 AU – this part of the paradigm is supported by observations of dusty discs around a number

of young T Tauri stars – and is expected to take about 10^5 – 10^6 years to form. The gravity of the protostar causes an infall of material from the disc, which in turn compresses the object, causing it to heat up until nuclear burning begins in the core on timescales of 10^5 – 10^7 years. The disc material is replenished from the rest of the surrounding cloud and a redistribution of mass and angular momentum results in a centrifugally supported 'Solar Nebula'.

- The Formation of the Dust Disc

  The next phase occurs as the dust grains in the disc, which start out $\sim 10\,\mu$m in size, undergo collisions with other dust grains and begin to grow while the dust is still "in suspension" in the gas. As the dust grains in the disc continue to grow they settle gravitationally into a dust disc in the midplane of the main disc. This allows an important increase of dust density, and hence collision rate, allowing the grains to grow more rapidly. At this stage, the average particle size is thought to be 0.01–10 m. Over the next 10^4 – 10^5 years these particles grow to ~ 1 km in size.

- The Formation of Planetesimals and Terrestrial Planets

  Gravitational interaction between these planetesimals can cause orbital changes, leading to further collisions. If a sufficient mass of planetesimals is present in the disc a runaway accretion process ensues whereby the planetesimals grow rapidly by self-gravity. By this process, terrestrial-sized planets are produced on timescales of 10^7 – 10^8 years.

- The Formation of Gas Giants

  A threshold is reached once a protoplanet reaches ~ 15 M_E in size. It then has sufficient gravitational pull to start accreting gas from the surrounding disc which is only halted when all the gas within the planet's gravitational grasp is exhausted, causing an annular gap in the disc. As the disc is expected to dissipate within 10^7 years, gas giants must logically form prior to this. Furthermore, they must form beyond the so-called "snow-line": the radius at which the temperature is low enough to allow the required volatile materials to condense to liquids/solids (Boss 1995). This produces additional material which increases the rate at which the planet core can reach the critical threshold, allowing the gas giants to form quickly, before the gas dissipates.

- Orbital Migration

For these reasons, gas giant planets are not generally thought to form close to their parent stars, which made the discoveries of 'hot Jupiters' all the more surprising. Some form of orbital migration is usually invoked to explain these planets, and a number of different possibilities have been suggested. Any form of migration would in all likelihood wreak havoc for any smaller planets forming inside the giant planet's initial orbital radius.

Planet–Gas Disc Interaction

One of the most popular theories, initially suggested by Goldreich & Tremaine (1980) and expanded by Lin & Papaloizou (1986) and others, involves the interaction of the planet with the surrounding disc from which it formed. The presence of the planet disturbs the disc, causing spiral density waves. The disc beyond the radius of the planet carries angular momentum away from it, while the inside disc loses angular momentum to the planet. From this stage, there are two possible outcomes. In type I migration, the disc response is linear, and the torque from the outer disc overcomes that from the inner disc, causing the planet to move rapidly inwards on timescales of $\sim 10^4$ years for a 10 M_E planet from 5 AU. Type II migration relies on a non-linear disc response, where the the tidal torques exceed the viscous torques internal to the disc. In these circumstances, an annular gap forms in the disc at the radius of the planet which reduces the accretion rate. If the planet is of less mass than the surrounding disc, then inward migration occurs at the viscous evolution timescale of the disc. See Nelson et al. (2000) for a more detailed discussion.

Planet–Planetesimal Disc Interaction

Alternatively, migration may similarly occur if the planets interact with a disc of planetesimals (Murray et al. 1998). This model hypothesises that the gas giants form beyond the snowline as usual. Migration occurs after the formation of an annular gap at the planet's radius, and the model presumes that most of the material has formed into planetesimals. The required exchange of angular momentum between the disc of planetesimals and the planet occurs when the planet's gravity causes interaction with planetesimals in resonant orbits inside the planet's orbital radius. The interaction induces chaotic perturbations in the planetesimals orbit which eventually crosses that of the planet. Gravitational interactions lead to the planetesimals colliding with the star or planet, or else being ejected from the system entirely.

Migration is halted when the local density of planetesimals falls, or when a large

fraction of the planetesimals collide with the star. The limitation of this theory is that it requires a very large mass of planetesimals to cause migration over large distances.

Planet–Planet Scattering

A further theory suggests that migration can occur without the presence of a disc. Rasio & Ford (1996) found that gravitational interactions between a system of two or more planets can cause the planets to transfer into closer orbits, often with large eccentricities similar to those observed in known planets, particularly if one of the planets is ejected.

- Stopping Orbital Migration

The rate of orbital migration is proportional to the orbital radius. However, planets have been observed in apparently stable orbits with very small orbital radii. This suggests that the inward migration can be stopped, or at least staved off long enough for the disc to dissipate.

There are several suggestions, which I briefly summarise below:

Planet–Planet Interactions

As part of the planet-planet interaction mechanism, Rasio & Ford (1996) hypothesised that migration might be stopped if a planet was scattered into an orbit with a small periastron distance. Tidal interactions with the star would then circularise the orbit.

Stellar Tides

Lin, Bodenheimer & Richardson (1996) theorised that the planet will spiral in towards the star on a relatively circular course. Once a planet has achieved an orbit with a small periastron radius, tidal friction can cause the transfer of angular momemtum between the spin of the star and the planetary orbit resulting in the outward migration of the planet. If this rate of gain of angular momentum equals that lost to the disc, the orbit will be stabilised. However, the star will continue to accrete the inner disc material. Once this reservoir is gone, the balance in angular momentum transfer will be lost unless the rest of the outer disc has dissipated by this time. If this is the case, the planet could be left in a very close, circular orbit about the primary. Ward (1997) suggested a variation on this theory, pointing out that even if protoplanets are too small to open an annular gap, they might still undergo Type

I migration. Once in short-period orbits and within in the inner edge of the disc, these protoplanets could then accrete to form a larger body, like the 'hot Jupiters' observed. The orbit of this body would gradually circularise as before.

Magnetic Field–Gas Interaction

Alternatively, Lin, Bodenheimer & Richardson (1996) suggested that the star's rotating magnetic field could clear annular holes in the hot gas disc around the star by causing the gas to flow along the field lines onto the star or away from the centre of the disc. If a sufficient gap around the star is caused, the planetary migration could stop after the radius of the inner disc, as the inward torques become negligible. However, this mechanism has trouble explaining planets orbiting at 0.1–0.2 AU, too far out to be affected by their star's field.

Planet to Star Mass Transfer

Trilling et al. (1998) pointed out that the planet could lose mass through its Roche lobe during its inward migration. Mass transfered from planet to star would cause the planet to move outwards. If the planet's orbital radius is equal to its Roche radius then the forces moving the planet inwards will balance the outward forces, and migration would be halted. If the planet has sufficient mass to maintain this mass transfer until the disc has dissipated, then a close, stable orbit may result.

However, there is some evidence that for some planets, the inward migration was inexorable. HD 82943 was found to have ^{6}Li present in its atmosphere (Israelian et al. 2001), which is thought to be quickly destroyed by stars of this spectral type (G0). Therefore, it is possible that the lithium came from a planet that got so close that it was torn apart by its star and the material engulfed. Also, a considerable difference has been found in the iron and lithium abundances of the otherwise very similar pair of dwarf stars 16 Cyg A and B, which could be due to the same process. As yet, there is insufficient evidence to draw firm conclusions.

1.4.2 Challenges for the Modern Paradigm

Much of the paradigm described above has not been established in great detail as yet, for instance the exact fragmentation mechanism by which stars form. Nevertheless, the last

decade's discoveries of extra-solar planets have revealed a number of problems, which I will briefly discuss here.

One of the most conspicuous problems with current formation theories lies in the unexpectedly large range of eccentricities observed for all planets outside the tidal circularisation radius of the star. It is expected that planets forming within a dusty gaseous disc would have circular orbits (de la Fuente Marcos & de la Fuente Marcos 1997). Some migration mechanisms do allow for the development of high eccentricities (planet-planet scattering for instance), but generally, they are not expected. There have been a number of theories put forward to explain these observations within the current paradigm:

- Planet-Planet Interactions

  In numerical simulations of the evolution of planetesimals, such as those by Levison, Lissauer & Duncan (1998), it has been found that planet-planet scattering is the chief cause of large eccentricities. Many interactions were found to lead to planetary ejections. This has been put forward as a likely explanation of the orbital parameters of the υ And multi-planet system (Butler et al. 1999).

- Planet-Accretion Disc Interactions

  Artmowicz (1993) investigated in detail the expected evolution of planetesimals in the Solar nebula, and found that the eccentricity evolution of planetary-mass bodies is dominated by interactions with the nebula via Lindblad resonances, and is increased by planetary close encounters and/or distant N-body resonances.

- Resonant Orbits

  Numerical simulations by Snellgrove, Papaloizou & Nelson (2001) and Armitage et al. (2001) indicate that pairs of planets in resonant orbits, such as those of Gliese 876 where the period of one is a near multiple of that of the other, can cause the eccentricities of the planets to grow.

- Stellar Binaries

  The discovery of a planet around 16 Cyg B, a member of a wide stellar binary, triggered speculation as to whether the stellar companion had anything to do with the planet's eccentricity of 0.63, the highest known at the time. Mazeh, Krymolowski & Rosenfeld (1997) found that, although the tidal forces exerted by the companion star are small, they can cause modulation of the planet's eccentricity (between ~ 0.2

– 0.8) over long periods of time. They also found the amplitude of the modulation to be strongly dependent on the angle between the orbital plane of the stellar binary and that of the planet. These findings were supported in work by Holman, Touma & Tremaine (1997).

- Stellar encounters in young clusters.

  Alternatively, de la Fuente Marcos & de la Fuente Marcos (1997) suggested that the high eccentricities could be caused by multi-star interactions in the open clusters in which the planetary systems formed. The predominant mechanism was found to be a four-body interaction between a planetary system and two single stars. One of the single stars usually gets ejected, carrying with it excess energy therefore allowing a hierarchical system to form. The momentum transfer of this event enables the planet to take on an eccentric orbit.

However, the current paradigm is applied solely to planetary objects. Conventional wisdom holds that brown dwarfs, by contrast, are the very-low-mass end of the stellar Initial Mass Function and as such form by fragmentation of the primordial cloud in the same way as stars.

The analysis conducted by Heacox (1999) and Stepinski & Black (2001), however, showed that in terms of orbital parameters, the populations of planetary candidates, brown dwarfs and stellar binary companions are indistinguishable. On this basis, Heacox (1999) recommended that the formation paradigm be reconsidered, and that the assumption that planets and brown dwarfs are separate classes of objects should be challenged. In qualification, the author notes that the similarities between the distribution of orbital parameters will probably be modified by orbital evolution.

On the other hand, a number of examples of long-period planetary systems with circular orbits have recently been discovered. This, combined with our Solar System, may mean that the suggested formation mechanisms will have to explain *both* high- and low-eccentricity systems.

The existence of two populations of low-mass objects appears to be supported by the evidence of the Brown Dwarf Desert. However, once again, statistical studies by Heacox (1999) and Stepinski & Black (2000) have shown that it could be a feature of the low-number statistics.

One feature of the exoplanet population that is not disputed is the frequency of high-metallicity stars with short-period giant planets. Murray & Chaboyer (2001) point out that this may be partly due to experimental biases. However, they conclude that it cannot fully explain the observed metallicity difference in the populations. The explanation for the difference, however, is not so easily agreed upon. There are two opposing theories:

- Primordial metallicity: This theory supposes that stars with planets form from clouds with intrinsically higher metal content. The higher the cloud's percentage of high-Z material, the theory goes, the more likely it is to form protoplanets, and hence short-period planets.
- Pollution theory: Alternatively, systems forming short-period planets might enrich their star's atmosphere as a natural by-product of the process. This could occur in several ways: (1) by the complete inward migration of metal-rich planets via disc interaction, (2) by the scattering of metal-rich planets onto the star by planet-planet interactions or (3) by the accretion of disc material onto the star in the form of planetesimals, comets, etc.

Perhaps the most tempting theory – that planets have migrated all the way to the star and been engulfed – could explain the evidence of ^{6}lithium in the atmosphere of the main sequence star, HD 82943 (Israelian et al. 2001). This element is expected to be destroyed during a star's pre- and main sequence lifetime. A number of authors have investigated the chemical abundances of stars with planets compared to a 'control' group of similar stars with no planets to investigate whether the atmospheres of stars with planets have been replenished with ^{6}lithium. Gonzalez & Laws (2000) for instance found that stars with planets tend to have less lithium, yet Ryan (2000) found no evidence of a difference, and criticized the previous author's choice of comparison field stars. Once again, the twin, Solar-type stars of 16 Cyg A and B are a useful test case, since these very similar stars presumably formed in a similar environment. Laws & Gonzalez (2001) found that 16 Cyg A has an enhanced metallicity relative to 16 Cyg B: $\Delta[Fe/H] = 0.025 \pm 0.009$, on the basis of which the authors favour the 'pollution' theory. Deliyannis et al. (2000) report a lithium enhancement seen in 16 Cyg A relative to B but could neither prove or disprove the slight enhancement of beryllium that would be expected if the pollution theory were correct. Unfortunately, the evolutionary processes which are thought to destroy the

primordial lithium in stars are not well understood (see a discussion by Deliyannis et al. 2000), so this is not a very conclusive test.

Laughlin (2000) and Murray & Chaboyer (2001) both note a possible positive correlation between metallicity and stellar mass. They both agree that this is most likely to be due to the accretion of between 6.5 and 30 M_E of material after the gaseous disc phase of formation has finished. Santos, Israelian & Mayor (2000) on the other hand, while agreeing that planet-hosting stars are metal-rich, finds no evidence of a relation between metallicity and stellar mass, and concludes that the metallicity difference cannot be explained by a "simple" pollution mechanism, favouring the primordial theory.

The one conclusion that can safely be drawn from this discussion is that the current sample of exoplanet systems is woefully small. Many more discoveries of new systems are required to reveal the full variety of planetary systems.

1.4.3 Planetary Atmospheres

The first theoretical predictions about the nature of exoplanet atmospheres were made prior to their discovery (for example, Burrows et al. (1995)), based on observations of the atmospheres of Solar System planets. Since the discoveries of the remarkable variety of real planets, these models have been modified and updated to include the strong heating effects of a star in close proximity. The models constructed based on the known planetary systems are now being used to determine their atmospheric structure, radii, equilibrium temperature, and luminosities, both reflected and emitted. It is also possible to determine the colours and spectra of the planets, raising the exciting possibility of measuring the atmospheric constituents of a distant planet. These important results and predictions ought to be testable by new experiments planned for the near future.

Significantly, Guillot et al. (1996) showed that even 'hot Jupiter' type planets have a sufficiently strong gravitational pull to hold onto their gaseous atmospheres against the evaporation caused by the star's heating, indicating that such planets are reasonably long-lived (providing their orbits are stable).

Atmospheric modelling has also revealed much about the planet's evolution. They show that, if a planet is far enough away from its host star that it is not substantially heated by it, the planet's temperature decreases and the planet evolves with a constant

radius. The models imply that the maximum radius that a gas giant can achieve occurs at a mass of about 4 M_{jup}; greater mass planets will have smaller radii because the corresponding increase in the planet's self-gravity requires electron degeneracy pressure to support it. If the planet does suffer significant heating by its host, the planetary radii is expected to be correspondingly larger. This is thought to be because the planet has migrated close to its star sufficiently early in life that the heat retarded the contraction that the cooling planet would otherwise undergo (Burrows et al. 2000).

The large range of temperatures that are expected of the known exoplanets (200 K – 1500 K) is considerably different from the comparable gas giants in our Solar System. It is therefore expected that the exoplanets will have correspondingly different atmospheric structures and composition, and hence, spectra. Accordingly, Sudarsky, Burrows & Pinto (2000) have defined 4 classes of gas giant exoplanets, based on their expected albedos. This classification will be important for experiments planning to observe planets by direct imaging and those attempting to obtain atmospheric spectra. Seager & Sasselov (1998) and Seager, Whitney & Sasselov (2000) have predicted reflected lightcurves and polarisation curves for some exoplanet systems, comparing highly irradiated 'hot Jupiters' to planets in longer period orbits.

1.4.4 Frequency of Extra-Solar Planetary Systems

Until very recently the age-old debate about the existence of other planets was still open. Now we know they're out there. But just how common are they?

The most prolific discoveries by radial velocity measurements imply that ~ 1 percent (Vogt et al. 2000) of all Solar-type stars harbour planets within a radius of about 4 AU of the star. Unfortunately, these surveys have not yet run for long enough to shed much light on the frequencies of planets further out, or of lower-mass planets.

The only other experiments which can currently draw any conclusions on these classes of planets are microlensing surveys, some of which have been running for ~ 10 years. As I will explain in Section 1.5, this technique is (theoretically) sensitive to planets of *any* mass with orbital radii similar to their star's Einstein radii. None of these surveys have produced an uncontested planetary detection, though there have been a number of suggested 'discoveries'. Albrow et al. (2001) have therefore been able to infer that less

than a third of their typically ~ 0.3 $M_\odot$ target stars have Jupiter-mass companions with orbital semi-major axes between 1.5–4 AU.

In an interesting recent development, Sahu et al. (2001), searching for microlensing events in the globular cluster M 22, discovered 6 mysterious, un-time-resolved events which they interpreted to be due to microlensing events by free-floating planetary-mass objects in the cluster. If this is the case, it implies that these planets account for ~ 10 percent of the cluster mass. However, Gaudi (2001) and de la Fuente Marcos & de la Fuente Marcos (2001) both conclude that if these were microlensing events they are unlikely to be caused by planets, bound or free-floating, in M 22 itself. Such an explanation would require the planet population of M 22 to be unfeasibly large as judged by present observations and theory. Both papers suggest that the events were either microlensing events caused by a massive, dark cluster of planets along the line-of-sight to M 22, or else were simply not microlensing events. Hopefully the nature of these puzzling events will be resolved by further observations.

1.5 Detecting Planets

Everyone attempting to detect new extra-solar planets is confronted by the same problem: even the largest planets are small, faint and a long way away. Undaunted, several techniques have been employed by various groups that exploit the known effects of the planet's presence on the host star. All have their own strengths and weaknesses, and I describe each technique briefly below and discuss the contributions made by it, in order to put the current work in its proper context.

1.5.1 Direct Imaging

The most obvious way of finding planets – by taking very high resolution images of suitable stars and their immediate surrounds – is rendered very difficult by the extreme star/planet brightness ratio and the small separations involved. To quote an example used by Marcy & Butler (1998), the magnitude of a Solar-type host star at a distance of 10 pc is $V = 5$ mag, while the magnitude of a Jupiter-analogue planet in orbit around it would be $V = 27$ mag, and the two objects would be separated by only $0\farcs5$. This is currently beyond

ground-based telescopes, for which the atmospheric seeing and the exozodical light are the limiting factors. The situation is much improved by observing in the infra-red, where the star/planet flux ratio is only(!) $\sim 10^{-4}$ at 20–100 μm. This is due to both a lower flux from the star and the residual thermal radition from the planet from its gravitational contraction. Unfortunately, the currently achievable spatial resolution in the thermal IR is of the order of $1\farcs0$.

A number of projects planned for the future promise to deliver the required resolution. From the ground, the Keck and Very Large Telescope (VLT) interferometers could be used to for high-resolution IR imaging. Coronagraphic adaptive optics presents one way of countering the detrimental seeing, and are currently under development (see for example Woolf & Angel 1998). Alternatively, a dark-speckle (Labeyrie 1995) IR camera on the Next Generation Space Telescope should produce direct detections of Jupiter-sized planets. In the future, planned IR space interferometers such as the Terrestrial Planet Finder TPF (NASA, Beichman 1996) and *Darwin* (ESA, Penny et al. 1998) will be able to detect even Earth-mass planets and perform analysis to detect the presence of life-sign molecules such as oxygen, ozone and methane.

1.5.1.1 Reflected Light Detection

An alternative approach to detecting light from 'hot Jupiter' type planets has been pioneered by Collier Cameron et al. (1999) and Charbonneau et al. (1999). In this approach, a series of high-resolution spectra are taken of the system, timed to coinside with the planet presenting its maximum observable phase from Earth (that is, when the planet reflects the maximum light from the star). By carefully modelling and removing the star's spectrum from the observations, the remaining data should contain the faint copy of the star's spectrum reflected off the planetary atmosphere. These spectral lines will appear red- and blue-shifted as the planet moves around its orbit. Moreover, superimposed on this spectrum will be the planet's own absorption spectrum, revealing much about its composition and albedo if the two can be clearly distinguished.

Both Cameron et al. and Charbonneau et al. have observed τ Boötes in this way. While neither were successful in clearly detecting the reflected spectra, the technique was used to place reasonably stringent limits on the planet's geometric albedo.

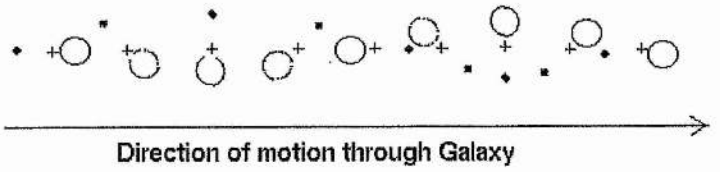

Figure 1.6: Illustration of the reflex motion of a star due to a companion planet, as seen by astrometric measurements.

1.5.2 Pulsar Timing

The first technique to produce an undisputed planetary detection by Wolszczan & Frail (1992) was that of pulsar timing. While wholly unexpected, this remains the only method to have discovered Earth-mass bodies outside our Solar System, owing to the extreme precision of timing achieved. The reflex motion of the pulsar due to the orbiting planet causes slight ($\pm$15 picosecond in the case of PSR B1257+12) but periodic variations in the arrival times of the light pulses from the star, due to the increase/decrease in the distance the pulses have to travel.

This is a powerful technique, able to detect planets of all sizes, even down to the largest asteriods (Wolszczan 1999)! The limitation of this method, however, is clear – it can only be applied to millisecond pulsars, which while fascinating objects in their own right, are unlikely to form planets in the same way as Sun-like stars (Podsiadlowski 1995) and are unlikely to harbour abodes of life "as we know it".

1.5.3 Astrometry

The astrometry technique also relies on the reflex motion of the star caused by the planet's orbital motion, but can be applied to any star. As shown in Figure 1.6, if the inclination of the planets orbit approaches zero (that is, the orbit appears to be in the plane of the sky), then over time as the star moves around the galaxy, it will move sinusoidally instead of in a straight line.

This "wobble" is proportional to the orbital radius and planetary mass, and inversely proportional to the Earth-star distance. Using the same example as above for comparision,

the Jupiter-analogue planet would produce a wobble only 0.5 milliarcsec (mas) in amplitude. The advantage of this technique is that it is sensitive to larger planets at greater radii (10–30 AU) than commonly surveyed by other methods. Furthermore, it can measure the true planetary mass and orbital inclination, in contrast to the more common radial velocity technique (see Gatewood 1987 for a review of this method). Unfortunately, the main disadvantage of this technique is the length of time required for the tiny amplitude wobble to manifest itself sufficiently to provide a concrete detection. Astrometric surveys require decades of painstaking work to gather sufficient data.

This was the first technique to be employed in the search for exoplanets, but while a number of claims of detection have been made (see Section 1.2), none have been corroborated. In part, this is due to the length of time necessary to provide confirmation. Gatewood (1987) demonstrated that it is possible to make ground-based astrometric measurements to an annually averaged precision of 1 mas. This precision could improve with the use of instruments such as the Multichannel Astrometric Photometer instrument on Keck II, and a further improvement to 20 μas could be achieved by using both Keck telescopes as an interferometer.

A number of space missions are currently being planned in NASA and the ESA. The NASA Space Interferometry Mission (SIM, Unwin, Turyshev & Shao 1998) aims for 4 μas measurements for stars down to 20^{th} magnitude. This mission is expected to find Neptune-mass planets within 5 AU of any star within $\sim$ 10 pc. The ESA mission, Gaia, plans to provide astrometry and radial velocities for one billion stars over a 4 year period. Sozzetti et al. (2001) discuss the planet-finding capabilities of this mission, which aims for $\sim$ 10 μas astrometry for stars brighter than 12^{th} magnitude. It should be able to detect single Jupiter-mass planets with orbital periods between 0.5 and 11.8 years for any Solar-type star within 60 pc.

1.5.4 Microlensing

The only other technique that can expect to find Earth-mass planets from the ground is microlensing.

Gravitational lensing occurs when an object, known as the lens, passes between a background star (the source) and the observer, as depicted in Figure 1.7(a).

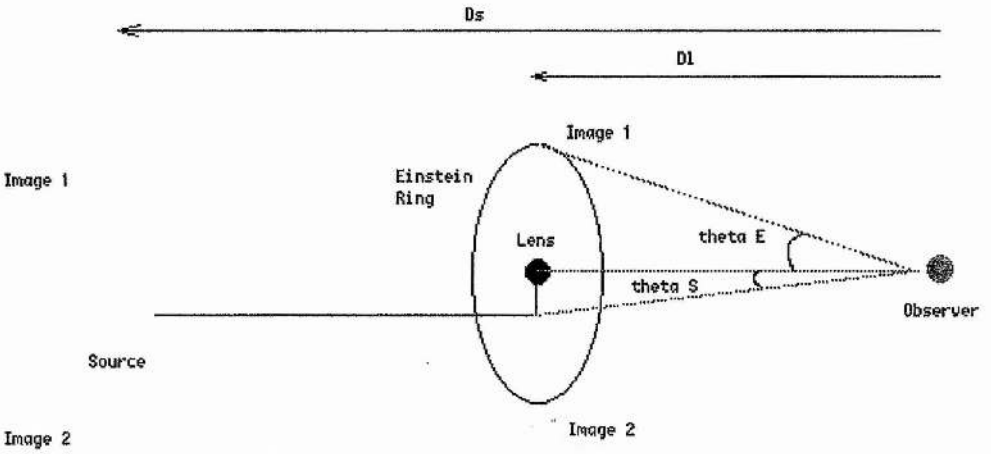

(a) Schematic diagram of a microlensing event

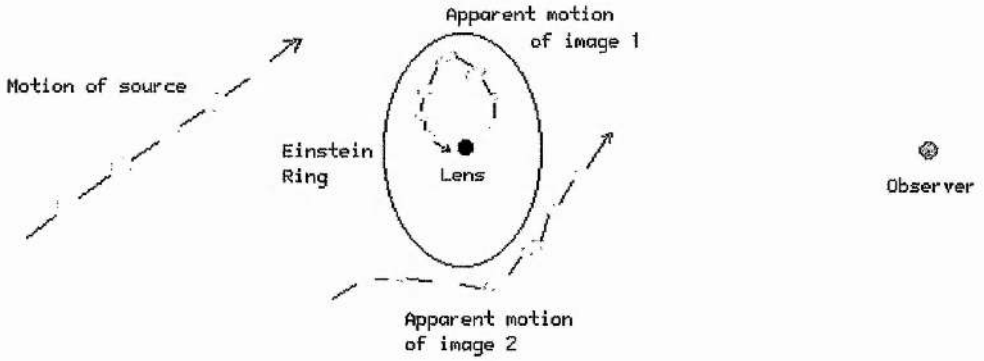

(b) The movement of the images during a microlensing event

Figure 1.7: Schematic illustrations of a microlensing event.

The mathematical description of the event is beyond my current purpose, but a good review was published by Sackett (1999). In conceptual terms, the gravity of the intervening source bends light so that the observer sees two images of the source (see Figure 1.7(b)), unless the source–lens–observer alignment is precise, in which case a ring is formed at a radius characteristic of the lens, the so-called Einstein radius. More light than usual reaches the observer is concentrated into these images. The images move as shown in Figure 1.7(b) as the lens–source relative motion carries them through alignment. When the lensing mass is a galaxy or galaxy cluster, it is possible to resolve the images. When the lens is only of stellar mass, the separation of the images is of the order of microarcseconds, and hence unresolvable. In this case, the observer sees only the amplification of the source's light as the lens passes, in a smooth, symmetrical and achromatic variation. If the lensing star is orbited by a planet, then the planet's gravity can contribute to the lensing effect. Theoretically, these planetary amplification events can be almost infinite, but of very short duration ($\sim$ few hours compared to the $\sim$ weeks–months duration of the stellar event).

The chances of two stars aligning so exactly are of course remote, so a number of survey teams have been photometrically monitoring rich star fields like the Galactic Bulge, Magellanic Clouds and globular clusters for the characteristic amplification events since 1992. Of the order of 100 events are now routinely identified each year by these surveys during the southern hemisphere Bulge observing season. Once an event in progress is identified, emailed alerts go out to the community so that high-cadence photometric follow-up can be carried out.

The primary drawback of this technique is that once the event has occured, it will never repeat, so all the required observations *must* be taken at the time. Furthermore, the technique requires no light from the lens system itself, which will almost certainly never be identified. The technique is good for survey work however, and the results after several years of monitoring can put strong constraints on the population of planets. It is also most sensitive to planets with orbital radii similar to their star's Einstein radii – approximately 5 AU for Solar-type stars, the regime of Jupiter-analogues.

After $\sim$ 10 years of surveying, no uncontested planetary candidates have emerged (see discussion in Section 1.4.4). There are plans for a space-based Galactic Exoplanet Survey Telescope or GEST (Bennett & Rhie 2000) which could detect Mars-mass planetary microlens events for all planets with orbital radii of $\gtrsim 1$ AU.

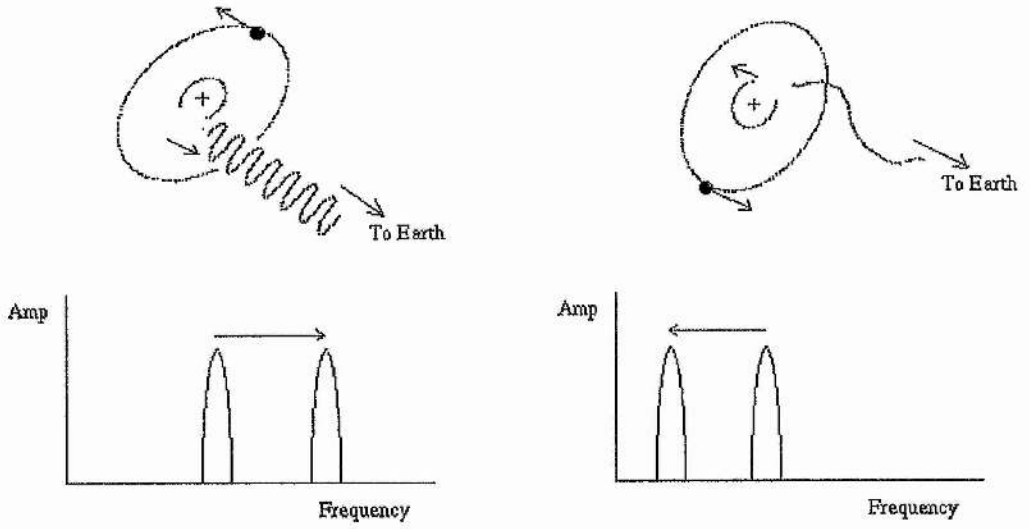

Figure 1.8: The reflex motion of a star due to a companion planet, as seen by radial velocity measurements.

1.5.5 Radial Velocity Measurements

The radial velocity technique produced the first planetary detection around a Solar-type star, and virtually all other detections since. This technique also relies on the star's reflex motion to the orbiting planet: as the planet moves away from the Earth, so the star moves towards us and the Doppler effect results in the light being blue shifted. The opposite red shift occurs as the planet's orbit brings it towards us again. This is illustrated by Figure 1.8.

The semi-amplitude of this wobble (K) is given by:

$$K = \left(\frac{2\pi G}{P}\right) \frac{\mathrm{M}_p \sin i}{(\mathrm{M}_* + \mathrm{M}_p)^{2/3}} \frac{1}{\sqrt{1-e^2}}, \tag{1.1}$$

where P is the orbital period, M_p and M_* are the planetary and stellar masses respectively and e is the eccentricity.

This technique is particularly sensitive to massive planets, close to their parent stars. For example, a Jupiter-mass planet with an orbital radius of 1 AU will cause an amplitude of 28 ms^{-1}. The first radial velocity surveys reached precisions similar to this, but methods have improved to allow measurement precisions of 3 ms^{-1}. This is thought

to be the limit of accuracy, as movements of the stellar photospheres produce velocity variations in Solar-type stars which are only slightly smaller than this. This means that the current surveys can detect Jupiter-mass planets out to radii of 5 AU and Saturn-mass planets within 1 AU.

Perhaps the greatest limiting factor of this technique is that without an estimate of the inclination of the planetary orbit, the mass cannot be determined unambiguously. Since most of the candidates are single stars and non-eclipsing binaries, where inclination is difficult to establish, this leaves one of the most important parameters unresolved (some of the known 'planets' could be brown dwarfs or stars!). The method, which obviously requires high-resolution spectroscopy, is also limited to the finite number of bright, Solar-neighbourhood field stars - it cannot investigate planet formation in younger open clusters or older globulars, for instance. It is also insensitive to planets at greater separations from their stars.

1.5.6 Transit Detection

The final weapon in the planet hunter's arsenal is the method of transits, where for suitable alignments, an exoplanet will eclipse its host star as seen from Earth, on a regular, detectable basis. A full detailed description of this method is given in Chapter 2. This technique has the advantages that it can yield unambiguous values for planetary radius and orbital inclination, and so together with radial velocity measurements, the technique can give the true mass and density of the companion, distinguishing between gas giants and solid planets and thus putting some constraints on the chemical composition. Furthermore, as the transit events re-occur regularly, the results can be confirmed by subsequent observations.

The technique's obvious drawback is the requirement for a very precise orbital alignment between the star, planet and Earth ($\sim 87° - 90°$ for a hot Jupiter). Therefore, to have any chance at all of detecting such a system, samples of thousands of stars must be studied in detail for long periods of time, similar to the large scale microlensing surveys. The method of transits covers a sensitivity range similar to that of the radial velocity technique, and can thus complement its results well. But it has the advantage that the purely photometric method can be extended to much fainted stars, and with reletively little in the way of equipment required.

Several projects are underway that survey large areas of sky for transit events. Most of these, such as the STARE[3] and VULCAN (Borucki et al. 2001) projects, are based around small CCD cameras with $\sim$ 10 cm apertures, often mounted on an equatorial tripod. These cameras can cover very wide fields of view, $\geq 6°$, and can provide the required 1 percent or better photometry for thousands of stars at a time. In addition, many of the radial velocity surveys organise photometric follow-up observations to test whether the system transits, owing to the significant amount of information to be gleaned from such a detection.

As yet, no planets have been discovered by this method, but its validity was spectacularly confirmed in 1999 November by Charbonneau et al. (2000) and Henry et al. (2000), who independently detected the transits of HD 209458b, following its prior discovery though radial velocity observations (discussed in Section 1.4).

Future transit projects are even more exciting. While atmospheric seeing limits the detection of planetary transits from the ground to Jupiter-mass or larger, the detection of Earth-mass planets is possible with high time-cadence observations from space. A number of missions are on the drawing board which propose to do this, for example *Kepler* (Borucki et al. 1997) which aims for 10^{-5} mag precision for Solar-type stars brighter than 12^{th} magnitude and hopes to find between 1000–2000 Mars- to Jupiter-mass planets. This mission has been proposed to NASA and, if formally selected, could be launched in 2004. A competing missions include *Eddington*[4], which has been recommended for inclusion in the ESA's science missions 2008-2013 and is currently being developed, and COROT (Deleuil et al. 1997). The latter craft is under construction in anticipation of a launch in $\sim$ 2005, and also expects to find "a few tens" of Earth-mass planets.

1.6 Summary

In this chapter, I have attempted to summarise the history as well as the current status of the search for extra-solar planets, and to illustrate how our understanding of planetary formation and evolution has been affected by the recent discoveries. I have also attempted to highlight the work in progress, and the unanswered questions that remain. It is in this

[3]http://www.hao.ucar.edu/public/research/stare/stare.html

[4]http://astro.esa.int/SA-general/Projects/Eddington/

context that I will present my work, and how it fits in with the larger picture.

I have concentrated on using the technique of searching for transits in a different environment from all other current search programs, which look at field stars. Instead, I have studied time-series photometric observations of large numbers of stars in intermediate–old age open clusters. This represents a very different stellar environment and a "missing link" in the formation of planets. As I discussed in Section 1.2, we have observations of the circumstellar disc where planets are thought to form, and we have (indirect) observations of the planets around middle-aged main sequence stars, but despite much theoretical work on the subject, no other experimental work is concentrating on the evolution of the planets between these times, and it is a period that the technique of transits is uniquely suited to investigating.

In the next chapter I will explain in detail the theory behind the method of transits, and discuss the merits of the various different approaches taken. In Chapter 3 I describe the work undertaken: the open clusters selected for observation and why, present simulations of the anticipated results and explain the observational strategy. I then cover the experiment as it was carried out in Chapter 4, and describe the data reduction. My results are presented in Chapters 5 – 6, regarding, separately, my findings in terms of exoplanetary science and the discovery of many other types of photometric variables which are a natural by-product of the project. Finally, I present my conclusions in Chapter 7.

CHAPTER 2

The Theory of Planetary Transits

2.1 Introduction

Qualitatively, planetary transits are easily understood; they are distant stellar eclipses. From a planet hunter's point of view, the limiting factor in detecting these events is the precise alignment required between the Earth, planet and star for the transit to be observed. As there is no reason to think that exoplanetary orbits should be preferentially inclined one way or the other relative to the Earth, this alignment condition implies that transits are inherently unlikely.

Therefore, in order to mount a search for these events, we first need to know the following:

- its duration, which determines the minimum sampling rate in any observations, and
- the amplitude, or photometric depth of the transit, which determines the quality of photometry required, and
- the probability that any given planetary system will display transits in order to estimate the numbers of stars which must be observed.

Figure 2.1 shows a schematic representation of a transiting planetary system which defines the parameters used in the following discussion.

The primary star (of radius R_*) to planet (radius R_p) separation, defined between their centres, is given by a. The orbital inclination, i, represents that angle between the plane of the sky and the planetary orbit; hence for transits to be seen, i must approach

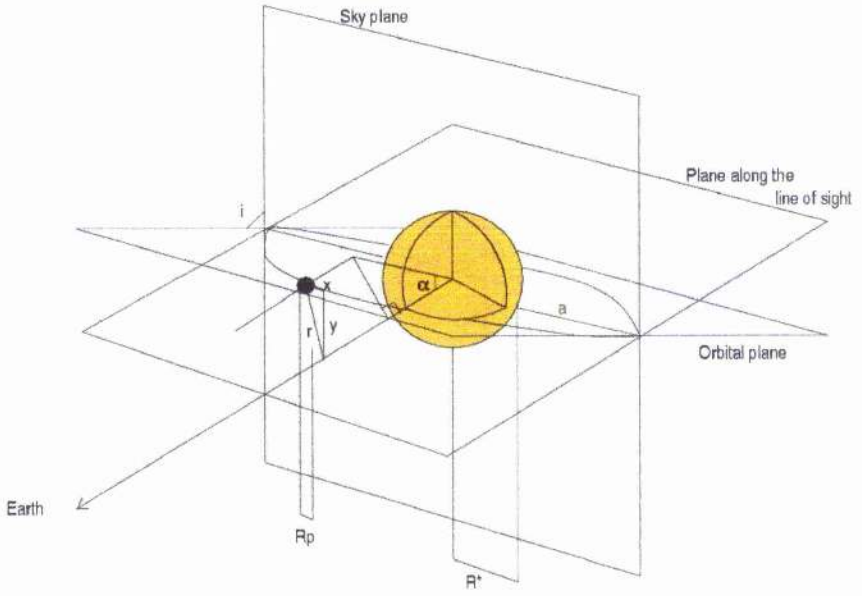

Figure 2.1: Schematic diagram of a transit event, illustrating the definitions of the relevant parameters.

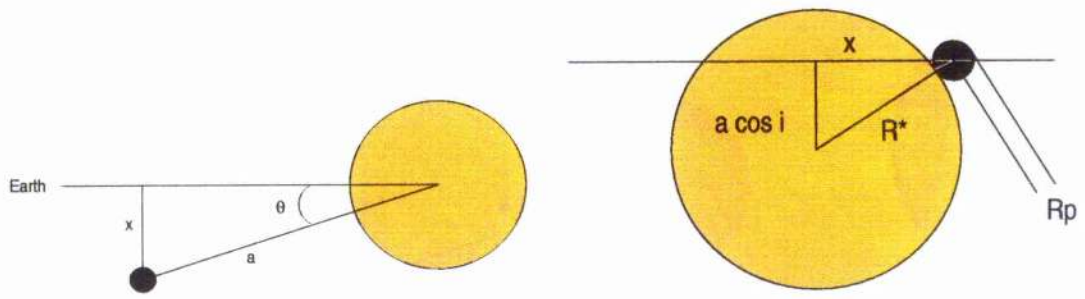

(a) TOP VIEW (b) PLAN VIEW

Figure 2.2: Top (a) and plan (b) views of the transit event.

90°. During a transit, the planet's disc is seen projected onto that of the star, horizontal and vertical distances x,y from the stars projected centre, and radial distance r. The angle α is taken from the actual centre of the star, as defined for limb-darkening.

2.1.1 Transit duration

A transit event lasts for the time when the projected planet–star separation, $r \leq (\mathrm{R}_p + \mathrm{R}_*)$. Examining Figure 2.2(a) shows that the planet subtends an angle of 2θ during a transit, out of the 2π that it subtends during a full orbit. The duration of a transit t_{trans} is therefore given by:

$$t_{trans} = P.\frac{2\theta}{2\pi}, \tag{2.1}$$

where P is the planet's orbital period. Comparing Figure 2.2 with Figure 2.1, it can be seen that the distance $y = a\cos i$. At the begining (and end) of a transit therefore, when $r = \mathrm{R}_p + \mathrm{R}_*$, the distance x is given by Pythagoras' rule and θ is given by:

$$\theta = \arcsin\left(\frac{\sqrt{(\mathrm{R}_* + \mathrm{R}_p)^2 - a^2\cos^2 i}}{a}\right). \tag{2.2}$$

Therefore, the duration of a transit is given by:

$$
\begin{aligned}
t_{trans} &= \frac{2P}{2\pi}.\arcsin\left(\frac{\sqrt{(\mathrm{R}_* + \mathrm{R}_p)^2 - a^2\cos^2 i}}{a}\right), \\
&= \frac{P}{\pi}\sqrt{\left(\frac{\mathrm{R}_*}{a}\right)^2 - \cos^2 i}, \qquad (2.3) \\
&\leq \frac{P\mathrm{R}_*}{\pi a}, \qquad (2.4)
\end{aligned}
$$

assuming that $a \gg \mathrm{R}_* \gg \mathrm{R}_p$.

To get an estimate for the length of a planetary transit, consider a simple example system consisting of a 'hot Jupiter' of radius 1.5 R_{jup} orbiting its parent star of 1.0 $\mathrm{R}_\odot$ in a circular orbit of period 3.5 days and radius 0.05 AU. Equation 2.4 gives an upper limit for the duration of a transit of ~3.5 hours. By contrast, a planet in a Earth–like orbit would have a transit lasting over 12 hours, while a Neptune–orbit transit would last ~3 days! These examples illustrate an observational bias. For a transit signature to stand out in time-series photometry, durations of a few hours are preferable. Furthermore, Equation 2.4 shows that for planets with large orbital radii, the $\cos^2 i$ term becomes increasingly significant – the apparent angular radius of the star from the planet's point of view becomes very small, so the alignment between observer, planet and star must become more precise. So the transit technique clearly favours planets which orbit very close to their parent star.

2.1.2 Transit amplitude and lightcurve morphology

In the following derivation, I make the assumption that the planet reflects no light from its star that might alter the photometric signature of the transit. Of course, this is not strictly the case; any transiting planet will show phases of illumination in the same way as our Moon throughout its orbit. However, even a 'hot Jupiter' of $\sim 1\,\mathrm{R}_{jup}$ at a small separation ($\sim$ 0.05 AU) and with an albedo of 1 is expected to reflect at most only $\sim 2 \times 10^{-5}.F_*$. Furthermore, the photometric signature during the transit could be slightly modified by refraction of starlight through the planetary atmosphere. This effect has also been ignored.

Looking at Figure 2.1 along the line-of-sight from Earth, we see the transit event as it is shown in Figure 2.3. From this it will easily be seen that the shape of the transit lightcurve is governed by the drop in flux, Δf, from the star of total flux f_0, which is

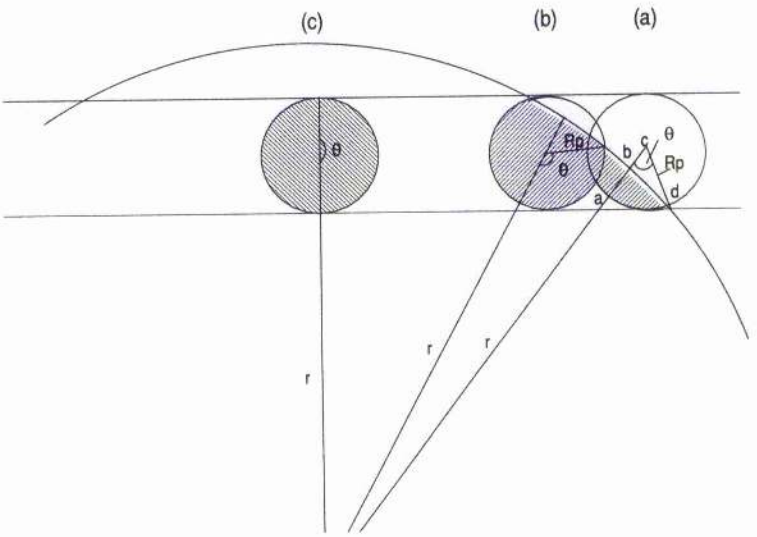

Figure 2.3: Schematic diagram of a transit event, as seen from the point of view of the observer.

in turn governed by the area of the star occulted by the planet, $f = f_0 - \Delta f$. In this expression, Δf equals the product of the area of stellar disc covered by the planet and the intensity of radiation at wavelength λ from the occulted region, F_{occ}.

Assuming that the planet is small when compared with the star, then the stellar limb can be assumed to make a straight chord across the planetary disc as the transit begins (position (a) in Figure 2.3). The line of separation of the stellar and planetary centres defines two sectors when it crosses this chord, one of which is labelled ACD on Figure 2.3. The area of this sector may be calculated in star-centred polar coordinates as:

$$\begin{aligned} A_{ACD} &= \frac{1}{2}\int_0^{\theta} \mathrm{R}_p{}^2 . d\theta \\ &= \frac{\theta}{2}\mathrm{R}_p{}^2, \end{aligned} \tag{2.5}$$

where the angle θ is related to the stellar and planetary radii in the following way:

$$\theta = \arccos\left(\frac{r - \mathrm{R}_*}{\mathrm{R}_p}\right). \tag{2.6}$$

The triangle BCD has an area given by:

$$A_{BCD} = \frac{1}{2}.(r - \mathrm{R}_*).(\mathrm{R}_p \,.\, \sin\theta). \tag{2.7}$$

Therefore, the occulted area A_{occ}, shown in Figure 2.3 (a), is given by:

$$\begin{aligned} A_{occ} &= 2.\left[\frac{1}{2}\int_0^{\theta} \mathrm{R}_p{}^2 . d\theta - \frac{1}{2}(r - \mathrm{R}_*).(\mathrm{R}_p \,.\, \sin\theta)\right] \\ &= \int_0^{\theta} \mathrm{R}_p{}^2 . d\theta - (r - \mathrm{R}_*).(\mathrm{R}_p \,.\, \sin\theta). \end{aligned} \tag{2.8}$$

As flux represents intensity over a given area, the drop in flux from a star of uniform brightness due to the transit is the product of the area and the stellar intensity from that area,

$$\Delta f = A_{occ} F_{occ}. \tag{2.9}$$

However, the effects of limb darkening ensure that the brightness of a stellar disc is far from uniform. To represent this, the linear limb darkening law:

$$I(r) = I_o. \left(1 - u + u\sqrt{1 - \left(\frac{r}{\mathrm{R}_*}\right)^2} \right), \tag{2.10}$$

can be combined with Equation 2.9. The effects of limb darkening on transit lightcurve morphology are discussed in more detail in Section 2.1.2.1.

It can be seen how the transit technique complements the radial velocity method by resolving the factor of $\sin i$ degeneracy in the planetary mass as both the radius and the orbital inclination can be determined.

But can we observe these transits? Do even the most massive planets cause a sufficiently large drop in star flux to be observable? To answer these questions, consider again the example system described in Section 2.1.1, assuming an orbital inclination such that the planet appears wholly surrounded by the stellar disc at mid-transit. Neglecting the smaller effects of limb darkening, it is easy to see that the maximum drop in flux is the ratio of the area of the planet's disc to that of the star, multiplied by the star's unocculted flux:

$$\begin{aligned} \text{Max } \Delta f &= f_0 \left(\frac{\pi \mathrm{R}_p{}^2}{\pi \mathrm{R}_*{}^2 + \pi \mathrm{R}_p{}^2} \right) \\ &\approx f_0 \left(\frac{\mathrm{R}_p}{\mathrm{R}_*} \right)^2. \end{aligned} \tag{2.11}$$

From this equation it can be seen that the transit technique is observationally biased towards large planets orbiting relatively small stars: approximately Solar-type stars and later. For our example system, the maximum flux drop is $\sim 0.01 f_0$, corresponding to a similar drop in magnitude. Photometry to better than 1 percent precision is achievable from ground-based telescopes, and so the photometric signature of transits is observable for 'hot Jupiter'–type planets. However, if we replace this 'hot Jupiter' with an Earth-radius

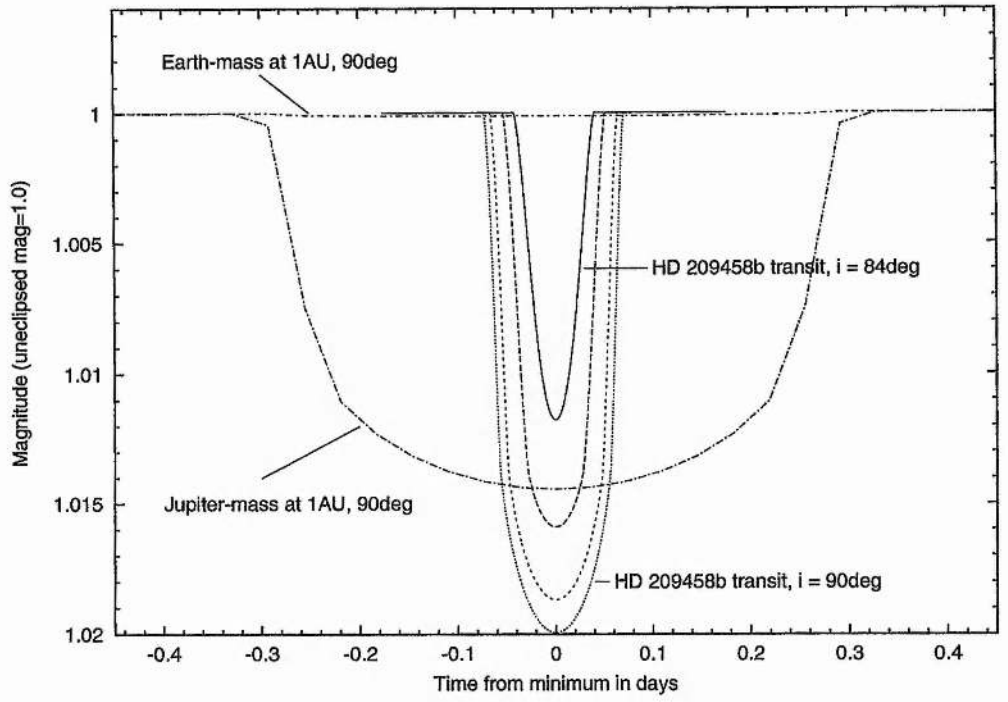

Figure 2.4: The photometric signatures of transits in various different systems. The known transiting system HD 209458 is shown at various orbital inclinations for comparison with Earth-mass and Jupiter-mass planets at a distance of 1 AU and an orbital inclination of 90°.

planet, the depth of the photometric signature is only $\sim 8 \times 10^{-5}$ mags. So detections of Earth-mass transiting planets will have to wait for the upcoming space-based missions. This is illustrated by Figure 2.4, which shows the shape, depth and durations of transits in a variety of systems. The one known transiting system, HD 209458, has parameters very similar to our example: $R_* = 1.146 \pm 0.050\,R_\odot$, $R_p = 1.347 \pm 0.060\,R_{jup}$, $a = 0.0468$ AU, $i = 86.68° \pm 0.14°$ (Brown et al. 2001) and $P = 3.524739 \pm 0.000014$ days (Robichon & Arenou 2000). For comparison, Figure 2.4 also shows the transits made by Earth- and Jupiter-sized planets at a distance of 1AU from their star and an orbital inclination of 90°. The Earth-transit is barely visible! Figure 2.4 also shows the effects of orbital inclination on the shape of the lightcurve; low inclination, 'grazing incidence' transits can mimic the shallower transit of a smaller radius planet in an edge-on orbit. The morphology of the lightcurve is then the key to determining the values of inclination and planetary radius which best fits the data.

2.1.2.1 Limb darkening

The effects of limb darkening on the shape of the transit lightcurve can be considerable and are obviously wavelength dependent. This is significant because the orbital inclination and planetary radius are determined by fitting a model to the data. Figures 2.5(a) and Figure 2.5(c) show how limb darkening in different wavelength changes the shape of the lightcurve. Photometry at the red end of the spectrum measures the cool, outer atmosphere of the star at a relatively large stellar radius to measurements made at shorter wavelengths. With a larger stellar radius the transit duration is correspondingly longer. Limb darkening is also less significant at red wavelengths so the lightcurve profile is less rounded, showing sharper ingress and egress "shoulders". This wavelength–dependent profile is similar to the change in profile caused by orbital inclination (c.f. Figure 2.4). Ignoring the effects of limb darkening can therefore lead to a model where the planet radius is overestimated and the inclination is correspondingly underestimated.

If a transit event can be well monitored in at least two colours, and if the star's type is known (giving estimates of its mass, radius, effective temperature and gravity), then the limb darkening effects during a transit can be modelled sufficiently well that the orbital inclination can be determined. In this case, a combination of Kepler's law and Equation 2.4 will yield the orbital period from the duration of only one transit. Figure 2.5(a) shows the transit lightcurves of HD 209458b through the filters U, B, V, R, I, J, H and K for an orbital inclination of 85° while the Figure 2.5(b) shows the $B-V$, $V-R$ and $U-K$ colour curves for the same phases. For comparison, the lower two panels of this figure show the same curves for an inclination of 90°.

Why do the colour curves vary in this way, according to wavelength and inclination? During ingress and egress, the planet obscures part of the reddened limb of the star, the colour of which appears correspondingly blue. Towards mid-transit the planet covers the less-limb darkened (bluer) central regions of the star, so the colour tends towards the red. Clearly the orbital inclination determines what region of the star will be eclipsed during the transit, hence the change in colour curve shape with inclination. Transits in which the planet only ever passes in front of the star's limb will cause the colour curve to remain blue throughout. If photometry of the transit was obtained in filters at opposite ends of the spectrum, such as U and K, then the colour effects of limb darkening are seen to reach their greatest amplitude. However, even disregarding the practical difficulties of obtaining

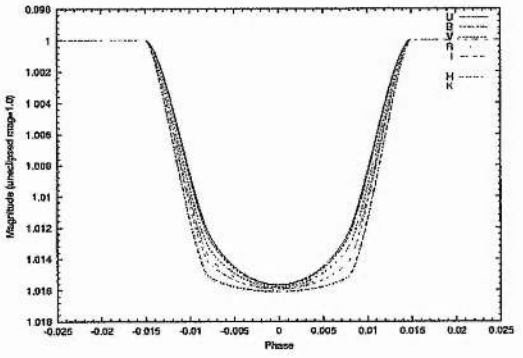

(a) Multifilter simulations of HD 209458b transits for $i = 85°$

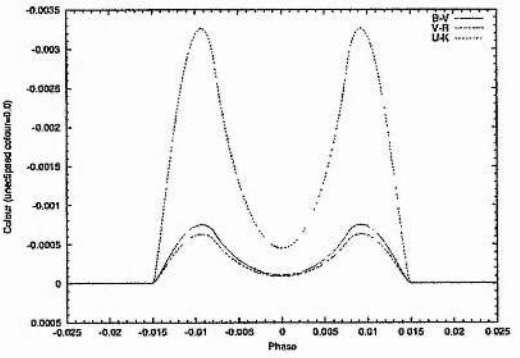

(b) HD 209458b transit colour curves for $i = 85°$

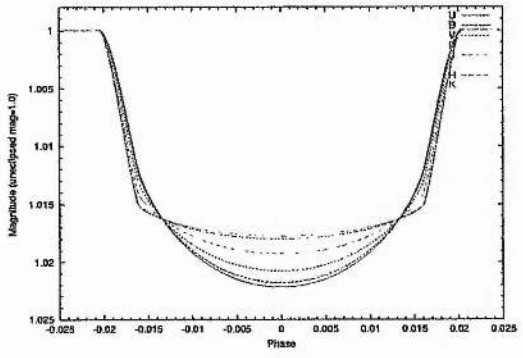

(c) Multifilter simulations of HD 209458b transits for $i = 90°$

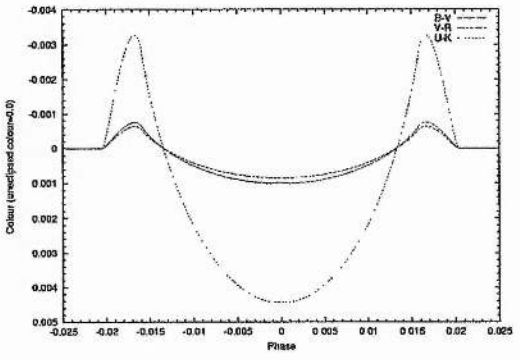

(d) HD 209458b transit colour curves for $i = 90°$

Figure 2.5: Simulations of multicolour transit lightcurves of HD 209458b

sufficient observations in both of these filters, the amplitude of this effect is at best only 3–4 millimags and probably only currently achievable from space.

One further point should also be noted. The linear limb darkening law used in the production of Figure 2.5 (with coefficients taken from Diaz-Cordoves, Claret & Gimenez (1995) and Claret, Diaz-Cordoves & Gimenez (1995)) works well enough when applied to main sequence, Solar-type stars but is less suitable for dwarf, low mass stars, for which the quadratic or logarithmic law should be used. This is important in the modelling of transits events, which are most obvious around dwarf stars.

2.1.3 The Probability of Detecting Planetary Transits

In a recent paper, Borucki et al. (2001) expounded a good explanation of the probability of finding transiting planets, based upon the following principles.

The rate at which planets may be detected is given by the product of the probabilities of the contributing factors, R:

$$R = P_d.P_p.P_a.P_o, \tag{2.12}$$

where P_d is the probability that a given star is a dwarf, P_p is the probability that that star has a 'hot Jupiter' planet in a 3-6 day period orbit, P_a is the probability that the planet's orbital inclination is such that transits will be seen and P_o is the probability that the transits will be observed during any given period of observation.

It is relatively easy to assign numerical values to the first two of these factors. As we saw in Sections 2.1.1 and 2.1.2, the transit method favours large planets orbiting very close to dwarf stars. About half of all stars in the field are dwarf stars, so we set $P_d \approx 0.5$ (Borucki et al. 2001). P_p may be estimated from the results of the ongoing radial velocity surveys, which have found that approximately 1–2 percent of Solar-type stars have 'hot Jupiter'–type planets (Borucki et al. 2001).

The probability of a planetary orbit having a suitable inclination is found from the geometry of the orbit (see Figure 2.2). In order for an observer to see transits, the orbital inclination must satisfy the condition $a.\cos i \leq \mathrm{R}_* + \mathrm{R}_p$, where $a.\cos i$ is the projected

vertical distance of the planet from the star's centre. As there is no reason to suppose that planetary orbits are in any way preferentially aligned, the probability P_a is given by:

$$\begin{aligned} P_a &= \frac{\int_0^{\left(\frac{R_* + R_p}{a}\right)} d\cos i}{\int_0^1 d\cos i} \\ &= \frac{R_* + R_p}{a} \\ &\sim \frac{R_*}{a} \end{aligned} \tag{2.13}$$

Adopting R_* and a values for the example 'hot Jupiter' system explained above, we estimate P_a to be $\sim$0.1.

Therefore, the probability that any given star will have a planet which undergoes transit events is $P_d.P_p.P_a \approx 7 \times 10^{-4}$, or to state it from an observer's point of view, around 1500 stars must be photometrically monitored in order to find the one star which will show transits.

However, the nature of the experiment also plays a strong role in determining how many planets are likely to be found, hence the factor P_o in Equation 2.12. To illustrate, if that 1 star in 1500 shows transits with a period and phase such that they occur during the day from the observer's location, then no transits will be found.

In order to make a reasonable estimate of P_o, I refer to Borucki et al. (2001), who simulated photometric observations for nights of various lengths (summer and winter) for a period of six weeks, assuming perfect weather throughout. Transits of periods between 3 and 6 days were introduced at all possible phases, and the fraction of events for which transits are observed was recorded. Observations of at least three transit events during the six weeks were required to count as a detection. Borucki et al. (2001) found a 65 percent chance of detecting any given transiting planet during the short summer nights, rising to 80 percent during the winter. It should be born in mind that this simulation includes no provision for unknown variables such as the weather, instrumentation problems etc, and therefore errs on the optimistic side. Furthermore, Borucki et al. (2001) showed that the detection probability was a strong function of orbital period for periods greater than about 4 days, in addition to the predictable drop in P_o for planets with periods that are integer or half-integer multiples of 1 day.

In this way, a reasonable estimate for the rate of transit detections, R, is found to be around $3 - 4 \times 10^{-4}$, depending chiefly on the number of hours available for observations per night. For the purposes of observations, this result implies that 1 transiting planet can be expected from every $\sim$2800 stars observed in the manner described above.

I include this estimate to give an idea of a "ball-park" figure for the numbers of stars which must be observed in order to find transits. However, as P_o is particularly sensitive to the design of the experiment undertaken, these calculations are reassessed in some detail in Chapter 3.

2.2 The Practical Aspects of Transit Observations

Single colour, high precision, high cadence photometric observations of a transit event yield values for the maximum amplitude (from which a lower limit on the ratio of the $\frac{R_p}{R_*}$ can be determined) and the duration (which places lower limits on the orbital period and hence the orbital radius) of the event. If multicolour observations are made, then in principle the orbital inclination can also be found, which in turn gives true measurements for these parameters. In practice however, observations of multiple transits will yield the orbital period, and hence the separation, a, from which the inclination may be estimated. This in turn allows the planetary radius to be determined.

However, we have assumed throughout this discussion that the primary star is a passive, unblemished (if limb darkened) disc of constant brightness. Of course, this is not always the case, and in the following section, I discuss the possible effects of a range of known stellar phenomena. With this in mind, I then move on to consider how best to target a search for exoplanetary transits.

2.2.1 Starspots and Other Opportunities for Confusion

Supposing a "dip" occurs in a star's lightcurve, of about the right amplitude and duration to be a transit event, how can we be *sure* that it was caused by a planet?

The first source of confusion might arise from binary stars. While most eclipsing binary systems have photometric amplitudes of a few hundreths to several magnitudes, it is possible to imagine a stellar binary with an inclination such that the secondary eclipsed the

primary causing photometric dips very similar to those expected from planetary transits, dips that would re-occur on the expected regular basis. Good multicolour observations of these events would allow a model to be fitted to the data which would yield the total mass and radii of the components and this ought to be sufficient to distiguish between these two possibilities. Confirmation would then be available from spectroscopy.

What about stellar spots? We know from Solar observations that spot groups rivalling the size of the Earth exist on Solar-type stars. Could a spot be mistaken for a planet? Firstly, spots are not permanent features. They come and go fairly rapidly and while they might be replaced with other spots, the phase and inclination of the resulting "transits" would vary considerably over time. Furthermore, for the Sun and stars like it, even at Solar Maximum the variation in flux due to spots is around the 0.001 percent level (Borucki, Scargle & Hudson 1985), and so is not likely to be confused with a gas giant planet. For later-type stars with more spots, or even for Solar-type stars and Earth-sized planet transits, the potential for confusion is higher. This might be resolved by spectroscopically measuring the star's rotation rate. Most sunspots travel with the rotation of the Sun, so any "planet" appearing to have an orbital period matching its star's rotation rate would be suspect.

Some stars, particularly the small, late-type stars most suited for a transit search, undergo pulsations, some of which can cause variations of similar amplitude and timescale to a transit. These variations are cyclic however, causing a constantly varying lightcurve which is easily distinguished from the more widely spaced transit "dips".

Finally, stellar flares. These of course cause a brightening, rather than a dimming of the star and will therefore not cause confusion, even in the more active late-type stars. However, flare events are blue in colour and might be a source of noise in any attempt to measure the colour change of a star during a transit due to limb darkening.

2.2.2 Selecting Targets for Observation

Before I consider search strategies for transit hunting, I would firstly indicate the philosophy of the approach taken. This can be simply stated: find the transit candidates first, follow-up later. While this may seem obvious, it does have an effect on the observing strategy. For example, we have seen in the theoretical discussion above that multicolour

observations are desirable for various reasons yet switching between filters constantly while conducting a survey of large number of stars would reduce the frequency of observations in any one colour. So would attempting to take images of standard star fields with a view to calibrating the photometry to the standard system. All that is needed to find transit events are high-candence, high-accuracy differential photometric observations. Once candidates are identified, true planetary transit events happen so regularly and predicatably that detailed spectroscopic and photometric follow-up can be obtained at leisure. So rather than obtain the full, multicolour dataset in the first instance, I take the approach that it is better, initially, to obtain very high frequency observations, without sacrificing precision in order to have the best chance of finding the tiny signature of these fleeting events.

The discussion in the preceeding sections has shown that the method of transits is biased towards the detection of large 'hot Jupiter'–type planets, orbiting very close to dwarf stars with periods of around 3–6 days. This detection distribution is very similar to that of the radial velocity method, and it has been shown how the two techniques complement each other. It has been shown that a search for these events requires high-precision (milli-mag) photometry with frequent ($\leq$ hourly) observations taken over long periods ($\sim$ weeks). Several thousand stars must be monitored in this way, so a wide field of observation or a dense starfield is necessary. However, the transit technique has the advantage over radial velocity measurements in that high-precision photometry is possible for far fainter stars than spectroscopy can measure. The number of potential targets is therefore much greater, and not limited to field stars alone.

2.2.3 High–density, small field targets

Using a large telescope enables us to monitor a greater range of stellar environments instead of just the local field stars, due to the increase in light-gathering power, and observations of the Galactic Bulge and stellar clusters become possible. Janes (1996) was the first to suggest that open clusters would make good targets for transit searches, and this has been supported by more recent theoretical work by Bonnell et al. (2001) and Davies & Sigurdsson (2001). Open clusters can offer rich starfields within a fairly compact region. Of course, globular clusters offer an even greater density of stars, but are less suitable as targets for ground-based observations due to the extreme blending

of stars. This objection can of course be overcome with space-based observations, but theory by Bonnell et al. (2001) suggests that the physical density of stars in globular clusters would disrupt the circumstellar discs during the process of planetary formation in addition to causing the ejection of many of the surviving planets. Furthermore, as we saw in Section 1, the planets discovered thus far all encircle metal-rich stars, whereas globular clusters comprise mostly of old, metal poor stars. Gilliland et al. (2000) performed a survey of $\sim 34,000$ stars the globular cluster 47 Tuc and found no transits, supporting the current theory. Ground-based observations of the Galactic bulge field are possible, where the environment ought to be appropriate for planet formation, but the faintness of the stars presents a limiting factor. Even if a candidate transit was detected, most of the stars in these fields are too faint for current spectroscopic follow-up. Without this, we cannot determine the orbital separation so crucial to solving for the system parameters, or the mass of the companion. We would therefore not be able to distinguish between a planetary transit and a grazing-incidence binary star.

Open clusters appear to offer an excellent compromise: the star density in suitable clusters is very high, but not so high as to cause disruption of planetary formation, nor excessive blending, so observations may be made from the ground, and spectroscopic follow–up is possible for any interesting candidates. Furthermore, the ages of these clusters can be established independently, allowing us to probe star and planet formation at a range of epochs, and in a different stellar environment from that targeted by radial velocity surveys.

2.2.4 Wide–field surveys

Alternatively, using a very small telescope ($\sim$ 10 cm primary mirror), it is possible to monitor stars across a very wide ($\leq 10°$) field of view. While the lesser light-gathering power of the small telescope places restrictions on the limiting magnitude of stars included in the survey, sufficient numbers of bright stars can be monitored within the field of view to make a useful transit survey. Spectroscopic follow-up is then an easy task. This approach has an additional advantage in that it does not depend upon observers obtaining large amounts of time on over-subscribed professional telescopes. The only equipment required is a commercially-produced telescope and driven mount plus a professional-quality CCD and ancillary computers. Once constructed, this instrument can be dedicated to transit

surveys for months on end.

2.3 Summary

In this chapter I have reviewed the theory describing a transit event and used this to present examples of transit lightcurves for various configurations of planet and star sizes and separations. These were used to illustrate the effects of planet radius, separation, orbital inclination, limb darkening and filter bandpass on lightcurve shape. I have also considered some of the practical aspects of hunting for transits, summarising the probability theory of detecting the events, possible causes of false alarms and considering different detection strategies.

In this work I have concentrated on a high-density, (relatively) small-field approach, focussing on open cluster target fields. In the next chapter, I discuss this strategy and the observations in detail.

CHAPTER 3

Transit Search in Open Clusters

3.1 Introduction

This search for transits stems from Janes (1996) work, suggesting that open star clusters would make good targets as I discussed previously in Chapter 2. A fairly large telescope is required to make good quality observations of open clusters, the brightest of which (with the exception of the Pleiades and Hyades which cover too wide a field of view) generally have stars $\sim$ 10 mag and fainter. For our purposes, the Wide Field Camera (hereafter WFC) available on the 2.5m Isaac Newton Telescope (INT), La Palma, offers an excellent combination of high resolution and light-gathering power together with an unusually wide field of view ($\sim 34' \times 34'$). As time on large telescopes is at a premium, we cannot assume that we will be able to get the ideal continuous observations over many weeks. Therefore, to assist in the design of an appropriate observing strategy, it is necessary to simulate the experiment and thereby predict what observations will maximise our chances of detecting transit events.

3.2 Simulating Open Cluster Observations

To this end, I have developed a program to simulate the INT observations and predict the chances of observing a transit. A similar study was recently published by Borucki et al. (2001), for the VULCAN project. This project is quite different from the current work, in that it is a very wide angle survey of bright stars, using a small camera set up. Furthermore, the predictions made in their paper are based on the continuous, high cadence observations which can be continued for periods of weeks and months on the

privately owned equipment. This approach was discussed in Chapter 2, Section 2.2.4. In contrast, observations such as ours, made on internationally owned instruments, are charateristically limited to days or weeks at best, often spaced out to achieve a long time-baseline of observations. With this in mind, it was necessary to write my own simulation. I have based the following arguments on a rather more realistic allocation of 10 nights per month for two to three months.

3.2.1 The Design of the Simulation

As I discussed in Chapter 2, Section 2.1.3, it is possible to predict the occurence frequency of transiting planetary systems: approximately 1 in 1500. To estimate the probability of actually *observing* one however, I have adopted a Monte Carlo approach. My program simulates 7000 transiting stars, generating the system parameters (such as planetary orbital period and radius) necessary to calculate the duration and depth of the transit, and the time at which it occurs. These parameters are generated in the following way:

- Planetary orbital period. As this experiment aims to detect 'hot Jupiters' in very short period orbits, I used a random number generator set to produce a Gaussian distribution with a mean period and standard deviation of 3 days. The periods were also required to be greater than 0.5 days.
- Time of mid-transit. For a given system, the time of the first transit was generated as a (uniform deviate) random fraction of the orbital period. Once it was determined whether this transit was detected or not, the time of the *next* transit event was calculated by adding the period. This was in turn tested for detectability, and the process was repeated until the time of mid-transit exceeded the specified end of observations.
- Star magnitude, distance and lightcurve RMS. Obviously, the observations will include stars with a range of magnitudes, and a corresponding range in the precision to which they are measured, which in turns affects the chances of being able to spot the transits. Once the program has generated a star's magnitude, it calculates the expected RMS of its lightcurve from an empirical function fitted to the RMS .vs. mean magnitude of the actual INT data. To generate the star magnitude, the program generates two separate distributions of stars: cluster members, at a known distance,

and field stars, whose distances are generated using a uniform random deviate function. Cluster members of G to M types are generated – all other types are either evolved off the Main Sequence given this cluster's age, and so bright that they are saturated in the INT data. Field stars are allowed to range between F and M types. The apparent magnitude of the star and its RMS is then calculated.

- Star mass and radius. Assuming that all the stars are main sequence, once the apparent magnitude and distances are known, so the mass and radius are derived.

Once these parameters were generated, then the amplitude of the transit is calculated from Equation 2.11, and the duration from Equation 2.4.

Given the time of mid-transit and its duration, the code then works out how many images were taken during each event, assuming that pairs of frames were taken of the field once an hour (thus allowing time for a number of fields to be observed in rotation). If the number of images taken during an event equals or exceeds three, and the transit is at least twice as deep as the RMS scatter of the star's lightcurve, then the transit was considered to be detected.

3.2.2 Deciding the Best Observing Strategy

There is a trade-off involved in deciding the optimum observing strategy. On the one hand, the demonstrated scarcity of transit events would argue for the observations covering many different fields in order to monitor as many stars as possible. On the hand, it is obvious that the frequency of observation must be high enough to spot the brief transit events. Simulated observations are key to deciding a suitable balance of these factors.

Firstly, the simulations described above allow me to quantify the probability of observing transit events as a function of the orbital period of the planet. A fixed range of planetary periods was selected, and for each period interval, 7000 transiting systems were generated by the procedure described above. The probability of detecting a transit of period P (inclination assumed to be 90°) is then given by the number of detected transits of that period divided by the number of trials. Figure 3.1 illustrates how this probability is affected by the sampling rate of the lightcurves.

These simulations assumed a single, 10-night run of 8 hours of observations per night

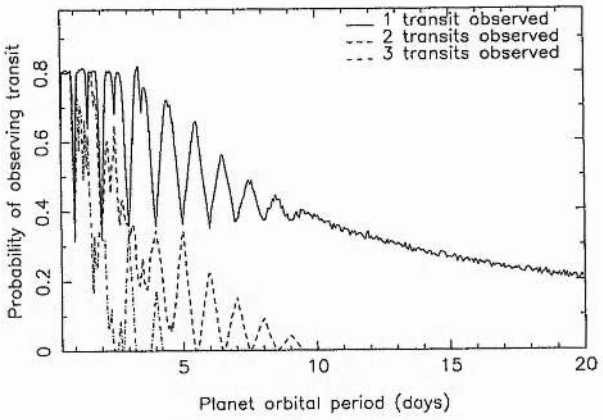

(a) Continuous observations made of one field

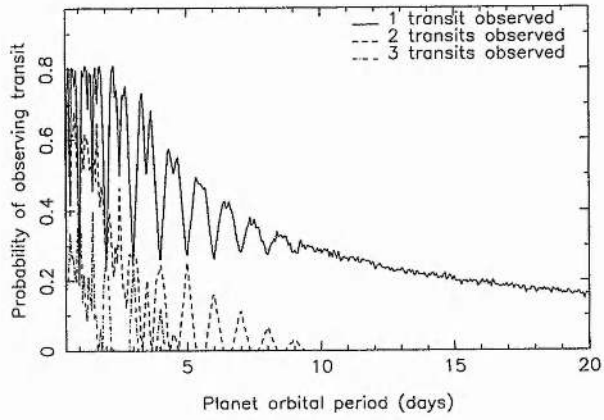

(b) Paired images taken at 1 hour intervals

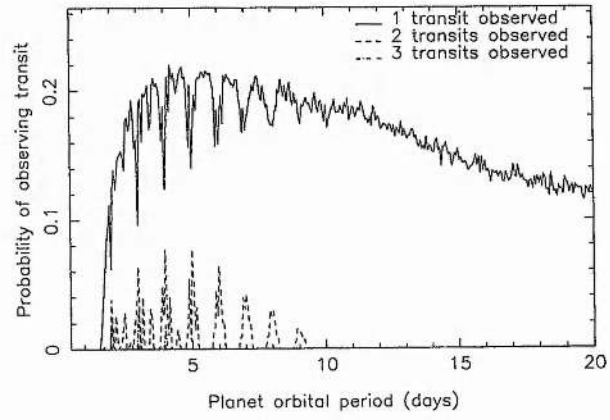

(c) Paired images taken at 2 hour intervals

Figure 3.1: The probability of observing transit events in a 10 night observing run with 8 hours of data/night as a function of planetary orbital period for a range of different image sampling rate.

firstly for continuous observations of a single field, and then for the case where a number of fields are observed in a rotation taking 1 and 2 hours respectively. These results show that the probability of observing a transiting planet of any given period is not greatly affected by a reduction in sampling rate of an hour or so, but would be strongly affected if the sampling rate is reduced any futher, particularly for short period planets.

These figures also illustrate the effects of the one day alias - planets with orbital periods of multiples of 1 day are less likely to be found, since significant numbers of the events will always occur during the day. These planets are beyond the scope of the current experiment - only observations from multiple locations on Earth, or from space could help.

The more significant question is how any reduction in sampling affects the detection of transits of various durations. To answer this a slight variation on the above simulation was made. A range of transit durations was taken and for each interval, 7000 transiting system generated. The probabilities are then calculated in the same way. The plots in Figure 3.2 show the impact of different sampling rates on the likelihood of detection.

These plots illustrate the true impact of the observing strategy. However they do not exclude the possibility of observing multiple fields. The transiting systems which would remain undetected by this method are obviously those with event durations less than the sampling rate or duty cycle. Refering to Figure 3.1 it will be seen that the probability of detection also drops considerably for very long-period systems, purely due to the limited duration of the observing run. For an experiment designed to detect 'hot Jupiters', not much is lost by choosing a duty cycle of 1 hour compared to the potential gains in sheer star numbers by observing multiple fields. On a cautionary note though, Figure 3.2(c) shows that a longer duty cycle would begin to compromise the detection of the short-period objects.

The other observing option available is whether to monitor stars continuously for many tens of nights in a row, or to split the time into several separate runs. The former option is unlikely to be favoured by telescope allocation committees particularly since it must include some (heavily oversubscribed) darktime. But will splitting the observing time have a detrimental affect on the likelihood of success?

Figure 3.3 shows the results of my simulation for two separate cases, plotted as a function of the number of hours observed per night (ranging from 6 hours in summer to

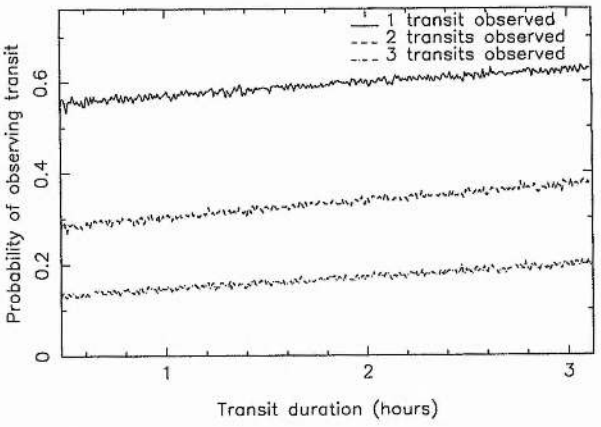

(a) Continuous observations made of one field

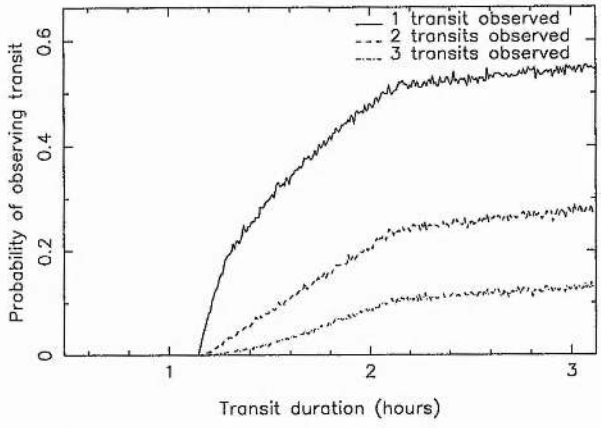

(b) Paired images taken at 1 hour intervals

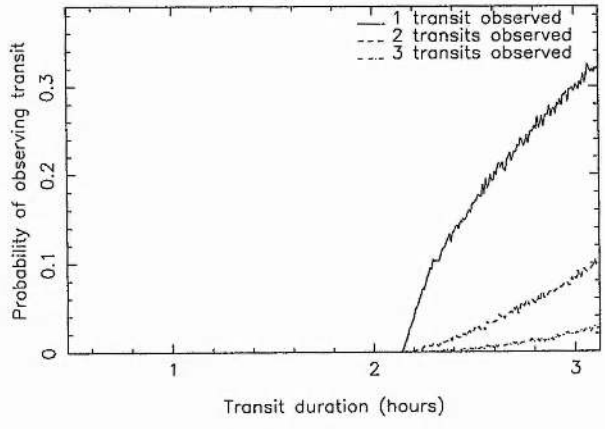

(c) Paired images taken at 2 hour intervals

Figure 3.2: The probability of observing transit events as a function of transit duration for a range of different image sampling rates. One 10-night run of 8 hours/night was considered, using a range of planet orbital periods generated from the Gaussian distribution described in the text.

16 hours in winter). Figure 3.3(a) shows the detection rate for twenty nights of continuous observations (using a duty cycle of 1 hour) while Figure 3.3(b) shows separate curves for 1, 2 and 3 runs of 10 nights per run. The runs are assumed to be spaced by 1 month so as to occur during (more readily available) bright-time.

These figures show that splitting a 20-night run in half this way does not seriously affect the chances of detecting transits, while increasing the probability of being awarded telescope time.

On the basis of these results, a good observing strategy would be to make observations during two runs of ~ 10 nights each separated by 1 month. Larger numbers of stars can be monitored by observing several fields in rotation, provided that the rotation cycle does not exceed ~ 1 hour.

3.2.3 Predicted Transit Detection Rate

Having settled on a good observing strategy, I can now use the simulations to estimate the transit detection rate of the experiment. The plots in Figure 3.4 show the probability of detecting transiting systems when 1, 2 and 3 transits are required to establish a detection respectively.

It is clear from these plots that the probability of detecting a transiting system levels out at a maximum of 0.8 and not 1.0, regardless of the length of observations. This is because transiting systems were generated with a full range of magnitudes corresponding to a range of lightcurve RMS scatters. As the transit is required to be at least twice as deep as the RMS scatter of the star's lightcurve in order to be detected, a certain subset of the 7000 trials will never be detected: low amplitude transits occuring to faint stars. This reflects observational reality.

From these results I estimate that P_o from Equation 2.12 is approximately 0.5. This assumes that two transit events must be detected in two runs of 10 nights per month during the summer. The probability of detecting a transit, R, from the INT observations is therefore approximately 1/3000. Observing during the longer winter nights can clearly strongly enhance this probability, and similarly with more observing runs.

On the face of it, this strongly suggests that at least two observing runs are required

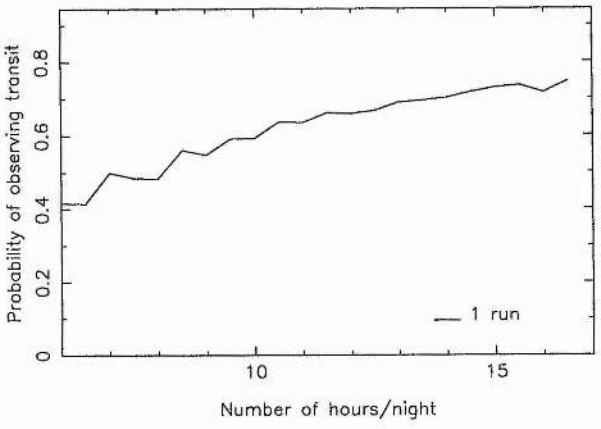

(a) Twenty nights observations taken at 1 hour intervals

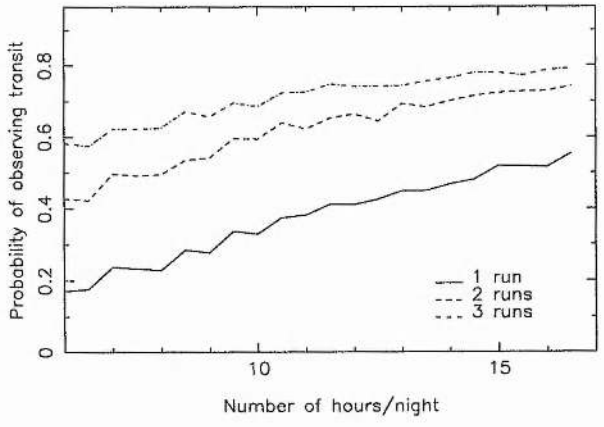

(b) Separate 10 night runs with data taken at 1 hour intervals

Figure 3.3: The probability of observing transit events as a function of the number of hours observed per night to compare the detection probabilities of observations made during 1 run of 20 sequential nights and several runs of 10 nights each at 1 month intervals. 8 hours of observations were assumed for each night and the planet orbital periods were taken from a Gaussian distribution described in the text.

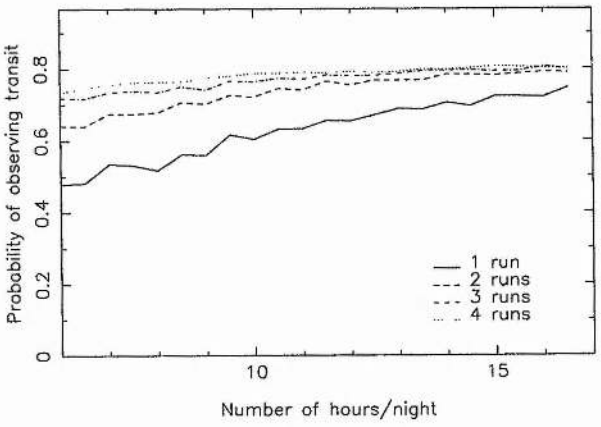

(a) 1 transit event required for detection

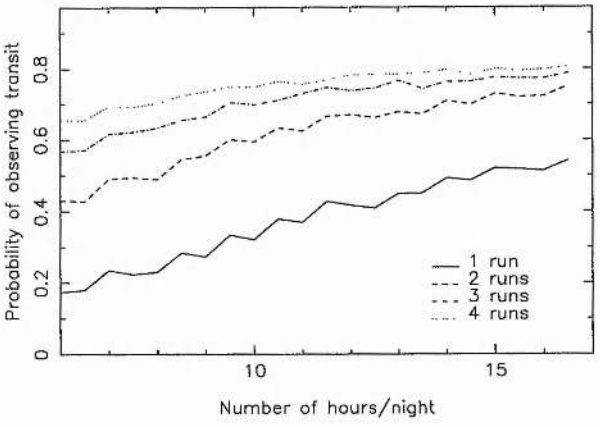

(b) 2 transit events required for detection

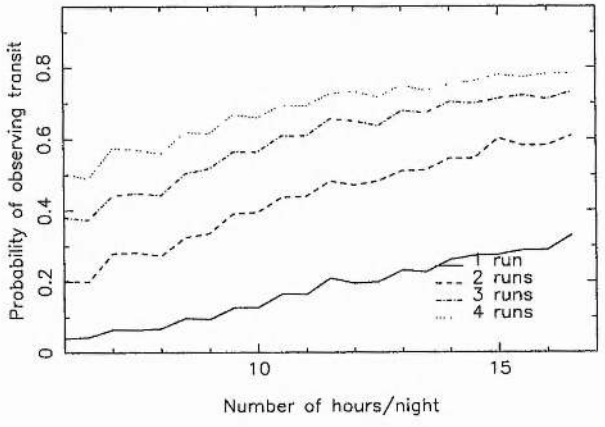

(c) 3 transit events required for detection

Figure 3.4: The probability of observing transit events in the field of an open cluster as a function of the number of hours observed per night and the number of 10 nights/month observing runs completed.

to have a realistic chance of detecting a transit. However, it is worth remembering that the purpose of these observations is to *detect transits candidates*, rather than characterise them fully as this may be done in follow-up observations. A single convincing transit event would be sufficient to put a star on the candidate list. In this case, the probability of detecting a transit event is much higher: $\sim 1/2100$.

3.3 The Observing Strategy and Targets

The simulations indicate that taking pairs of images (to minimise the effects of cosmic ray hits) once an hour is a sufficient sampling rate. It was therefore decided that, in order to monitor as many stars as possible, we would observe 3 clusters in rotation. The target clusters were selected on the basis of the following criteria.

- The magnitude of Solar-type stars at the distance of the cluster, to ensure that enough photons would be received from these stars within reasonable exposure times,
- Cluster age, which needed to be as great as possible so that planets had had a chance to form
- Cluster metallicity, as planets were thought to form from dusty debris discs. This has since been borne out by the growing numbers of exoplanets almost all of which orbit stars of high metallicity.
- Cluster radius and number of member stars. We selected star-rich clusters with fairly small radii in order to get as many stars as possible within the field of view of the telescope.
- When and for how long they were visible from La Palma.

In selecting target clusters, it was necessary to make a trade off between the first three criteria and the fourth. The clusters NGC 6819, NGC 6940 and NGC 7789 were choosen as the best targets, although unfortunately, these clusters are most visible from La Palma during the shorter summer/autumn nights. While longer nights clearly increase the chances of observing transits, it is also worth considering that poor winter weather conditions would be likely to reduce the amount of data actually obtained. So having to observe the targets in summer is less of a drawback than it seems. Basic physical data on

Table 3.1: The basic physical parameters for the selected target open clusters.

	NGC 6819	NGC 6940	NGC 7789
RA (J2000.0)	$19^h\ 41^m$	$20^h\ 35^m$	$57^h\ 00^m$
Dec (J2000.0)	$+40°11'$	$+28°\ 18'$	$+56°\ 43'$
l	73.°97	69.°90	115.°48
b	+8.°48	-7.°17	-5.°37
Distance (pc)	2500	770	2337
Radius	$\sim 9.5'$	-	-
Age (Gyr)	2.5	7.2	1.7
Metallicity	+0.07	+0.03	-0.08
$E(B-V)$	0.10	0.214	0.217
Trumpler class	I 1 r	III 2 m	II 1 r

these clusters is presented in Table 3.1, including their Trumpler (1930) classifications to give an indication of the richness of the clusters ((p)oor, (m)edium or (r)ich), the degree of central concentration of their stars (I – most concentrated to V – widely scattered) and whether the cluster appears well detached from the background star field (1) or not (5).

3.4 The INT Observations

The group involved with this search, lead by Keith Horne, Alan Penny, Andreas Quirrenbach and Andrew Collier Cameron, applied for time on the INT Wide Field Camera instrument and received three, 10-night observing runs: 1999/06/20–30, 1999/07/21–31 and 2000/09/10–20. A team of observers was sent for each run: Alan Penny, Andreas Quirrenbach and Rachel Street (Run 1), Keith Horne, Yianni Tsapras and Neda Safizadeh (Run 2) and David James, Kevin Pearson and David Mitchell (Run 3). During the first two runs all three cluster fields were observed in rotation as planned. Prior to the third run however, it was decided that due to the higher airmass of NGC 6819 and NGC 6940 in August and in order to achieve a faster sampling rate, only NGC 7789 would be observed.

The WFC consists of four thinned 2048×4096 pixel EEV CCDs, covering a 0.28 square degree field of view with a pixel size of 13.5 μm (corresponding to a plate scale $0.33''\,\mathrm{pix}^{-1}$), and is mounted at the prime focus of the INT. The CCDs are cooled by liquid

Table 3.2: The gain and noise parameters of the four INT-WFC CCDs during the 1999 runs. Taken from the Cambridge Astronomical Survey Unit (CASU) webpage

Science CCD	Bias level	Gain (e-/ADU)	Readout noise (e-)	Max ADU
1	1559	3.12	7.9	58000
2	1636	3.19	6.4	59000
3	1744	2.96	8.3	59000
4	1190	2.22	8.4	58000

Nitrogen to around 150K and the resulting dark current is negligible. During the first night of the first run the camera was used in STANDARD or NONASTRO mode, giving a read out time of 155s. We then switched to the default SLOW or TURBO read out recommended by the observatory technical staff for all subsequent observations. This gave a read out time of 160s.

The gain and readout noise values differ slightly for each chip. The values presented in Table 3.2 were taken from the Cambridge Astronomical Survey Unit (CASU) webpage[1] and were adopted during the data reductions.

As the hunt for transits requires only differential photometry in one colour-band, the vast majority of observations were made using the Sloan r' filter. Pairs of 300 s exposures were taken of each cluster in turn from the time they became visible. In this way, NGC 6819 and NGC 6940 were observed for $\sim$ 7 hours each night (NGC 7789 for $\sim$ 5 hours), typically resulting in $\sim$ 16 frames per night. The average gap between pairs of exposures of each cluster was, at most, roughly an hour and we had good observing conditions on all nights.

These observations resulted in approximately 500 science frames (roughly 160 on each cluster) per run, giving a total science dataset of $\sim$ 185 Gb. Such a huge dataset requires the data reduction pipeline to be more or less completely automated. In order to develop such a pipeline, I decided to work on a more easily managed subset of the data and concentrated on the CCD-4 data taken of the centre of cluster NGC 6819. As my results presented in subsequent chapters stem from this work, it is appropriate to briefly summarise the previous work done on this cluster.

[1]http://www.ast.cam.ac.uk/~wfcsur/ccd.html

3.5 Previous Studies of NGC 6819

The basic physical parameters of NGC 6819 are provided in Table 3.1. The earliest reference I can find to this cluster is Trumpler's original work classifying it as I 2 r, implying a centrally concentrated and rich cluster with a moderate range in star brightnesses (Trumpler 1930). The first photometric study of the cluster was made by Barkhatova (1963) and was followed by similar studies by Purgathofer (1966) and Burkhead (1971). The latter published two colour (V, B) photoelectric and photographic observations of 530 stars in the field of the cluster, a colour magnitude diagram and an estimate of $m - M_V = 11.55$ for an assumed $E(B-V) = 0\overset{m}{.}12$. Barkhatova & Vasilevsky (1967) announced the discovery of the first variable in the cluster, which was later confirmed and classified an an M4 giant of irregular variation by Lindoff (1971).

In 1972 Sanders (1972) published what would become one of the seminal studies of NGC 6819: membership probabilities for 189 stars (limiting magnitude of V$\approx 14\overset{m}{.}5$) based on their proper motions. This was followed by two photoelectric and photographic studies which have also been often cited. Lindoff (1972) published three-colour photometry down to $V_{lim} = 15\overset{m}{.}25$, and derived an estimate for the extinction of $E(B-V) = 0\overset{m}{.}3$, while the work by Auner (1974) produced values for the parameters $E(B-V) = 0\overset{m}{.}28$ and $m - M_V = 11\overset{m}{.}76$ with a $V_{lim} = 16\overset{m}{.}6$. These were the last significant photometric studies of this cluster until recently.

Since that time the tendancy has been to concentrate on open clusters as tracers of Galactic structure, metallicity, chemical abundances and evolution, for example Janes & Adler (1982), Strobel (1991) and Janes & Phelps (1994). NGC 6819 has also played its part in resolving the controversy over the origins of blue stragglers, being one of a number of clusters whose blue stragglers' radial velocities were measured in the effort to identify close binaries. Manteiga et al. (1991) found that the blue straggler star 889 in NGC 6819 (numbering from Auner (1974)) had a anomalous photometric colours which could be due to binarity, but concluded that the photometric errors were too large to be sure.

Kaluzny & Shara (1988) obtained the first time-series photometric dataset on NGC 6819; 8 and 10 V frames of two fields covering 854 stars of $V \leq 17\overset{m}{.}5$ were taken over two nights in August 1986. This study revealed 3 possible variables thought by the authors to be short period detached eclipsing binaries. A further 5 possible variables were identified in

a radial velocity study by Glushkova, Kulagin & Rastorguev (1993), who also use Sanders (1972) numbering. However, one of the stars listed as variable is given the number 79, whereas Sanders (1972) states that there is no star 79 in his numbering.

A number of studies have produced a range of values for the extinction coefficient, metallicity and mean radial velocity of NGC 6819. Canterna et al. (1986) found $E(B-V) = 0.15$ most appropriate, with a metallicity of $[Fe/H] = -0.03$, whereas Friel & Janes (1993) measured a value of $[Fe/H] = +0.05 \pm 0.11$ and found the mean radial velocity to be $V_r = -7$ kms^{-1}. Glushkova, Kulagin & Rastorguev (1993) determined a value of $V_r = 4.8 \pm 0.9$ kms^{-1}, and Thogersen, Friel & Fallon (1993) found $V_r = +1 \pm 6$ kms^{-1}. More recently, Rosvick & Vandenberg (1998) found $[Fe/H] \approx -0.05$, $E(B-V) = 0.16$, distance modulus $m - M_V = 12.35$ and a cluster age of 2.4 Gyrs. Bragaglia et al. (2001) has since derived values of $[Fe/H] = +0.09 \pm 0.03$ and $E(B-V) = 0.14 \pm 0.04$ from high-resolution spectra of red clump stars in the cluster. Finally, Kalirai et al. (2001a) has derived $E(B-V) = 0.10$ and $m - M_V = 12.30 \pm 0.12$, consistant with an age of 2.5 Gyrs. I have adopted these most recent values in the table above. Rosvick & Vandenberg (1998) and Kalirai et al. (2001a) represent the most recent in-depth photometric studies of NGC 6819, with limiting magnitudes in V of $\sim 19\overset{m}{.}5$ and $\sim 25\overset{m}{.}0$ respectively. The Kalirai et al. (2001a) is particularly notable as it employed the CFHT mosaic CCD camera covering an area of $42' \times 28'$ on the sky. Neither study however, provides time-series photometry.

All of the previously identified variable stars are saturated in our data, so we are unable to provide further information on them. My current work provides longer baseline photometry on this cluster to fainter magnitudes than previously available, and therefore provides a more complete tally of the variables within this field.

3.6 Summary

In this chapter I have presented simulations of INT-WFC observations which were used to assess different observing strategies. The observations made, in three separate runs, according to the decided strategy were described.

In order to process the very large resulting dataset it is necessary to develop the reduction pipeline to be as automated as possible. I have concentrated on a subset of the data in order to develop this pipeline – this is described in the next chapter. As the data

subset is that of NGC 6819 I have presented a summary of previous work on this cluster.

CHAPTER 4

Data Reduction Pipeline

4.1 Introduction

To develop the data reduction pipeline, I initially concentrated on the nine nights (1999/06/ 22–30) of data from chip-4 of the WFC of the centre of NGC 6819. In this chapter I describe the data reduction procedure in detail, using the 18 images of NGC 6819 from the night of 1999/06/25 to illustrate where appropriate. Once the pipeline was in place, it was used to reduce a much larger dataset, the results of which are presented and discussed in Chapter 5.

4.2 INT Data Reduction Pipeline

Although the INT data is very large, it can be conveniently split into subsets which can be stored "on disc". This has the advantage that it allows for some level of human interaction with the data in the form of "quality control" rather than relying entirely on algorithms to spot and correct unexpected flaws in the data. My pipeline takes advantage of this, while leaving robust programs to deal with the majority of process automatically. The various stages of the procedure are discussed below.

4.2.1 Producing Master Bias and Flat Fields

Sky flat fields and bias frames were taken at the begining and end of each night. Following close examination of the bias frames, microphonic signals were found at the $\sim \pm$ few counts level which were not constant between frames. These were later found to be caused

by electronic interference from the telescope's autoguider. Although small enough to be insignificant to the photometry, this is believed to be the reason why no satisfactory gain and noise values could be determined from these data. Other than this, the bias was stable during the run, and a masterbias frame was constructed from the 31 bias frames. This was done by subtracting the median number of counts per pixel from the overscan region from each frame before using the STARLINK package FIGARO (Shortridge et al. 1998) command *medsky* to produce the median of all the frames. Subtracting the overscan median from all data frames first allows for the bias level, while subsequently subtracting this masterbias allows for pixel-to-pixel variations across each frame.

After subtracting the overscan median and masterbias from the raw flat fields, a correction for the nonlinear response of the chip was applied of the form:

$$\begin{aligned} C_{corr} = 0.995565 C_{obs} &- 1.10012 \times 10^{-6} C_{obs}^2 \\ &+ 5.77076 \times 10^{-12} C_{obs}^3, \end{aligned} \tag{4.1}$$

where C_{obs} and C_{corr} refer to the observed number of counts and the corrected number of counts, respectively, for a given pixel after bias subtraction. This correction was taken from the "Wide Field Camera - Known Problems" webpage [1].

Manual examination of the flat fields revealed that an adjustment was necessary due to a read out problem, which caused extra pixels to be included in the overscan region on one side of the image and removed from the other side. The features of the flat fields therefore moved between frames. To counteract this, all the flat fields were collapsed and cross-correlated with a selected reference flat field in order to calculate trim limits to ensure that all the frames were correctly aligned.

At this stage it was realised that virtually all of the flat fields contained some star images. These stars were in different places on each frame due to the telescope being moved between flats exposures each night, but it was found that they did not "average out" sufficiently well when the flats were combined. To cure this problem, masks of all the pixels above a certain threshold were made for each given flat field. These pixels were set to zero in the flat field. This mask was then multiplied by another flat field where the

[1] http://www.ast.cam.ac.uk/~wfcsur/foibles.html

stars were in different positions. This produced a frame where all pixels had a constant value except those of the stars. The star-covered pixels in the mask now had the values of the same pixels from the second flat. The mask was then scaled to match the median value of the first flat and added to it. This produced a flat field where the star-covered regions were replaced with similar but unaffected regions from another flat.

Once all the star images were removed in this way, MEDSKY was used to create the masterflat. This process was carried out by a pair of interactively-operated C-shell scripts.

4.2.2 Pre-processing the Science Frames

Manual examination of the science frames revealed the frame taken during the best conditions; this frame was adopted as the reference frame. The following procedure was adopted for each science frame and executed in an automated fashion by C-shell script once masterbias and masterflat frames were available. The overscan median was measured and subtracted, followed by the subtraction of the masterbias. The correction for the non-linear chip response given in Equation 4.1 was then applied and the frame was divided by the masterflat. The resulting image was 'collapsed'; that is, the values of all pixels in each row/column were summed. The resulting 1-dimensional spectra (collapsed in x and y directions) were then cross-correlated with spectra of a reference frame selected from the night of best seeing, and trim limits were calculated and applied accordingly. Finally, the pre-processed NDF-format frame was converted into IRAF format using the Starlink package CONVERT (Currie et al. 2000).

4.2.3 Processing the Reference Frame

The reference frame was reduced manually using IRAF's DAOPHOT task (Stetson 1987). DAOFIND was run to identify objects in the frame; this output was then adopted as the full starlist. After performing aperture photometry on this list, approximately 100 isolated stars were manually chosen for the derivation of the point-spread function (hereafter PSF). The process of selecting PSF stars, generating, refining and subtracting the PSF was iterated until a satisfactory PSF was obtained – the accepted stars then comprised the PSF starlist. After some experimentation (described in detail below), it was found that DAOPHOT's "penny2" function gave the best residuals across the frame when allowed to

vary quadratically with x and y. This is a two component model, consisting of an elliptical Gaussian core and Lorentzian wings. Both parts of the model are aligned along separate and arbitrary position angles. These PSF stars were used to generate such a PSF for all subsequent frames.

4.2.4 Performing photometry on the dataset

DAOPHOT requires certain frame-dependent parameters in order to perform good quality photometry, for instance the exposure time, the standard deviation of the background count value, maximum and minimum good data values to determine when saturation occurs, etc. These parameters are stored in separate files for each frame and called by the routine as required. In order to provide a suitable file for each frame, I wrote a C-shell script which called various FIGARO and KAPPA (Currie & Berry 1998) routines to measure these parameters and produce an IRAF-format parameter file for each image. These files were then automatically called during the reduction.

At this stage another C-shell script was run which noted the following parameters from the image headers: the UT of the start of the exposure, the RA and Dec, the exposure time, the date and equinox (i.e. 2000.0). Heliocentric Julian Dates (hereafter HJD) were then calculated for the frames by a FORTRAN code.

Once the parameter files, the full starlist and the PSF starlist were in place, PSF photometry was performed on the rest of the dataset by a fully automated IRAF script, with the star positions re-fitted independently in each frame. The process followed was the same as that described for the reference frame, using the same PSF starlist for each frame. Once the PSF photometry on each frame was completed, my IRAF script wrote out results into ASCII text files including the star identifier, its x,y position, magnitude and magnitude error, the χ^2 value of the PSF fit and the sky background in counts. These output files then formed the basis of the post-processing analysis.

4.2.5 Post-processing

DAOPHOT does not measure all stars in every image; some are very faint, blended etc., and are only measurable in images taken in very good conditions. Furthermore, due to the way nearby stars are placed into groups for measurement, the stars are not always

measured in the same order. For these reasons, the pipeline output files require sorting to establish which stars are measured in which images. This is done by a FORTRAN code which tries to identify every star in each output file by both its DAOPHOT identity number and position. If no entry is found for a star in any given image then zeros are entered in the output file. All subsequent processing codes are designed to look for and exclude these non-measurements.

Once the DAOPHOT output is obtained and sorted, it is necessary to self-calibrate the data, to remove the time-variable effects such as atmospheric extinction as the airmass of the target changes through the night. In order to do this, I initially developed a post-processing code that uses all the data on all stars. Firstly, the mean magnitude $m_o(j)$ of every star j within the magnitude range $17\overset{m}{.}0 - 20\overset{m}{.}0$ is calculated from the magnitude $m(i,j) \pm \sigma(i,j)$ in each image i using $\frac{1}{\sigma(i,j)^2}$ weights as in Equation 4.2.

$$m_o(j) = \frac{\sum_i \frac{m(i,j)}{\sigma(i,j)^2}}{\sum_i \frac{1}{\sigma(i,j)^2}}. \tag{4.2}$$

The fainter stars were excluded due to large amount of noise dominating their lightcurves. The magnitude residuals $\delta m(i,j)$,

$$\delta m(i,j) = m(i,j) - m_o(j), \tag{4.3}$$

of each star in each image are then calculated. From this quantity, the average residual for each image, $\Delta m(i)$, is found:

$$\Delta m(i) = \frac{\sum_i \frac{\delta m(i,j)}{\sigma(i,j)^2}}{\sum_i \frac{1}{\sigma(i,j)^2}}. \tag{4.4}$$

These $\Delta m(i)$ values are then subtracted from the magnitude of every star in each image to correct for the time-variable extinction, giving $m_{corr}(i,j)$:

$$m_{corr}(i,j) = m(i,j) - \Delta m(i). \tag{4.5}$$

As this amounts to a correction in the zero point of the magnitude scale for each image, I have come to call the $\Delta m(i)$ values the 'zero points' of the images. Once these corrections have been made, the code offers various output options for later analysis.

4.2.5.1 Positional Dependence of the Magnitude Residuals

Once this self-calibration had been performed, the residuals (that is, the $\delta m(i,j)$ of the stars post-correction) were examined to test how well the corrections had been made.

My first reduction of the data used a constant, purely Gaussian PSF function. However, after self-calibration, examination of the magnitude residuals made it clear that improvements could be made. Figures 4.1(a) and 4.1(b) show the RMS scatter of each star's lightcurve against its mean magnitude and the magnitude residuals plotted against x, y pixel position respectively. The latter plot clearly shows a position-dependency in the residuals, particularly strong in the y-direction.

In response, I experimented with several PSF functions. DAOPHOT's "penny2" function appeared to give the cleanest star-subtraction from the image. This model consists of an elliptical Gaussian core with Lorentzian wings where the position angles of both components are aligned separately. Post-processing the data resulting from this model produced Figures 4.1(c) and 4.1(d). The use of this model did cause some improvement in the residuals, but there are obviously still positional variations in the data.

Adopting the "penny2" model in order to better handle the extended wings of the stellar images, the next stage of sophistication was to allow the PSF to vary across the frame in such a way as to best fit the data. The DAOPHOT options to allow linear and quadratic variations were both tested and the latter was found to produce the best residuals; Figures 4.1(e) and 4.1(f) show greatly improved results.

Nevertheless, some positional variations remain in the residuals, particularly dominant along the long (y) axis of the CCD. To counteract this problem, I developed some software to compute position-dependent magnitude zero points ($\Delta m(x,y,i)$) for each image in the dataset. This was done by splitting each image into 500 $\times$ 500 pixel sectors, and calculating the zero point for each sector in each image independently, using only the stars found within it. The principle behind this was that, whatever the cause of the position-dependency be it varying levels of extinction due to light cloud or airmass

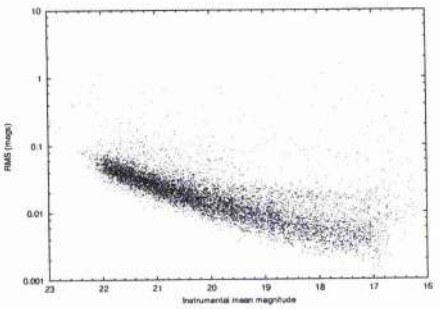

(a) Constant Gaussian PSF

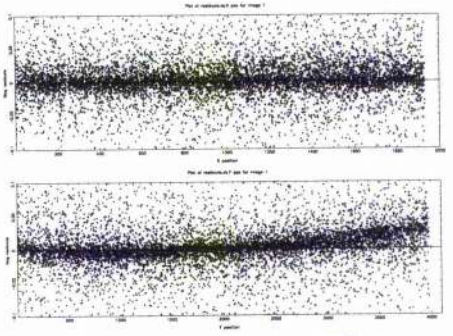

(b) Constant Gaussian PSF

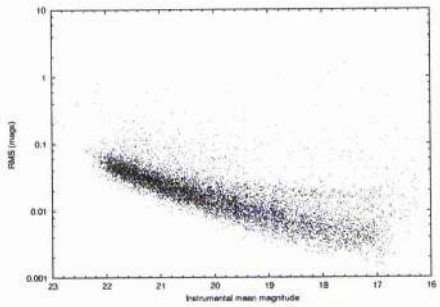

(c) Constant "Penny2" PSF

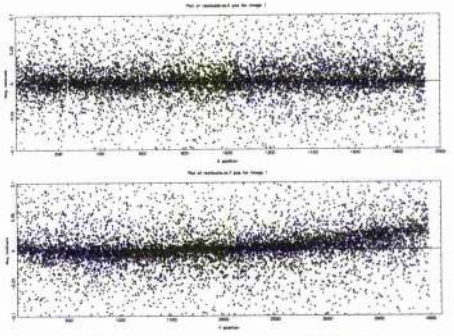

(d) Constant "Penny2" PSF

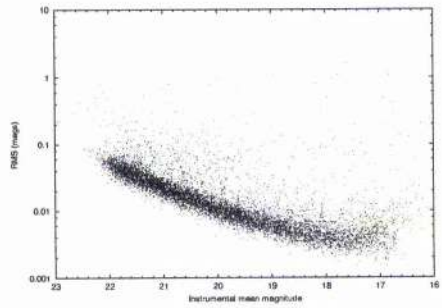

(e) Variable "Penny2" PSF

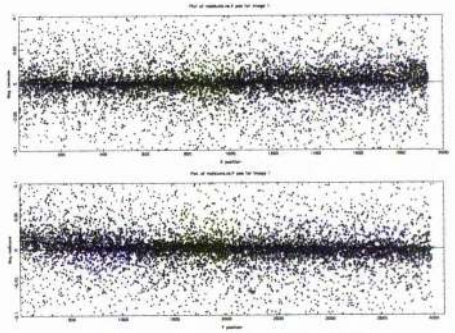

(f) Variable "Penny2" PSF

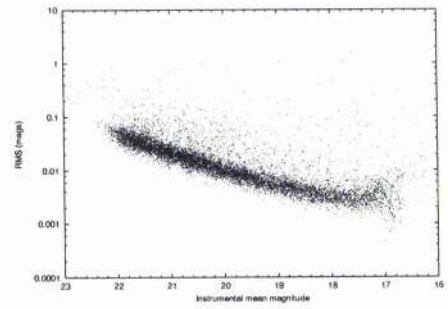

(g) Position variable PSF/zero points

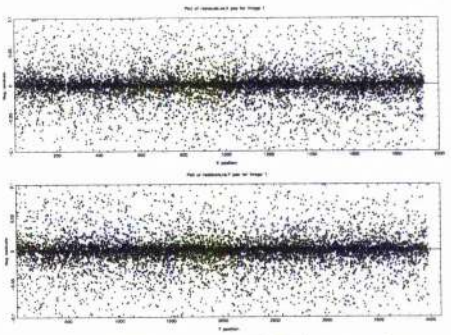

(h) Position variable PSF/zero points

Figure 4.1: Plots of RMS .vs. mean magnitude (left-hand column) and magnitude residuals .vs. x, y pixel position (right-hand column) for successively more advanced reduction and post-processing.

etc., stars close together should be similarly affected. Of course, stars of different colours would be differently affected by such extinction, but this is a secondary effect since a filter was used. Sectors of this size were decided upon after some experimentation as the best balance between considering the variations over small regions of the images and having sectors that incorporate enough stars to calculate meaningful statistics.

The zero points for each sector of each image are calculated as follows. The mean magnitudes and RMS of all the stars throughout the dataset are first calculated, as before. All stars within the given sector with magnitudes in the range $17\overset{m}{.}0 - 20\overset{m}{.}0$ are then identified and the magnitude residuals calculated.

The uncertainty on $\delta m(i,j)$ equals the quadrature sum of the uncertainties on $m(i,j)$ and $m_o(j)$. The median $med_{\delta m}$ of all the $\delta m(i,j)$ values for this sector is then found, along with the weighted standard deviation, $\sigma_{\delta m}$. The median is used in this first instance in order to be less sensitive to outliers. The mean value of these δm values is then calculated, weighted with the inverse varience uncertainty on each $\delta m(j)$, and rejecting all stars which do not meet the criterion:

$$(med_{\Delta m} - \sigma_{\Delta m}) < \Delta m(i,j) < (med_{\Delta m} + \sigma_{\Delta m}). \tag{4.6}$$

This mean is taken to be the magnitude zero point $ZP(s,i)$ of sector s in the current image.

The procedure is iterated by calculating each star's magnitude according to the formula:

$$m(i,j) = m_{\mathrm{DAOPHOT}}(i,j) - ZP(s,i), \tag{4.7}$$

starting with all $ZP(s,i) = 0.0$. The mean stellar magnitude is calculated from the resulting $m(i,j)$, from which the zero points are recalculated, and so on, until the mean magnitudes of all stars in that sector change by less than $0\overset{m}{.}001$ between iterations. The procedure then moves onto the next image sector.

Comparable results from this post-processing are presented in Figures 4.1(g) and

4.1(h). I find that the last of the positional dependency is adequately removed by this technique.

4.2.5.2 Catching the Cosmic Rays

Cosmic ray hits at the position of a star during an exposure are partly removed by DAOPHOT's PSF fit - the software employs a procedure which de-weights any point which does not converge towards the model as it is fitted. Nevertheless, some cosmic ray hits are visible in the lightcurves which, due to their high amplitude, can disrupt the post-processing.

Unambiguously identifying and removing cosmic ray hits can be difficult, since any dataset contains statistical outliers and I want to avoid removing good datapoints as much as possible. With this in mind, my post-processing code employs the following, rather conservative approach.

For a given star j, the code works its way through the lightcurve taking each image i at a time, using the datapoints on either side to calculate the local mean $\overline{m_{local}}$ and standard deviation σ_{local} in order to 'predict' the value of the mid-point. If the actual magnitude of the mid-datapoint $m(i,j)$ passes the following condition:

$$m(i,j) < \overline{m_{local}} - 5\sigma_{local}, \tag{4.8}$$

then the datapoint is identified as a cosmic ray hit and the code removes the point from the data. The whole procedure is then repeated, removing the greatest outlier each time until the lightcurve RMS changes by less than 1×10^{-5}.

The post-processing code applies this algorithm in the following way. Once the zero point-corrected magnitudes of all stars have been calculated according to Equation 4.7, the lightcurves are 'cleaned' of cosmic rays using the procedure described above. The code then goes on to calculate the zero points in the usual way, which are then applied to the data and so on. As the code iterates, no datapoint is permanently removed from a lightcurve until the final iteration. In this way, as the mean magnitude of a star shifts from one iteration to the next, all the datapoints are re-tested for inclusion so as not to exclude good data.

For the sake of clarity, this stage of the pipeline is hence forward referred to as the "self-calibration" of the data.

4.3 Minimising the Systematic Residuals

At this stage in the process, the lightcurves can show some residual systematic scatter, mostly due to periods of poor seeing, high sky background, etc. The following procedure is adopted in order to minimise this effect.

Each lightcurve is correlated with every other lightcurve in order to identify the closest matches. However, the purpose here is to find those *constant* lightcurves which most closely match the pattern of systematic *residuals* rather than the most closely matching *lightcurve*. This is particularly important with variable stars, where one W UMa lightcurve would correlate very well with other W UMas for example though this would not necessarily reproduce the pattern of residuals. To avoid this problem, the correlation co-efficient, ρ, is weighted by the product of the RMS values of both the current working lightcurve and that of the matching lightcurve:

$$\rho_w = \frac{\rho}{RMS(star_1).RMS(star_2)}. \tag{4.9}$$

The values of ρ_w for all stars relative to the working lightcurve are then sorted in order to identify the twenty most positive correlations. The residuals of these lightcurves (each lightcurve minus its own mean value) are then summed to obtain an estimate of the systematic residuals in each image $res(i)$:

$$res(i) = \frac{\sum_{j=1}^{N_*} \left(\frac{m(i,j) - \overline{m}(j)}{\sigma(i,j)} \right)^2}{\sum_{j=1}^{N_*} \left(\frac{1}{\sigma(i,j)^2} \right)}. \tag{4.10}$$

These residuals are then fitted to the working lightcurve by the following χ^2-minimisation technique. The model fitted to the lightcurve can be represented as:

$$\begin{aligned} m(i,j) &= m_o(j) + \Delta m.res(i) \\ &= \sum_{n=1}^{Np} P_n.C_n, \end{aligned} \tag{4.11}$$

where the adjusted parameters, P_n are the offset magnitude $m_o(j)$ and amplitude Δm. Np is the number of parameters while N_{im} is the number of images. The goodness of the fit is then calculated from the χ^2:

$$\chi^2 = \sum_{i=1}^{N_{im}} \left(\frac{m(i,j) - \sum_{n=1}^{Np} P_n.C_n}{\sigma(i,j)} \right)^2. \tag{4.12}$$

The values of the parameters for the best fit model can be derived by equating the first derivative of Equation 4.12 with respect to each parameter to zero, giving:

$$\sum_{i=1}^{Nim} \frac{m(i,j)}{\sigma(i,j)^2}.C_m = P_n. \sum_{i=1}^{Nim} \frac{C_n.C_m}{\sigma(i,j)^2}, \tag{4.13}$$

which may be conveniently represented in matrix form as:

$$\mathbf{b} = \mathbf{P}.\mathbf{M}. \tag{4.14}$$

It is a simple matter to solve the equation:

$$\mathbf{P} = \mathbf{b}.\mathbf{M^{-1}}, \tag{4.15}$$

algebraically to give the values of the best fit parameters $\mathbf{P}$:

$$\begin{aligned} P_1 &= b_{11}.detM.M_{22} - b_{21}.detM.M_{21} \\ P_2 &= b_{21}.detM.M_{11} - b_{11}.detM.M_{12}. \end{aligned} \tag{4.16}$$

This produces the mean magnitude and amplitude factors which best fit the pattern of residuals to the working lightcurve. The model is multiplied by the amplitude factor and subtracted in order to remove the systematic residuals.

Following this processing, the precision achieved is typically very close to the theoretical limit. This is discussed further in Section 5.

4.3.1 Astrometry

In order to provide RA and Dec positions for any stars for which follow-up observations might prove to be interesting, an astrometric fit to the INT data was performed. A Digital Sky Survey–II image covering the INT CCD field of view was obtained from the ESO Online Digitized Sky Survey webpage[2], and a list of star x,y positions was identified from this image using the PISAFIND task within the PISA package (Draper & Eaton 1999). A list of stars covering the whole frame was then identified from the Guide Star Catalogue 2.1[3] (Morrison et al. 2001), and these RAs and Decs were matched with their PISAFIND x,y positions. This list was fed into ASTROM (Wallace 1998), in order to produce more accurate local RA and Dec positions for all the stars identified in the DSS frame. Around 100 stars common to the DSS image and the INT reference frame were then identified, and their INT x,y positions and RAs and Decs were fed into ASTROM using an 8-parameter solution to calculate RA and Dec positions for all the stars found in the INT reference frame plus the field centre coordinates. The radial distortion coefficient required for this solution was taken from the Cambridge Astronomical Survey Unit webpage[4]

4.4 Testing the Pipeline

Most of the software used in the pipeline is part of either the STARLINK or IRAF collections. As such, the pre-processing and DAOPHOT reduction of the data is carried out using well-tested and documented software. My post-processing software, on the other hand, is new. How can I be sure that the results it produces are genuine?

[2]http://archive.eso.org/dss/dss

[3]http://www-gsss.stsci.edu/gsc/GSChome.htm

[4]http://www.ast.cam.ac.uk/~mike/casu/WFCsur/distortion.html

To address this question, I have developed software to simulate the pipeline photometry output of DAOPHOT for the INT data. The advantage of knowing the exact nature of all the noise sources in the data allows me to assess the performance of the post-processing software. These noise sources, described below have therefore been designed to be as close to reality as possible.

4.4.1 FAKEGEN: Data Simulation Software

The DAOPHOT-based output of the reduction pipeline is in the form of one text-file per image listing the magnitude, uncertainty, position and ID number of each star measured in that image. FAKEGEN was designed to produce similar files, simulating star lightcurves by the following process:

- The first stage is to generate a set of HJDs of the times for the 'images'. With a cycle time of about an hour, the INT dataset characteristically has between 16 and 25 images per cluster per night. FAKEGEN generates pairs of HJDs during the night and calculates the correponding airmass of the cluster from the INT. The code checks that the cluster was visible, ie had an airmass less than 2. If the cluster is not visible, the code moves on to the next night, generating appropriate numbers of images per night. This routine also simulates the INT observing strategy by generating up to 10 nights of observations in a single run. If more images are required, separate runs of up to 10 nights are generated spaced at one month intervals.
- The next stage is to generate random mean magnitudes for the required number of stars, according to a distribution derived from the INT data.
- Once the mean magnitude of each star has been established, FAKEGEN generates a magnitude per image using a Gaussian distribution centred on the star's mean and with a standard deviation computed from the theoretical RMS of the INT data, and assigns magnitude error bars on each point from similar theoretical calculations (described in Section 4.4.2).
- Pixel positions for each star are then generated by randomly assigning mean x,y values to each star within the limits of the image, and generating ~ 0.5–pixel shifts in a Gaussian random distribution to simulate the small differences in position due to seeing fluctuations in each image.

- A user-choosen number of variable stars can be added to the dataset at this point by convolving a star lightcurve (selected at random) with a sine function (for a BY Draconis-type lightcurve) or a sum of a sine and a cosine for an eclipsing binary for randomly generated periods and amplitudes. Transits can also be included in the dataset by adding the bottom half of a cosine function.

- FAKEGEN accounts for the effects of atmospheric extinction by applying the Bouguer Law (Jimenez, Gonzalez Jorge & Rabello-Soares 1998):

$$m = m_o + 1.086.K_\lambda.A, \tag{4.17}$$

where m is the apparent magnitude of a star of magnitude m_o above the atmosphere, K_λ is the extinction coefficient for the given wavelength λ, and A is the current airmass of the target.

I adopted a value of $K_\lambda = 0.075$ for a central wavelength of 680 nm and filter width of 10 nm for borderline clear/cloudy conditions from Jimenez, Gonzalez Jorge & Rabello-Soares (1998). This was the closest listed wavelength to that of the Sloan r' filter (central λ = 624 nm, width = 134.7 nm) with which the INT observations were made. In practise, this difference will mean that magnitude extinction in the fake data will differ slightly from those in the real data. Nevertheless, the lightcurve of every star still follows the inverse quadratic-shaped curve throughout the night. As the post-processing code is not filter-specific, these lightcurves provide a suitable test of that code.

- To simulate the effects of cosmic ray hits, FAKEGEN generates a certain number of cosmic ray hits proportional to the number of stars and images. It then chooses star and image numbers at random to which the cosmic rays are added, of randomly generated amplitude (between 0 and 2 mags).

- FAKEGEN also simulates the effects of having a pattern of magnitude residuals systematically affecting all lightcurves to a varying degree. This might be caused by, for example, night-to-night variations in seeing, Moon light etc. Systematic residuals are added by generating a random number for each night of data. This number is set to zero 65 percent of the time so that, as with the real data, some nights will be more affected by residual scatter than others. For each image within each night of data,

this value is then added to a random number generated from a uniform distribution to lie between 0 – 0.01. This gives a "residuals pattern" lightcurve, scattered about zero. This pattern is then multiplied by a final random factor (lying between 0 and 1) in order to vary the amplitude of the systematic residuals affecting each star. The pattern is then added to all the generated star lightcurves.

- When DAOPHOT produces the output files, the stars are not always in the same order, and if a star was not measured in that image for whatever reason, it will not produce an entry at all. To simulate this, the data are passed through a scrambling routine which results in the order of the star measurements for each image being re-sorted at random. Separate arrays of the data prior to scrambling and the addition of noise are kept to provide a 'control' to compare to the output of the post-processing code.

The FAKEGEN code produces all same outputs as the post-processing code so that comparison can be made: predictions of the RMS and mean magnitudes for all stars, plots of their lightcurves both with noise sources added and without. It also produces the same text-files of star measurements of the fake data per image that DAOPHOT produces so that the fake data can be run through the post-processing code.

4.4.2 The Noise Model

An integral and important part of generating fake datasets is the calculation of realistic magnitude errors for each datapoint, and by extension, predicting the RMS scatter expected in the lightcurve of a star of given magnitude. FAKEGEN addresses these questions by considering a purely Gaussian, two dimensional PSF. The volume contained within this function is given by V_G:

$$V_G = \int_{-\infty}^{+\infty} \int_{-\infty}^{+\infty} \exp\left(-\frac{x^2+y^2}{2\Delta^2}\right) dxdy, \tag{4.18}$$

where Δ is the standard deviation of the Gaussian which is integrated over all pixels x, y out to infinity. This volume is equivalent to the volume of a cylinder of unit height and radius Δ so that the volume of the cylinder, $V_{Cyl} = 2\pi\Delta^2$. A normalised Gaussian PSF function may therefore be written:

$$P(x,y) = \frac{1}{2\pi\Delta^2} \exp - \left(\frac{\frac{1}{2}(x^2+y^2)}{\Delta^2} \right). \tag{4.19}$$

During the PSF fitting process, this function is scaled to fit the flux of a star such that the flux contributed by each pixel equals $P(x,y).f_{star}$. f_{xy} is the number of counts in pixel x, y. The flux measured by PSF fitting of this star is therefore given by the weighted mean of the flux over all affected pixels:

$$f_{star} = \frac{\sum_{xy}(P_{xy}f_{xy}/\sigma^2_{xy})}{\sum_{xy}(P^2_{xy}/\sigma^2_{xy})}, \tag{4.20}$$

where:

$$\sigma^2_{xy} = \sigma^2_o + \frac{f_{sky} + f_{star}.P_{xy}}{G}, \tag{4.21}$$

where σ_{xy} is the total noise on the flux in pixel x,y. This consists of a number of independent noise sources: σ_o, the readout noise of the CCD, the noise due to the background flux from the sky, f_{sky} and the inherent photon noise from the star flux, f_{star}. G is the gain of the CCD device used in photons/ADU.

The variance of this weighted mean (and consequently the uncertainty on the flux measurement) is then given by the standard equation:

$$\sigma(f_*)^2 = \mathrm{Var(f_{star})} = \frac{1}{\sum_{\mathrm{xy}}(\mathrm{P^2_{xy}}/\sigma^2_{\mathrm{xy}})} \tag{4.22}$$

FAKEGEN calculates the error by summing over a series of 1000 annuli of area $2\pi r dr$ begining at the centrepoint of the star and extending out to a radius of 6 pixels. Since the full-width-half-maximum (fwhm) of stellar images in the INT data was typically ~ 3 pixels, this maximum radius includes the vast majority of the star's light. Equation 4.19 is then used to compute the value of $P(x,y)$ and hence the value of $P(x,y)^2.dxdy$ for each pixel. The quantity Δ is estimated from the full-width-half-maximum, S, of the Gaussian. The hwhm $(S/2)$ of the function is given by:

$$\begin{aligned} \exp\left(-1/2\frac{(x^2+y^2)}{\Delta^2}\right) &= \frac{1}{2} \\ -\frac{1}{2}\left(\frac{S/2}{\Delta^2}\right) &= \ln 2. \end{aligned} \tag{4.23}$$

From this, Δ can be determined by using the image seeing to estimate the fwhm:

$$\Delta = \frac{S}{\sqrt{8\ln(2)}}. \tag{4.24}$$

The variance on f_{star} is given by Equation 4.22, where the star flux and $P(x,y)$ are known and the readout noise, sky flux per pixel and gain are all reasonable estimates derived from typical INT values. Once the sum is completed, the uncertainty on the datapoint is added in quadrature to the systematic noise (a user-set parameter of the order of 3–4 millimags). The uncertainty in the flux, f, measurement is converted to an error in magnitudes by considering that:

$$m = m_o - 2.5\log(f) = m_o - 2.5\left(\frac{\ln(f)}{\ln(10)}\right). \tag{4.25}$$

By differentiating with respect to the flux we obtain:

$$\begin{aligned} dm &= \frac{2.5}{\ln(10)}.\frac{1}{f}.df, \\ \sigma(m) &= \frac{2.5}{\ln(10)}.\frac{\sigma(f)}{f}. \end{aligned} \tag{4.26}$$

4.4.3 Pipeline Performance with Fake Data

Figures 4.2 and 4.3 show a selection of fake lightcurves produced by FAKEGEN. The left-hand panels show the generated lightcurves before extraneous noise sources were added; ie, what the post-processing code should ideally produce. These lightcurves include only the Gaussian noise appropriate to a star of that magnitude. For the sake of clarity I shall refer to these as the "ideal" lightcurves. The right-hand panels show the lightcurves with

added variations due to atmospheric extinction, systematic residuals and cosmic ray hits added at random. The first four lightcurves illustrate typical constant stars with mean brightnesses at roughly one magnitude intervals. The latter four stars in this example are typical examples of the four different types of variable stars included in the dataset: W UMa and Algol-type eclipsing binaries, BY Draconis-type stars and planetary transit events. The arrows in plots of the transit lightcurve indicate when the transits occur.

These stars were included as part of a 9000-star, 350-image dataset that was run first through the self-calibration code. Among the output of this code are the lightcurves of all the stars; Figures 4.4 and 4.5 (left-hand panel) show the lightcurves of our example stars produced by this code for comparison. In the right-hand panel, I have subtracted the original noiseless data from this lightcurve and plotted the residuals on the same magnitude scale, offset to zero.

The same dataset, now self-calibrated, was then run through the systematics compensating stage of the pipeline. Figures 4.6 and 4.7 show lightcurves comparable to those in Figures 4.4 and 4.5 after this final stage.

These figures show that the constant-star lightcurves retrieved by the self-calibrating code match still show signs of systematic residuals relative to the 'ideal' lightcurves, but that the scatter in the residuals of the large-amplitude variables is well below the amplitude of the variations. After compensating for these residuals, Figures 4.6 and 4.7 show a much reduced scatter in the cases where most of the lightcurve is constant (those for constant stars plus transits and Algol-type eclipsing binaries). The lightcurves for the large amplitude variables however, do not benefit from this technique because the data correlates poorly with all other star lightcurves.

The example of the transit lightcurve is particularly interesting. In the right-hand panels of Figures 4.3 and 4.5 for this star, the transits are all but indistinguishable from the noise variations in the lightcurve. Nevertheless, Figure 4.7 shows that the transits are retrieved by the post-processing.

A more general test of the code is to plot the RMS and reduced χ^2 of each star's lightcurve against the mean magnitude, using $\frac{1}{\sigma(i,j)^2}$ as the weight. Figures 4.8(a) and 4.8(b) show such plots produced by FAKEGEN for the dataset before the noise sources were added. As a result, these plots represent the ideal that the post-processing code should

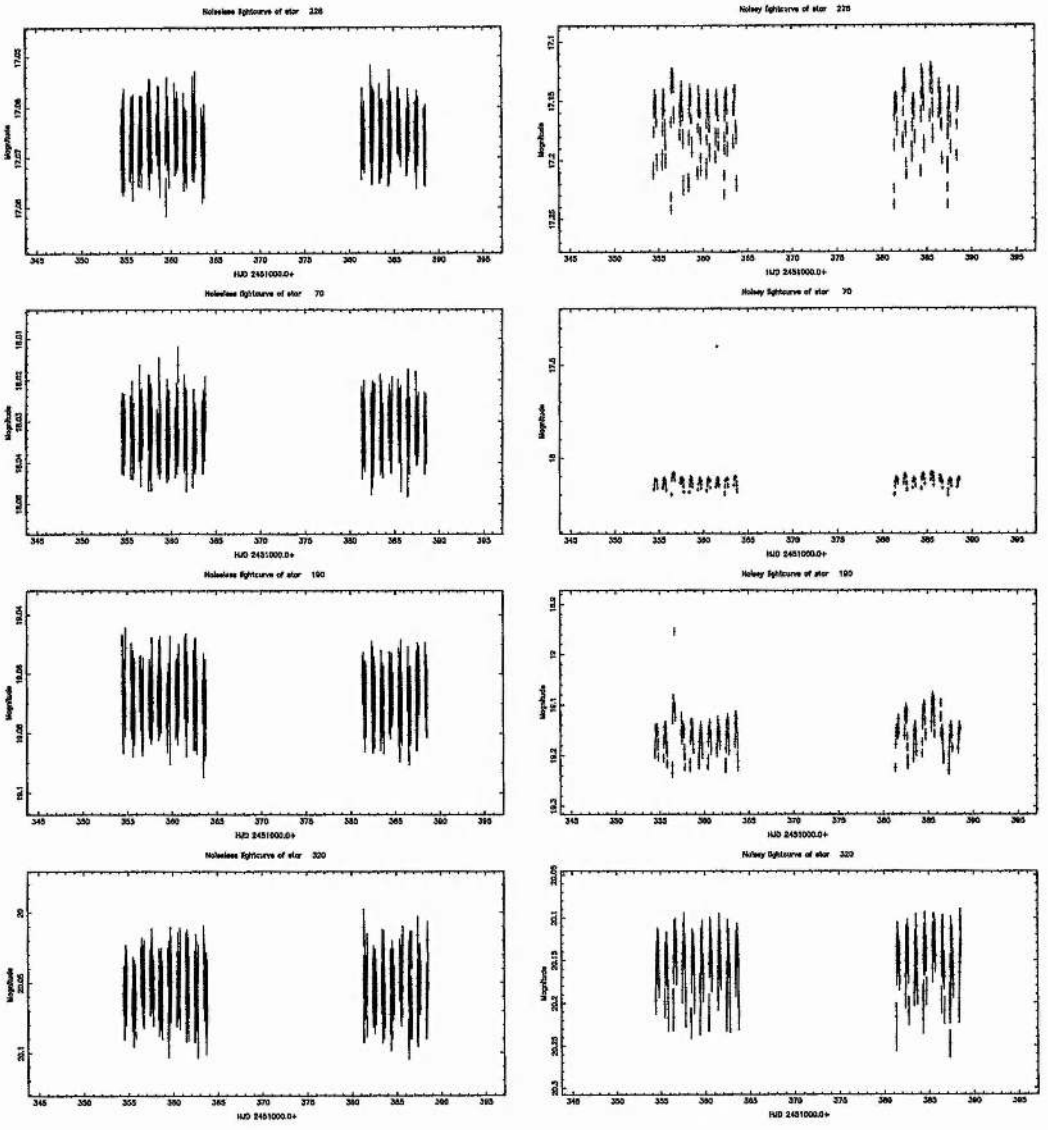

Figure 4.2: FAKEGEN-generated example lightcurves. The left-hand panels show the ideal lightcurves. The right hand panels show the same lightcurves with various noise sources added: atmospheric extinction, cosmic rays and systematic residuals.

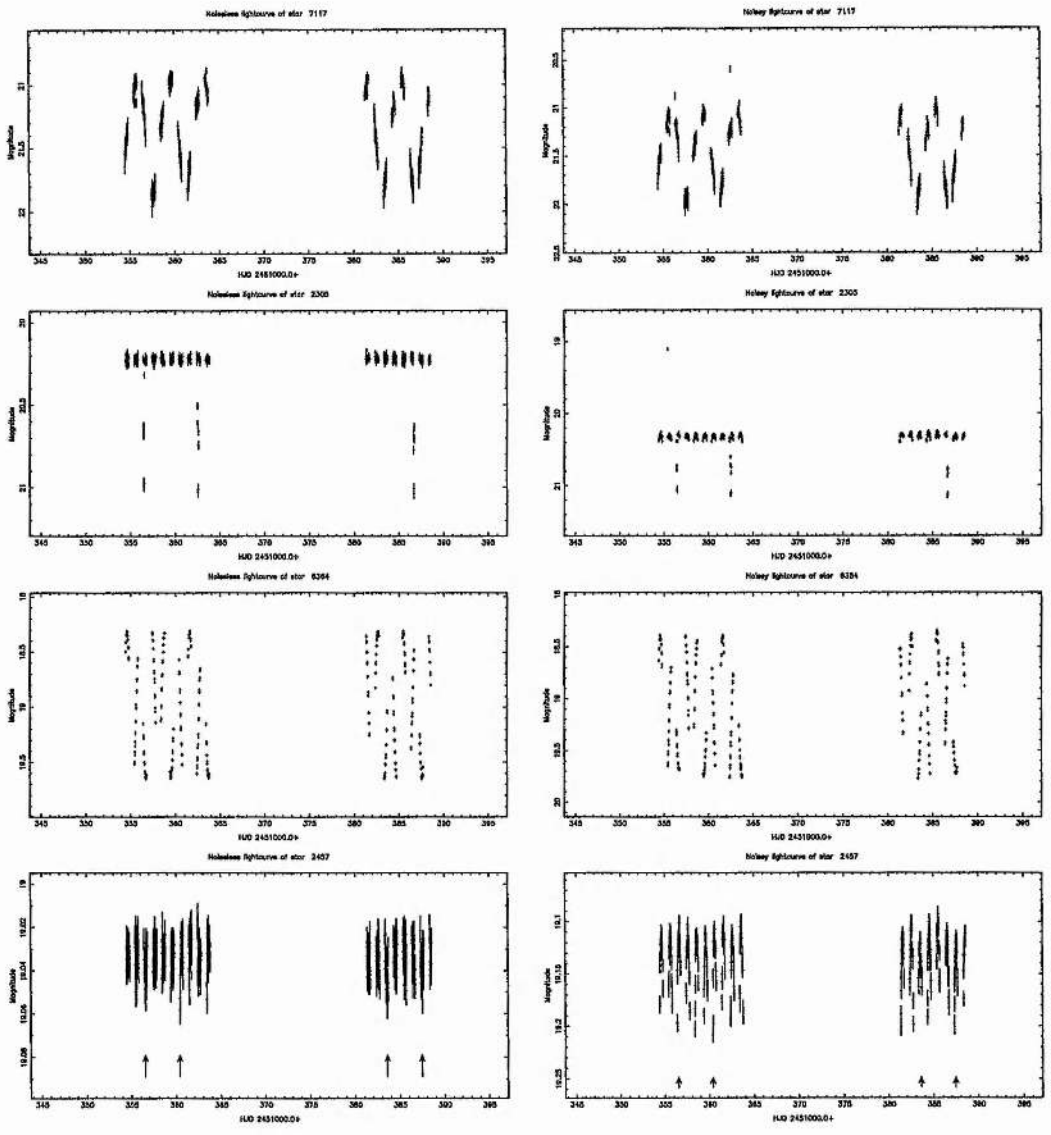

Figure 4.3: FAKEGEN-generated example lightcurves. The left-hand panels show the true lightcurves. The right hand panels show the same lightcurves with various noise sources added: atmospheric extinction, cosmic rays and systematic residuals. The variable types are, in order from the top, W UMa, Algol-type eclipsing binaries, BY Dra star and planetary transit. The arrows in the transit lightcurve indicate when the transits occur.

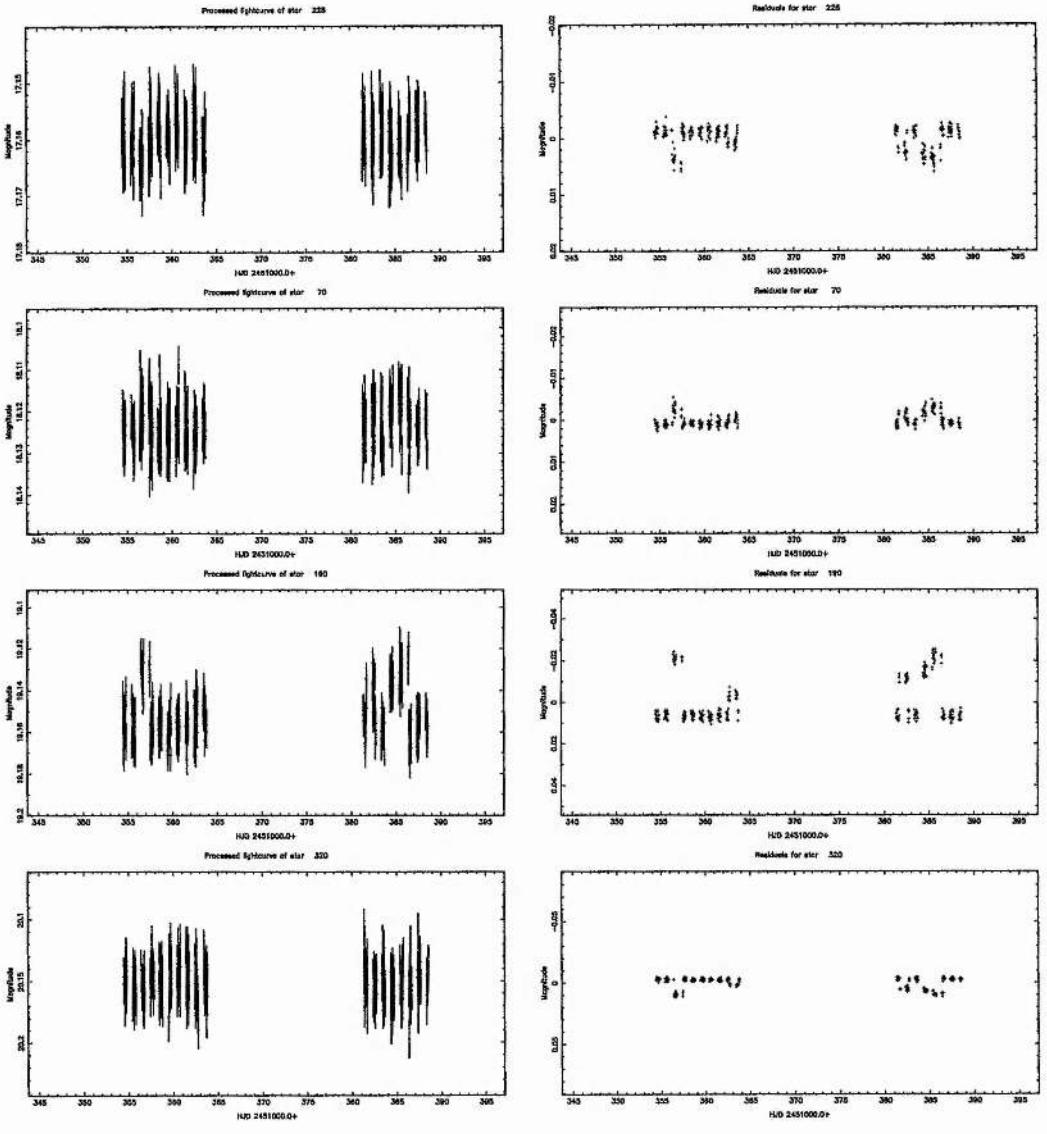

Figure 4.4: The same set of example stars after self-calibration with the pipeline. The left-hand panels show the retrieved lightcurves while the right-hand panels show the residuals between the retrieved and original (noiseless) lightcurves, displayed on the same axis range for comparison.

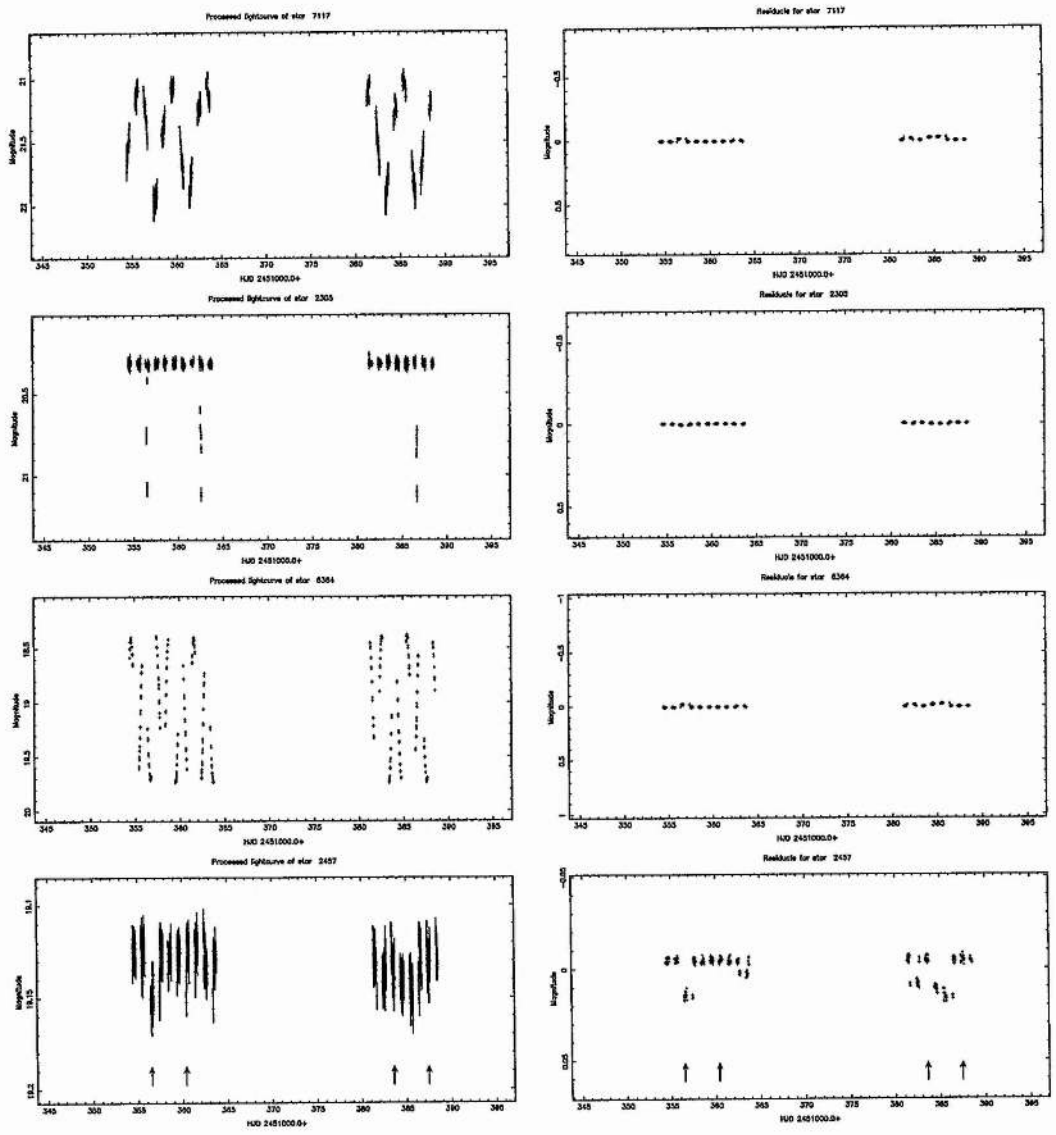

Figure 4.5: The same set of example stars after self-calibration with the pipeline (continued).

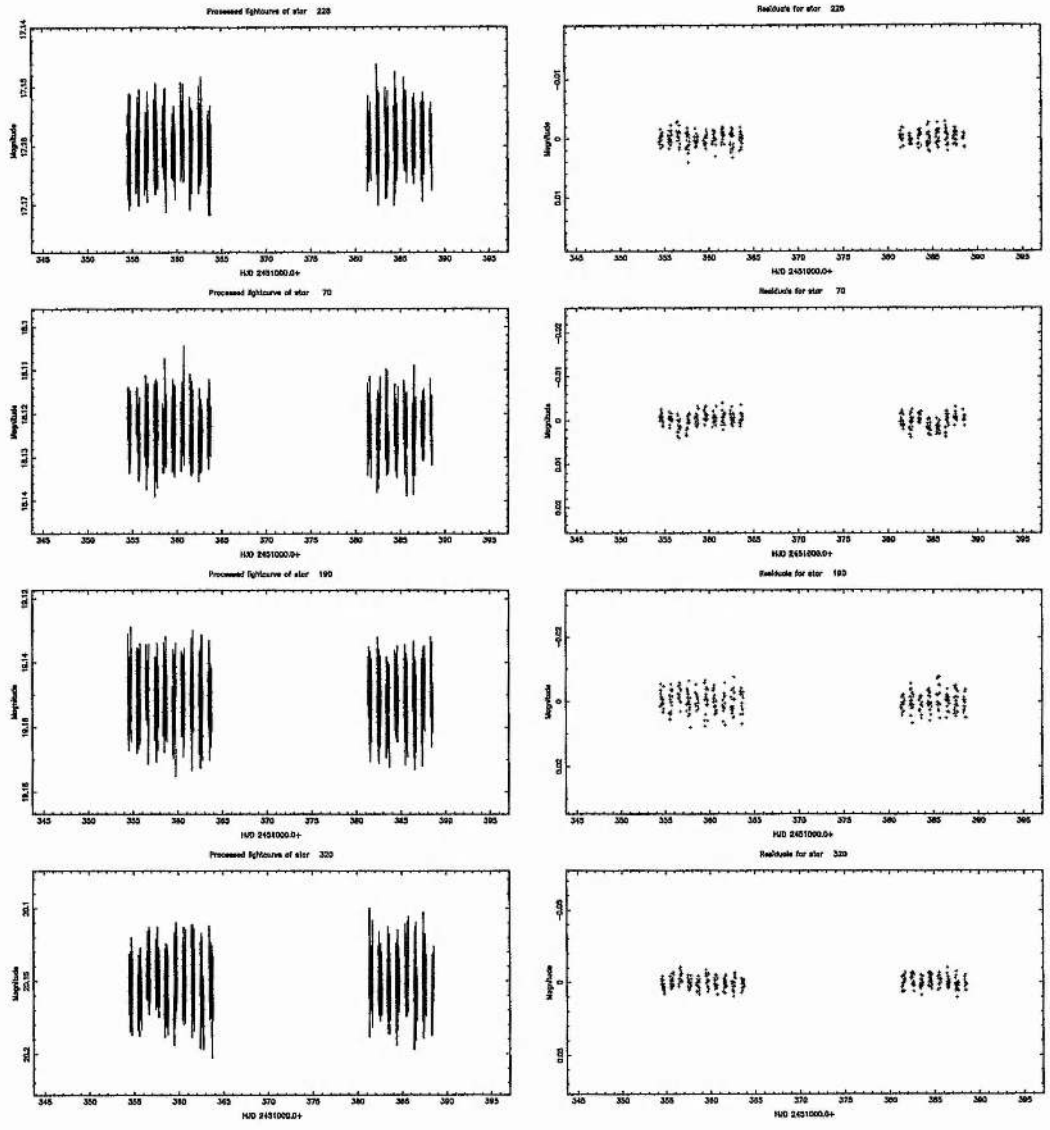

Figure 4.6: The same set of example stars after compensating for systematic residuals. The left-hand panels show the retrieved lightcurves while the right-hand panels show the residuals between the retrieved and original (noiseless) lightcurves, displayed on the same axis range for comparison.

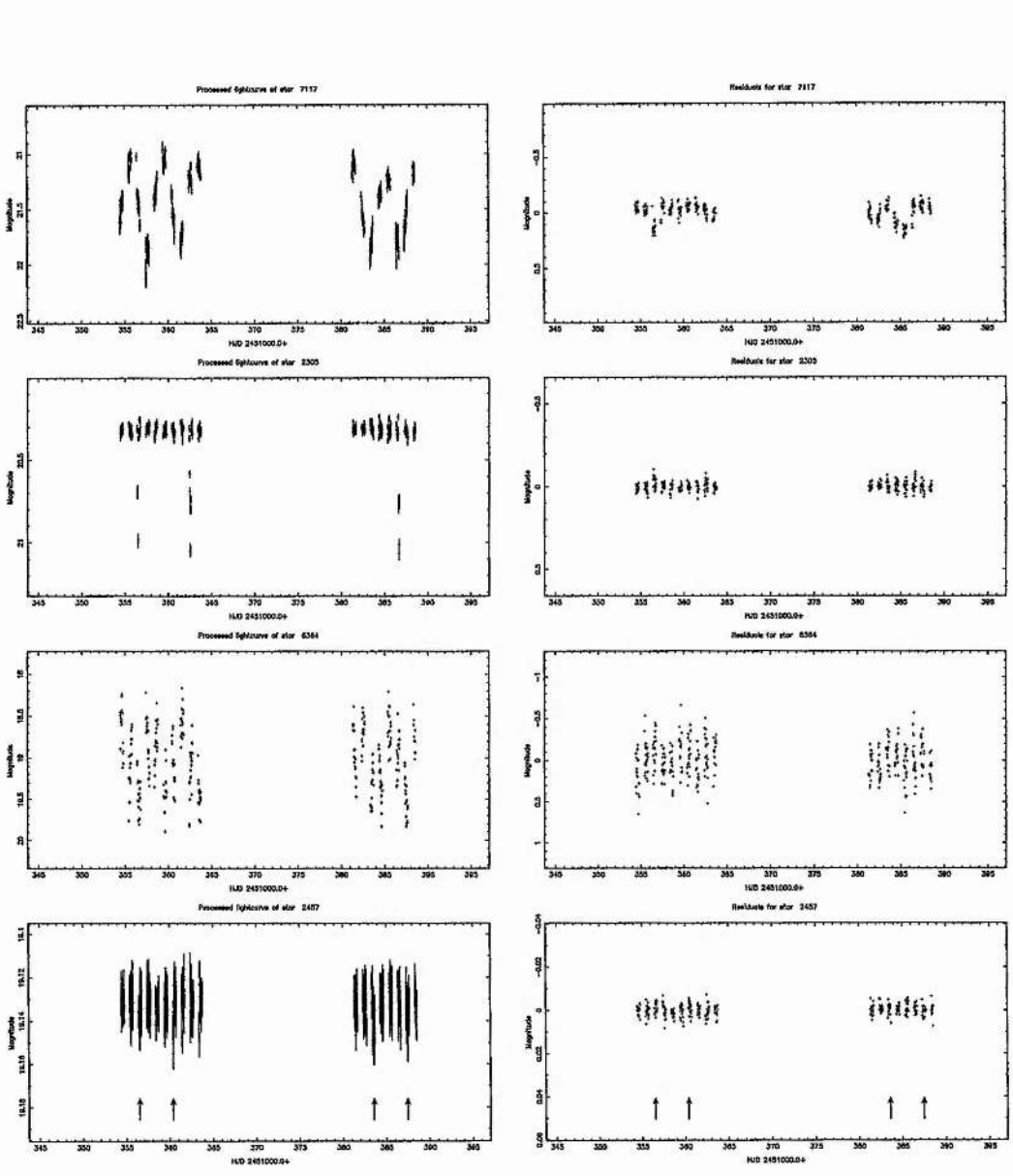

Figure 4.7: The same set of example stars after compensating for systematic residuals (continued).

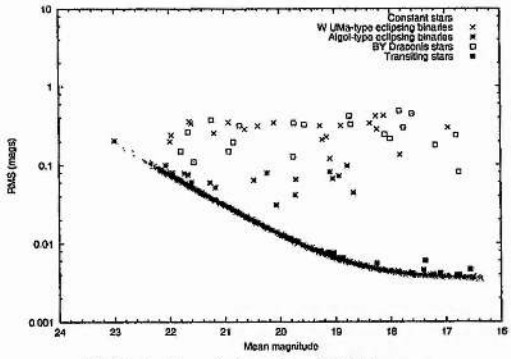

(a) Noiseless fake-data RMS curve

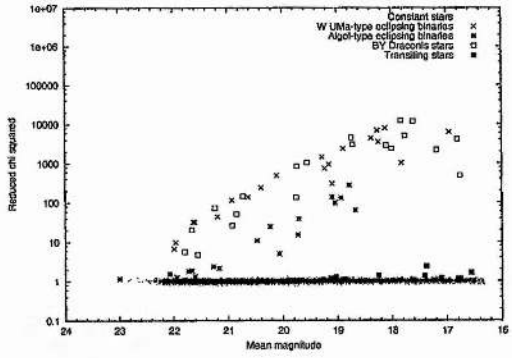

(b) Noiseless fake-data reduced chi squared curve

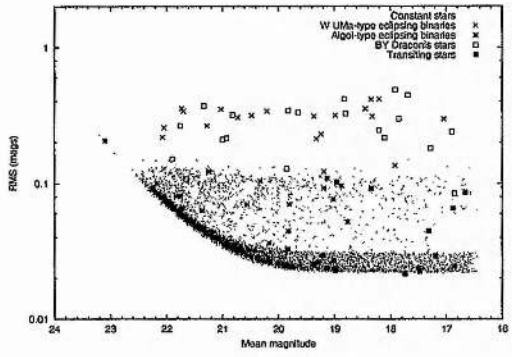

(c) Fake-data RMS curve including noise sources

Figure 4.8: RMS and reduced χ^2 plots of a 9000-star, 350-image fake dataset including 20 variables of each of the types shown. The top two curves were plotted before noise sources such as airmass extinction and cosmic ray hits were added to the data, while the curve below shows the noise-added RMS curve.

produce. The superimposed symbols represent the various types of fake variables included in the dataset.

The third plot, Figure 4.8(c) shows the RMS .vs. mean magnitude curve after the noise sources have been added. The effects of the noise sources are clearly visible: the large density of points immediately above the main curve is due to the systematics variations added while the fringe of points with higher RMS is due to the addition of cosmic rays of various amplitudes. Also the curve clearly levels off at around $0\overset{m}{.}035$; this is due to the nightly variation in magnitude due to atmospheric extinction. This is similarly consistant for all stars, colour terms not being included as the narrow filter band pass used in the real data makes these terms less important. For fainter stars the curve turns up as the

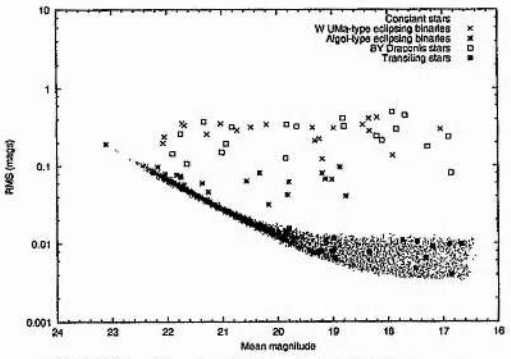

(a) Self-calibrated fake-data RMS curve

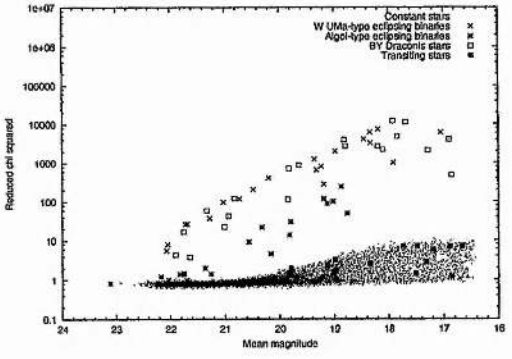

(b) Self-calibrated fake-data reduced chi squared curve

Figure 4.9: The RMS and reduced χ^2 plots produced after the self-calibrating code was applied to the same fake dataset (noise sources included). The positions of the variable stars are again highlighted.

sky background noise dominates.

Figure 4.9 shows RMS and reduced χ^2 curves plotted after the self-calibration code was applied to the fake dataset. While there are similarities between these and Figures 4.8(a) and 4.8(b) some important differences are immediately obvious. The self-calibration code is able to remove the realistic noise sources applied to the data reasonably well, but both RMS and reduced χ^2 curves are broader in the second pair of plots, indicating the presence of residual systematics.

Figures 4.10 show similar RMS and reduced χ^2 curves plotted after the compensation for systematic residuals. These plots compare favourably with the ideal plots in Figures 4.8(a) and 4.8(b).

These results indicate that the post-processing code performs very well, and does not introduce any systematic variations.

4.5 Summary

In this chapter I have described the data reduction pipeline and illustrated how it developed using the data subset. I have also described the simulation code developed to test the post-processing sections and displayed the quality of the results achievable using these codes. In

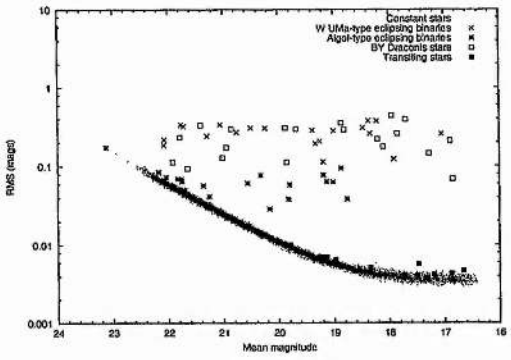

(a) Systematics compensated fake-data RMS curve

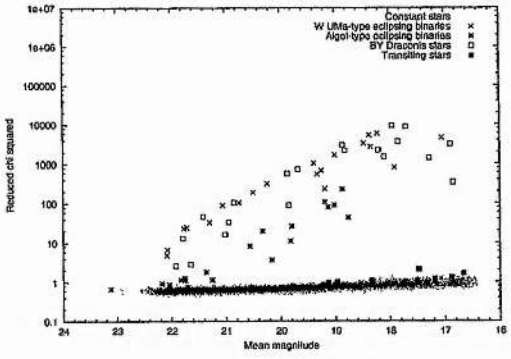

(b) Systematics compensated fake-data reduced chi squared curve

Figure 4.10: The RMS and reduced χ^2 plots produced after compensating for systematic residuals (noise sources included). The positions of the variable stars are again highlighted.

particular, Figure 4.2, when compared with Figure 4.4, shows that the very low amplitude transit events can be retrieved, even when the systematic errors completely obscure the transits in the un-processed lightcurve. Everything is now in place to begin the reduction of the full dataset.

CHAPTER 5

Results

5.1 Introduction

The data reduction pipeline described in Chapter 4 has been applied to reduce the NGC 6819 data for two of the four WFC CCDs (CCDs 2 and 4, refer to Figure 5.1). A total of 19 nights of data have been processed in each case: 1999/06/21–30 and 1999/07/21–31, the first and second runs respectively.

The pipeline deals with each CCDs data separately, as this approach is computationally convenienent. In the first sections I present and discuss the main photometric results before moving on to dealing with the detection of transits in Section 5.5.

5.2 Photometric Precision

Figure 5.2 shows the RMS against mean star magnitude diagrams for both CCDs. Both plots are superimposed with theoretical curves representing the contributions of various known noise sources. These were calculated in an almost identical manner to the noise models used in my simulations (described in Chapter 4), except that the sky background count, seeing etc, were measured for each image and these values were used to calculate the noise model.

The principal difference between these two fields can be seen at a glance from Figure 5.1. The CCD4 frame is dominated by the bright foreground star (HD 186307, V=$6\overset{m}{.}230$) and the bright central cluster stars. Together these cause a relatively high background making it difficult to observe faint stars. In contrast, the CCD2 field is less

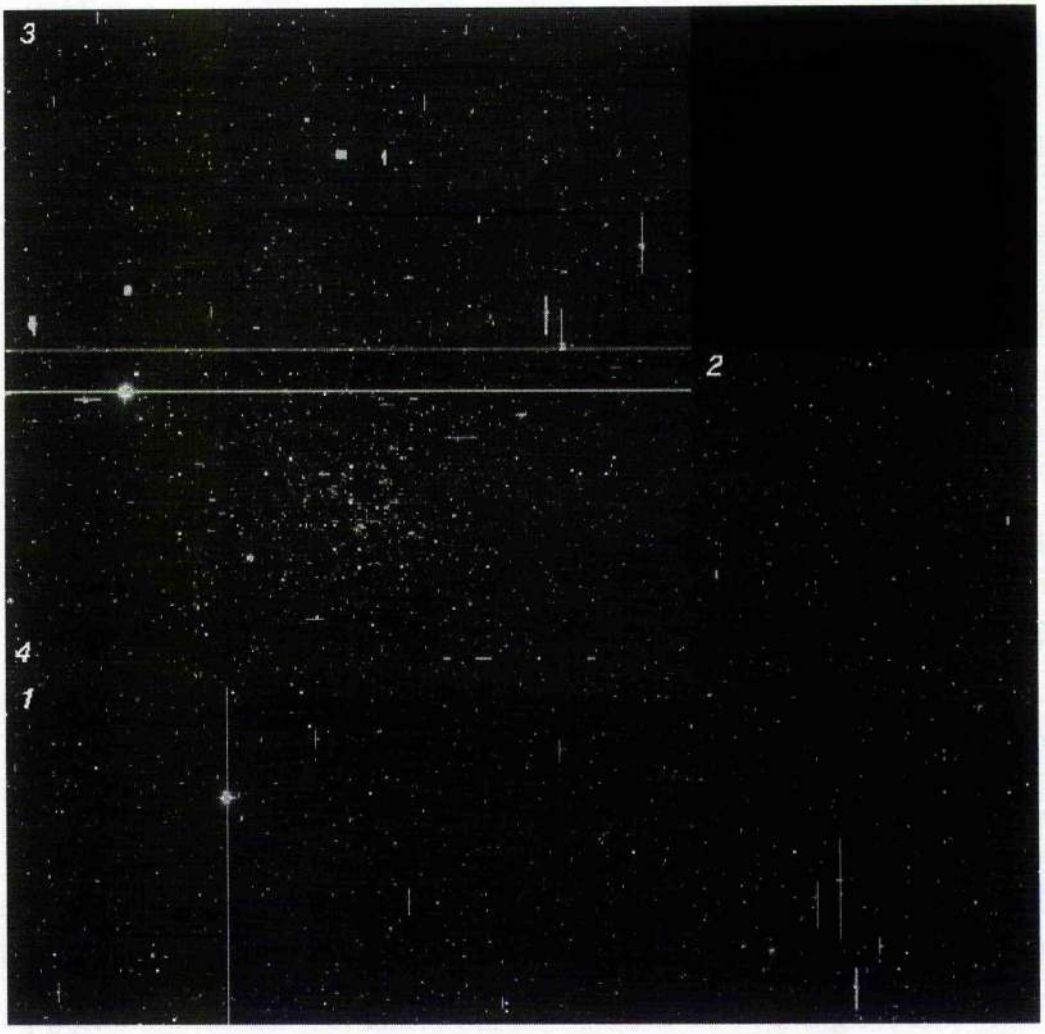

Figure 5.1: Mosaic image of NGC 6819 combining the four INT-WFC CCDs. The CCD numbers are given in the corners of the frames.

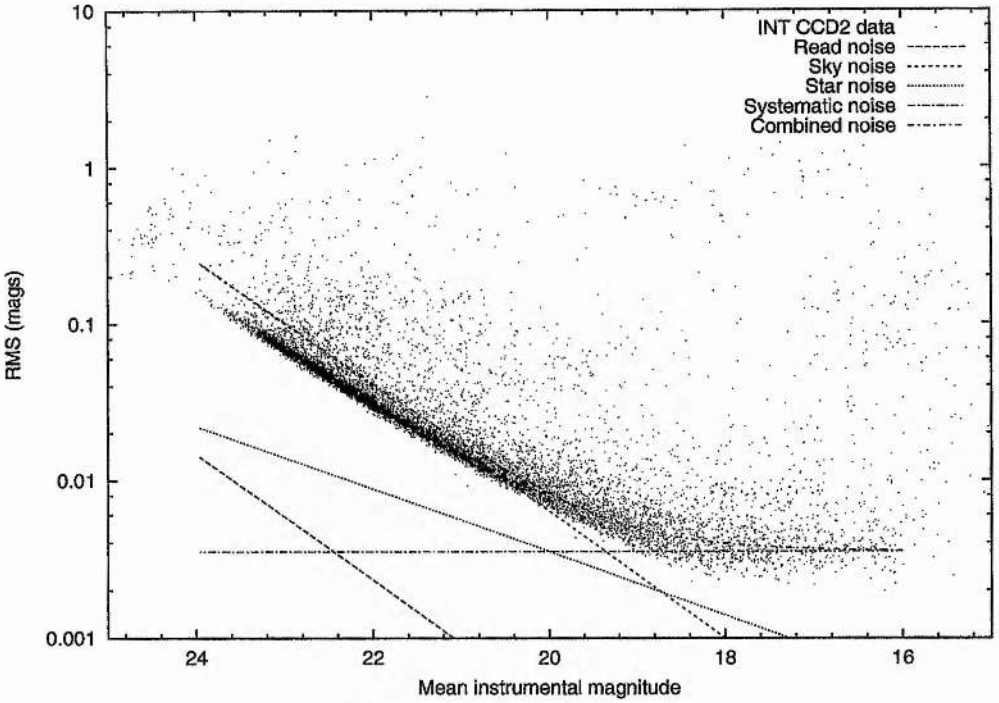

(a) RMS diagram for CCD-2

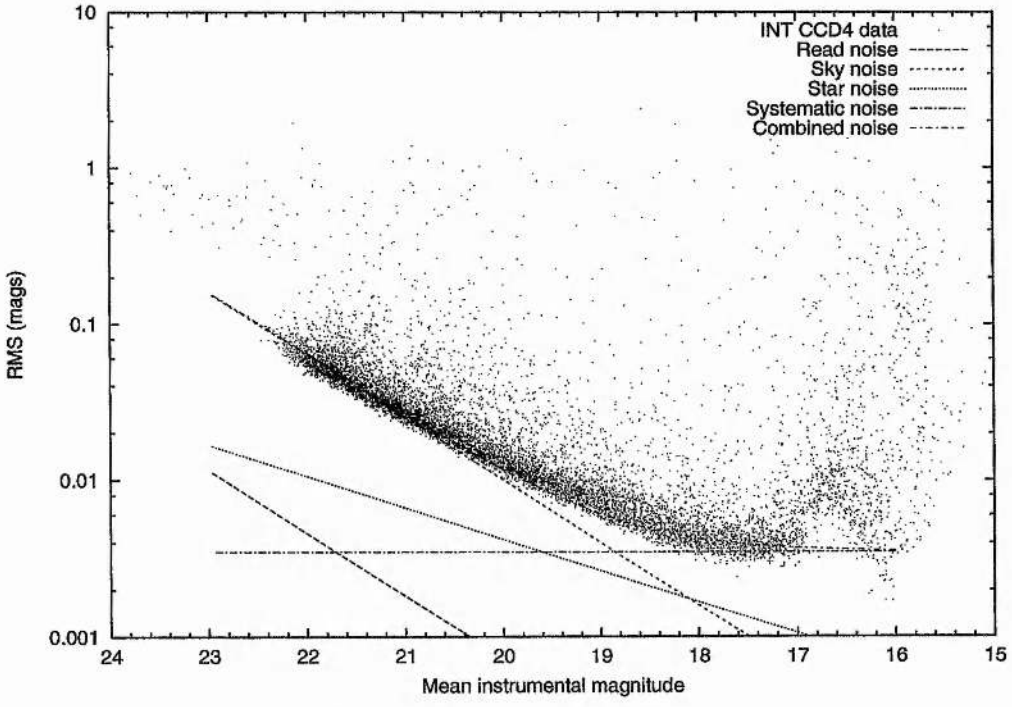

(b) RMS diagram for CCD-4

Figure 5.2: RMS against mean magnitude diagrams for CCDs 2 and 4. The superimposed curves indicate the contributions of various known noise sources.

dense and has no particularly bright stars, and so star magnitudes down to $\sim$ 24 mag have been well measured. This in turn highlights the growing gap between the noise model and the data at faint magnitudes. After investigation, I believe this to be due DAOPHOT over-estimating the magnitude errors on the datapoints.

It will immediately be seen from Figure 5.2 that the photometry of most stars is sky-noise limited, while that for stars brighter than $\sim$ 19 mag departs from the predicted Poisson-noise limit. The photometry for these brighter stars appears to be dominated by residual systematic noise at the level of $\sim$ 3.5 millimags. The origin of the noise is unknown, though possible causes include the effects of differential extinction on star of different colour. This limitation of ground-based photometry can be seen in work by other authors (see for example, Borucki et al. (2001)), who encounter systematic noise at similar levels of precision.

The important question is whether the precision is sufficient to detect planetary transits. This can be gauged by calculating the depth of transit (from Equation 2.11) caused by planets of various radii around stars of various spectral type, and plotting this against the apparent magnitude of the star at the distance of the cluster. These curves have been superimposed on the RMS diagrams for both CCDs in Figure 5.3. These plots show that for stars brighter than $\sim$ 19 mag, the scatter in the lightcurves is smaller than the depth of transits caused by planets of $\gtrsim 1\,\mathrm{R}_{jup}$ implying that these events should be apparent.

5.3 Colour Data

The detection of transit events requires only differential photometry in one filter. For this reason, virtually all the data taken was through the Sloan r' filter, although a small amount of other filter data was taken of each cluster.

5.3.1 The CFHT Colour Data

Coincidentally, however, during the course of this work, Kalirai et al. (2001a) published (non-time series) deep, wide-field photometry for NGC 6819 taken with the CFHT12K mosaic CCD camera on the Canada-France-Hawaii Telescope (hereafter CFHT) on Mauna

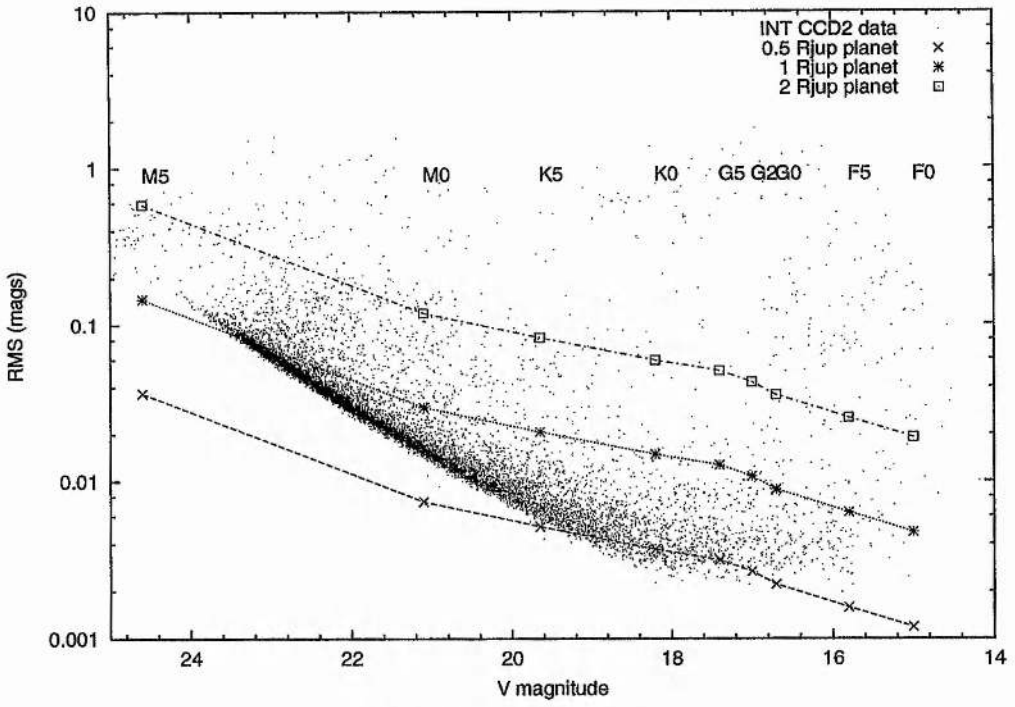

(a) RMS diagram for CCD-2

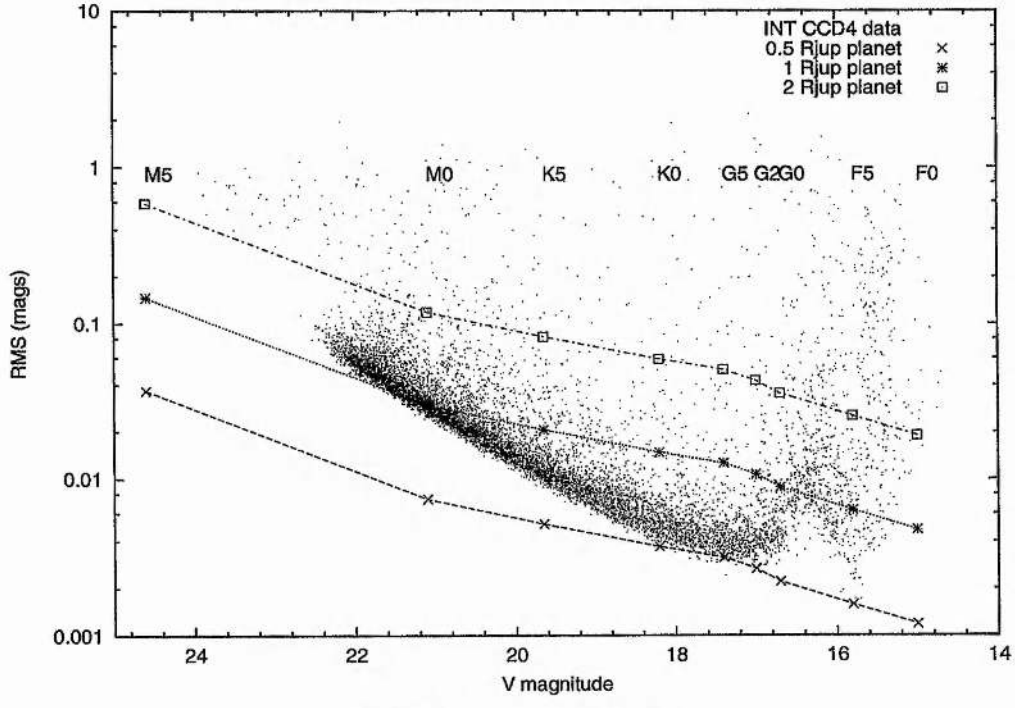

(b) RMS diagram for CCD-4

Figure 5.3: RMS curves for CCDs 2 and 4 superimposed with curves showing the predicted depths of transits for various planet and star radii.

Kea. Jasonjot Kalirai was kind enough to share this data with me (Kalirai 2001). Thanks to the increased light-gathering power of the CFHT, this data provides good quality calibrated photometry, particularly for the fainter stars. As this data was available, I have made use of it by identifying stars from the INT data. A full description of the CFHT dataset and reduction procedure is available in Kalirai et al. (2001b) and Kalirai et al. (2001a).

The photometric datafiles provided lists of star x,y pixel position (on the CFHT mosaic CCD camera), V magnitude and error, (B–V) and error and B, V stellarity indices. As no comparable WCS or RA/DEc coordinate data was available, it was necessary to compute the transformations between the x,y pixel positions from the CFHT CCDs which overlapped those of the INT.

I have developed my own software in order to identify the stars from the INT sample in the CFHT results. This software works by computing the following 6–parameter linear transformation between the INT and CFHT coordinates of about 8 reasonably bright, isolated stars manually identified in both datasets:

$$\begin{aligned} X_{CFHT} &= X_{INT} + p_1 + p_2.X_{INT} + p_3.Y_{INT} \\ Y_{CFHT} &= Y_{INT} + p_4 + p_5.X_{INT} + p_6.Y_{INT} \end{aligned} \tag{5.1}$$

The code then applies this transformation to the stars in the INT sample, and searches through the CFHT data to identify a star at that position. The predicted star positions are typically accurate to less than 1 CFHT pixel ($0.206''\,\mathrm{pix}^{-1}$), although if no star was found within a 4 pixel square box centred on the predicted coordinates, it was assumed that the star was not measured in the CFHT data. Furthermore, stars poorly measured in the INT data, without reliable values of weighted mean magnitude or RMS were also not identified in the CFHT colour data. From those stars where colour data was available, I have determined the relationships:

$$\begin{aligned} V &= 1.0604.r_{INT} - 1.9057 \ (CCD2), \\ V &= 1.0621.r_{INT} - 1.3239 \ (CCD4), \end{aligned} \tag{5.2}$$

between the INT instrumental magnitudes ($r_{\rm INT}$) and the calibrated V magnitudes from the CFHT. Using this relationship, I have been able to provide the roughly calibrated V magnitudes for stars without colour data. These magnitudes are noted in the appropriate tables.

It was also possible to derive a more accurate calibration, using the colour information:

$$\begin{aligned} V &= r_{INT} + 0.5159.(B-V) - 1.2136, \\ V &= r_{INT} + 0.4976.(B-V) - 0.6504. \end{aligned} \tag{5.3}$$

I have used these relations to ensure that the instrumental magnitude r_{INT} for each star, plus that for its check and comparison stars, was converted to a standardised system before the differential photometry was derived.

With colour information on so many stars in each CCD frame it is useful to plot colour-magnitude diagrams (Figure 5.4).

The cluster main sequence is clearly visible in Figure 5.4(b), although these data saturate before the cluster turn-off. This main sequence is notably missing from Figure 5.4(a), highlighting the centrally dense cluster morphology. The lower density of points in this diagram is due to the imperfect overlap of the CFHT frames with INT CCD2 (CCD4 was better placed in the centre of the CFHT mosaic) rather than the sparsity of the field. These figures provide clues towards the cluster membership of any given star, and this will be considered in greater detail when I discuss the variable stars found in these fields in Chapter 6. The diagrams also illustrate the large population of field stars in the survey. This will allow us to compare the cluster and field populations.

5.3.2 INT Colour Data

While $B-V$ colour data is extremely useful in, for example, helping to classify stars (see Chapter 6), it has limitations. In Section 5.5 I will discuss the need to know the radius of each star in the INT dataset in order to calculate the depth of transit we might expect. Barnes, Evans & Moffett (1978) showed that the $B-V$ index becomes very insensitive to

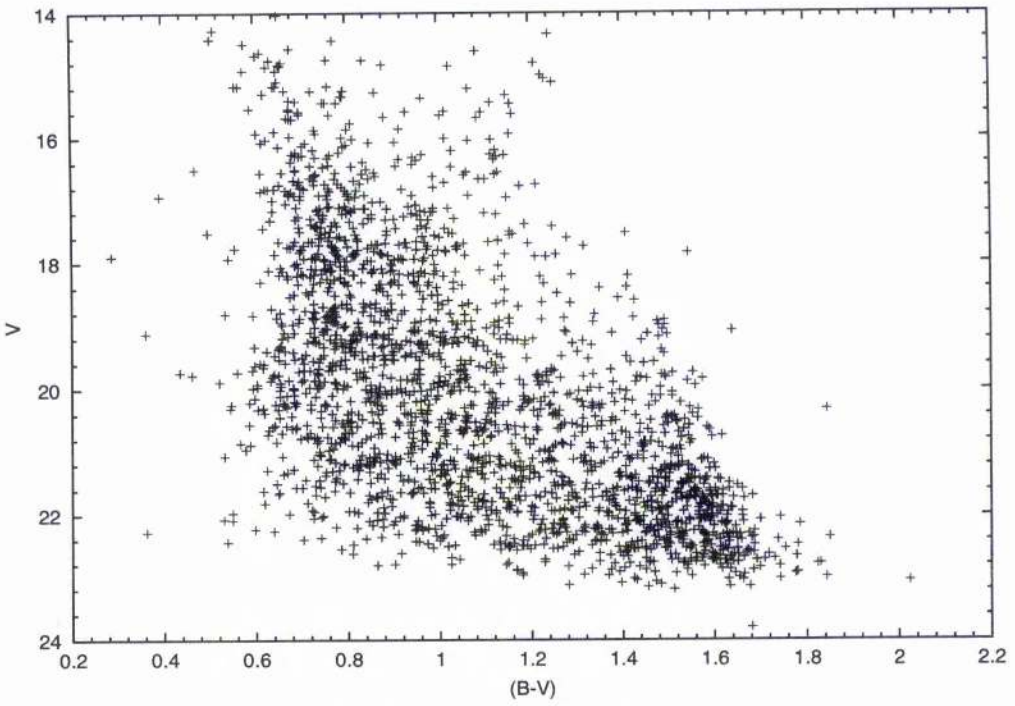

(a) B-V HR diagram for CCD-2

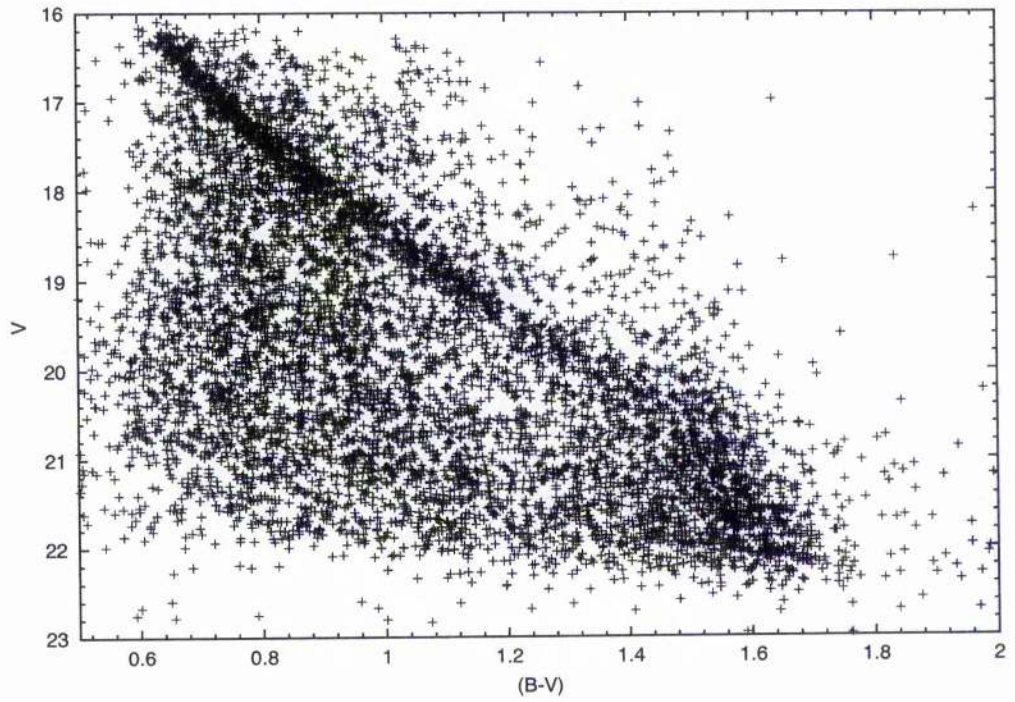

(b) B-V HR diagram for CCD-4

Figure 5.4: $B - V$ colour-magnitude curves for CCDs 2 and 4.

changes in stellar angular diameter (related via their surface-brightness index) at values of ≥ 1.5. Their work indicates that the $R-I$ and $V-R$ indices are more sensitive to stellar radius across the full range of colour values. However, they also comment that the scatter in the relationship for $R-I$ is larger for late spectral types than for $V-R$, and so I have adopted the latter index for my purposes.

In addition to the Sloan r data, some frames of each clusters were taken with U and Sloan i filters. While the U passband is of limited use in this work, three frames of i-band data of NGC 6819 have been reduced to provide Sloan $r-i$ colours for all the INT stars. This reduction was carried out using the same starlist used for the r-band data, using the same procedures described in Chapter 4. This provided instrumental Sloan $r-i$ colours for all stars which were adequately measured in both bandpasses (16964 stars).

To calibrate these instrumental $R-I$ colours, I have made use of theoretical calculations from the program XCAL, written by Keith Horne. XCAL makes use of known passband functions, $P(\lambda)$, and the Bruzual, Persson, Gunn and Stryker atlas of star spectra, written as $f_\nu(\lambda)$ in order to calculate the mean broadband flux, $\overline{f_\nu}(P)$. This represents the level of flux which, constant across all wavelengths, λ, gives the same number of photons as the given star's spectra in the current passband. $\overline{f_\nu}(P)$ is given by:

$$\overline{f_\nu}(P) = \frac{\int f_\nu(\lambda) P(\lambda) d\lambda/\lambda}{\int P(\lambda) d\lambda/\lambda}. \tag{5.4}$$

The mean broadband flux was then used to calculate theoretical magnitudes for a range of stellar spectral types relative to the flux from Vega in that passband, e.g. for the V-band:

$$m_V(\mathrm{star}) = -2.5 \log \left[\frac{\overline{\mathrm{f}_\nu}(\mathrm{P_V}, \mathrm{star})}{\overline{\mathrm{f}_\nu}(\mathrm{P_V}, \mathrm{Vega})} \right]. \tag{5.5}$$

Star magnitudes (e.g., m_V) through various different filters were computed in this way and used to calculate theoretical colours for a range of stellar spectral types. The INT instrumental Sloan $r-i$ colours were calibrated by superimposing the XCAL plot of Sloan $r-i$ against $B-V$ over that of the INT stars, as shown in Figure 5.5.

Vertical and horizontal offsets were then applied to the XCAL data such that the

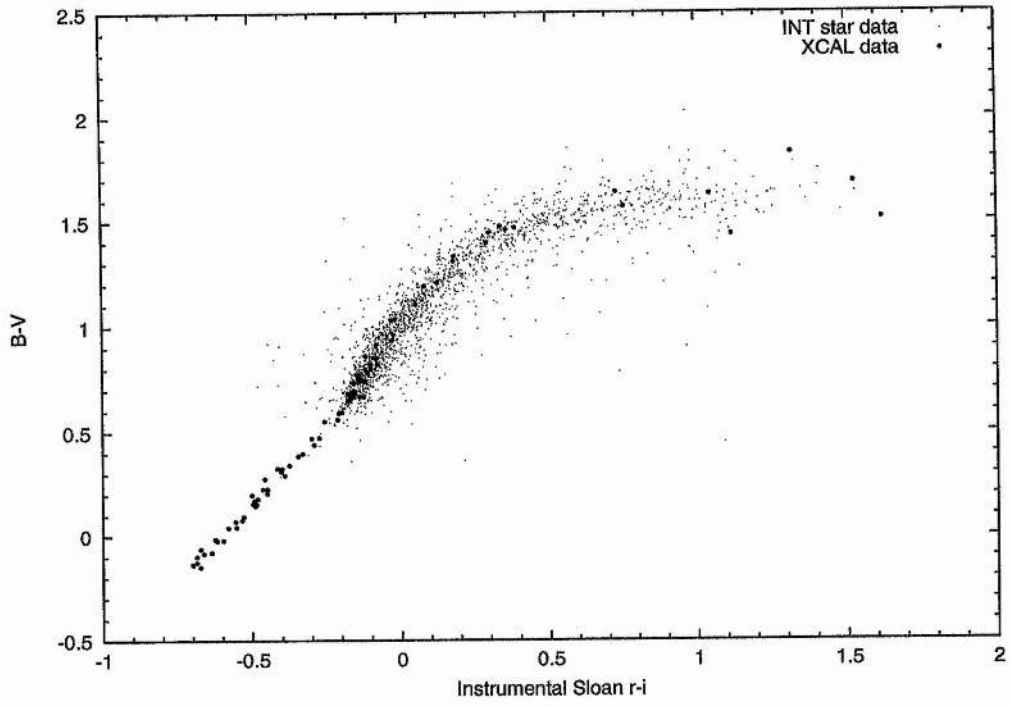

(a) Calibrating instrumental Sloan $r-i$ for CCD-2

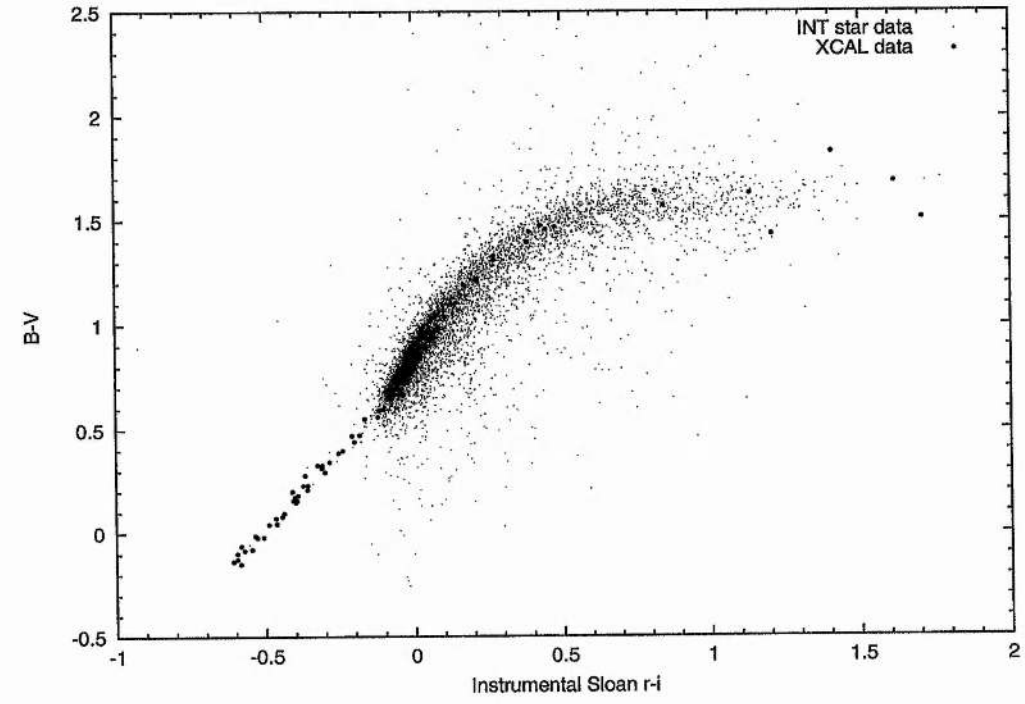

(b) Calibrating instrumental Sloan $r-i$ for CCD-4

Figure 5.5: Calibrating the instrumental Sloan $r-i$ colours for CCDs 2 and 4 by superimposing theoretical Sloan $r-i$.vs.$B-V$ curves and offsetting the latter until the two datasets matched.

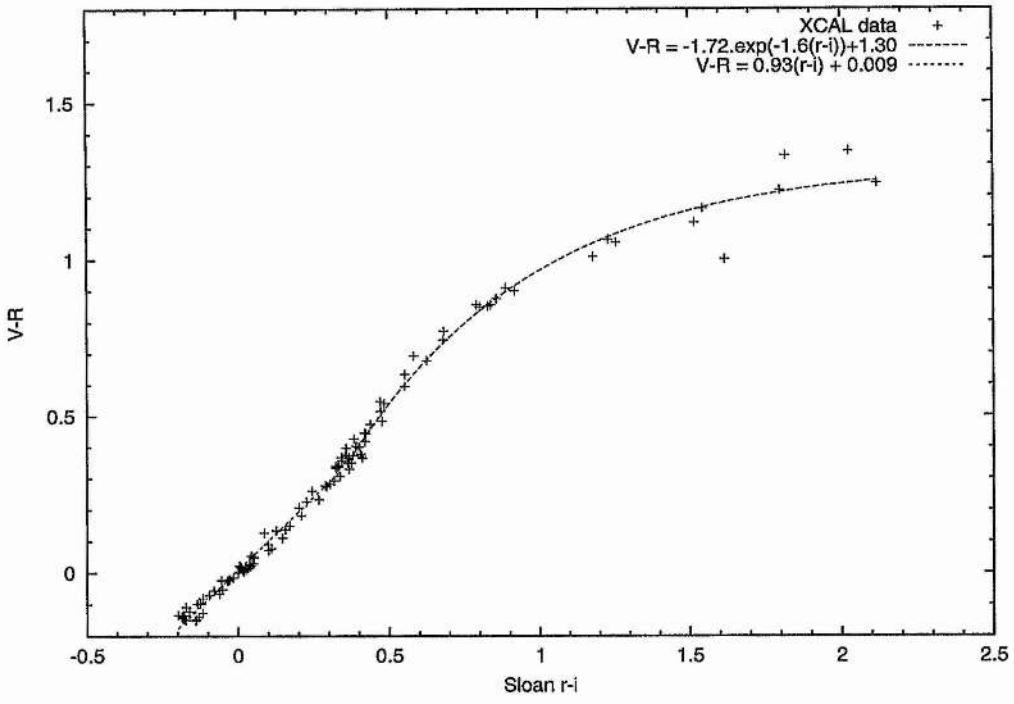

Figure 5.6: Converting calibrated Sloan $r-i$ colours into Johnson $V-R$.

datapoints lined up with the INT data. The horizontal offset provided the calibration factor for the INT data, in the sense that the true Sloan $r-i$ colour of a star $(r-i)$ is found from the instrumental one $(r-i_{inst})$ by adding the offset, Δ_{r-i}:

$$r-i = r-i_{inst}+\Delta_{r-i}. \tag{5.6}$$

Δ_{r-i} was found to be $0\overset{m}{.}50$ for the CCD2 data and $0\overset{m}{.}41$ for the CCD4 data. In both cases, the vertical offset (the difference between the theoretical and measured B-V) was found to be $0\overset{m}{.}2$. This is attributed to extinction in the direction of the cluster and is not very different from the value of $E(B-V)=0.1$ measured by Kalirai et al. (2001a).

A similar method was used to convert the now-calibrated Sloan $r-i$ colours into Johnson $V-R$. XCAL was used to produce a dataset of $V-R$ and corresponding Sloan $r-i$ values, which are plotted in Figure 5.6.

To derive a formula to convert Sloan $r-i$ colours into Johnson $V-R$, a function was fitted to this data using the method of least squares. As the shape of the curve changes at $r-i\sim 0.4$, two functions were fitted; a straight line for $r-i$ values $\sim -0.2 \sim 0.4$ and

an exponential function for the remaining curve:

$$V - R = 0.93(r - i) + 0.009, -0.2 \leq r - i \leq 0.356 \quad (5.7)$$

$$V - R = -1.72e^{-1.6(r-i)} + 1.30, 0.356 \leq r - i \leq 2.5. \quad (5.8)$$

These relations were then used to calculate $V - R$ colour indices for all INT stars with Sloan $r - i$ colours. I describe how these colours were used further in Section 5.5, and I present $V - R$ colour magnitude diagrams in Figure 5.7.

Finally, it was possible to calculate $R-I$ colours for all the stars using the calibrated Sloan $r-i$ values and the relationship bewteen the two bandpasses presented by Fukugita et al. (1996):

$$r - i = 0.98(R - I) - 0.23, (R - I) < 1.15$$

$$r - i = 1.40(R - I) - 0.72, (R - I) \geq 1.15. \quad (5.9)$$

The three colour indices were used to plot the colour-colour diagrams presented in Figures 5.8 – 5.9.

5.4 Astrometric Results

Astrometric solutions were performed separately for both CCDs using the method described in Chapter 4. Since the rotation centre of the WFC field of view lies in one corner of CCD 4, it was found that the best way to obtain a solution for CCD 2 was to treat the WFC as a single field and translate the pixel coordinates of the CCD 2 stars into the CCD 4 system. This was achieved using the translations available on the INT WFC survey webpage[1]. The INT WFC field is known to suffer from radial distortion. While an 8-parameter astrometric fit was employed to compensate somewhat for this, the resulting astrometric uncertainties increase with increasing distance from the optical axis. In practise, this means that the central CCD 4 has slightly better astrometry than the other

[1]http://www.ast.cam.ac.uk/~wfcsur/astrometry.html

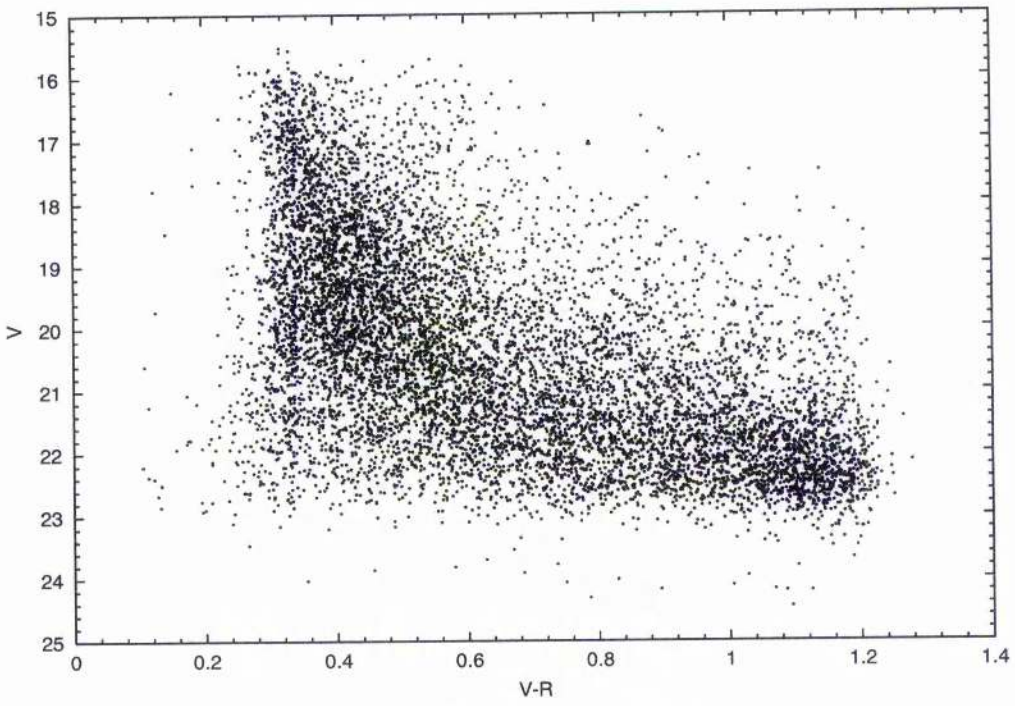

(a) $V - R$ HR diagram for CCD-2

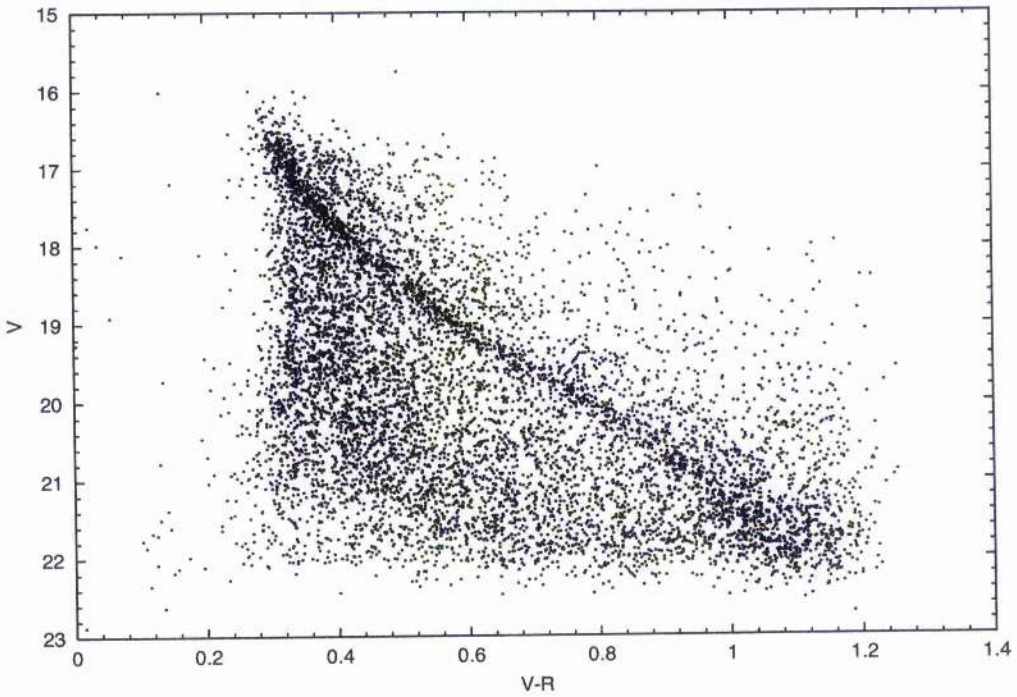

(b) $V - R$ HR diagram for CCD-4

Figure 5.7: $V - R$ colour-magnitude curves for CCDs 2 and 4.

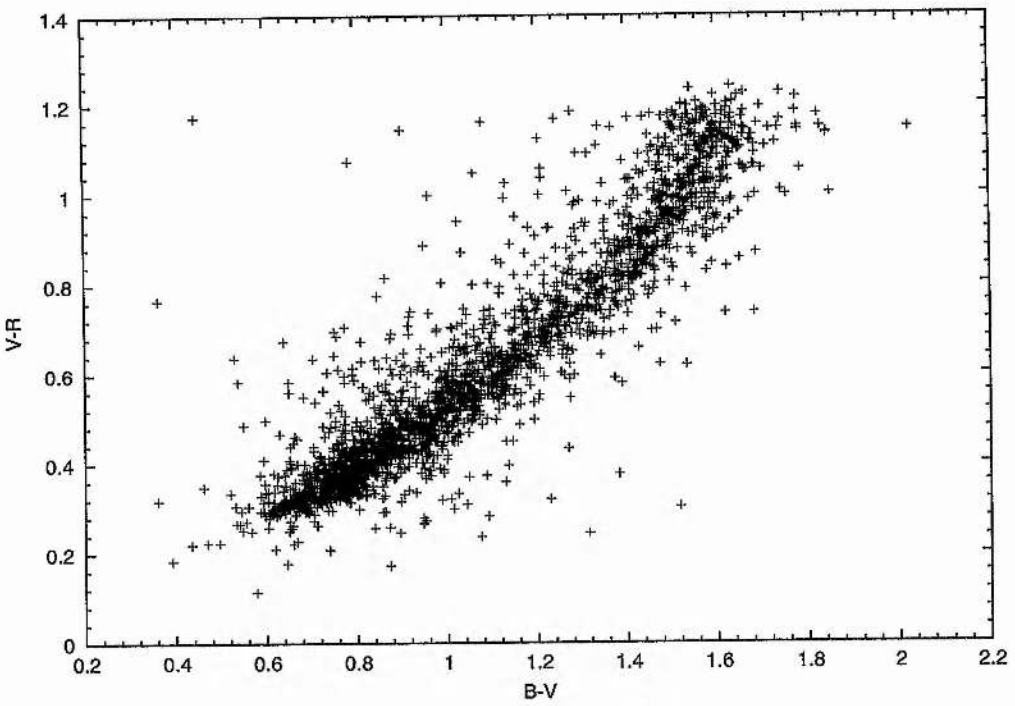

(a) $V - R$ HR diagram for CCD-2

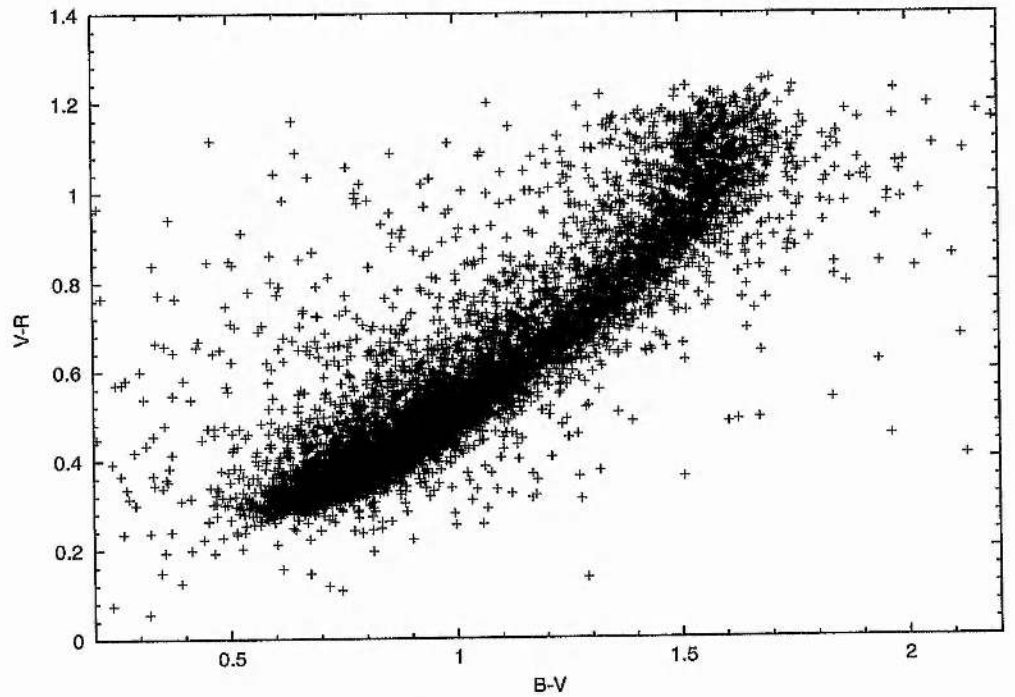

(b) $V - R$ HR diagram for CCD-4

Figure 5.8: $V - R$.vs.$B - V$ colour-colour curves for CCDs 2 and 4.

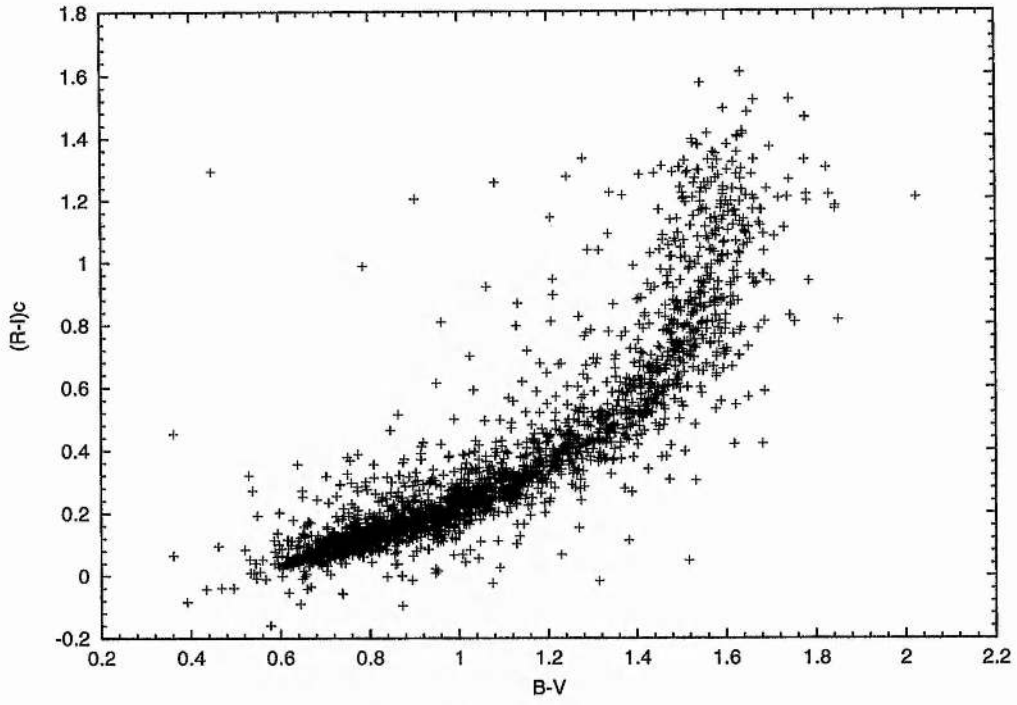

(a) $R-I$ HR diagram for CCD-2

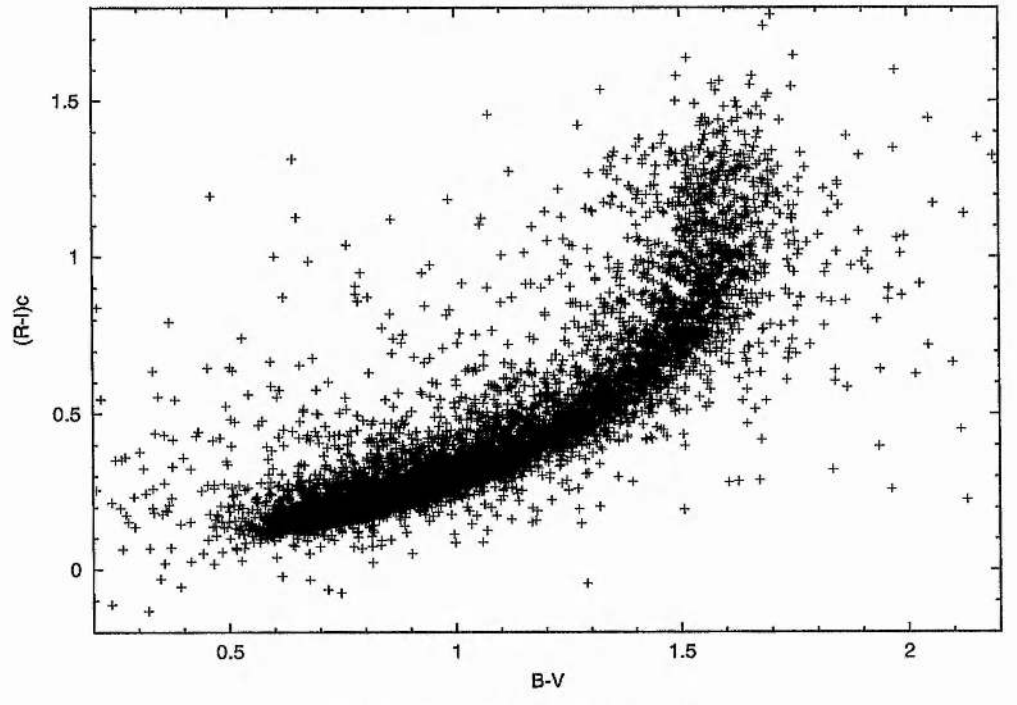

(b) $R-I$ HR diagram for CCD-4

Figure 5.9: $R-I$.vs.$B-V$ colour-colour curves for CCDs 2 and 4.

CCDs. The RMS error in the resulting RA and Dec positions was found to be $0.172''$ and $0.180''$ respectively for CCD 4 and $0.232''$ and $0.363''$ respectively for CCD 2.

5.5 Hunting for Planetary Transits

The lightcurve of example star 2457 in Figure 4.2, Chapter 4 illustrates the difficulty of detecting transit events even by eye in well-sampled lightcurves. The task of detecting these events in an automated fashion with an algorithm should therefore not be underestimated. A number of recent papers have described various different approaches to detecting the brief, shallow dips of transit events. For descriptions of these techniques, see for example Borucki et al. (2001), Gilliland et al. (2000), Doyle et al. (2000) and Defaÿ, Deleuil & Barge (2001). I am adopting the matched-filter approach to detecting transits as the most statistically optimal method. While many authors have resorted to other (less optimal) statistical techniques on the basis that the matched-filter approach is computationally too time-consuming, I have found that the method described below can hunt for and detect transits on reasonable timescales.

5.5.1 The Matched Filter Algorithm

This technique consists of the following stages:

- the generation of large numbers of model transit lightcurves for a reasonable range of transit parameters followed by
- the fitting of all these models to all star lightcurves. The 'goodness of fit' in each case is judged by calculating the value of χ^2.
- The data for each star are also fitted with a constant lightcurve at the mean magnitude of that star.
- Transit events are highlighted by comparing the difference, $\Delta\chi^2_{tf}$, between the χ^2 of the best-fitting model (χ^2_M) and that of the constant lightcurve (χ^2_C):

$$\Delta\chi^2_{tf} = \chi^2_C - \chi^2_M. \tag{5.10}$$

Ultimately, the most optimal transit models would be full star-eclipse solutions incorporating the effects of limb-darkening, etc. However, this approach is computationally very expensive and something of an over-kill for relatively sparsely-sampled lightcurves. I have adopted a simpler model, consisting of half a cosine curve representing the transit and a constant value of magnitude at all other times, as described by Equation 5.11.

$$m_{model}(i) = \begin{cases} m_{out}(j) + a.\cos(\frac{d}{\pi}(t(i) - t_o)) & t_{\text{start}} < t(i) < t_{\text{end}} \\ m_{out}(j) & \text{otherwise,} \end{cases}$$

where $m_{model}(i)$ is the magnitude of the model for star j in image i of out-of-transit magnitude $m_{out}(j)$. d gives the duration of the transit in days, starting and finishing at times t_{start} and t_{end} respectively. $t(i)$ is the time of a given image, t_o is the time of mid-transit and a is the amplitude of the event.

The key parameter spaces which my algorithm searches are those of transit duration and time of mid-transit. The orbital period is also clearly an important parameter, but secondary for the following reason. Fitting models consisting of a single transit event will identify the best-sampled transit in the lightcurve by causing the required high $\Delta\chi^2_{tf}$ value. It is of course true that fitting a model with transit events spaced at period intervals would cause a greater jump in $\Delta\chi^2_{tf}$, but this comes at a high computational price and slows the algorithm down considerably without significantly improving the chances of detection. The other main transit parameters, amplitude and out-of-transit magnitude, are determined during the fit of each model to every lightcurve.

The algorithm begins by performing a least-squares fit of a constant lightcurve (of gradient zero) to all star lightcurves. This provides a measure of the mean magnitude for each star. It then calculates the χ^2 value of the fit to the data.

Model lightcurves are then generated for transit durations between 2 and 5 hours and mid-transit times spanning the full HJD-range of the dataset, in intervals of 1/4 of the duration. This interval was chosen as a trade-off between having sufficient intervals so as not to miss transits and having the models spaced out in order not to waste time fitting models with mid-transit times separated by less than the gap between successive frames.

Each model fitted to a given lightcurve can be represented as:

$$\begin{aligned} m(i,j) &= m_{out}(j) + a.m_{model}(i) \\ &= \sum_{n=1}^{Np} P_n.C_n, \end{aligned} \tag{5.11}$$

where the adjusted parameters, P_n are the offset magnitude $m_{out}(j)$ and amplitude a. Np is the number of parameters. χ^2 can then be minimised by the same technique explained in Section 4.3 to determine the best-fit values of the parameters P_n.

This process yields the amplitude of the transit and the out-of-transit magnitude. The χ^2 value of the fit of each model to the data is then calculated and the parameters and χ^2 of the best-fitting model are stored.

Finally, the $\Delta\chi^2_{tf}$ for each star is calculated from Equation 5.10, ignoring any stars already labeled as variables.

5.5.1.1 Selecting Transit Candidates

Once the code has produced a value of $\Delta\chi^2_{tf}$ for all stars, the next stage is to decide on a suitable cut off $\Delta\chi^2_{tf}$ threshold between constant stars and transit candidates.

This decision was made by answering the question: "At what value of $\Delta\chi^2_{tf}$ does the false alarm rate drop below a minimum acceptable level?" In this context a false alarm would be a chance formation of Gaussian-scattered points forming a transit-like dip and hence producing an unusually high $\Delta\chi^2_{tf}$ value for a constant lightcurve.

To answer this question, I simulated constant, Gaussian-noise lightcurves for 33 magnitude bins between $16\overset{m}{.}0$ and $24\overset{m}{.}0$, with 2000 stars per bin. These lightcurves were then input to the TRANSITFINDER algorithm in order to calculate the $\Delta\chi^2_{tf}$ for all stars. This gave a realistic evaluation of the amplitude in the scatter of $\Delta\chi^2_{tf}$ values for Gaussian-noise lightcurves at all magnitudes.

For comparison, I then had the code add an example transit to all of the simulated lightcurves, of fixed parameters similar to those of HD 209458: period = 3.4 days, duration

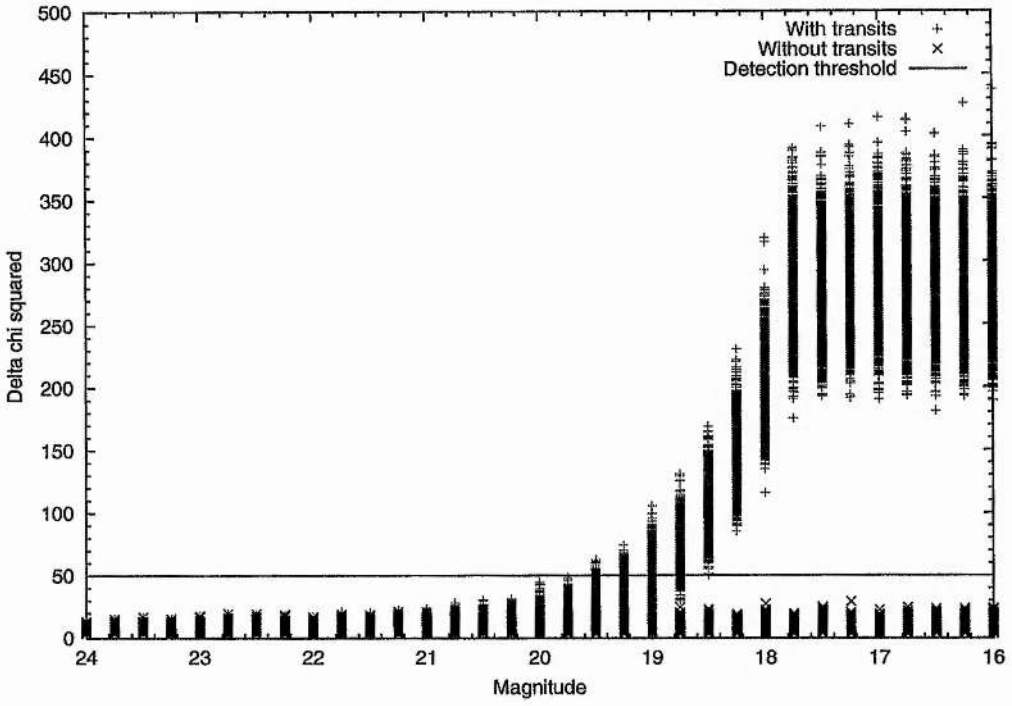

Figure 5.10: Plots of $\Delta\chi^2_{tf}$ .vs. magnitude for a Gaussian-noise only dataset, and one with a fixed parameter transit added to lightcurves of various mean magnitudes. The cut off threshold of $\Delta\chi^2_{tf} = 50.0$ was established, above which Gaussian-noise lightcurves produced no false transit detections.

= 2.4 hours, amplitude $0\overset{m}{.}02$ and HJD of mid-transit 2451355.65. These lightcurves were also run through the TRANSITFINDER algorithm.

Figure 5.10 shows the two resulting $\Delta\chi^2_{tf}$ distributions plotted against magnitude. It is immediately apparent that stars with transits have very much greater $\Delta\chi^2_{tf}$ values than purely constant lightcurves for magnitudes brighter than ~ 19 mag. The flattening off of the former distribution at bright magnitudes is due to the scatter in the lightcurves becoming systematic-noise dominated. It is also clear that no constant lightcurve produces a $\Delta\chi^2_{tf}$ values above ~ 40. A $\Delta\chi^2_{tf}$ threshold of 50.0 should therefore guarantee zero false alarms from Gaussian-noise lightcurves while detecting the vast majority of transit events.

While all lightcurves above this threshold should be carefully examined, another plot could provide a useful guide in selecting the most likely candidates. If a transit is present in a lightcurve, the reduced χ^2 of the best-fit model should be small. Furthermore, the $\Delta\chi^2_{tf}$ value should be high as it departs from a constant lightcurve. In a plot of reduced

χ^2(model) against $\Delta\chi^2_{tf}$ the transit events should cluster around the top left, separating them from constant lightcurves which should show no great change in $\Delta\chi^2_{tf}$.

5.5.2 Predicting the Expected Number of Transit Events

In order to discover the efficiency of the detection algorithm, I simulate a large number of trials of a known range of transit events. I then run the TRANSITFINDER code over the simulated lightcurves in order to evaluate what fraction of the total number of trial transit events are detected with a $\Delta\chi^2_{tf}$ above the threshold of 50.0.

The probability of detecting a transit may be written as a function of four parameters: the planetary and stellar radii (R_p and R_*), the planetary orbital period (P) and the magnitude of the star (m_*); this may be written as $P(det|R_p, R_*, P, m_*)$. The planetary and stellar radii determine the amplitude of the event, the period defines the frequency and the distance to the star determines the apparent magnitude. The orbital inclination, i, is, of course, a factor in both the amplitude and duration of the transit and I describe how this parameter is handled below.

Firstly, I make the assumption that all the stars in the INT data are on the main sequence. In terms of class III giants, this is fairly safe, since the least luminous giant star has an absolute magnitude of $\sim$+0.0. Given this dataset's maximum limiting apparent magnitude is $\sim$ $17\overset{m}{.}0$, the star would have to be at a minimum distance of $\sim$25 kpc – outside the Galaxy.

Similar calculations reveal that class IV subgiant stars could be present in the data, and a more careful treatment is required. Taking the known absolute magnitudes of subgiants of all types it is possible to calculate the range of distances over which these stars could be measured within the limiting apparent magnitudes: $17\overset{m}{.}0$ – $23\overset{m}{.}0$. The maximum distance was taken to be 8.5 kpc – the distance to the Galactic Centre. The volume of space from which these stars could be measured was then calculated, while identical calculations were made for various main sequence star types.

Allen (1973) lists a table giving the space densities of stars of different spectral and luminosity classes. Although this data was derived from Solar neighbourhood rather than whole galaxy observations, it was the best readily available and should be adequate for an order of magnitude estimate. Furthermore, the table data lists the space densities of class

IV and brighter stars as a single group and so results in an over-estimate in that sense. Using these densities, it was possible to estimate the number of subgiants in the sample as a percentage of the total number of stars visible of all luminosities. It was found that subgiants should comprise no more than 0.6 percent of the total sample, and therefore the assumption of main sequence stars is safe.

From this assumption, I have used the $V-R$ colour index computed for all stars (see Chapter 5) to find an estimate for the radius of each star. This was done by interpolating between measured values of $V-R$ and R_* for the range of main sequence star types from Gray (1992). These values were supplemented at the low-mass end by data from Reid & Gizis (1997), who list $V-R$ index, absolute magnitude and spectral type for 106 low-mass systems. The absolute magnitude was then used to calculate the radii of these stars. An exponential curve was least-squares fitted to the Reid and Gizis data and used to calculate values of stellar radii at fixed intervals of $V-R$ in order to provide one smooth, continuous dataset, which is plotted in Figure 5.11. The slight break in the curve at $V-R \sim 0.8$ is the region where the two datasets join and intervening data is sparse. Interpolation over this dataset was then used to compute main sequence star radii from $V-R$ colour index. Similarly, interpolating over a table of absolute magnitude and main sequence star radii and mass from Binney & Merrifield (1998) provided the absolute magnitude and mass of a star of given $V-R$ index.

Finally, the assumption that all stars are main sequence means that the apparent magnitude of a star of given $V-R$ colour is simply a function of distance. The implications of this are that the probability of detecting a transit for any given star may now be written as a function of the observable parameters, $V-R$ and m_*: $P(det|R_p, V-R, P, m_*)$.

To assess this probability, I begin with suitable guesstimate values of R_p and P, initially using values of $R_p = 1.3\,\mathrm{R}_{jup}$ and $P = 3.5$ days to be similar to HD 209458 as an illustrative example. I then generate 1000 constant Gaussian-noise lightcurves at $0\overset{m}{.}5$ intervals between 14–24 mag and for a range of $V-R$ colours between 0.0–2.3 mag at $0\overset{m}{.}1$ intervals. For each of these trials I generate a random value of $\cos i$, where i is the orbital inclination from a uniform deviate between 0–1. Having determined the appropriate radius, absolute magnitude and mass of the star from its colour, I then calculate the duration of the transit from Equation 2.4. The maximum amplitude of the transit is found by calculating the flux drop caused by the planet covering an area of the stellar surface at

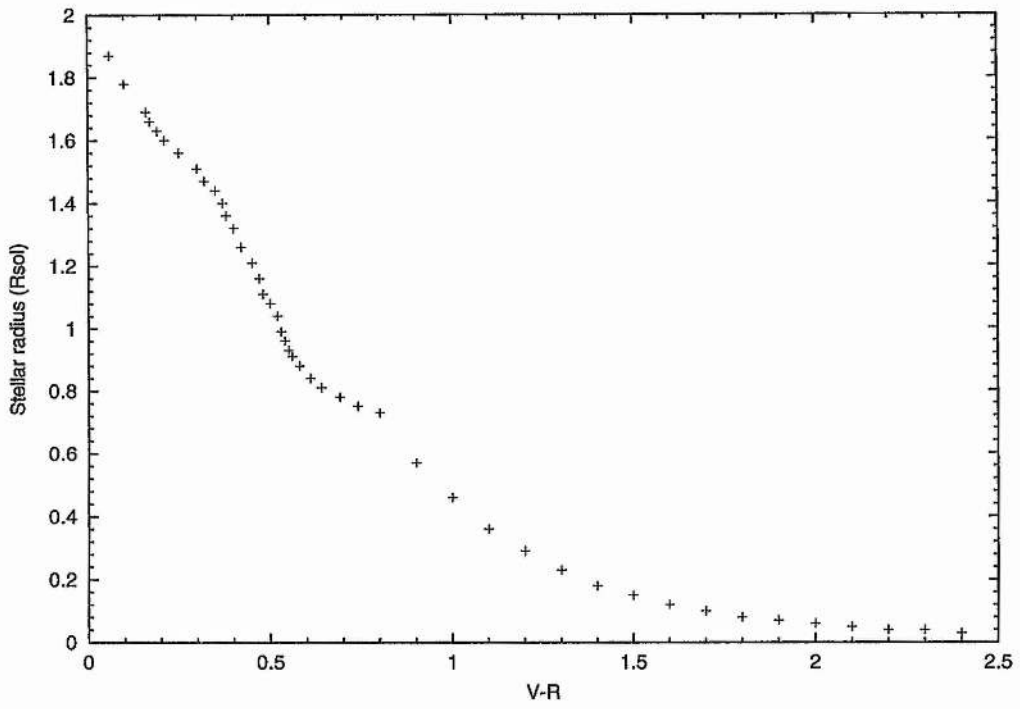

Figure 5.11: Plot of the final, combined dataset of main sequence star radius and $V-R$ colour index used to estimate the stellar radius of each star in the INT dataset.

the minimum impact parameter, taking limb darkening into account. If this amplitude is greater than zero, then transit events are added to the lightcurve at appropriate intervals using Equation 5.11. If not, then the lightcurve is left unchanged from Gaussian noise. In this way, I simulate a realistic distribution of transit lightcurve morphologies and orbital inclinations.

Once 1000 lightcurves have been generated for each combination of magnitude and colour, the TRANSITFINDER algorithm is run, producing an array of $\Delta\chi^2_{tf}$ values. The code calculates the detection probability, $P(det \mid R_p, P, \text{V-R}, m_*)$, as the fraction of these which produce a $\Delta\chi^2_{tf}$ greater than the threshold.

The resulting probabilities can be used to estimate the number of planets I can expect to find in the INT data in the following way. The program adds a planet to every star lightcurve, even if no transit is seen due to unfavourable inclination. If this was the true distribution of planets of this P and R_p, and assuming that my detection algorithm is 100 percent efficient at detecting the transits, then the number of planets detected would equal the number of planets with favourable inclinations. More generally, the number of planets expected, N_E of given P and R_p can be written

$$N_E = N_{ps} \sum_{i=1}^{N_*} P(det\ |V-R, m_*), \tag{5.12}$$

where N_* is the number of stars and N_{ps} is the actual fraction of stars with such planets.

The number of planets with $R_p = 1.3\,\mathrm{R}_{jup}$ and $P = 3.5$ days that I expect from the INT data was estimated by using interpolation to compute a probability of detection for each star from its $V-R$ and m_* from the grid of probabilities calculated beforehand. These were then summed over all stars.

From this analysis, I would expect to see 180.9 and 85.7 transits from CCDs 2 and 4 respectively if all stars had one such planet. This simulation predicted more transits from CCD 2 because it used realistic functions of RMS .vs. magnitude, derived from the data from each chip, to estimate the scatter on simulated lightcurves of given magnitude. As the higher blending in CCD 4 caused greater scattering in the lightcurves, the signal to noise ratio of the transits was reduced, making them harder to find. Assuming that the frequency of these planets is the same in this field as radial velocity studies have found for the Solar neighbourhood, then $N_{ps} \sim 1$ percent. I therefore expect to see 2–3 transits of HD 209458-like planets in the INT data, 0–1 of which should orbit cluster-member stars.

While this result suggests a fairly disappointing number of planet detections from this dataset, the number of planets expected is a strong function of period. To illustrate this I have run multiple simulations for $R_p = 1.3\,\mathrm{R}_{jup}$-planets using a range of periods, and plotted the resulting planet expectancy rate against period for both CCDs in Figure 5.12. These plots show the same drop in detection rate at integer multiples of one day and half-day as do similar plots presented in Chapter 3. For this reason, the detection rate for planets with non-integer multiple periods (unlike HD 209458b, the example used here) should be considerably higher.

5.6 The Transit Candidates

The TRANSITFINDER code, using a threshold of $\Delta\chi^2_{tf} \geq 50$, identified 74 candidate transit events in the CCD 2 data and a further 162 in the CCD 4 data. The lightcurves of these

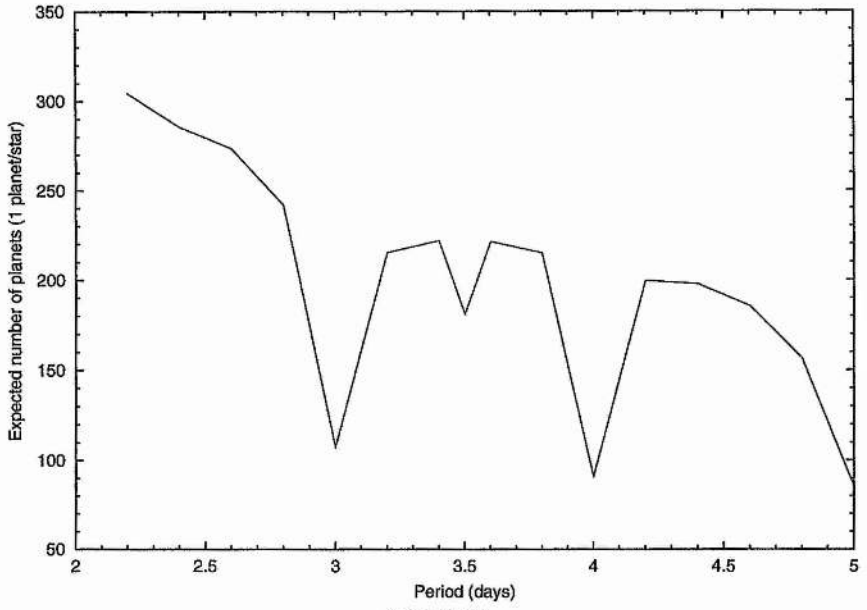

(a) CCD2

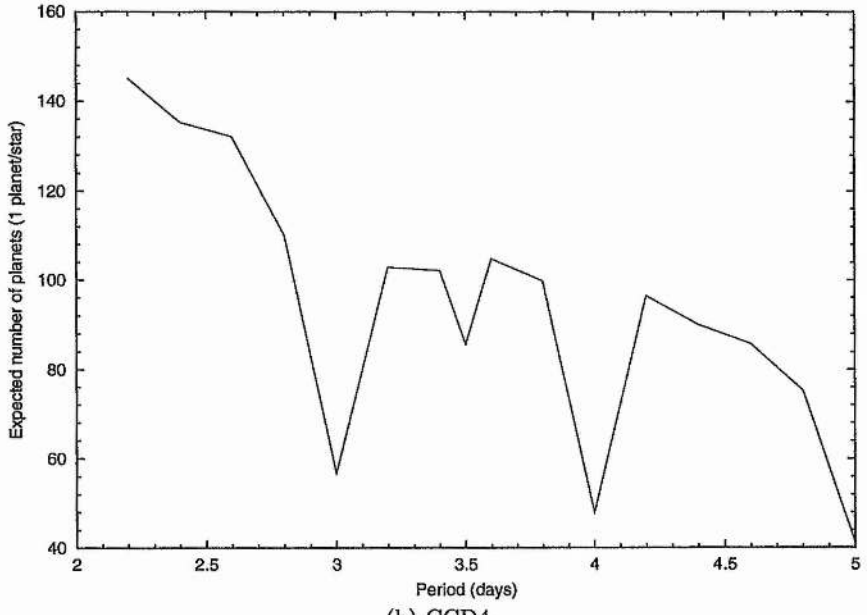

(b) CCD4

Figure 5.12: The variation of the expected number of planet detections with period, assuming that all stars have one hot Jupiter.

stars were subsequently closely examined, and were found to fall into a number of clear categories: 8 eclipse events, 22 active stars and 206 blended stars. These are discussed below.

5.6.1 Eclipse Events

Four stars from each CCDs were found to show brief, low amplitude eclipses in otherwise constant lightcurves. These stars were also found to be isolated and cleanly measured so that there is no reason to doubt the validity of the results. As these stars are the strongest transit candidates, they are discussed individually below, and the lightcurves are presented in Figures 5.13 and 5.14. Periods have been estimated in each case using the Lomb method (Lomb 1976).

- CCD 2 Star 328, $\Delta\chi^2_{tf} = 1471.733$:

  This lightcurve shows only a single eclipse event, $\sim 0\overset{m}{.}215$ in depth and $\sim$ 4.8 hours in duration. While transits of this amplitude are possible, it is only for the combination of large planet orbiting a late-type star. The $V-R$ colour of this star, 0.553, indicates $\sim$ G6 type star of radius close to that of the Sun. It is most likely, therefore, that this eclipse is due to a detacted stellar companion. With only one eclipse, the orbital period cannot be established.

- CCD 2 Star 2179, $\Delta\chi^2_{tf} = 252.486$:

  This lightcurve appears to show four eclipses of similar depth ($\sim 0\overset{m}{.}05$) and duration ($\sim$ 4.8 hours) which are marked with arrows on Figure 5.13(b) at intervals of approximately 7 days. At a first glance, this would appear to be a promising transit candidate. However, the $V-R$ colour of this star is 0.397, indicating a $\sim$ F5 star. Re-arranging Equation 2.11 and taking the radius of an F5 star to be $1.32\,\mathrm{R}_{\odot}$ it is possible to estimate the minimum radius of the eclipsing body: $\sim 2.5\,\mathrm{R}_{jup}$. This would suggest that the companion is a low-mass star or possibly a brown dwarf. This would be an interesting object for follow-up work as the properties of the more massive component can be used to constrain the properties of the secondary (Gizis et al. 2000). The lightcurve of this system is presented phased in Figure 5.13(c), using a time of mid-eclipse of 2451382.534 ± 0.004 and a period of 4.602 ± 0.01 days. The eclipses are of such similar depth that together with the fairly sparse sampling it

is difficult to distinguish which is the deeper. After close examination I have phased the lightcurve on the eclipse I think to be primary.

- CCD 2 Star 3731, $\Delta\chi^2_{tf} = 1570.585$:

  Only two eclipse-like events appear in this lightcurve, both in the second half of the data. The first, at HJD$\sim$ 2451386.5 with a depth of $\sim 0\overset{m}{.}04$, appears to be a secondary eclipse. The primary eclipse at HJD$\sim$ 51390.4 has a depth of $\sim 0\overset{m}{.}09$. The $V-R$ of 0.314 suggests an early F-type star, although this colour is estimated from the combined light of both stars. This object is therefore likely to be a stellar Algol-type eclipsing binary. Both eclipses are poorly sampled during ingress, which might explain why it was not identified in the search for variables (see Chapter 6). This also made it difficult to determine the period of the binary, which I estimate to be 8.28 ± 0.2 days. The phased lightcurve is presented in Figure 5.13(e); the epoch of the primary eclipse was found to be 2451390.420 ± 0.005. The secondary eclipse seems to be centered slightly after phase 0.5, suggesting that the orbit may be elliptical, though better sampled eclipses are necessary to confirm this.

- CCD 2 Star 6690, $\Delta\chi^2_{tf} = 1311.166$:

  This star also appears to be an Algol-type eclipsing binary with a period of 6.98 ± 0.09 days. The eclipses all appear to have a similar depth of $\sim 0\overset{m}{.}07$. The shallow depth of the events indicates that the orbital inclination is close to the limit of $a.\cos i \leq R_* + R_p$ – a "grazing incidence" binary. The stellar nature of the companion is inferred from the $V-R$ colour of 0.408 as before, which corresponds to a mid-F type star. The phased lightcurve of this star is presented in Figure 5.13(g); the time of mid-eclipse was taken to be 2451387.418 ± 0.003. The period of this object has resulted in only primary eclipses being observed.

- CCD 4 Star 4686, $\Delta\chi^2_{tf} = 3452.777$:

  This lightcurve shows a single, relatively deep ($\sim 0\overset{m}{.}52$) eclipse, about 4.8 hours in duration. Its $V-R$ colour of 0.923 indicates an early M-type star and an eclipse this deep could therefore be caused by an M-type companion in a long period orbit.

- CCD 4 Star 4913, $\Delta\chi^2_{tf} = 544.449$:

  This star appears to be another Algol-type eclipsing binary, with one primary eclipse of depth $\sim 0\overset{m}{.}52$ seen together with three secondary eclipses (depth $\sim 0\overset{m}{.}245$) in this fashion because the period is close to a multiple of one day: 3.024 ± 0.001. The signs

of sinusoidal variations in the second half of the lightcurve seem to be due to stellar activity. The phased lightcurve is presented in Figure 5.14(c); the time of mid-eclipse was taken to be 2451359.173 ± 0.002.

- CCD 4 Star 6234, $\Delta\chi^2_{tf} = 173.896$:

  This star appears to be a short period (0.417 ± 0.0003 days) eclipsing binary, with eclipses lasting only ∼ 1.2 hours. The $V - R$ colour of 0.695 indicates an early-mid M, while the eclipse depths (∼ $0\overset{m}{.}04$ and ∼ $0\overset{m}{.}18$) for secondary and primary respectively) suggest a small M-type or brown dwarf companion. The lightcurve phased on an epoch of 2451359.460 ± 0.003 is presented in Figure 5.14(e).

- CCD 4 Star 7332, $\Delta\chi^2_{tf} = 333.875$:

  7332 seems to be a binary similar to 6234; it shows eclipses of depth ∼ $0\overset{m}{.}12$ and very fast duration: ∼ 1.5 hours. The lightcurve phased on an epoch of 2451357.067±0.006 is presented in Figure 5.14(g). The period is longer than that for 6234: 3.199 ± 0.005 days and the $V - R$ colour of 0.418 indicates a late G or early K-type components. The phased lightcurve also seems to exhibit sinusoidal variations of roughly $0\overset{m}{.}06$ peak-to-peak amplitude. This is not unexpected from a star of this spectral type and the question of stellar activity is address in Section 5.6.2.

Some caution must be exercised with these objects. The low amplitude and sparse sampling of the eclipses did in some cases make it difficult to determine the period; in these cases I have presented phased lightcurves folded on the most likely period. I also note that stars 2179 and 6690 both show eclipse-like events apparently at the same time, on nights 1 and 9 of the first run data, and that star 3731 shows some fainter points on these nights also. I have noticed in the course of the analysis that lightcurves often show a few such faint points at the begining or end of a night, when the object is observed at high airmass at dawn or dusk, and that the nights in question show this effect (seen in the lightcurve of 3731). With these very quick, low amplitude eclipses it becomes important to be able to distinguish true eclipses. In the cases of stars 2179 and 6690, the fainter data points consistantly resemble multiple eclipse events which fall towards the middle of the night. Also the events on nights 1 and 9 do not fall at exactly the same time on both lightcurves and the subsequent eclipses fall at different times. I have therefore decided to include these events, but with the caveat that better-sampled follow-up photometry should be gathered before these stars are firmly classified.

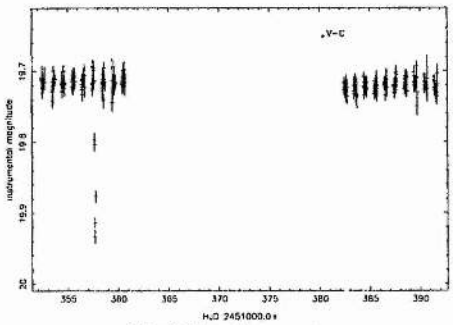

(a) CCD2 Star 328

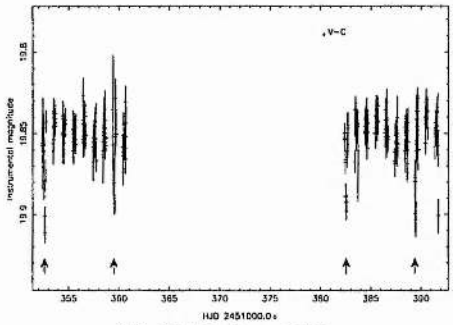

(b) CCD2 Star 2179

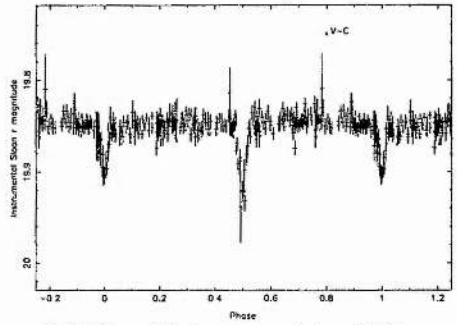

(c) Phased lightcurve of star 2179

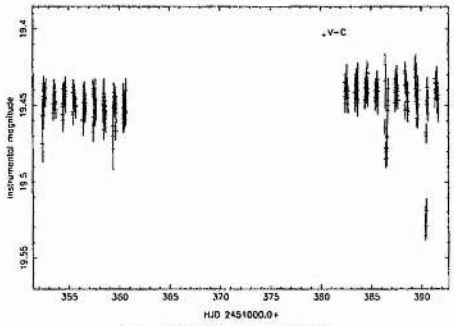

(d) CCD2 Star 3731

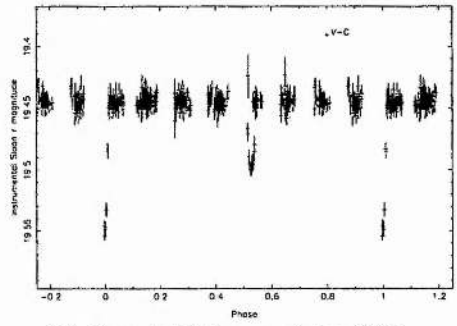

(e) Phased lightcurve of star 3731

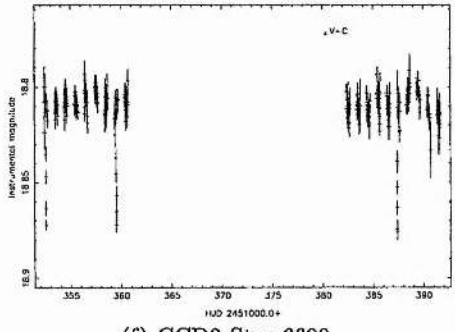

(f) CCD2 Star 6690

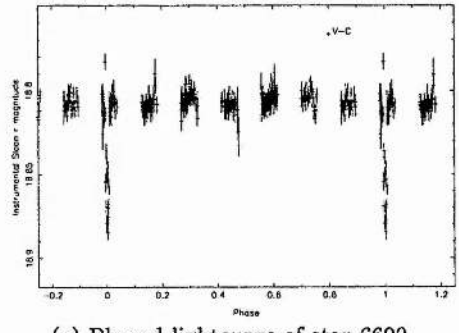

(g) Phased lightcurve of star 6690

Figure 5.13: Lightcurves of candidate transit events from CCD 2.

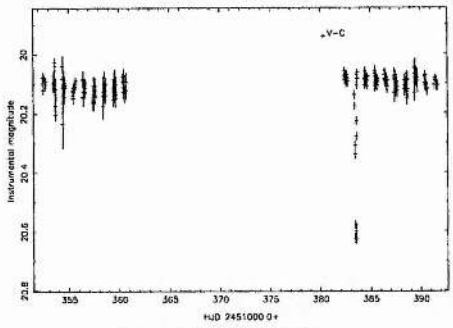

(a) CCD4 Star 4686

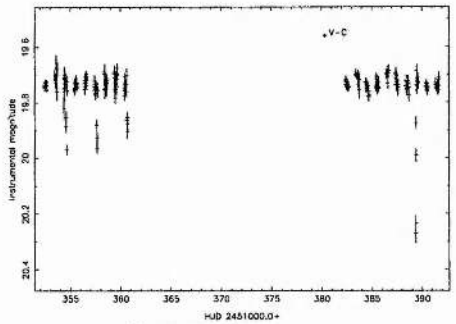

(b) CCD4 Star 4913

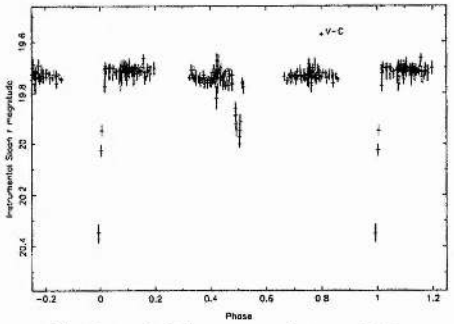

(c) Phased lightcurve of star 4913

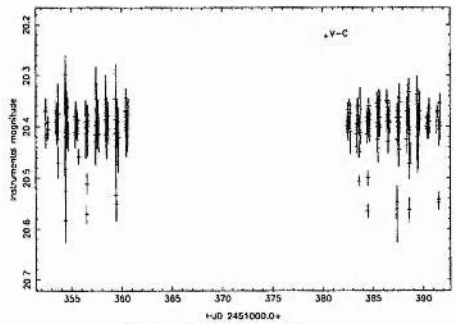

(d) CCD4 Star 6234

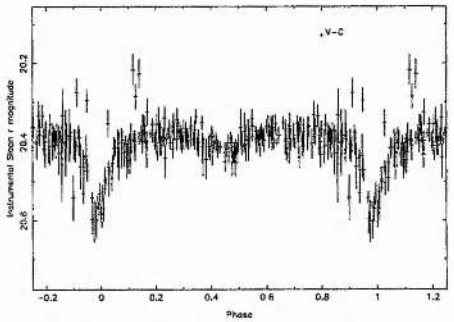

(e) Phased lightcurve of star 6234

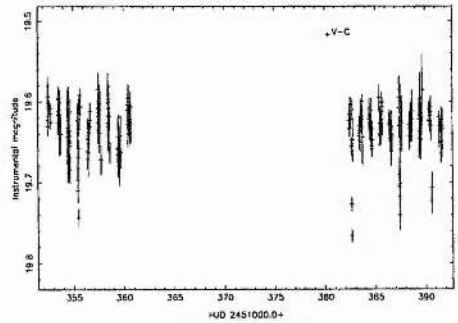

(f) CCD4 Star 7332

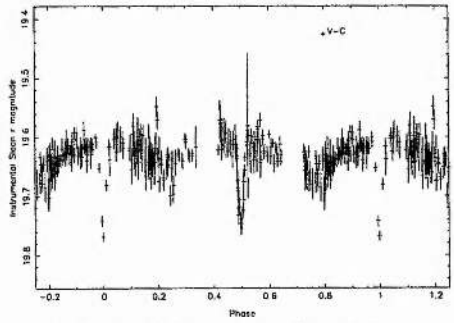

(g) Phased lightcurve of star 7332

Figure 5.14: Lightcurves of candidate transit events from CCD 4.

None of the events in the lightcurves of these stars appear to be due to a planetary transit. However, the TRANSITFINDER code has found examples of very-low-mass companions in binary systems. These systems are interesting in their own right, as I will discuss further in Chapter 6 when I consider the large amplitude variables. These results show the algorithm does find these brief, low-amplitude eclipse events in real data, indicating that it is capable of finding planetary transits if any occurred in the data.

5.6.2 Active Stars

The next catagory of objects found by the TRANSITFINDER code is that of active stars such as BY Draconis objects (BY Dra) – 22 such objects were identified in total. The larger amplitude versions of these objects were identified in my variable-star search, and these are covered in detail in Chapter 6. The TRANSITFINDER code tends to find the lower-amplitude objects where the lightcurve can be well fitted by a long-period, shallow 'transit' model.

Figures 5.15, 5.16 and 5.17 present the lightcurves of the stars showing signs of activity identified by transitfinder.

All the stars presented in this section are variable stars which were not revealed by the search for variables described in Chapter 6, mostly due to their low amplitude. Stellar activity is therefore a significant cause of false alarms. In a future search it might be desirable to take this into account. In Figure 5.18 I have plotted the measured peak-to-peak amplitude of variation of these stars against their $V - R$ colours.

This plot shows an increase in amplitude towards later stellar types. As the variations are thought to be due to star spot coverage, indicating stellar activity, this is expected. The plot illustrates that the amplitudes and durations of the variations can mimic those of a transit event sufficiently well to be a cause of false alarms. It must be remembered that due to the long period nature of these variations, some of these stars may have larger amplitudes than measured here. Also, the amplitude and shape of the variations can change over timescales of weeks to months as the size, position and area of the spot groups changes. These characteristics can be used to distinguish these stars from true planetary transits, although longer periods of observations may be required.

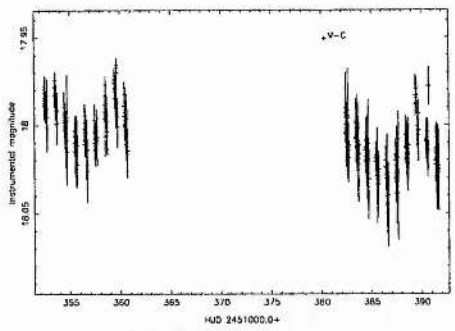

(a) CCD2 Star 171

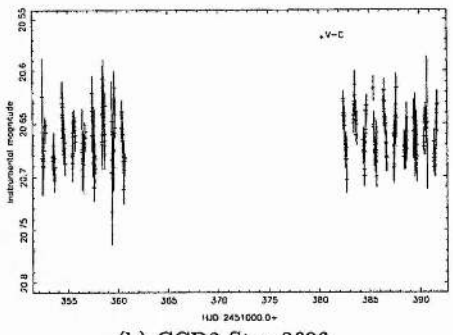

(b) CCD2 Star 2696

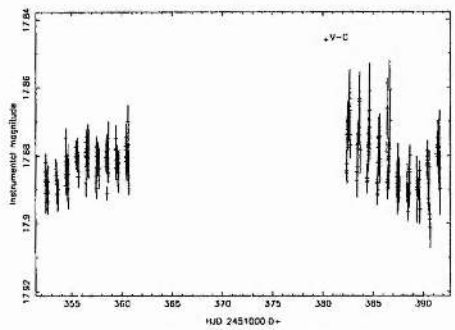

(c) CCD2 Star 3236

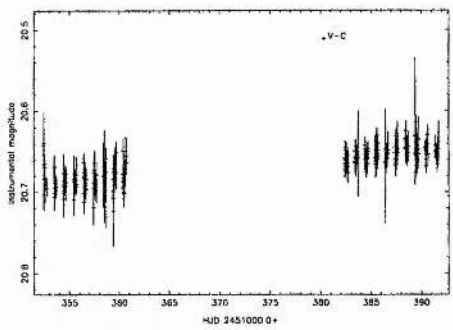

(d) CCD2 Star 4112

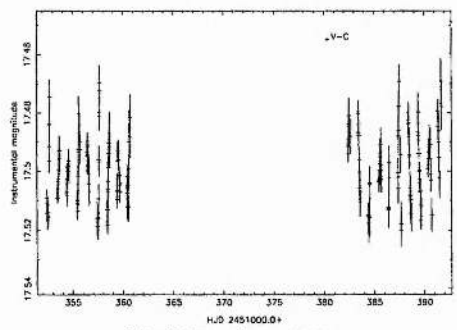

(e) CCD2 Star 4483

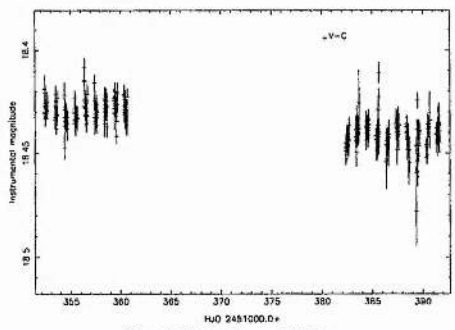

(f) CCD2 Star 5423

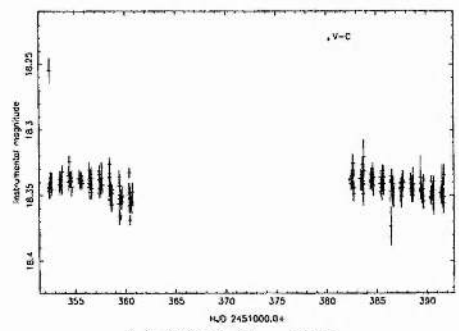

(g) CCD2 Star 8075

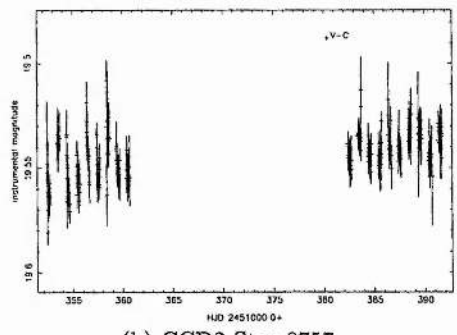

(h) CCD2 Star 8757

Figure 5.15: Lightcurves of active stars from CCD 2.

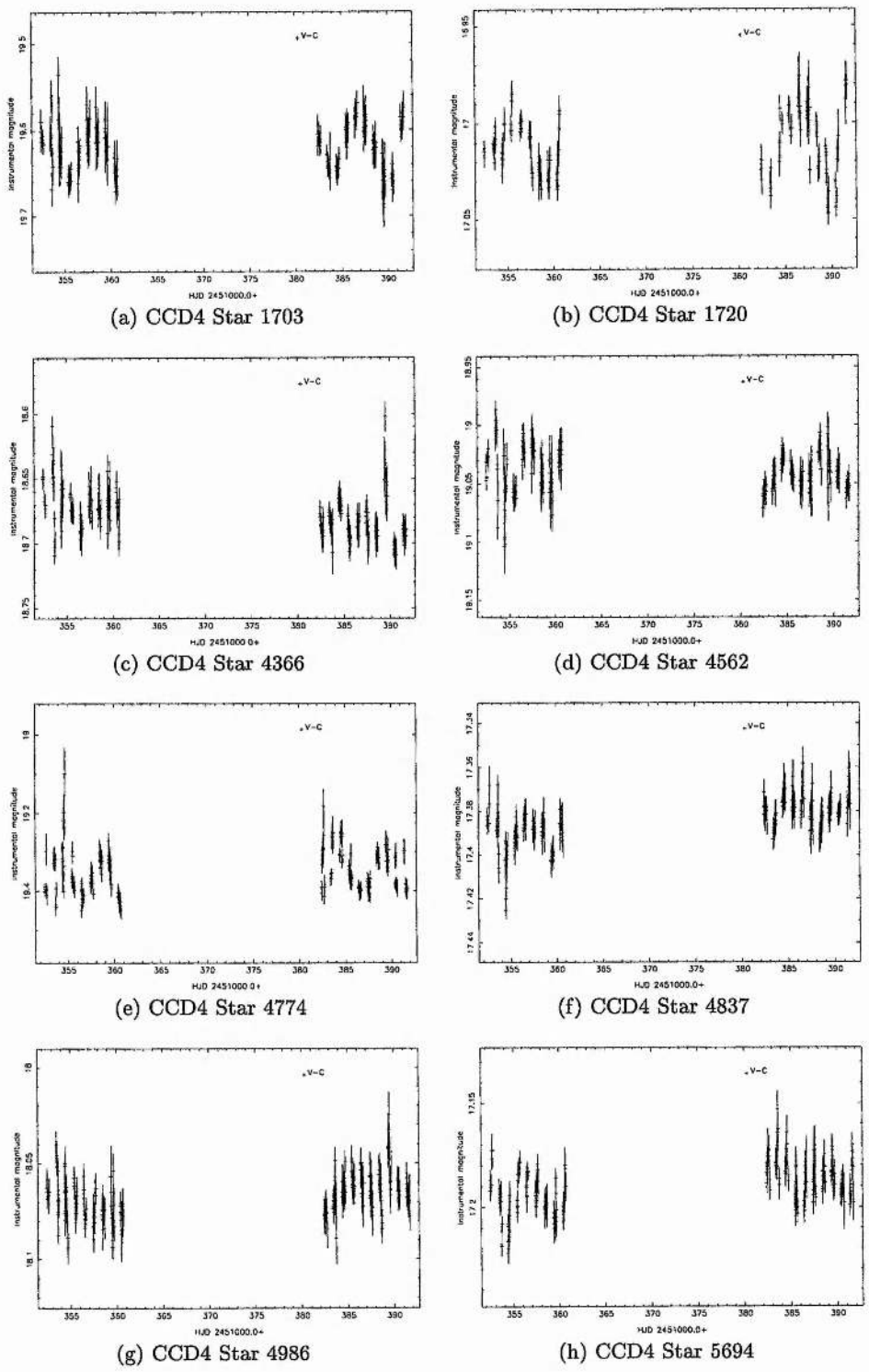

(a) CCD4 Star 1703

(b) CCD4 Star 1720

(c) CCD4 Star 4366

(d) CCD4 Star 4562

(e) CCD4 Star 4774

(f) CCD4 Star 4837

(g) CCD4 Star 4986

(h) CCD4 Star 5694

Figure 5.16: Lightcurves of active stars from CCD 4.

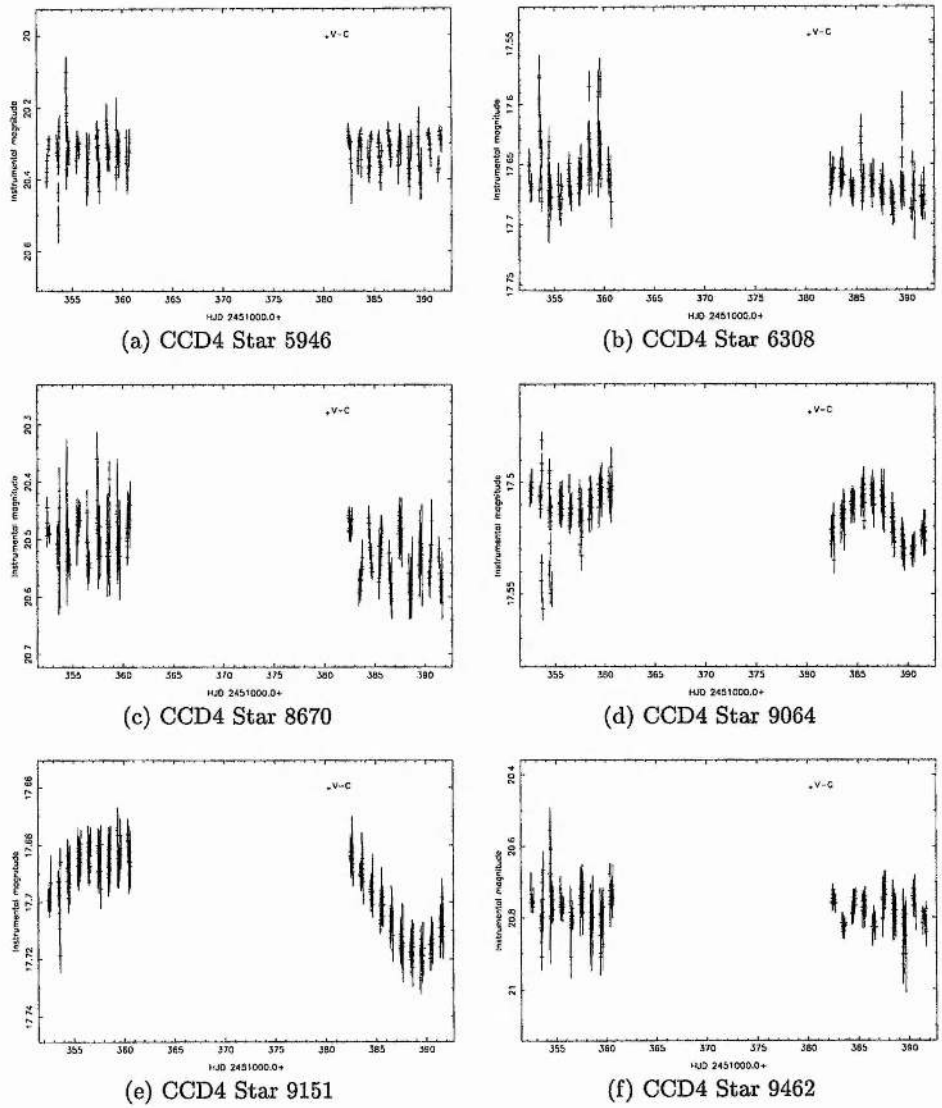

(a) CCD4 Star 5946

(b) CCD4 Star 6308

(c) CCD4 Star 8670

(d) CCD4 Star 9064

(e) CCD4 Star 9151

(f) CCD4 Star 9462

Figure 5.17: Lightcurves of active stars from CCD 4 (continued).

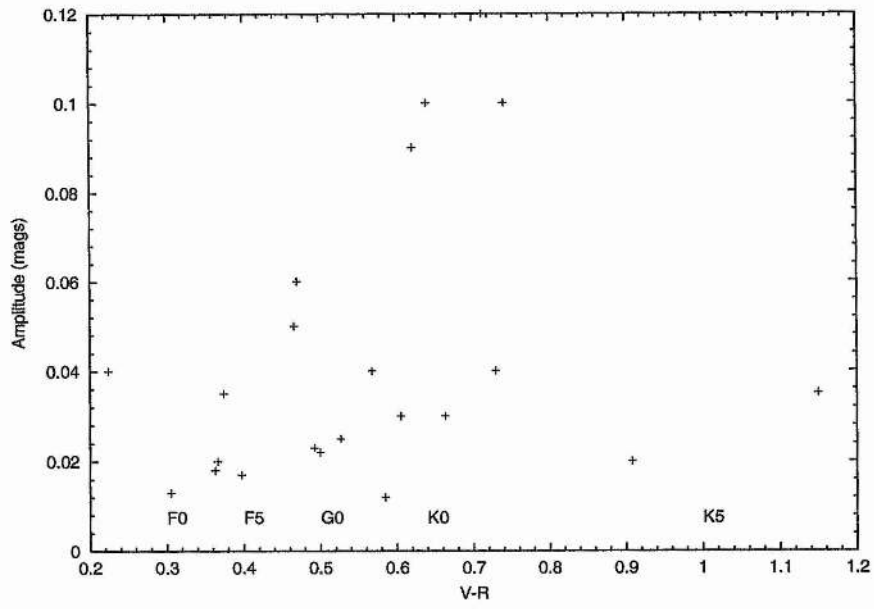

Figure 5.18: Plot of peak-to-peak amplitude .vs. $V - R$ for active stars found by TRANSITFINDER

5.6.3 Blended Stars

Around 75 percent of the transit candidates were found to have relatively bright companion stars very close by (within $\sim$ 20 pixels) or else were found to lie close to a dead or bleeding column – in short, blended. Examining the lightcurves of these objects revealed a number of non-random distortions which can be explained by the close proxmity of another light source and which can resemble a transit event sufficiently well to fool the search algorithm.

In order to quantify this, I have developed a 'blending index', C, defined as follows:

$$C = \left[\sum_{j=1}^{N_*} \frac{\Delta}{r} \frac{f_c}{f_*} \right] B_*, \tag{5.13}$$

where the contributions by the number of companion stars within 20 pixels, N_* are added together. f_c and f_* refer to the fluxes of each companion and the target star respectively, while Δ is the average value of seeing in pixel units and r is the radial separation of each companion. This sum is then multiplied by $B_*/\overline{B}$ where B_* is given by:

$$B_* = \sum_{i=1}^{N_{im}} \frac{B_*(i)}{B_o(i)}, \tag{5.14}$$

where $B_*(i)$ is the background count measured for the target star by DAOPHOT in each image i of N_{im} images and $B_o(i)$ is the median background for each image. B_* therefore quantifies whether the local background level is higher or lower than the median. This is useful in taking into account moonlight contamination and nearby bright stars which raise the background level without being close enough to crowd the target star. The blending index, C, therefore has a high value for badly blended objects.

In Figure 5.19 I have plotted this index against my transitfinder index, $\Delta\chi^2_{tf}$.

These figures show a positive correlation between the two indices. To illustrate how this can happen, I present the lightcurves of an example of a blended pair of stars, 8405 and 8410, in Figure 5.20 and a thumbnail image of the region surrounding these stars in Figure 5.21. The TRANSITFINDER code identified a possible transit event at HJD$\sim$ 2451389.5 in the lightcurve of 8410. Figure 5.20(d) shows the lightcurve of star 8410 at this time. This clearly shows why the TRANSITFINDER code identified a $\sim 0\overset{m}{.}26$ transit-like event. However, the lightcurve of star 8405 at the same time shows a strong correlation. It would seem that DAOPHOT measurements of blended stars have difficulty in separating the light from these two stars, and the resulting lightcurves can produce a high $\Delta\chi^2_{tf}$ index.

Effectively measuring or else eliminating badly blended stars from the dataset would considerably reduce the TRANSITFINDER false alarm rate. One possible way of achieving this would be to modify the algorithm to take account of the blending index data. This must be done with caution, however, as occasionally a blended star is found to show genuine variation. This should be a primary consideration when selecting target fields for future transit searches. Alternatively, the χ^2(model) .vs. $\Delta\chi^2_{tf}$ plot can prove useful. These plots are presented in Figure 5.22.

These plots show the expected grouping of constant stars to the lower left. They also show that the stars discussed in Sections 5.6.1 are clustered towards the upper left, away from the main group of points. The majority of blended points tail away to the upper right, though a few blended stars are mixed up with the eclipsing lightcurves. These

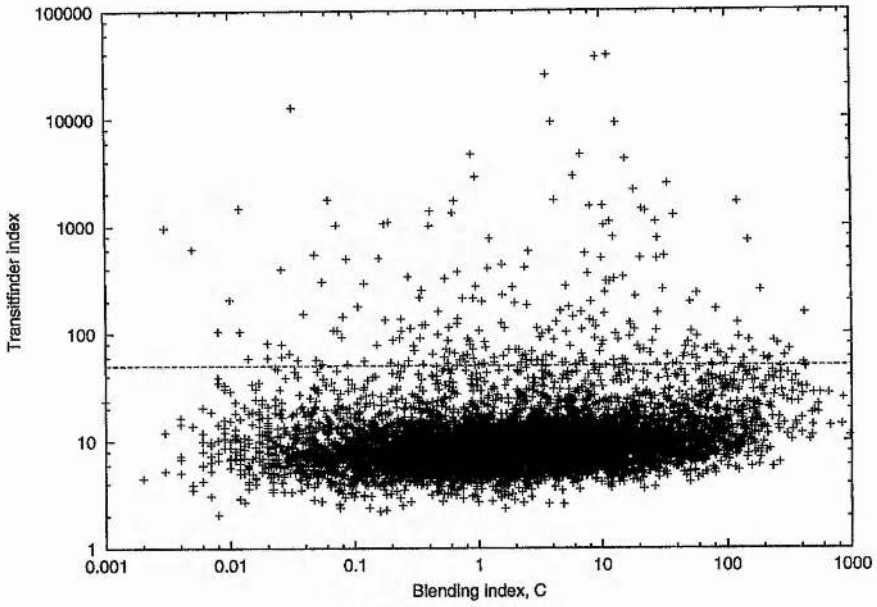

(a) Blending in CCD 2

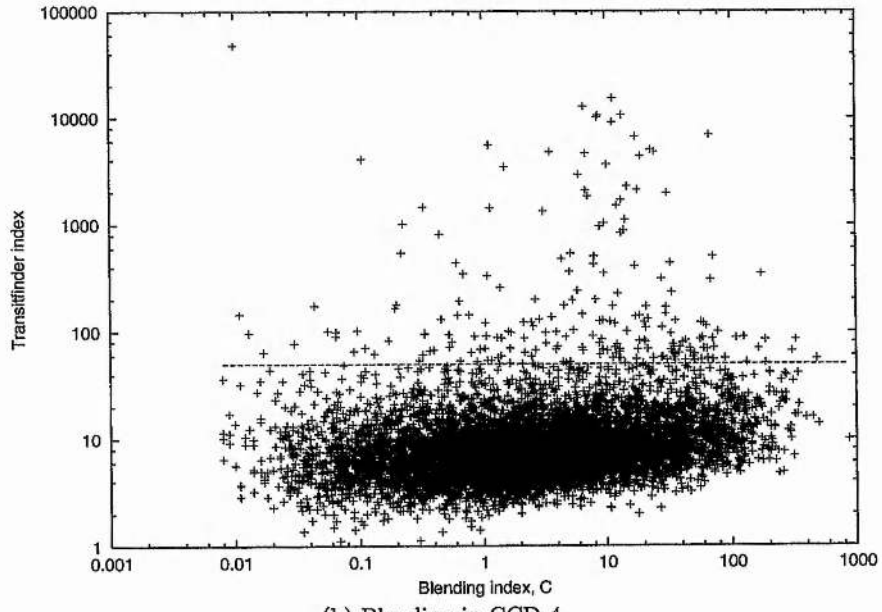

(b) Blending in CCD 4

Figure 5.19: The relationship between blending and $\Delta\chi^2_{tf}$ indices. The horizontal lines represent the cut-off for transit candidate detection.

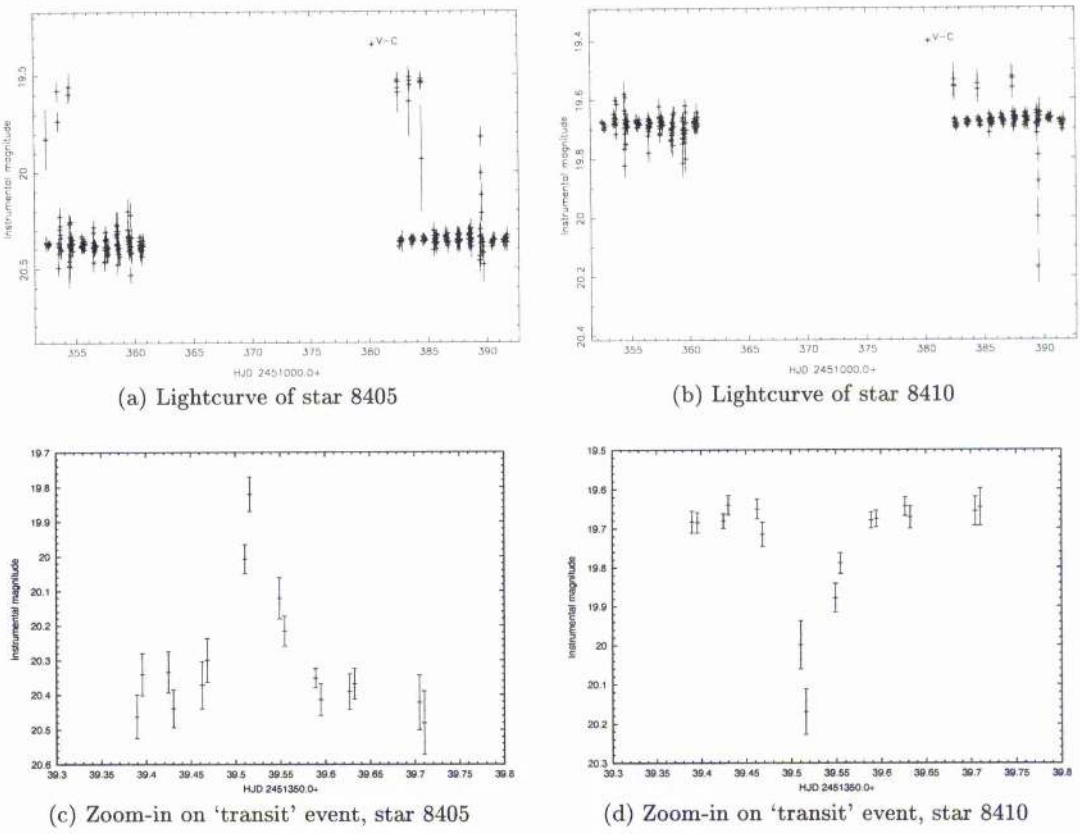

(a) Lightcurve of star 8405

(b) Lightcurve of star 8410

(c) Zoom-in on 'transit' event, star 8405

(d) Zoom-in on 'transit' event, star 8410

Figure 5.20: Example lightcurves of a blended pair of stars, 8405 and 8410. The lower two plots show the lightcurves at the time of the transit-like event detected by TRANSITFINDER.

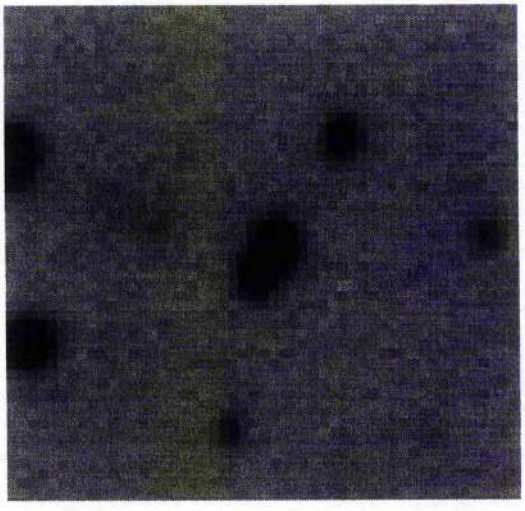

Figure 5.21: Thumbnail image of the two blended stars, 8405 and 8410 (centre).

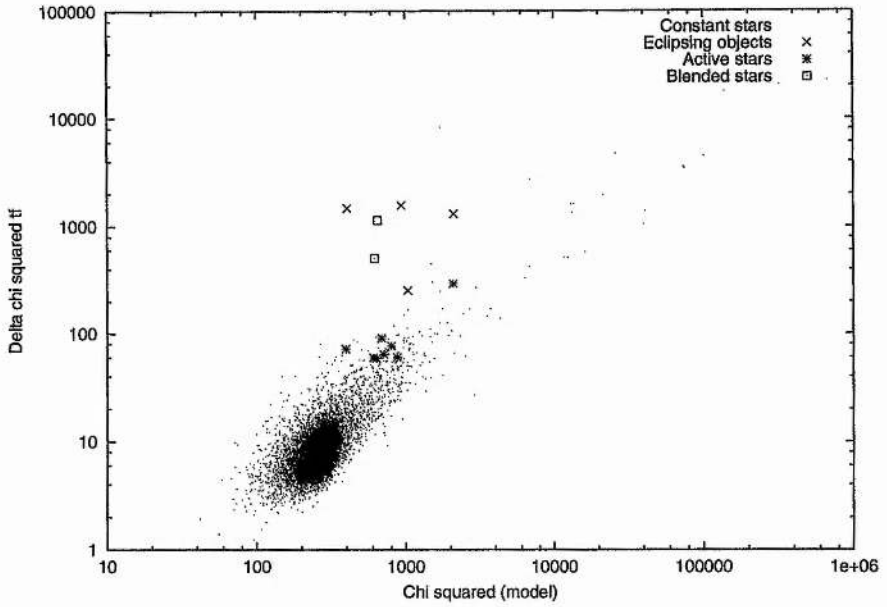

(a) CCD 2

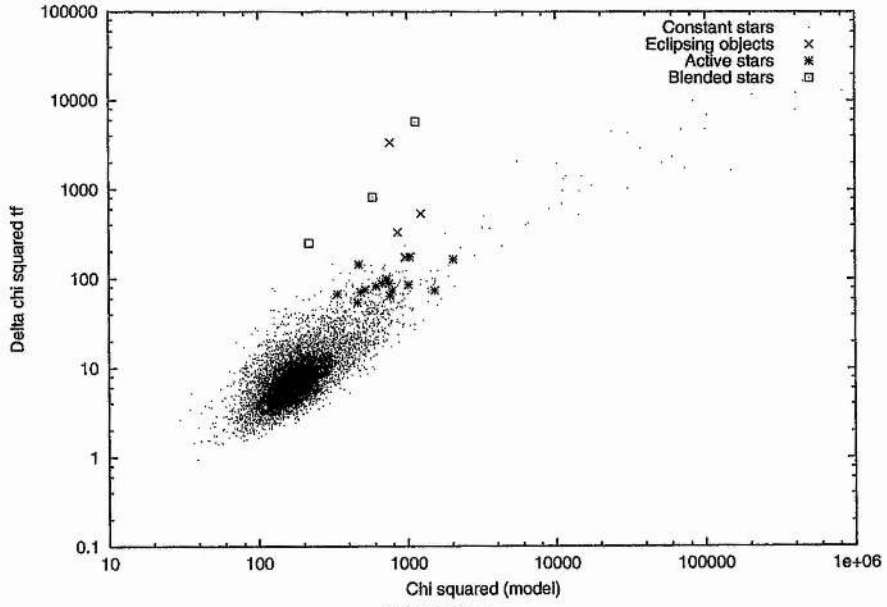

(b) CCD 4

Figure 5.22: χ^2_{red} .vs. $\Delta\chi^2_{tf}$ plotted for CCDs 2 and 4. The postions of the variable stars identified by TRANSITFINDER are marked.

diagrams therefore make a useful guide when examining transit candidates.

Genuine transits would be expected to have low values of χ^2(model), indicating a good fit in addition to showing a considerable improvement in fit between the model and a straight line - i.e., a high value of $\Delta\chi^2_{tf}$. I have therefore carefully examined the lightcurves of all stars in the region of both plots; that is stars with χ^2(model) > 50.0 and $\Delta\chi^2_{tf} < 400.0$. These lightcurves are shown in Figures 5.23 – 5.28. More candidates were identified on CCD4 than CCD2 due to the detrimental effects of the greater degree of blending.

A number of these stars fall into this interesting region due to the effects of low-level stellar activity – for example, stars 171 and 545. A significant number of the selected sample – such as 5288 and 8291 – are so faint as to lie on the limit of detectability in this data and have a correspondingly large degree of scatter in their lightcurves. It can be seen from all the lightcurves that nights of poor conditions can cause a series of widely scattered datapoints; HJD 2451353 is a common culprit. Naturally, in some cases this scatter can mimic a transit and the algorithm is drawn towards these points. This is the case for many of these candidates (see, for example, stars 918 and 1759) but close inspection reveals that the "transit" is unconvincing. Similarly some stars like 1356 show 2 or 3 consecutively faint datapoints but this is insufficient to identify a convincing transit event. Follow-up data with a greater sampling rate is required, and as yet, no convincing transits have been discovered.

5.7 Summary

In this chapter I have discussed the photometric accuracy achieved by the pipeline and derived colour information on all the stars. I have described how my TRANSITFINDER algorithm finds transit events and established a suitable threshold in the transit statistic, $\Delta\chi^2_{tf}$, for finding these events.

I have presented an analysis predicting the number of transits I would expect to see in this dataset if every star had a planet similar to HD 209458b orbiting with a 3.5 day period. Assuming that the frequency of such planets is the same in this field as in the Solar neighbourhood ($\sim$ 1 percent according to radial velocity surveys), then I would expect to find between 2 and 3 transiting planets, 0–1 of which should be a cluster member. I note however, that the probability of finding transits drops significantly for periods which are

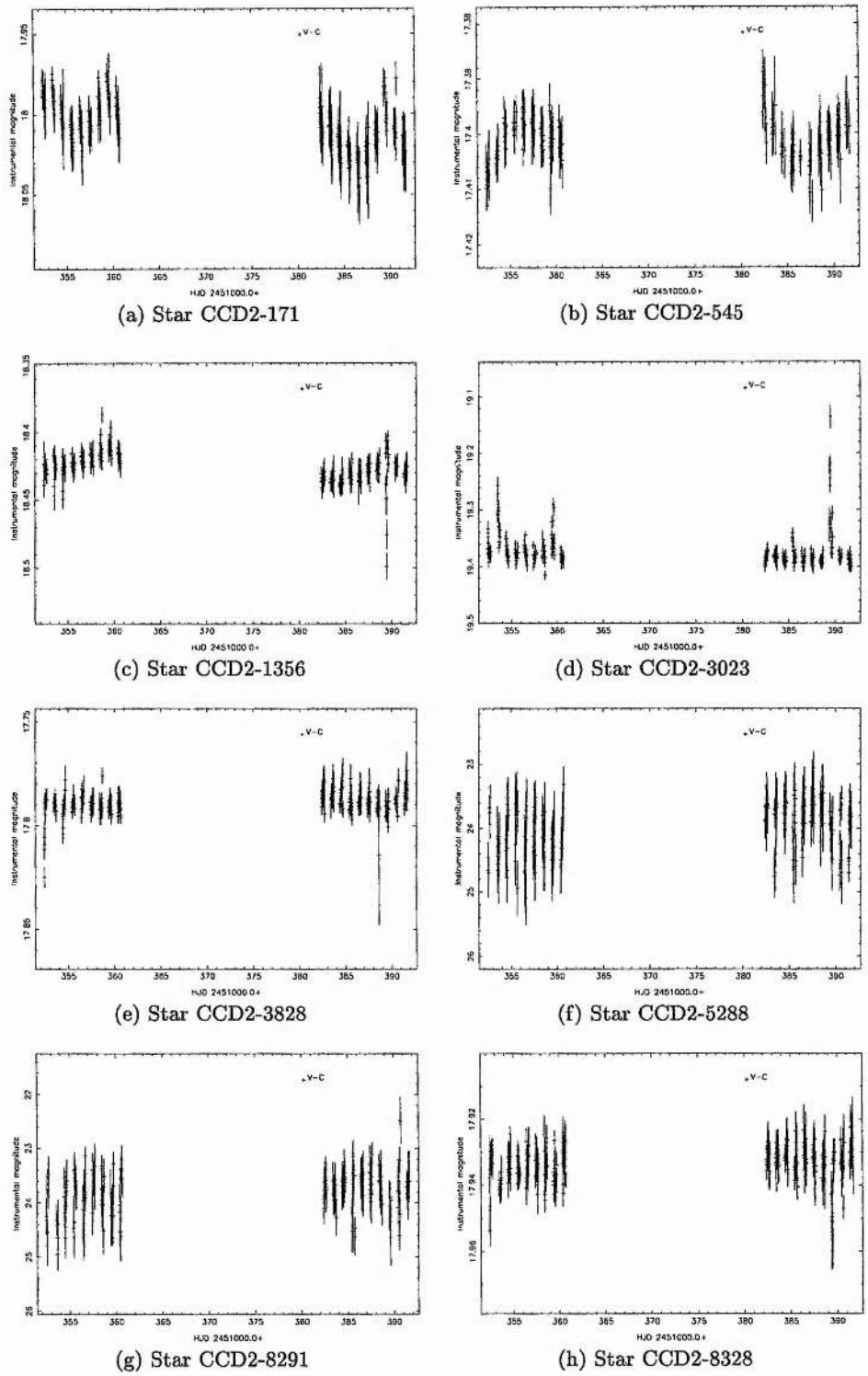

(a) Star CCD2-171

(b) Star CCD2-545

(c) Star CCD2-1356

(d) Star CCD2-3023

(e) Star CCD2-3828

(f) Star CCD2-5288

(g) Star CCD2-8291

(h) Star CCD2-8328

Figure 5.23: Lightcurves of stars from region of χ^2_{red} .vs. $\Delta\chi^2_{tf}$ plots where planetary transits are expected.

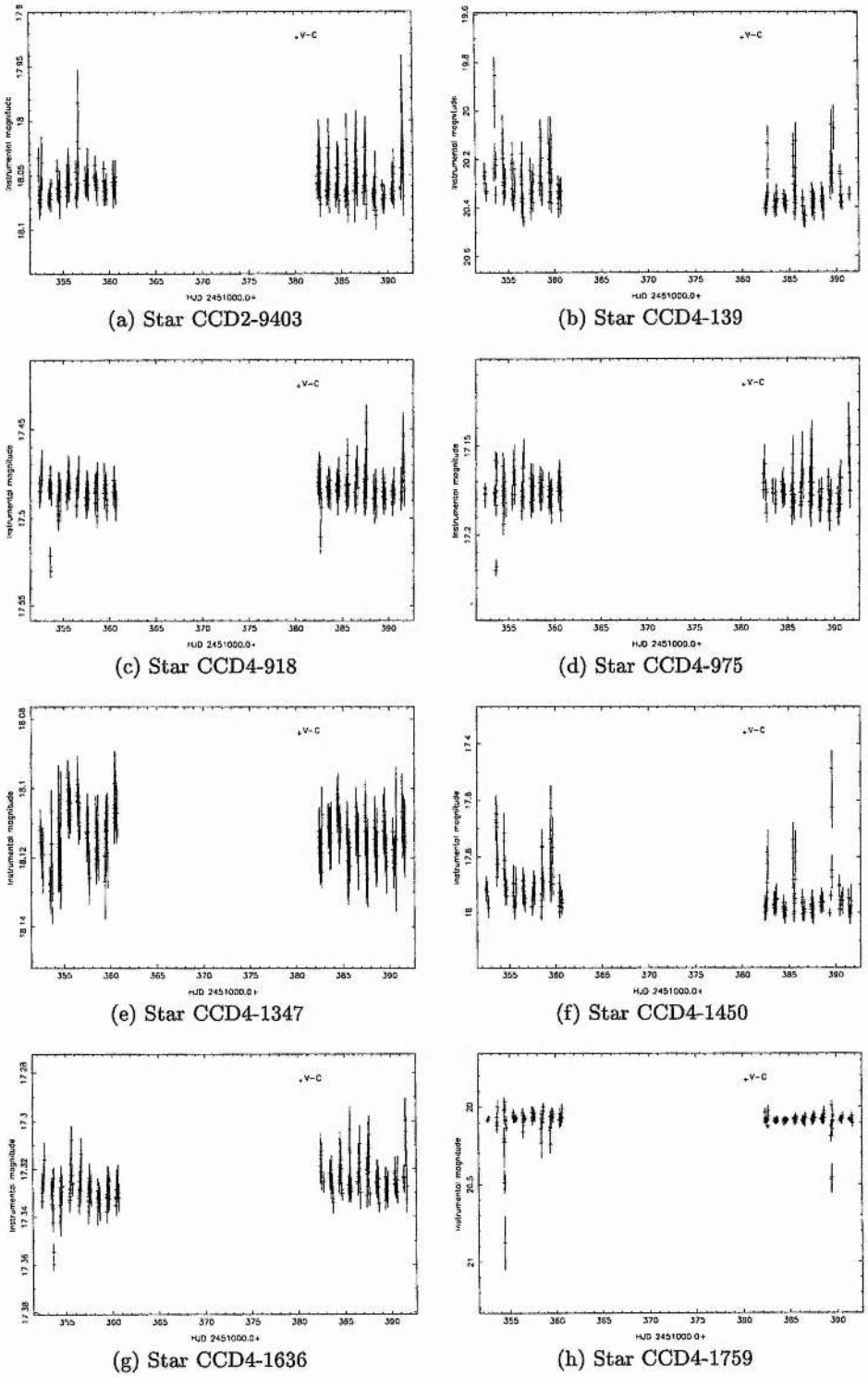

(a) Star CCD2-9403

(b) Star CCD4-139

(c) Star CCD4-918

(d) Star CCD4-975

(e) Star CCD4-1347

(f) Star CCD4-1450

(g) Star CCD4-1636

(h) Star CCD4-1759

Figure 5.24: Lightcurves of stars from region of χ^2_{red} .vs. $\Delta\chi^2_{tf}$ plots where planetary transits are expected.

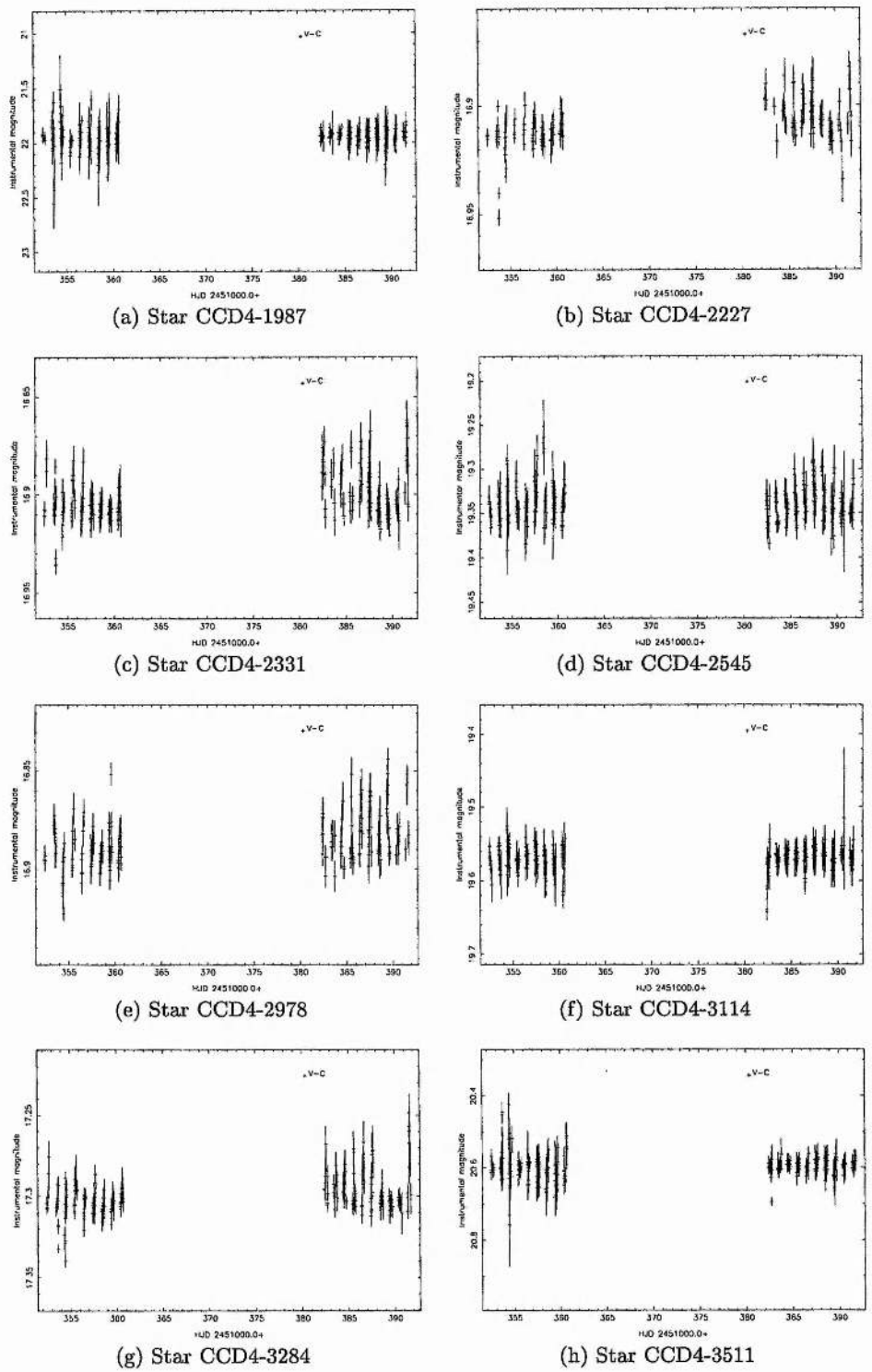

(a) Star CCD4-1987

(b) Star CCD4-2227

(c) Star CCD4-2331

(d) Star CCD4-2545

(e) Star CCD4-2978

(f) Star CCD4-3114

(g) Star CCD4-3284

(h) Star CCD4-3511

Figure 5.25: Lightcurves of stars from region of χ^2_{red} .vs. $\Delta\chi^2_{tf}$ plots where planetary transits are expected.

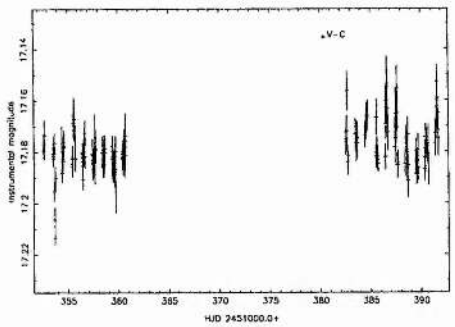

(a) Star CCD4-3616

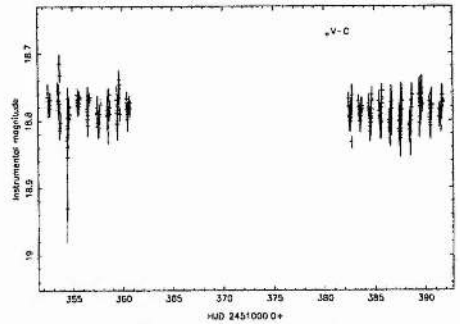

(b) Star CCD4-3844

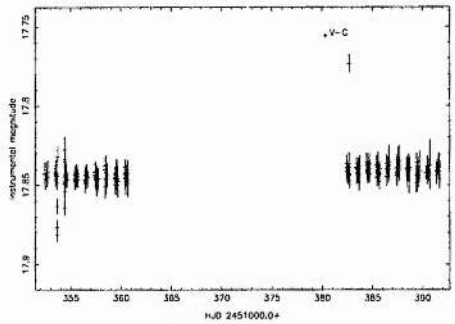

(c) Star CCD4-4303

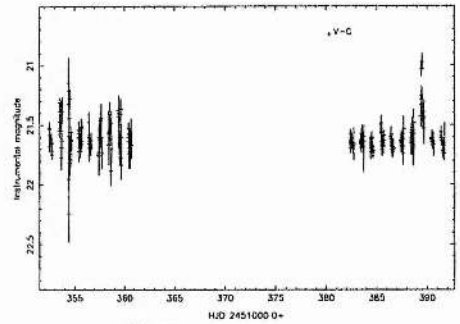

(d) Star CCD4-4347

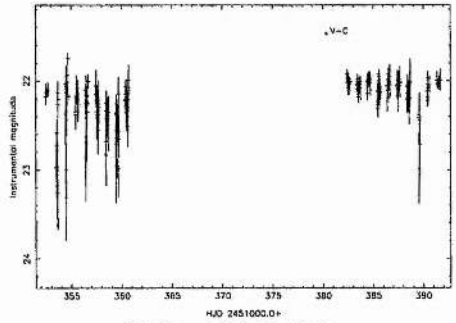

(e) Star CCD4-4376

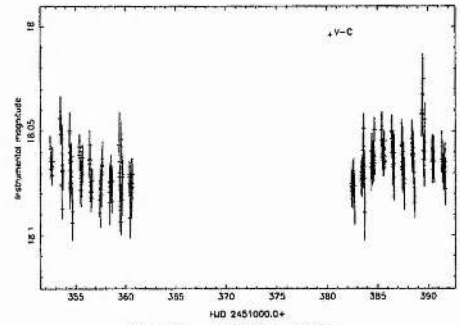

(f) Star CCD4-4986

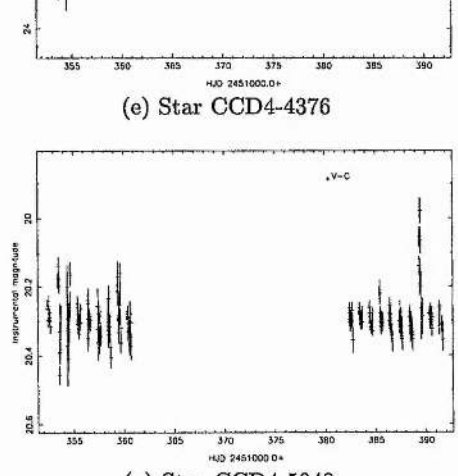

(g) Star CCD4-5048

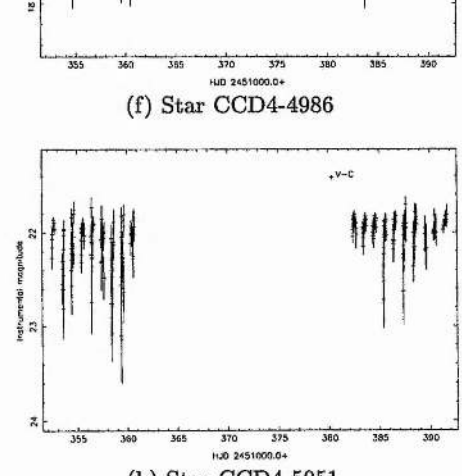

(h) Star CCD4-5051

Figure 5.26: Lightcurves of stars from region of χ^2_{red} .vs. $\Delta\chi^2_{tf}$ plots where planetary transits are expected.

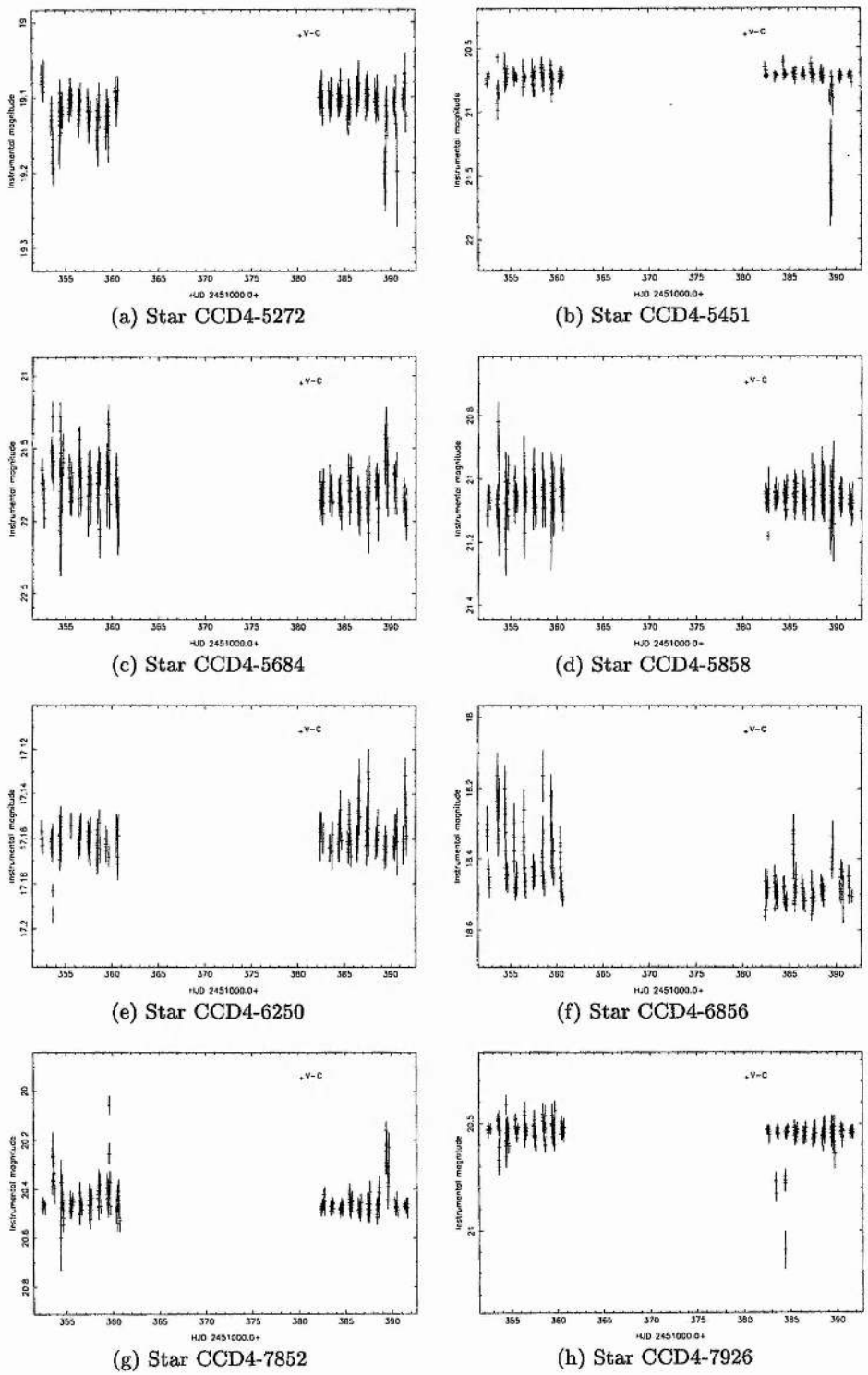

(a) Star CCD4-5272

(b) Star CCD4-5451

(c) Star CCD4-5684

(d) Star CCD4-5858

(e) Star CCD4-6250

(f) Star CCD4-6856

(g) Star CCD4-7852

(h) Star CCD4-7926

Figure 5.27: Lightcurves of stars from region of χ^2_{red} .vs. $\Delta\chi^2_{tf}$ plots where planetary transits are expected.

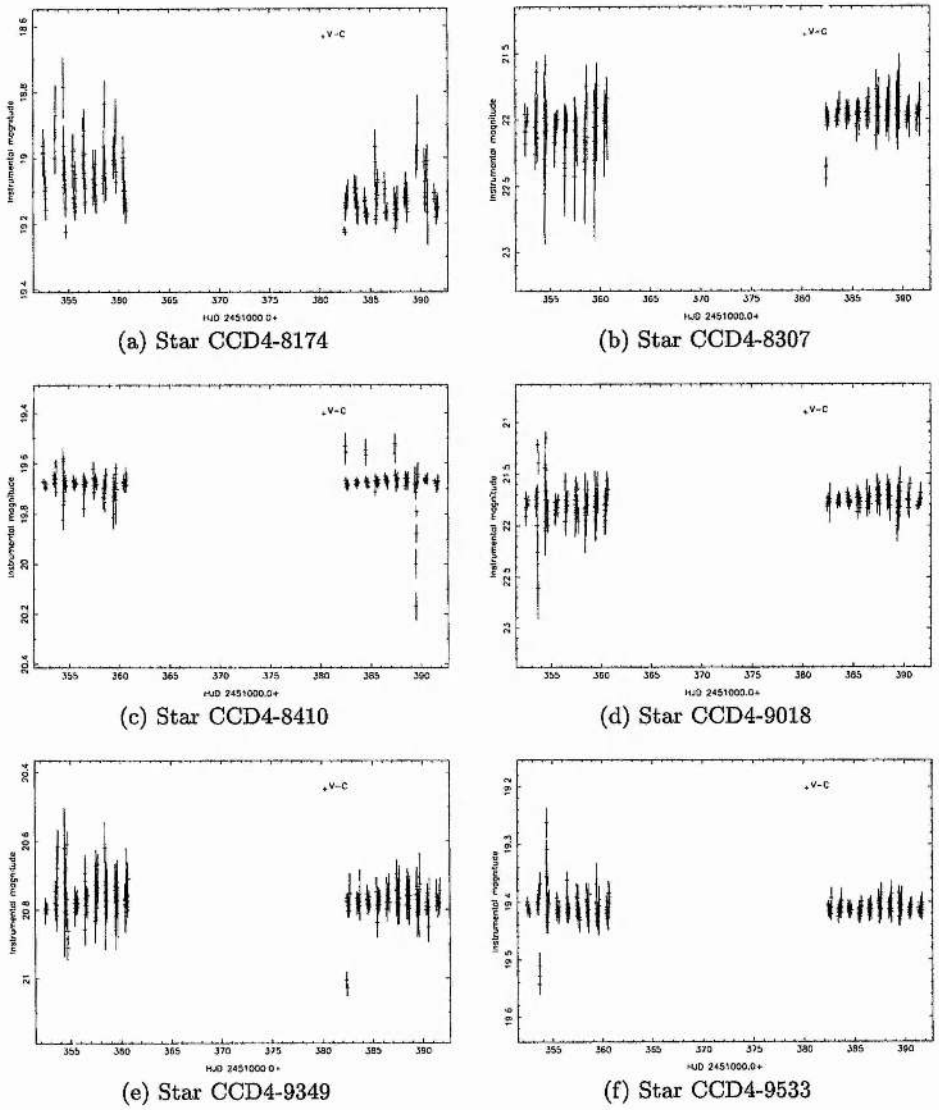

(a) Star CCD4-8174

(b) Star CCD4-8307

(c) Star CCD4-8410

(d) Star CCD4-9018

(e) Star CCD4-9349

(f) Star CCD4-9533

Figure 5.28: Lightcurves of stars from region of χ^2_{red} .vs. $\Delta\chi^2_{tf}$ plots where planetary transits are expected.

integer multiples of half or one day. The expected transit rate for different orbital periods is therefore higher.

In practise, I have found no planetary transits events. At first glance, this would tend to suggest that the frequency of 'hot Jupiter' type planets in the NGC 6819 field is different from that of the Solar neighbourhood. However, the number of stars surveyed means that the expected number of transits is sufficiently low that no firm conclusion can yet be drawn. Several stars were found to display eclipses however. Although the companion body in all cases was found to be of stellar mass, the algorithm proved its ability to identify brief, low-amplitude eclipses in real data. Several of these companion objects are thought to be very-low-mass stars (M-dwarfs) or possibly even brown dwarfs, and are worthy of follow-up study in their own right. I note that the threshold for detection was set fairly high for this study, in order to have zero false alarms from Gaussian statistics. Correspondingly, the amplitudes of the eclipses found were relatively high by planetary transit standards (a few hundredths of a magnitude). By using χ^2_{red} .vs. $\Delta\chi^2_{tf}$ diagrams to identify candidates in future, an alternative threshold may be set which would be more sensitive to low amplitude events while screening out most of the false alarms.

The TRANSITFINDER algorithm found 236 transit candidates in total. The vast majority ($\sim$ 75 percent) were found to be due to blending-distorted lightcurves, and I have found that my blending index shows a positive correlation with $\Delta\chi^2_{tf}$. Eliminating these false alarms, either by screening for affected stars and removing them from the dataset or making suitable improvments in the measurement technique, will be an important future development in transit detection. The other major source of false alarms proved to be stellar activity. Some 22 low-amplitude variable stars (mostly of the BY Dra class) were highlighted by the TRANSITFINDER. These were found to have variations which can be reasonably well fitted by a transit lightcurve model; that is, with similar durations and amplitudes. It was also noticed that the occasional night of poor-quality data (due to bad seeing for example) could cause lightcurve variations of similar or larger amplitude to those of a genuine transit. In this case, the algorithm can be drawn towards the larger amplitude spurious event, resulting in the transit being missed.

CHAPTER 6

Variable Star Discoveries

The results for CCD4 presented in this section are the subject of a paper, "Variable Stars in the Field of Open Cluster NGC 6819", which has been accepted for publication by *Monthly Notices of the Royal Astronomical Society.*

6.1 Introduction

While these observations were specifically designed to find transiting planets, long baseline time series photometry is also ideally suited to the discovery of many types of variable stars. In this respect, the field of an open cluster is extremely interesting as it provides a useful experimental ground for the investigation of star formation and evolution, not least for the eclipsing binaries that are the subject of work by Kaluzny and others (see for example Kaluzny, Mazur & Krzemiński 1993, Kaluzny & Ruciński 1993, Kaluzny, Krzemiński & Mazur 1996). These and other works suggest that some close cluster binaries evolve considerably with time due to the gradual loss of angular momentum and eventually coalesce into a single star. Since the ages of clusters can be established independently, the progress of this evolution can be charted by conducting photometric studies of binaries in clusters of known age. As NGC 6819 is an intermediate age cluster, we might expect to see signs of close/contact binaries in reasonable numbers.

6.2 Identifying Candidate Variable Stars

In order to identify variable star candidates, we first needed to eliminate from our sample stars that were poorly measured. Whatever the reason for this, be it saturation, blending,

close presence of a dead column etc., only stars measured in at least 60 percent of frames were considered. This eliminated approximately 16 percent of stars.

The reduced χ^2 of each star relative to the star's mean magnitude was then calculated; these parameters are plotted in Figure 6.1. I notice that the main body of points on the reduced χ^2 plot are below the expected value of 1. I believe that this is due to the over-estimation of the magnitude errors produced by DAOPHOT, which include default co-efficients for the flat-fielding and PSF errors.

A straight line of variable offset and gradient was fitted using the method of least-squares to the 'backbone' of points in this diagram. A good fit was obtained by iteration. The standard deviation of the points around the line ($\sigma_{\chi^2_{red}}$) was computed and in the following iteration, points more than 2σ away from the line were excluded. This process was repeated until the fitted parameters changed by less than 10^{-5} between iterations. Finally, I identified all stars fulfilling the criterion:

$$\chi^2_{red}(j) \geq \chi^2_{red}(\overline{mag(j)}) + \sigma_{\chi^2_{red}}, \tag{6.1}$$

where $\overline{mag(j)}$, and $\chi^2_{red}(j)$ are respectively the mean magnitude and reduced χ^2 of star j and $\chi^2_{red}(\overline{mag(j)})$ is the χ^2_{red} predicted for a star of this magnitude by the fitted lines.

The corresponding cut-off lines are plotted in Figure 6.1. 785 stars were found above this cut off line in CCD4; 2596 were found in CCD2. These objects were all considered candidate variables. The reason for this increase in the numbers found is due to the much tighter clustering of non-variable stars in Figure 6.1(a), resulting in a much smaller value of $\sigma_{\chi^2_{red}}$. This clustering is in turn thought to be due to the lesser degree of blending in CCD2, away from the concentrated centre of the open cluster. The lightcurves of these stars were then examined to eliminate those showing spurious or residual systematic effects. I believe the main reasons for stars showing unusually high scatter are blending, the presence of CCD flaws such as dead columns, and the differences in atmospheric extinction of stars with different colours.

This left genuine variable stars plus a further set of stars showing signs of variability. In these latter cases the photometry is insufficient to be sure (for instance, when the

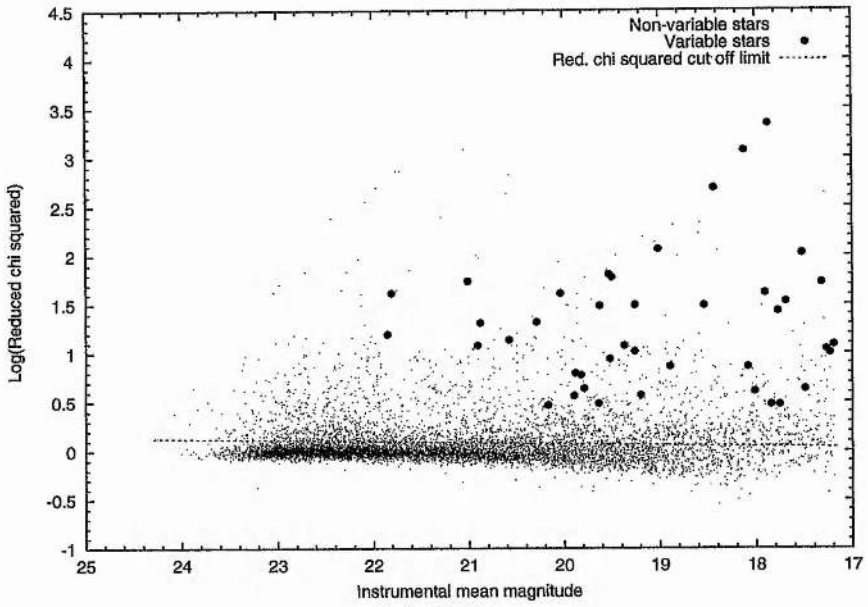

(a) CCD2

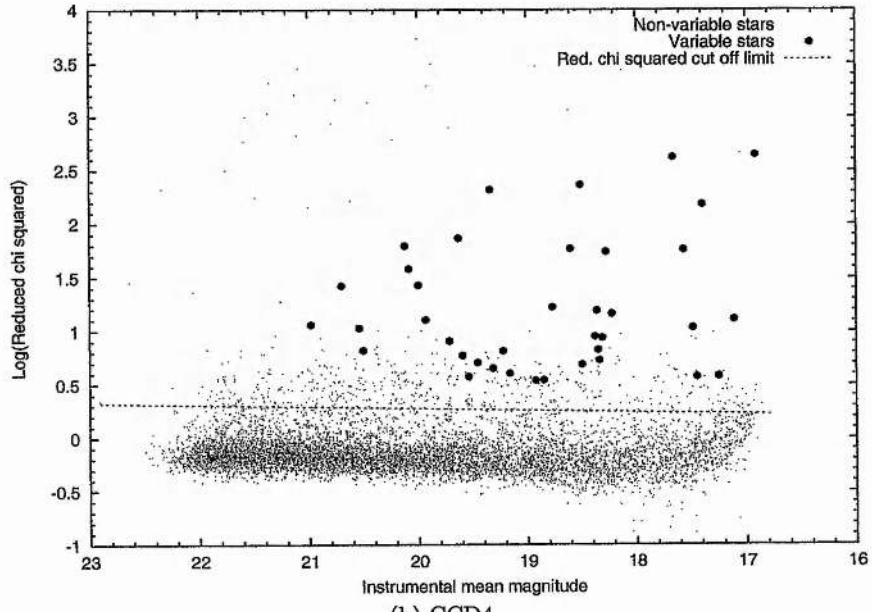

(b) CCD4

Figure 6.1: Plots showing the variation of χ^2_{red} with instrumental mean magnitude and the cut off limits between constant stars and candidate variables. The highlighted points mark the variables discussed in this chapter.

variations are of low amplitude). We attempt to classify these stars below, with the caveat that our lack of spectroscopic data means that the classes should be considered tentative until further work can be carried out. Astrometric results (discussed below) and finder charts are presented in Appendix B. Lightcurves of the differential photometry for the stars are presented in the relevant sections (6.4 – 6.7). In order to plot these, comparison and check stars were selected close to each variable; each lightcurve shows the variable-comparison (V-C) data as the upper curve and the comparison-check (C-K) data as the lower curve. The C-K curves have been displaced in magnitude by the amount shown for the sake of plot clarity.

Visual inspection of the lightcurves indicated those that show a high degree of periodicity. A period-finding program was then applied to the data for these stars. This program uses the Lomb method (Lomb 1976) to obtain a frequency spectrum where the highest peak occurs at the inverse of the period of variability. A Gaussian was then fitted to the highest peak in each spectrum to accurately determine the peak frequency and hence the period. The periodograms of some stars showed more than one strong frequency, indicating more than one possible period. This was usually because the period was close to the one-day alias, or due to very short duration eclipses with few datapoints, or else because the period of the variation was greater than the length of the dataset. In these cases, I have folded the lightcurves on the most likely period, and present the periodogram next to the lightcurve. For the sake of comparison, Figure 6.2 shows the window function of the dataset.

6.3 Colour Information

Once the variable stars were identified, a search was made for their entries in the Kalirai $B-V$ colour data. This information is presented with the stars in the relevant sections below. As I described in Chapter 5, colour data is not available for all stars; in the case of CCD2 in particular, this is chiefly due to the lack of overlap of the INT CCD2 field with that of the CFHT. However, for those stars where $B-V$ colour information is available, I have highlighted their positions on the respective CCD colour-magnitude diagrams in Figure 6.3.

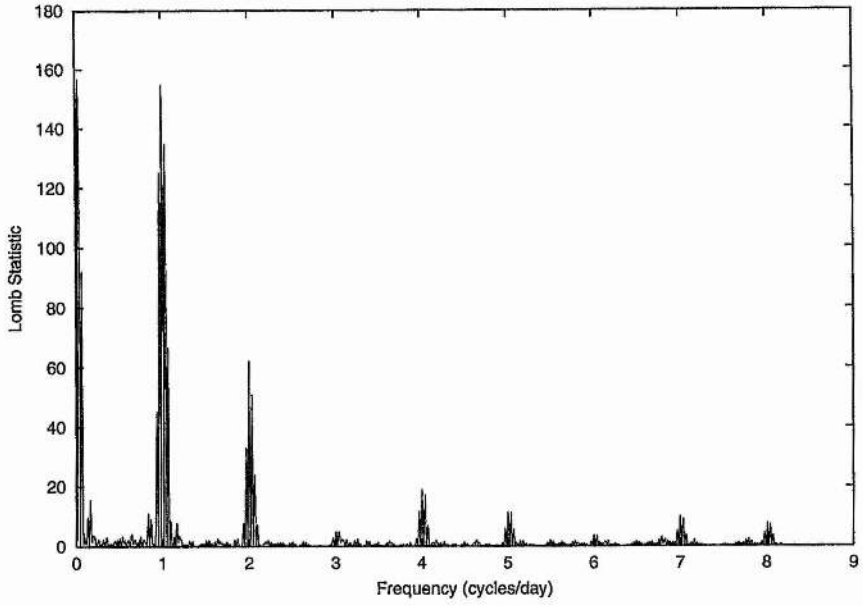

Figure 6.2: Plot showing the window function for the INT observations.

6.4 Eclipsing Binaries

I have found 25 eclipsing binary systems, plus a further 3 systems which I suspect to be eclipsing binaries. Their details are listed in Tables 6.1 and 6.2, where in the case of the suspected systems, the reason for caution in my identification is noted. For those stars where colour data and calibrated V magnitudes were available, they are listed in columns 4 and 5 of the tables; for those stars where none was available I have computed a V magnitude using Equations 5.2. Columns 7 and 8 give the radial distance of each star from the cluster centre (measured by Kalirai et al. (2001a) to be $\alpha_{J2000} = 19^{\rm h}41^{\rm m}17.7^{\rm s}$, $\delta_{J2000} = +40°11'17''$), and the magnitude difference of each star from the cluster main sequence. In the latter column, a positive value indicates that the star lies above the main sequence, a negative one indicating it lies below the main sequence. These data are intended to be a guide to the likelihood of cluster membership for each star. In particular, the radial distance can be compared to the cluster radius for $15 \leq V \leq 20$ of $\sim 9.5'$ (Kalirai et al. 2001a), where the star density falls to that of the field. However, it should be noted that the colours of the binaries were obtained at unknown phase and so the positions of these stars relative to the main sequence is only intended as a rough guide to cluster membership. This is particularly important for some of the larger amplitude binaries.

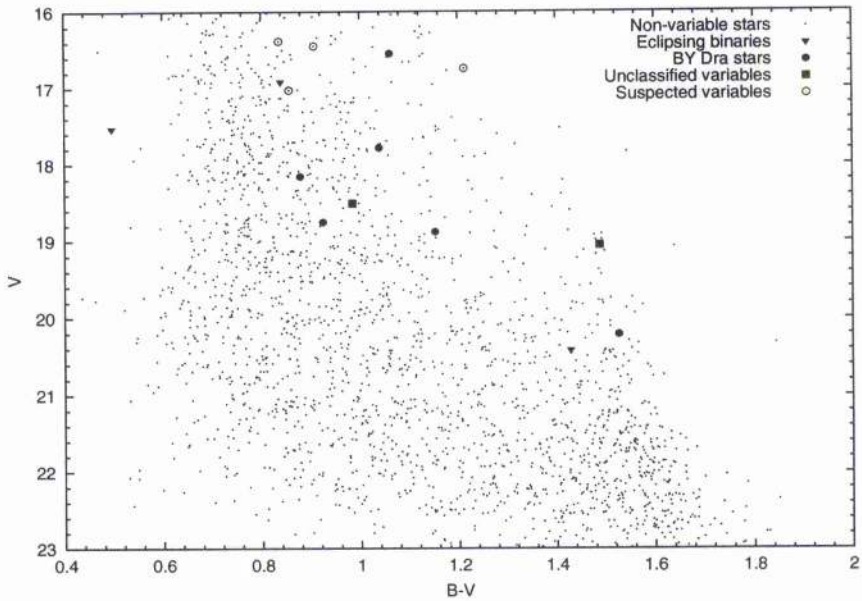

(a) CCD2

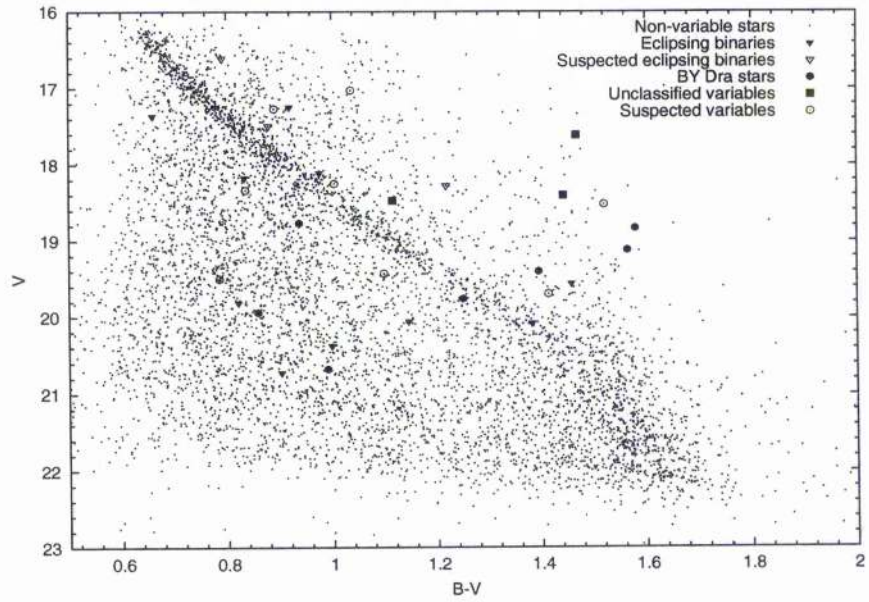

(b) CCD4

Figure 6.3: The colour-magnitude diagrams for each CCD. The highlighted points mark the variables discussed in this chapter.

Table 6.1: Details of the eclipsing binary systems found in CCD2 data, classified into the following categories: W Ursae Majoris type (EW), Algol-type (EA) and β Lyrae type (EB). The error on the last decimal place is given in brackets.

Star	Epoch (HJD)	Period (days)	V mag	$(B-V)$	Type	R′	δm_V (mag)
324	2451353.549(1)	0.2475(1)	21.2(2)		EW		
935	2451357.506(1)	2.92(6)	18.90(7)		EA		
946[1]	2451356.4974(9)	0.2982(2)	19.60(8)		EW		
1283	2451358.467(2)	0.2585(1)	21.3(1)		EW		
2155[1]	2451385.5621(6)	0.2445(1)	17.0(2)		EW		
2160	2451354.563(4)	0.2590(1)	20.4(1)		EW		
2876	2451357.721(3)	0.3828(4)	20.27(8)		EW		
3590	2451354.5444(7)	0.3903(3)	16.68(7)		EW		
4305	2451386.5897(7)	0.910(2)	20.420(3)	1.429(9)	EA		0.00
5291	2451352.5619(9)	0.5757(9)	17.526(3)	0.496(5)	EW		> -1.5
5362[1]	2451354.4718(5)	0.3117(2)	17.08(6)		EW		
7298	2451354.461(1)	0.3656(3)	16.915(2)	0.839(4)	EW		0.64
8124	2451356.5857(5)	0.2491(1)	17.3(2)		EW		

[1] Blended

Table 6.2: Details of the eclipsing binary systems found in CCD4 data, classified into the following categories: W Ursae Majoris type (EW), Algol-type (EA) and β Lyrae type (EB). The error on the last decimal place is given in brackets.

Star	Epoch (HJD)	Period (days)	V mag	$(B-V)$	Type	R $'$	δm_V (mag)
1753	2451358.6315(4)	0.2751(2)	20.078(3)	1.382(8)	EW	6.8	0.15
3856	2451356.4608(34)	0.293(1)	17.246(1)	0.920(1)	EW	5.6	0.82
4441[1]	2451358.5536(21)	0.2562(8)	18.275(1)	1.218(2)	EW	3.6	1.18
4448[2]	2451359.519(2)	0.3032(2)	17.494(1)	0.880(1)	EW	1.0	0.36
5302[3]	2451383.326(4)	0.6742(38)	18.106(1)	0.976(2)	EB?	1.3	0.24
5660	2451359.6924(8)	0.3384(2)	18.172(1)	0.834(2)	EW	4.7	-0.58
5834[4]	2451387.726(1)	0.3660(3)	16.610(2)	0.792(3)	EW	4.2	0.73
6230	2451382.4676(8)	0.2814(2)	20.724(4)	0.903(8)	EW?	2.7	-2.75
6728	2451359.516(1)	0.2637(9)	19.811(2)	0.822(8)	EW	4.4	-2.29
7333	2451385.607(1)	0.3571(2)	20.056(2)	1.146(6)	EA/RS	4.6	-0.92
7916	2451391.6151(3)	1.468(2)	17.359(3)	0.660(5)	EA/RS	6.4	-0.92
8080	2451355.5551(5)	0.2899(2)	20.374(3)	0.999(7)	EB	6.9	-1.92
8864	2451354.569(3)	1.332(3)	20.5(5)		EA	8.8	
8943	2451383.567(1)	0.2705(1)	19.559(2)	1.458(5)	EB	10.2	1.06
9440	2451355.628(9)	1.451(4)	20.6(5)		EB?	10.5	

[1] Suspected; sits on dead column, [2] Suspected; close to bright star, [3] Crowded field, [4] Suspected; blended, close to dead column

The phase–folded lightcurves for these systems are presented in Figures 6.4 - 6.7. Those for the suspected systems are shown in Figure 6.8. Most of the eclipsing binaries identified are of the W UMa (EW) type, consisting of ellipsoidal stars filling their Roche lobes, with their atmospheres in direct contact. These systems show smooth, continuously varying lighcurves where it is impossible to locate the exact begining and end of eclipses, which are usually of virtually the same depth. At least 3 systems seem to be Algol-type (EA) variables and the 4 are thought to be detached eclipsing binaries (EB). The components of EB or β-type eclipsing binaries are also ellipsoidal, causing continuously varying lightcurves, but not neccesarily in contact and there can be considerable difference in the depth of the eclipses. EA or Algol-type are composed of near-spherical, completely detacted stars, resulting in eclipses with sharply defined edges and little out of eclipse variation.

Stars 5660 and 5291 stand out as being particularly worthy of further attention. They display flat-bottomed eclipses of nearly equal depth, suggesting total eclipses, and hence an edge-on orbital inclination. With this in mind, it should be possible to perform a fit to the lightcurve in order to provide information on mass ratio, temperature etc. The attempt was made using the current dataset, but no reliable solution was obtained owing primarily to the lack of time-series data with another filter.

Although the stars 7916 and 7333 were initially classified as Algol-type eclipsing binaries, the distortion in the lightcurves and inequality of the maxima suggests that they may be eclipsing RS Canum Venaticorum (RS CVn) stars. These binary stars often show similar distortions in their lightcurves due to the presence of starspots, but spectroscopy is required to distinguish between these possible types. The photometry for stars 5302 and 9440 is similarly inconclusive about their classifications.

It is interesting to note the distribution in the periods of the W UMa systems. Ruciński (1997) presented a histogram of the period distribution of the W UMa type stars found by the OGLE experiment (Udalski et al. 1995a and Udalski et al. 1995b). This indicated that the most frequent period for W UMa systems was around ~ 0.4 days, and a sharp period cut-off at ~ 0.25 days. While the data suffers from the smallness of the sample, the values in Tables 6.1 and 6.2 suggests that the W UMa systems found in this field have periods shorter than the most common ~ 0.4 day period.

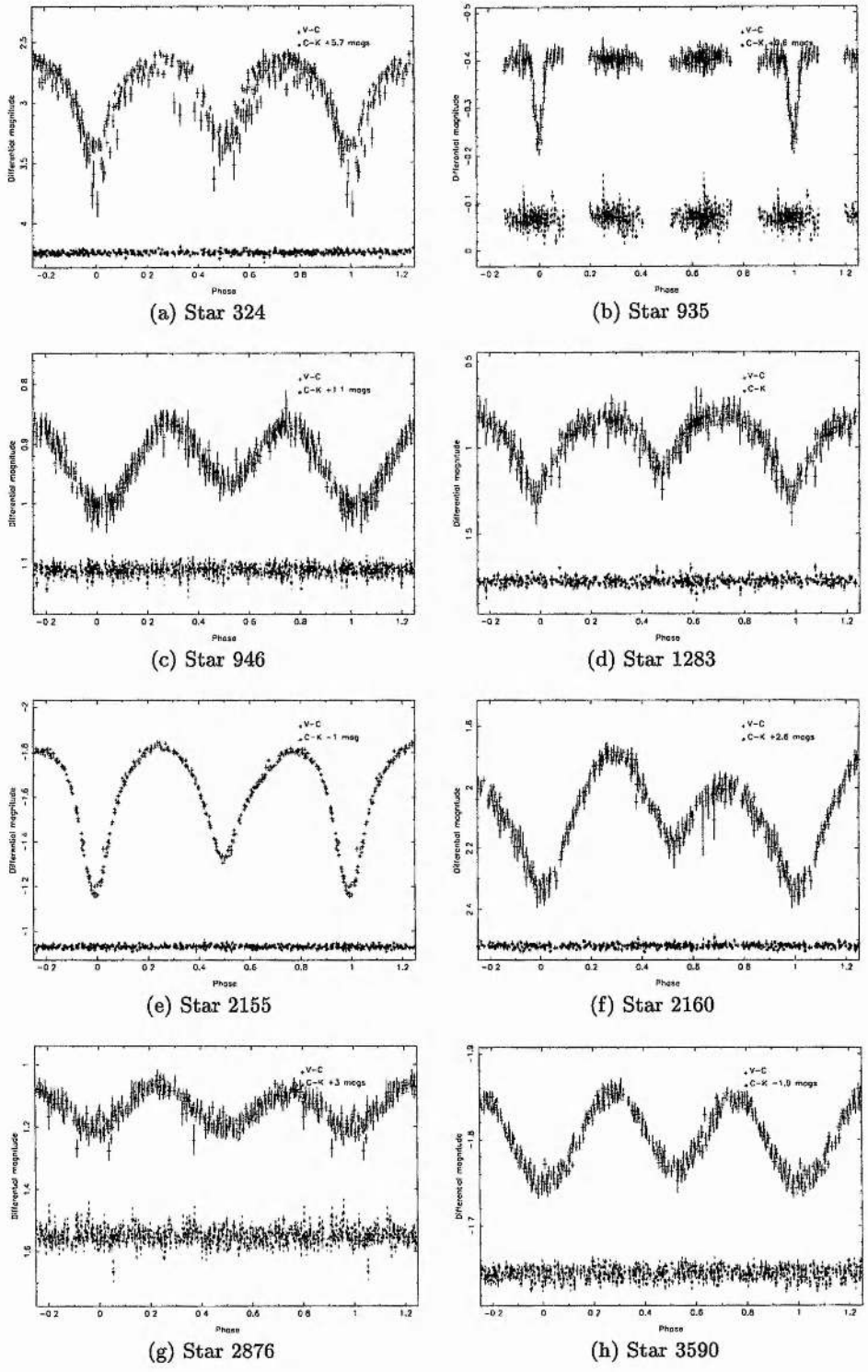

(a) Star 324

(b) Star 935

(c) Star 946

(d) Star 1283

(e) Star 2155

(f) Star 2160

(g) Star 2876

(h) Star 3590

Figure 6.4: Phased lightcurves for eclipsing binary systems from CCD2.

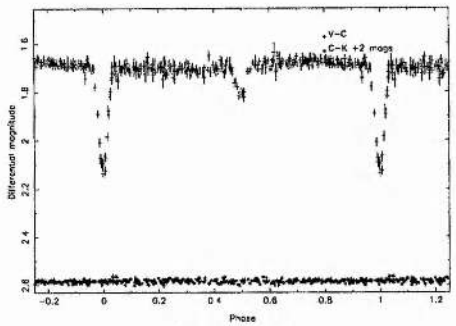

(a) Star 4305

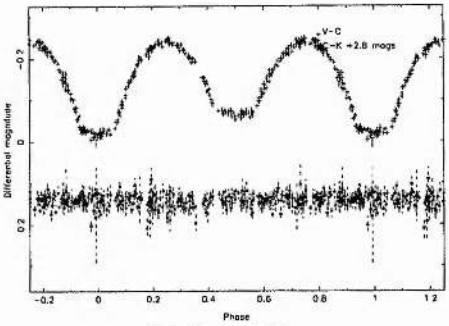

(b) Star 5291

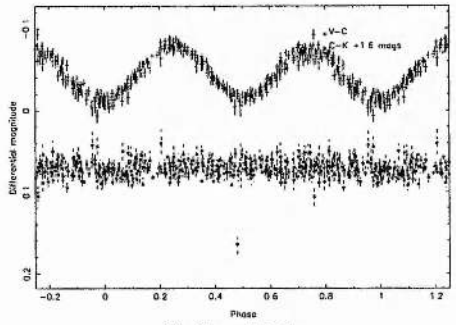

(c) Star 5362

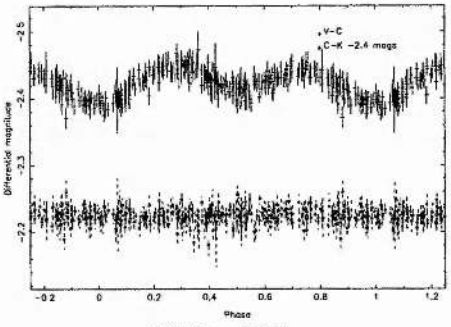

(d) Star 7298

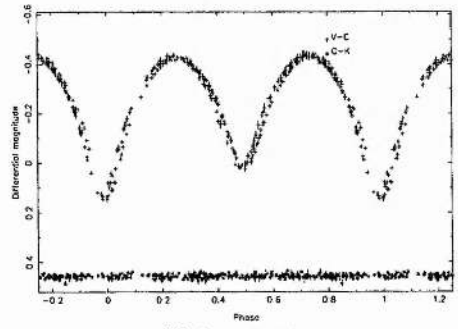

(e) Star 8124

Figure 6.5: Phased lightcurves for eclipsing binary systems from CCD2 (continued).

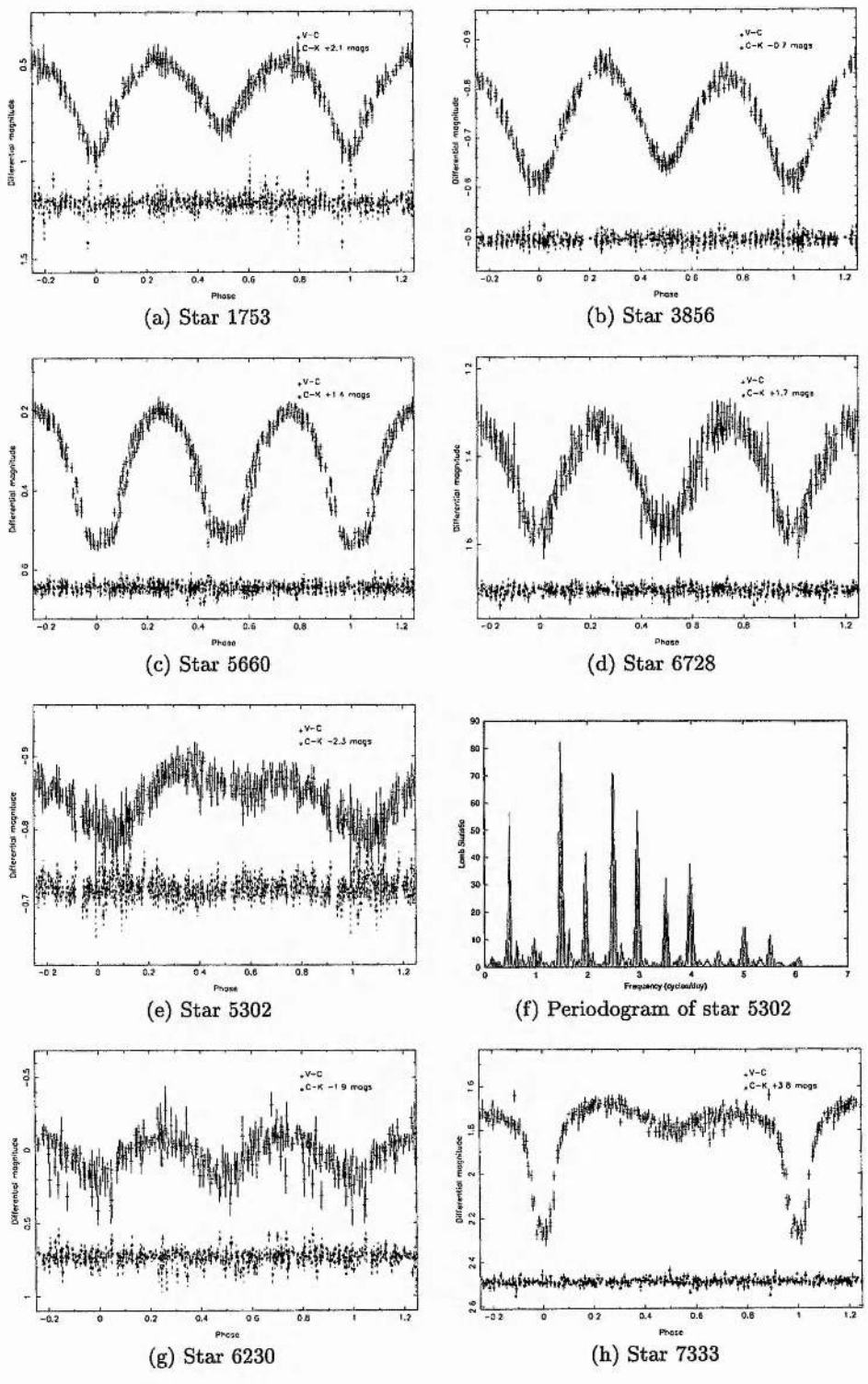

(a) Star 1753

(b) Star 3856

(c) Star 5660

(d) Star 6728

(e) Star 5302

(f) Periodogram of star 5302

(g) Star 6230

(h) Star 7333

Figure 6.6: Phased lightcurves for eclipsing binary systems from CCD4.

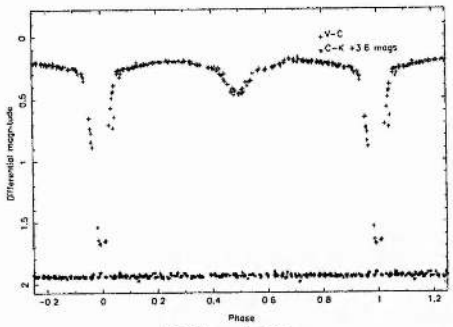

(a) Star 7916

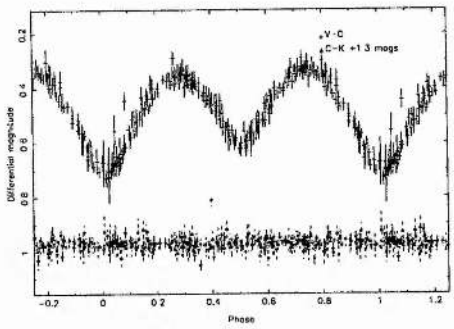

(b) Star 8080

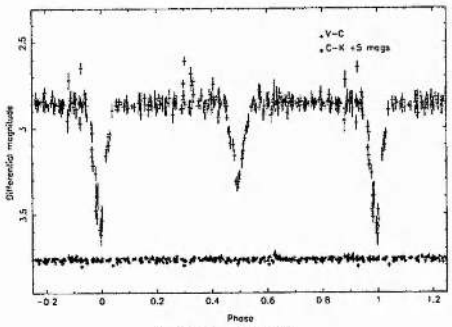

(c) Star 8864

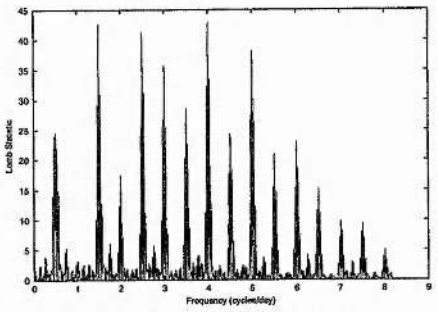

(d) Periodogram of star 8864

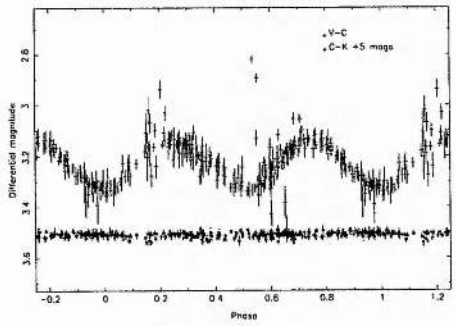

(e) Star 9440

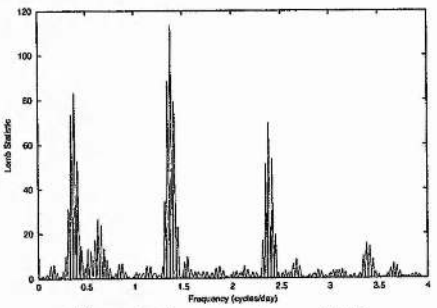

(f) Periodogram of star 9440

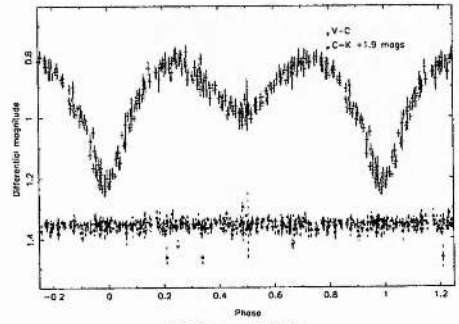

(g) Star 8943

Figure 6.7: Phased lightcurves for eclipsing binary systems from CCD4 (continued).

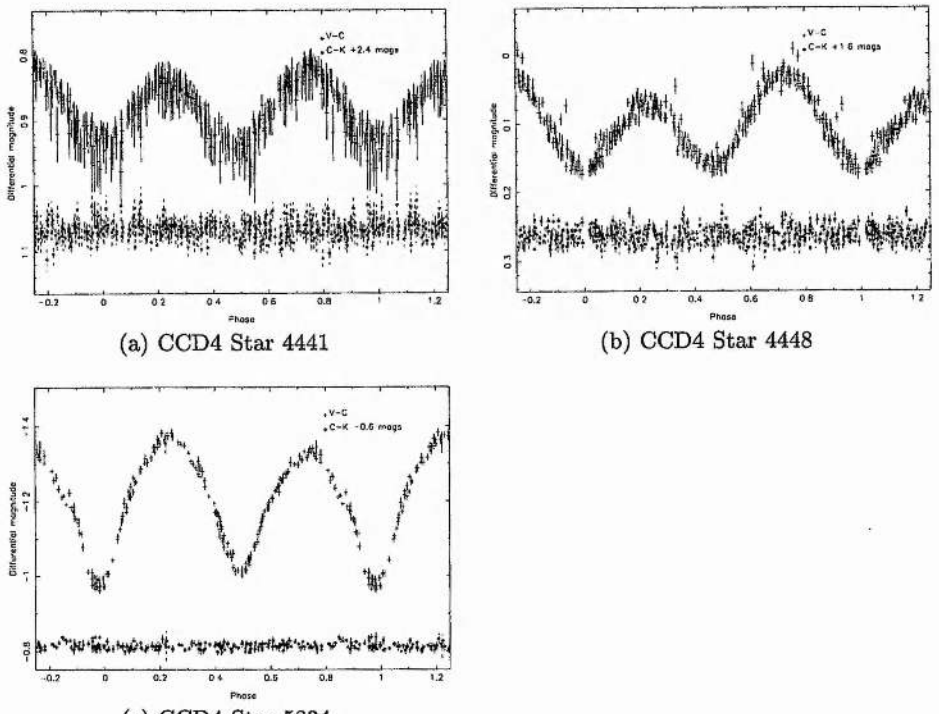

(a) CCD4 Star 4441

(b) CCD4 Star 4448

(c) CCD4 Star 5834

Figure 6.8: Suspected eclipsing binary systems.

6.4.1 Eclipsing Binary Cluster Membership

On the issue of cluster membership, the data in Tables 6.1 and 6.2 togther with Figure 6.3 indicate that stars 5291, 6230, 6728, and 8080 are most likely to be non-members, but is inconclusive about those positioned around the main sequence. Stars 8943 and 9440 are also probably non-members, judging by their large separations from the cluster centre. For the remaining W UMa-type stars in the sample, however, an alternative approach is available thanks to the period-colour-luminosity relation inherent to these stars. Ruciński (1997) derived the following relationship:

$$M_V = -4.44\log(P) + 3.02(B-V)_o + 0.12, \tag{6.2}$$

where M_V is the absolute magnitude of the W UMa, P is the period in days and $(B-V)_o$ is the dereddened colour of the system. Ruciński (1997) quotes an uncertainty of $0\overset{m}{.}22$ on absolute magnitudes calculated from this equation. Supposing that all the W UMa systems in this work that lie above the cluster main sequence are indeed cluster members, I adopt the value of reddening for NGC 6819 derived by Kalirai et al. (2001a),

Table 6.3: Determinations of distance to W UMas using the period-colour relation.

Star	CCD no.	Period (days)	m_V	$(B-V)$	M_V $\pm 0^m.22$	Distance (pc)
5291	2	0.5757(9)	17.526(3)	0.496(5)	2.38	9226±949
7298	2	0.3656(3)	16.915(2)	0.839(4)	4.29	2888±297
1753	4	0.2756(2)	20.078(3)	1.382(8)	6.48	4531±466
3856	4	0.293(12)	17.246(1)	0.920(1)	4.96	2468±252
4441	4	0.2562(8)	18.275(1)	1.218(2)	6.12	2326±237
4448	4	0.3032(2)	17.494(1)	0.880(1)	4.78	3016±308
5660	4	0.3384(2)	18.172(1)	0.834(2)	4.43	4844±494
5834	4	0.3662(14)	16.610(2)	0.792(3)	4.15	2683±275
6230	4	0.2814(2)	20.724(4)	0.903(8)	4.99	12100±1250
6728	4	0.2637(9)	19.811(2)	0.822(8)	4.87	8395±860
8080	4	0.2899(2)	20.374(3)	0.999(7)	5.22	9251±952

$E(B-V) = 0.10$ mag. It is then possible to calculate the absolute V magnitudes and hence the distances of these stars, assuming cluster membership. Any stars for which the calculated distance matches that of the cluster are considered probable cluster members. Table 6.3 gives the results of these calculations for all the W UMa systems for which I have colour information. In practice, three stars prove to have distances consistant with that of the cluster (2500 pc): 3856, 4441, and 5834. All of these stars fall on or slightly above the cluster main sequence on the colour–magnitude diagram, as expected for binary stars.

6.4.2 Possible M-Dwarf Binaries

Binary systems 4305 (CCD2) and 8864 (CCD4) also deserve special attention. The shape of their lightcurves seems to indicate detached systems of two spherical stars, and yet the periods were found to be 0.910 and 1.332 days respectively. It must be pointed out that the periodogram for the latter star, shown in Figure 6.7(d), has a number of strong peaks and therefore potential periods. This structure is believed to be due to the scarcity of datapoints obtained during the brief eclipses. All of the periods highlighted by the strong peaks have been used to phase the data for this star: only the peak at ~ 1.5 produced

a phased lightcurve and not scattered datapoints. The period implied is an harmonic of this peak. For two stars to remain undistorted at what must be a fairly small separations suggests that both stars are of low radius. The mean out-of-eclipse magnitude of $20\overset{m}{.}5$, and the likelihood that it consists of two small stars, suggests that the system is relatively nearby and not a cluster member (this is supported by its wide separation from the cluster centre). The duration and depth of the eclipses are ~ 5 hours and $0\overset{m}{.}75$, $0\overset{m}{.}45$ respectively. It is possible to derive a range of possible component masses for this system, using Kepler's law written in the form:

$$P = \frac{0.116(a/R_{\odot})^{3/2}}{(M/M_{\odot})^{1/2}}, \tag{6.3}$$

where P is the period of the system in days, a is the orbital separation, M is the sum of the component masses and $R_{\odot}$, $M_{\odot}$ are the solar radius and mass respectively. By rearranging Equation 6.3 it is possible to calculate the orbital separation of the stars for various component masses. Furthermore, knowing that the stars are undistorted implies that they must have radii, $R_* \lesssim 0.1a$ (Hilditch 2001). It is therefore possible to estimate the maximum undistorted radius for components of various spectral types. The estimated maximum radius can then be compared with the radius of a star of the type used. If the radius of the spectral type concerned is greater than the maximum calculated, then it implies that stars of that type are too large to remain undistorted given the period of this system. In this way, we find that star 8864 most probably consists of a pair of late-M dwarfs. However, this analysis assumes that the the stars are spherical, indicated by a flat lightcurve between eclipses. I note that if this system consisted of a pair of larger stars, they would be distorted, and the lightcurve would show a more rounded profile. The $V-R$ colour of this star (0.334) tends to suggest that this might be the case, although it should be remembered that this is derived from the combined light of two stars. Unfortunately, the star is too faint for the photometry to distinguish between these possibilities; further study is required.

Applying the same geometric analysis to star 4305 I find that this object is also likely to be a late-type star binary. In this instance however, colour data is available to assist in classification. The $(B-V)$ of 1.429 corresponds to an M-type star, although this colour also represents the combined light of the system. The difference in the depth of the

Table 6.4: Details of BY Draconis systems in CCD2 data. The error on the last decimal place is given in brackets.

Star	V mag	$(B-V)$	R′	δm_V (mags)	Amp. (mags)	Epoch (HJD)	Period (days)
56[1]	18.63(6)				0.08	2451386.14(1)	2.38(3)
90[2]	18.26(9)				0.18	2451357.30(1)	4.7(2)
681	19.11(6)				0.06	2451387.21(1)	2.32(4)
863	16.94(6)				0.08	2451385.02(1)	3.52(9)
2848	18.45(6)				0.04	2451356.89(5)	4.7(2)
3450	17.785(3)	1.039(7)		0.92	0.06	2451356.089(6)	1.39(2)
4698	16.548(2)	1.061(4)		2.20	0.04	2451358.42(6)	2.74(5)
4843[3]	18.755(1)	0.924(2)		-0.66	0.09	2451384.82(3)	5.332(7)
4977	19.34(8)					2451389.54(1)	0.461(2)[1]
5786	20.212(3)	1.527(8)		0.79	0.12	2451360.594(6)	0.3278(8)
6142	18.884(1)	1.152(3)		0.32	0.06	2451383.06(1)	1.29(2)
6694	18.157(1)	0.878(2)		-0.36	0.05	2451353.29(3)	0.660(3)
7662	19.19(6)				0.05	2451354.51(6)	2.93(7)

[1] Blended, [2] Close to bright object, [3] Possible RS CVn.

eclipses indicates two stars of different temperature. Nevertheless, the evidence suggests a very low mass star binary.

Very few M-dwarf binaries are currently known, yet their study forms a crucial foundation for much of astronomy. Detailed photometry and spectroscopy of such systems can be used to determine the physical dimensions of the component stars which in turn can be used to constrain models of stellar properties (Anderson 1991). The low mass end of these models is constrained chiefly by only two points; the M-dwarf binaries CM Dra and YY Gem. The handful of other such systems known have mostly not been studied in sufficient detail. Therefore, the addition of more very low mass binaries, if confirmed, would be a significant improvement, and further study of these systems is strongly recommended.

Table 6.5: Details of BY Draconis systems in CCD4 data. The error on the last decimal place is given in brackets.

Star	V mag	$(B-V)$	R $'$	δm_V (mags)	Amp. (mags)	Epoch (HJD)	Period (days)
1815	19.400(2)	1.395(5)	6.6	0.90	0.06	2451388.61(1)	0.733(4)
2393	18.765(1)	0.938(3)	6.0	-0.61	0.04	2451356.56(4)	1.9(2)
2576	18.833(1)	1.580(4)	6.2	2.49	0.14	2451389.6(3)	1.37(1)
3126[1]	19.939(2)	0.859(5)	6.2	-2.20	0.05	2451384.62(6)	5.4(2)
3127	19.758(2)	1.250(6)	4.4	-0.16	0.08	2451386.19(2)	3.5(1)
4003	18.2(4)		1.9		0.08	2451384.49(2)	3.9(1)
4484	19.1(4)		1.4		0.09	2451357.31(4)	6.3(3)
5861	19.120(2)	1.565(4)	1.6	2.11	0.06	2451387.11(5)	6.5(3)
7711	20.677(4)	0.991(8)	7.4	-2.26	0.39	2451357.39(3)	4.2(1)

[2] Close companion

6.5 BY Draconis Stars

I have found 21 stars which appear to be of the BY Draconis (BY Dra) type; their details are tabulated in Tables 6.4 and 6.5, and their lightcurves are presented in Figures 6.10 - 6.13. BY Dra variables are single, chromospherically active red dwarf stars. The photometric variations caused by the chromospheric activity (starspots, flares, etc.) can change in amplitude with the appearance/disappearance of spot groups. While periods have been determined for these new BY Dra stars, in some cases the periods are a sizable fraction of the length of the dataset. Therefore, as few cycles were observed, the periods show a higher degree of uncertainty. Columns 4 and 5 of Tables 6.4 and 6.5 refer to radius from the cluster centre and magnitude difference from the main sequence, as described in Section 6.4. Most of these stars show the classic characteristics of BY Dra stars – sinusoidal photometric variations (of amplitudes given in column 7) attributed to starspot activity on timescales of a few to tens of days, with photometric amplitudes between $0\overset{m}{.}05$ – $0\overset{m}{.}5$. Alekseev (2000) found that the majority (80 percent) of BY Dra stars do not exceed an amplitude of $0\overset{m}{.}15$, and these data conform to this finding. Only one star, 7711, displays an unusually high amplitude of nearly $0\overset{m}{.}4$. However, this is similar to the amplitude of BY Dra itself ($0\overset{m}{.}38$, Alekseev (2000)), and other examples of $\sim 0\overset{m}{.}4$ amplitude BY Dra

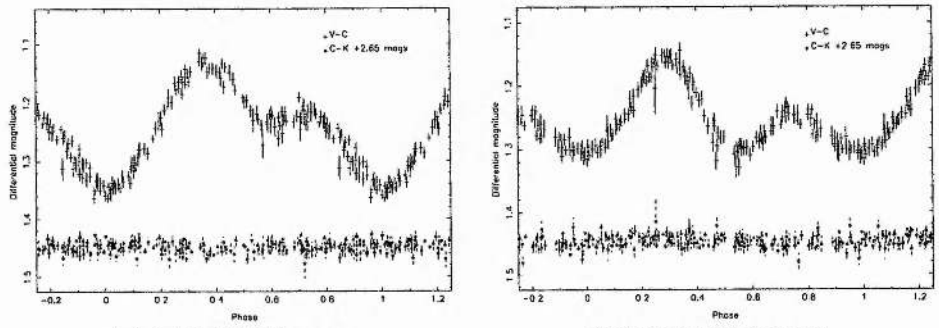

(a) 1st half lightcurve (b) 2nd half lightcurve

Figure 6.9: Phased lightcurves for BY Dra star 4977 for both halves of the dataset.

stars are known, so I retain this classification for 7711, in lieu of further data on this star. Furthermore, the $(B-V)$ colour information available for these objects indicate late–type stars, which is consistant with this classification. Some of these stars show a change in the amplitude of the variations between the two datasets, most notably star 4977. In the process of determining the periodicity of this object I found that the lightcurve morphology changed significantly between the first and second halves of the dataset. Figure 6.9 shows the phased lightcurves resulting from each half of the data. This variation makes sense in terms of the constantly changing area and latitude of spot coverage of the star.

Star 4843 shows some unusual features. The lightcurve (Figure 6.10(h)) shows two dips where the star appears to get $\sim 0\overset{m}{.}3$ fainter for a very brief ($\sim$ 2.5 hours) period. Close examination of these events shows that the datapoints follow a smooth eclipse profile. The eclipses have an approximate duration of 2.5 hours and a depth of about $0\overset{m}{.}35$ while the colour data on this object gives a $B-V$ of 0.924 ± 0.002. As the sinusoidal variations indicate a BY Dra primary star, this colour implies a star of type ~K2-3. Eclipses of this depth and duration could then be caused by an object of radius ~ 0.4 R_* or a late M-type star. If this is confirmed then this object could be re-classified as an RS CVn.

Figure 6.3 highlights 5786, 6142, 3450, 1815, 2576, 3127 and 5861 as possible cluster members, and while I have no colour information for 4003 and 4484, both have small projected distances from the cluster centre. The remaining stars are unlikely to be cluster members.

Several of these stars have periods considerably shorter than $\lesssim 2$ days. Star 5789 in particular has an unusually short period for a BY Dra star, and indeed it was initially classified as a W UMa until the colour was found to be 1.527. If further work confirms

Table 6.6: Details of the unclassified systems in the CCD2 data. The error on the last decimal place is given in brackets.

Star	V mag	$(B-V)$	R′	δm_V (mags)	Amp. (mags)	Epoch (HJD)	Period (days)
50	19.18(6)				0.08	2451356.00(6)	8.5(5)
2435	18.52(6)				0.07		
4694[1]	19.058(1)	1.488(4)		1.44	0.12	2451356.36(2)	6.9(4)
5567[2]	18.513(1)	0.984(2)		-0.21	0.09		

[1] Close pair with 4690, [2] Near bright object.

this classification, it may be that these stars have been spun up as part of binary systems, or they may simply be younger objects and unrelated to the cluster. I note, however, that the period of 2393 in particular is such that I obtained similar phase observations each night, and the resulting gaps in the phase coverage precludes firm classification.

I note that RS CVn and FK Comae Berenices (FK Com) stars can show similar lightcurve morphology to BY Dra stars, if the binary is non-eclipsing in the case of an RS CVn. FK Com stars differ from BY Dra in that they are giant chromospherically active stars, while RS CVn stars are close binary stars which show eruptive behaviour as well as the chromospheric activity which gives rise to sinusoidally varying lightcurves. While the high frequency of binary stars would argue for at least some of the stars in this section being RS CVn stars, I have currently have no evidence for this being the case. The possibility of an FK Com classification can be ruled out for most of the candidate BY Dra stars on the basis of their colours which indicate late-type stars. Until spectroscopic data is available for these objects, I classify them as BY Dra stars.

6.6 The Unclassified Variables

I found 8 stars showing significant variability for which the classification remains tentative. The details of these stars are given in Tables 6.6 and 6.7, and their various lightcurves may be found in Figure 6.14.

The lightcurve of star 8132 (Figure 6.14(g)) appears to be that of a Cepheid. While

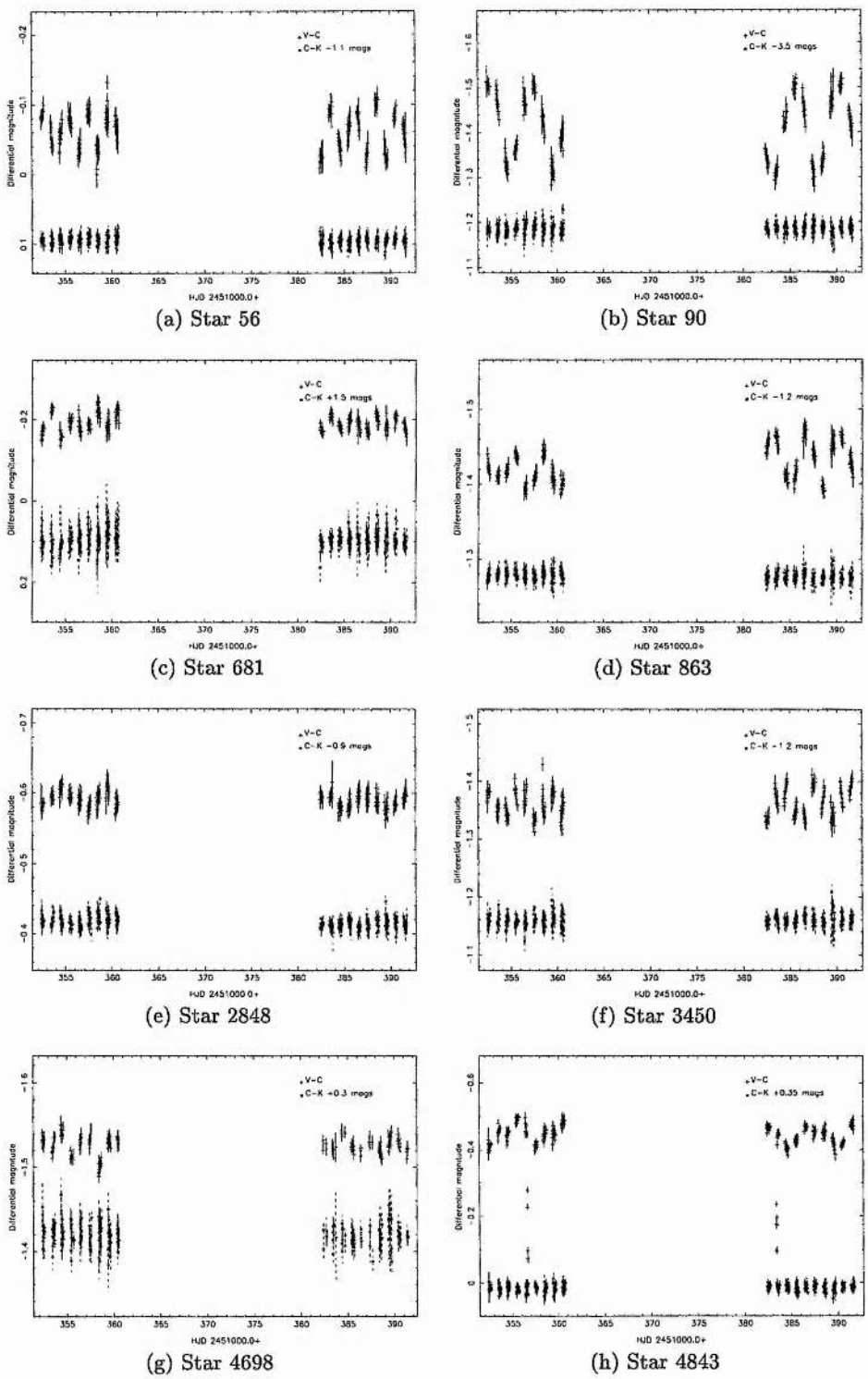

(a) Star 56 (b) Star 90

(c) Star 681 (d) Star 863

(e) Star 2848 (f) Star 3450

(g) Star 4698 (h) Star 4843

Figure 6.10: Lightcurves of the BY Dra systems in CCD2 data.

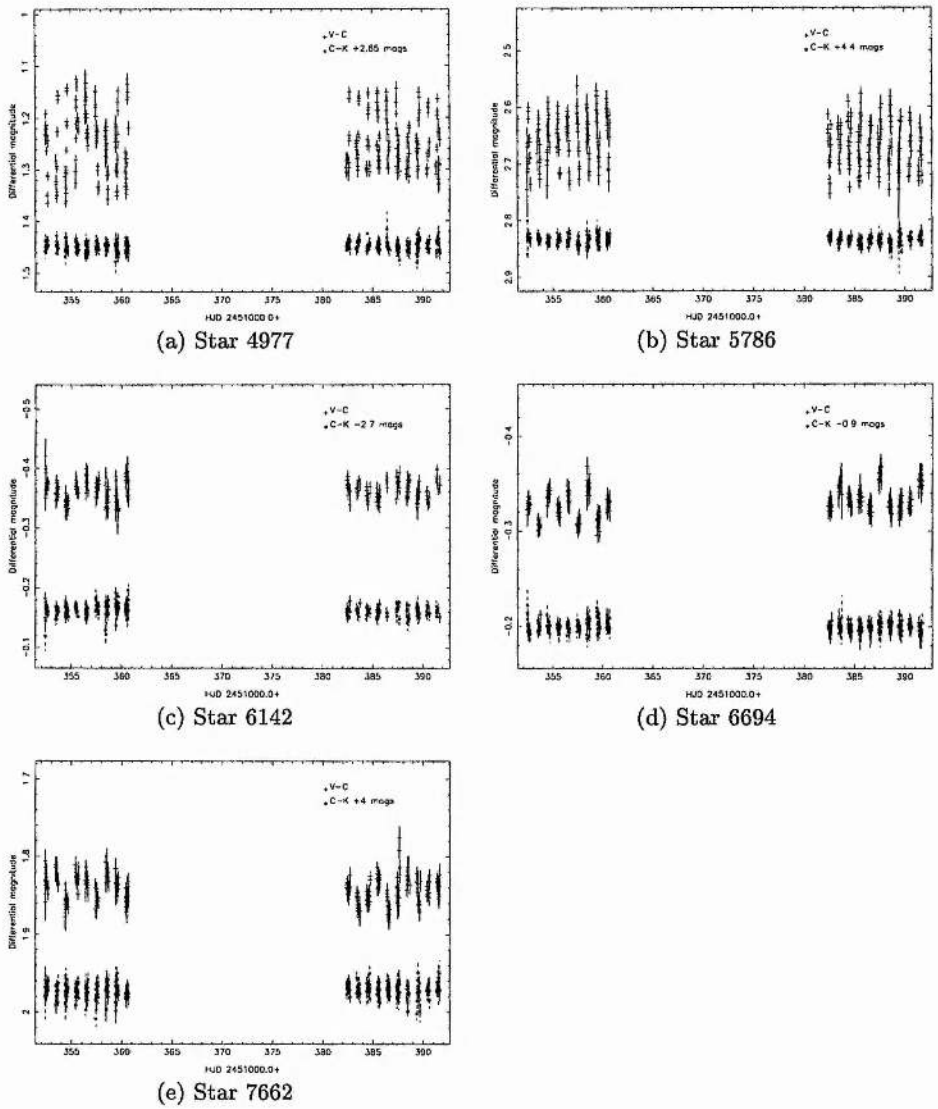

(a) Star 4977 (b) Star 5786

(c) Star 6142 (d) Star 6694

(e) Star 7662

Figure 6.11: Lightcurves of the BY Dra systems in CCD2 data (continued).

Table 6.7: Details of the unclassified systems in the CCD4 data. The error on the last decimal place is given in brackets.

Star	V mag	$(B-V)$	R $'$	δm_V (mags)	Amp. (mags)	Epoch (HJD)	Period (days)
224	17.611(1)	1.468(2)	11.3	3.07	0.02	2451384.323(5)	11.5(20)
2605[1]	18.474(1)	1.116(2)	4.7	0.52	0.04	2451389.64(5)	9.6(6)
8132[2]	19.2(5)		7.6		0.45	-	-
8830	18.402(1)	1.443(3)	8.6	2.14	0.15	2451384.61(1)	10.9(8)

[1] Near diffraction spike, [2] Cepheid?

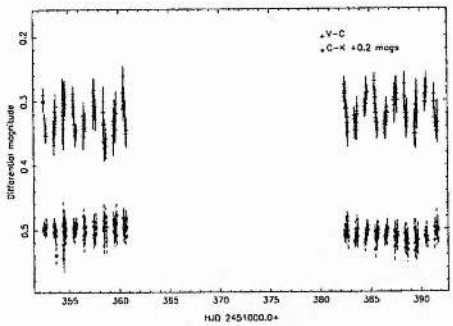

(a) Star 1815

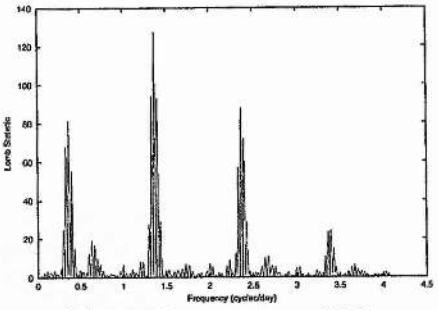

(b) Periodogram of star 1815

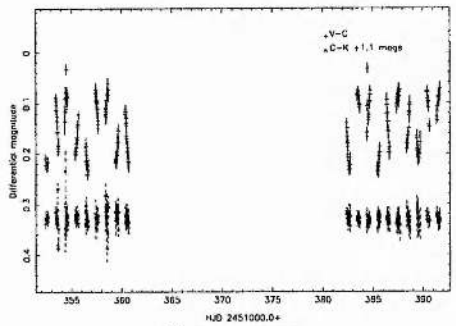

(c) Star 2576

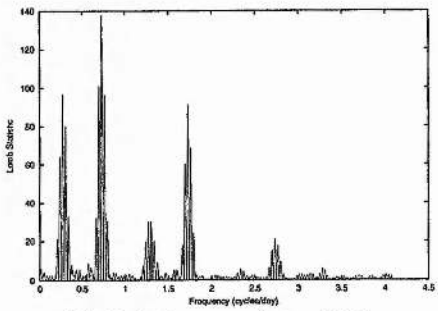

(d) Periodogram of star 2576

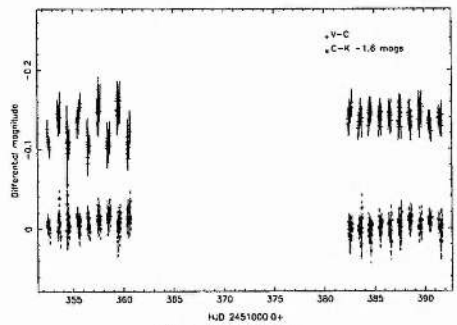

(e) Star 2393

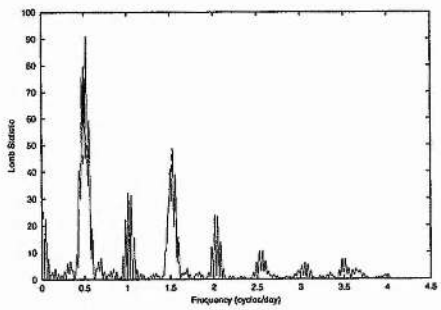

(f) Periodogram of star 2393

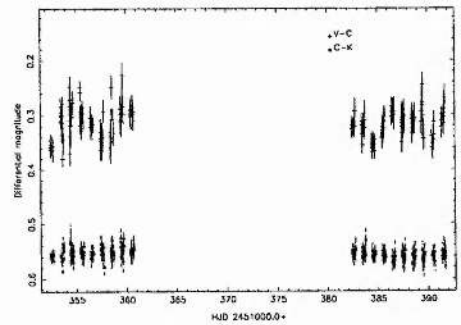

(g) Star 3126

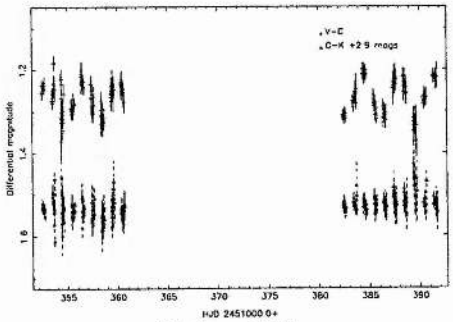

(h) Star 3127

Figure 6.12: Lightcurves of the BY Dra systems from CCD4 data.

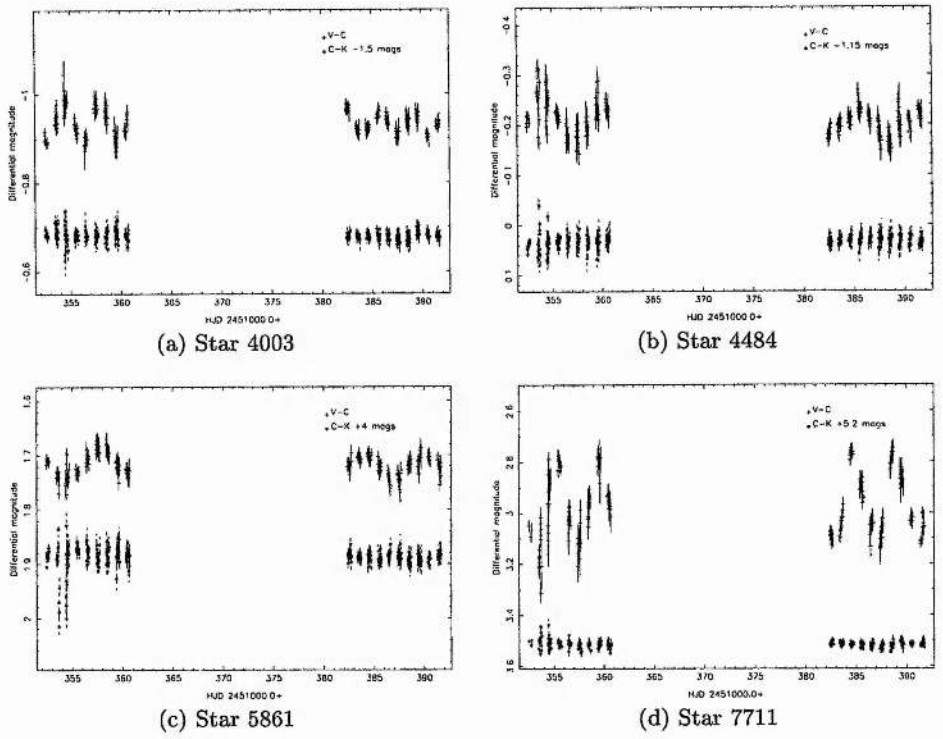

(a) Star 4003 (b) Star 4484

(c) Star 5861 (d) Star 7711

Figure 6.13: Lightcurves of the BY Dra systems from CCD4 data (continued).

I have no $B-V$ colour to indicate cluster membership for this star, if our classification is correct, then it is a pulsating giant star of high luminosity (class Ib – II) and spectral type F – K, according to Kholopov et al. (1985). Gray (1992) quotes the absolute V magnitude of F5 – K5 Ib giants to be -4.6 to -4.5 mag. At its faintest, therefore, and including the effects of extinction ($E(B-V) = 0.10$, Kalirai et al. 2001a), a Cepheid member of NGC 6819 would have an apparent magnitude of ~ 8 mag. For comparison, the brightest stars present in this field have magnitudes reaching ~ 16 mag, and stars brighter than these were completely saturated in all exposures. If further observations prove that star 8132 is a Cepheid, it is certainly not a cluster member.

The other three unclassified stars remain enigmatic, owing to the long period and low amplitude nature of their variation. I consider that they are most likely to be early type contact binaries with low orbital inclination or possibly ellipsoidal variables. The colour data available place the stars above the main sequence and so the question of membership remains open, but the large projected separations of 224 and 8830 suggest that they are not cluster members. Star 4694 is some distance from the main sequence and the cluster centre, suggesting it too is not a member.

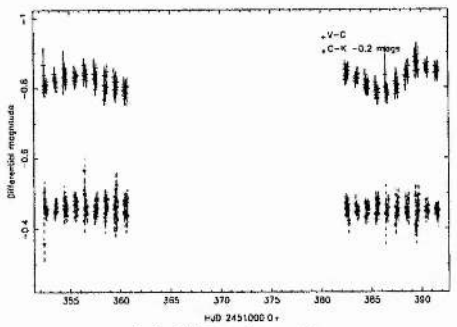

(a) CCD2 Star 50

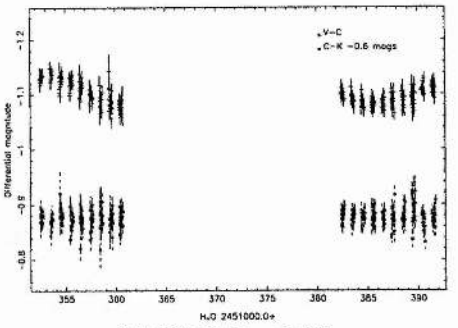

(b) CCD2 Star 2435

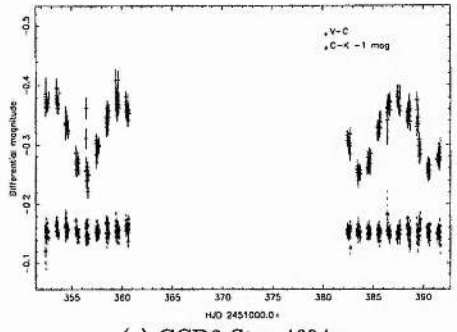

(c) CCD2 Star 4694

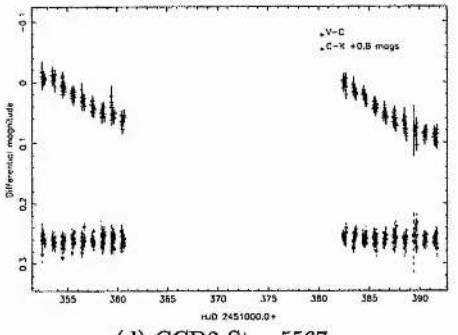

(d) CCD2 Star 5567

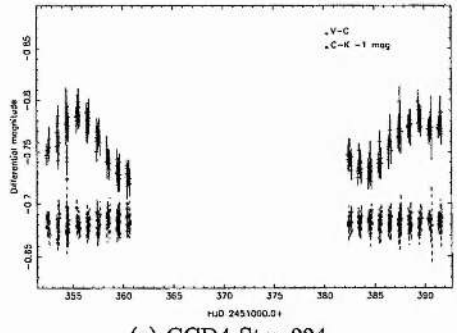

(e) CCD4 Star 224

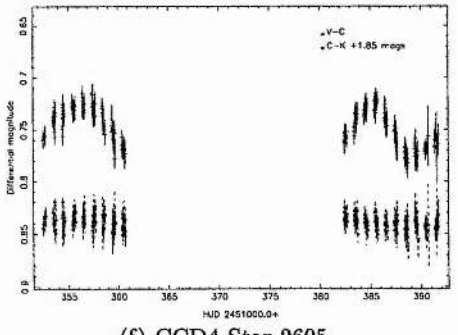

(f) CCD4 Star 2605

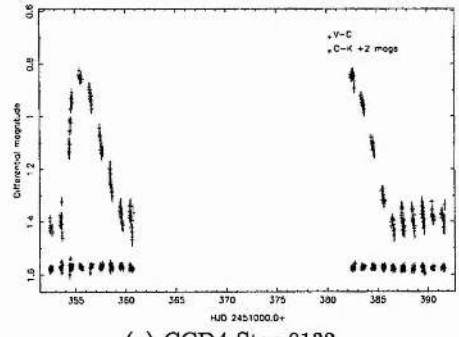

(g) CCD4 Star 8132

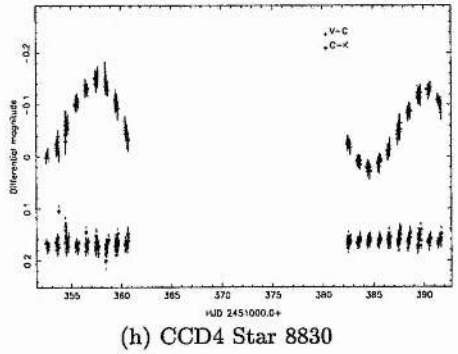

(h) CCD4 Star 8830

Figure 6.14: Lightcurves of the unclassified variable stars

Table 6.8: Details of suspected variable stars in CCD2 data. The error on the last decimal place is given in brackets.

Star	V mag	$(B-V)$	R′	δm_V (mags)
145	16.64(6)			
1220	17.27(6)			
2422	18.92(6)			
3240[1]	17.20(6)			
4690[2]	17.025(1)	0.856(1)		0.63
5132	16.745(2)	1.212(4)		2.66
5137	19.08(6)			
5171	16.92(6)			
6336	16.447(2)	0.907(3)		1.55
7090	16.384(2)	0.836(3)		1.22
7767	19.48(6)			

[1] Blended, [2] close pair with 4694.

6.7 The Suspected Variables

Tables 6.8 and 6.9 lists the details of stars I suspect may be variable but where the photometry is not sufficient to confirm this, owing to low amplitude variations or poor measurements due to faintness, blending, etc. Their lightcurves are presented in Figures 6.15 – 6.18. Due to the nature of the photometry, I have not attempted to classify these stars, but 5 of the CCD4 candidates (2825, 3236, 3878 and 5371) could be cluster members from their colour data and projected separations, and I recommend their further study. Three of the candidates from CCD2 could also be members from their colours (4690, 6336, 7090), although these objects are further from the cluster centre.

Star 5590 is particularly worthy of interest. This object has been classified as a suspected variable due to the unusual nature of its variations combined with the star's position in the densest part of the cluster where blending is considerable. Nevertheless, with these caveats in mind, the data appear to justify its inclusion. As Figure 6.18(b) illustrates, the variability appears to be periodic. Figure 6.18(c) shows the lightcurve

Table 6.9: Details of suspected variable stars in CCD4 data. The error on the last decimal place is given in brackets.

Star	V mag	$(B-V)$	R′	δm_V (mags)
2031	18.334(1)	0.836(2)	6.7	-0.73
2501	19.427(2)	1.099(4)	5.5	-0.51
2825	19.693(2)	1.414(6)	4.7	0.70
3236	17.027(1)	1.037(1)	5.6	1.61
3878	17.269(1)	0.891(1)	2.4	0.64
4339	17.0(4)		1.4	
5371	18.247(1)	1.005(2)	1.1	0.24
5590	18.7(4)		1.2	
8152	19.499(2)	0.786(3)	7.1	-2.19
8741	18.520(1)	1.521(3)	9.5	2.45

phased on this period. The lightcurve is incomplete because this period is so close to one day: 1.04 ± 0.10 days. These plots seem to indicate an eclipsing binary system, possibly consisting of a small object such as a white dwarf (indicated by the short primary eclipses) and a large, cool body (the lack of secondary eclipse indicates that most of the light is contributed by the primary). The curious dip shortly before the primary eclipse could be the eclipse of a 'hot spot' on the secondary star caused by the heating of the primary. However, this is by no means certain; if this periodicity proves correct, extended study will be necessary to acquire complete data on this object.

6.8 Summary

I find evidence for 55 variable stars within this dataset plus a further 24 where variability is suspected. Of these 79 stars, 25 appear to be eclipsing binaries with an additional 3 suspected, 22 are BY Draconis systems, and 8 remain unclassified due to long-period variation, though 1 of these is believed to be a Cepheid. However, I must urge caution regarding these classifications until confirmation is possible via spectroscopy and/or further photometric observations. I have determined that 3 of the W UMa-type eclipsing binaries

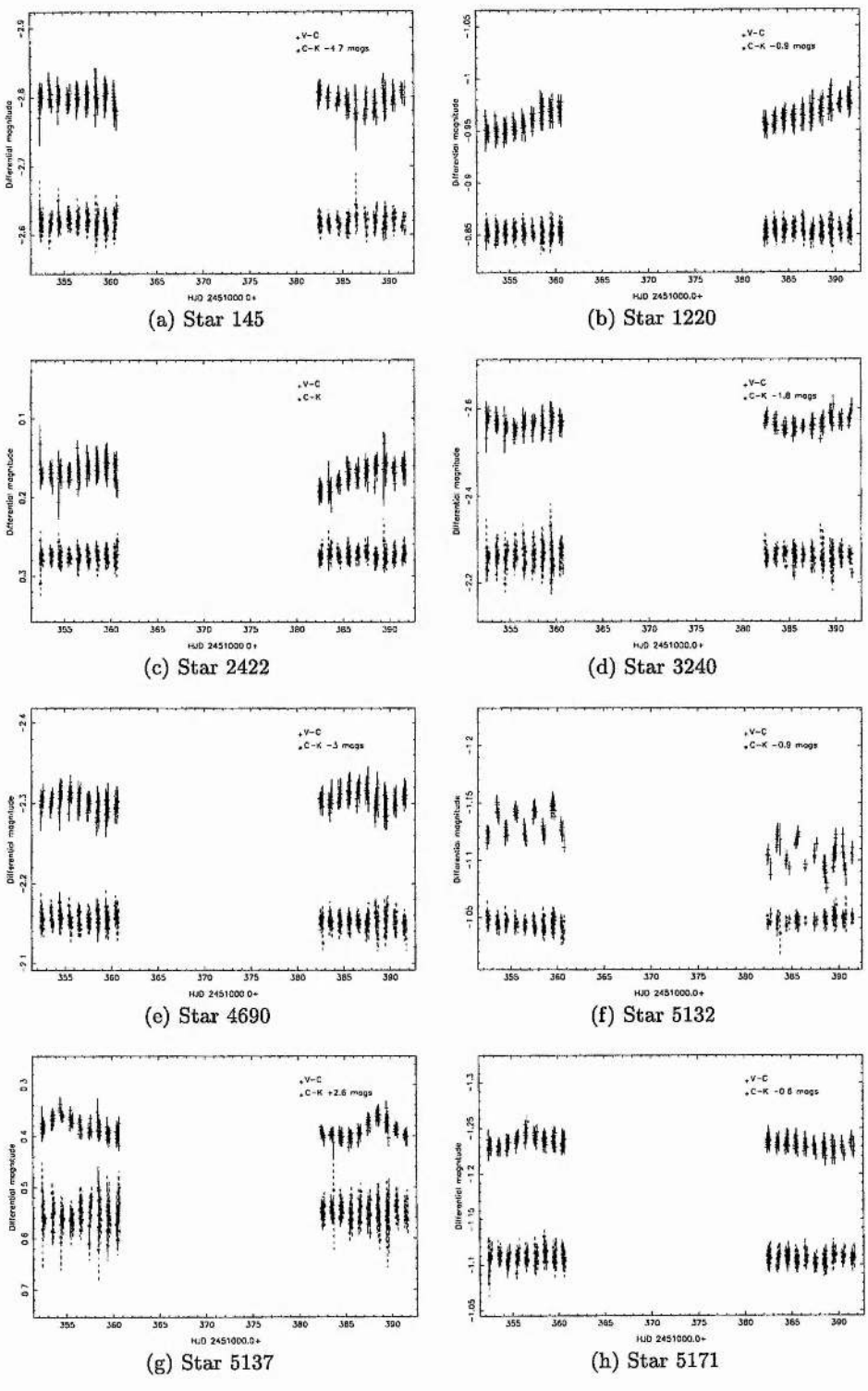

(a) Star 145 (b) Star 1220

(c) Star 2422 (d) Star 3240

(e) Star 4690 (f) Star 5132

(g) Star 5137 (h) Star 5171

Figure 6.15: Lightcurves of the suspected variable stars from CCD2.

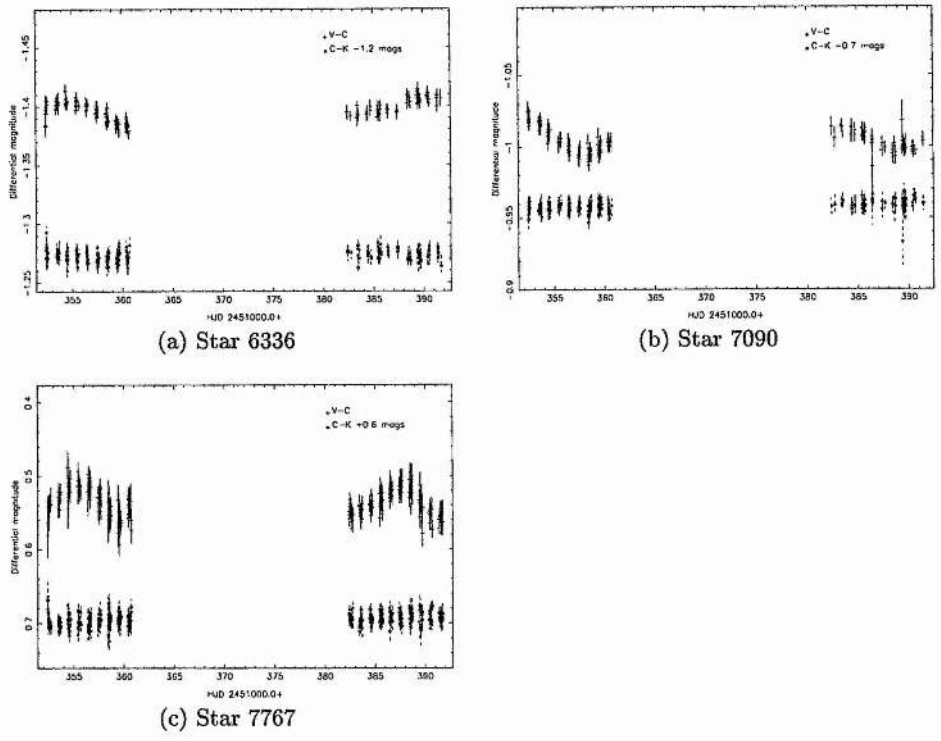

(a) Star 6336

(b) Star 7090

(c) Star 7767

Figure 6.16: Lightcurves of the suspected variable stars from CCD2.

are likely to be cluster members from their $(B-V)$ colours and periods, and have ruled out membership for at least 12 variables of other types, including the Cepheid, should the classification prove correct.

These results support the work of Kaluzny and others, which suggest that W UMa systems form in significant numbers in open clusters of around 4–5 Gyr (see Kaluzny, Mazur & Krzemiński 1993, Kaluzny & Ruciński 1993, Kaluzny, Krzemiński & Mazur 1996). It will be seen that such systems, which form from initially detached binaries, are just beginning to appear in cluster NGC 6819, which is only $\sim$ 2.5 Gyr old. Following up this work with spectroscopic and further photometric observations would be valuable, as cluster variables can potentially reveal much about stellar formation and evolution in this environment, and many basic details remain to be confirmed, such as our initial classifications and membership indications.

These data also included two Algol-type eclipsing binaries which could be M-dwarf binaries. The colour of 4305 indicates a very late-type star, consistent with an M-dwarf. Formal classification must wait however, as this is the colour of the combined light of the two component stars. Nevertheless, these are important objects for follow-up investigation

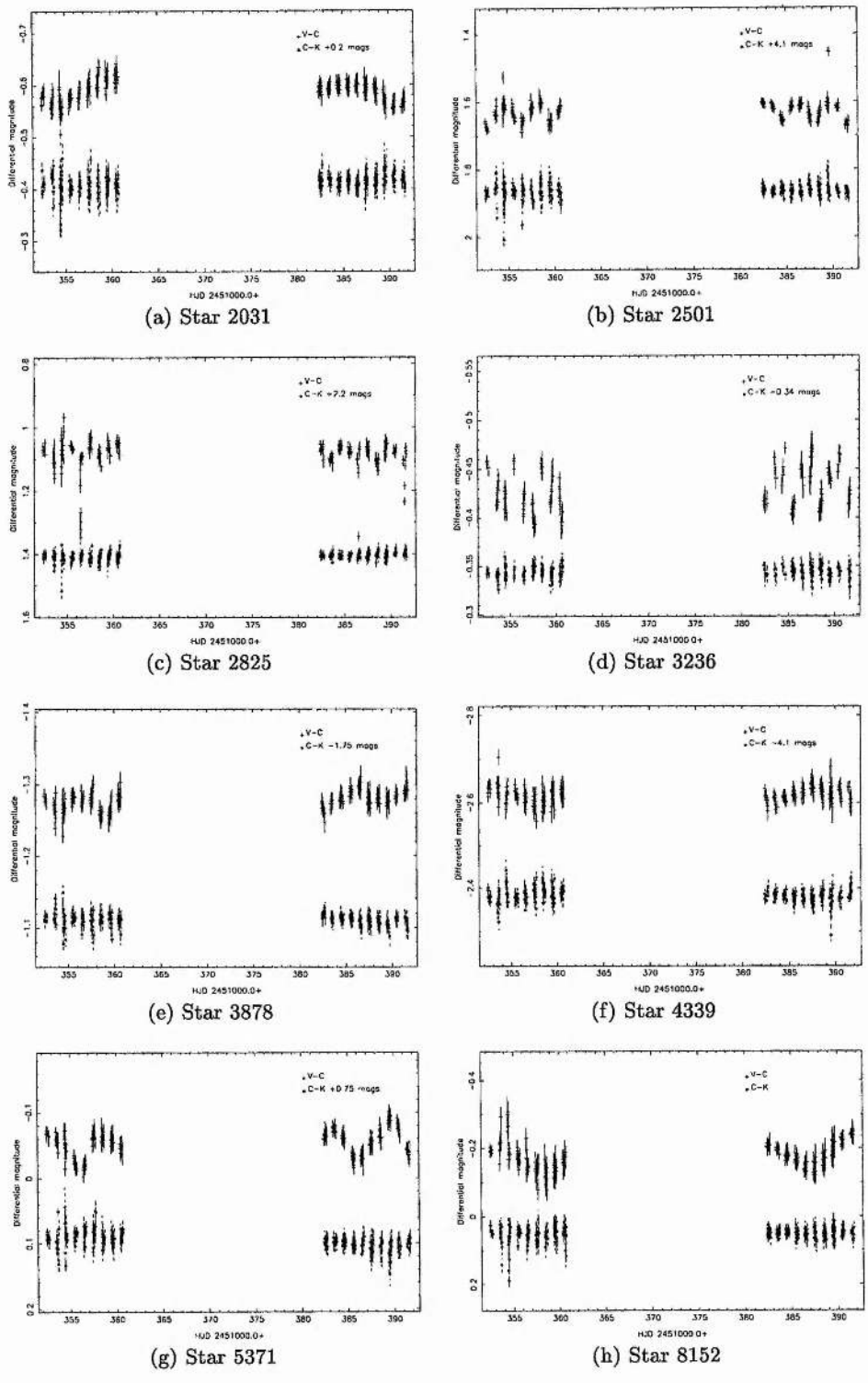

(a) Star 2031

(b) Star 2501

(c) Star 2825

(d) Star 3236

(e) Star 3878

(f) Star 4339

(g) Star 5371

(h) Star 8152

Figure 6.17: Lightcurves of the suspected variable stars from CCD4.

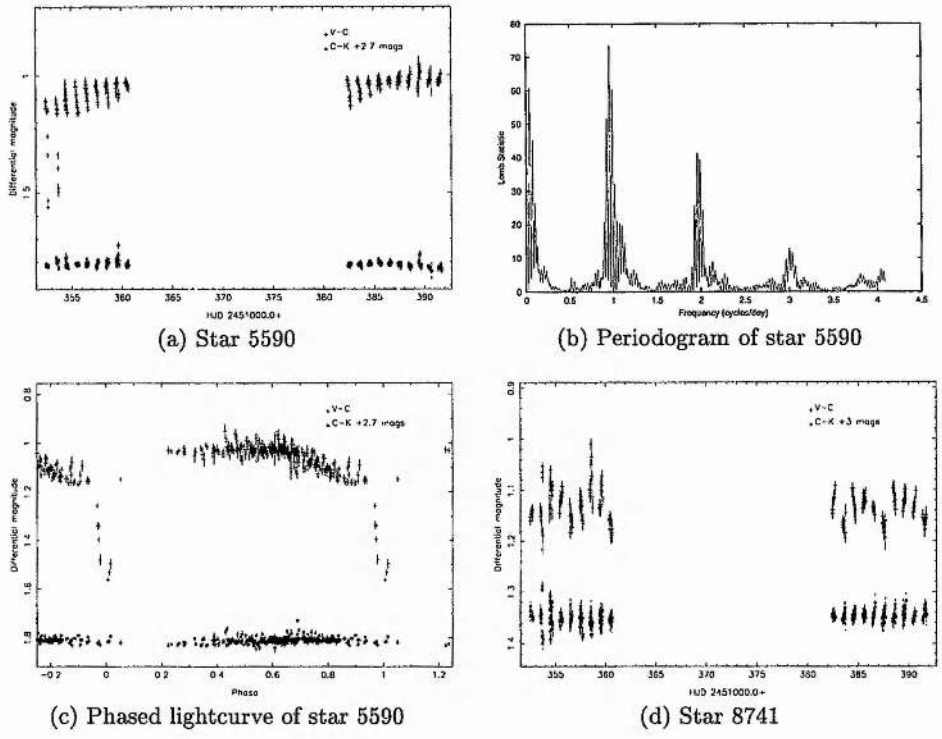

(a) Star 5590

(b) Periodogram of star 5590

(c) Phased lightcurve of star 5590

(d) Star 8741

Figure 6.18: Lightcurves of the suspected variable stars from CCD4.

as they could significantly contribute to our knowledge of the physical sizes of very low mass stellar objects.

CHAPTER 7

Conclusions

In this work I have focussed on the technique of identifying the photometric signature of a planetary transit from the lightcurves of several thousand stars at a time and applied it to the field of the open cluster, NGC 6819. In the process I have identified a considerable number of new variable stars, some of which are particularly interesting in their own right.

7.1 Hunting for Planetary Transits

The method of searching for transits to identify extra-solar planets has a strong advantage over the radial velocity technique in that it relies solely on photometry, and can be applied to fainter stars. The technique can therefore be used to extend the search for planets beyond the Solar neighbourhood. Furthermore, very large numbers of stars can be surveyed at once, and the dataset is extremely useful for research in other fields of astronomy. However, the technique's disadvantage is that it cannot rule out grazing incidence stellar eclipses, and follow-up observations are necessary to confirm and characterise the initial detection.

In Chapter 4 I presented and tested a method of achieving the highly precise time-series photometry required to detected transits for several thousand objects over a wide field. I have constructed a semi-automated data reduction pipeline by which the whole of the INT dataset can now be reduced and which I have tested using a subset of the data. In Chapter 5 I then described and tested an algorithm for identifying the short, shallow transit events from the resulting lightcurves. I have applied these techniques to the stars in the field of the open cluster NGC 6819.

The TRANSITFINDER algorithm succeeded in finding a number of brief, low amplitude eclipse events. While all of these appear to be grazing-incidence eclipses of stellar companions, the events themselves are very similar to transit events. The algorithm can therefore identify transit events in real data, should they occur. From the simulations described in Chapter 5, I expected to see 266.6 transits in this dataset, assuming that every star had one 'hot Jupiter' planet with the radius ($1.3\,R_{jup}$) and orbital period (3.5 days) similar to those of the one known transiting system, HD 209458. In the Solar neighbourhood, roughly 1 percent of stars are thought to have such planets, judging by the radial velocity results. If such planets are as common in this star field as they are in the Solar neighbourhood, then I should have found between 2 and 3 transits in my data, including between 0–1 transits from the cluster. The rather low number of expected transits is partly due to the relatively low number of stars analysed in this work; now that the reduction pipeline is in place, this will be rectified as soon as possible. However, it is also due to the fact that HD 209458 has an orbital period which is a multiple of a half-day. The plots in Section 5.5.2 show that this experiment is less likely to detect planets with orbital periods which a integer multiples of 1 or half a day as a large fraction of such planets will always transit during gaps in observations. If a similar period of 3.4 days is considered, then I should expect to find between 3 and 4 transits, with the number increasing towards shorter periods.

The fact that I have found no planetary transits in this data seems to argue for a lower frequency of 'hot Jupiter' type planets in the field of NGC 6819 relative to the Solar neighbourhood. Unfortunately, the number of stars surveyed so far is insufficient to give a strong indication as to whether the 'hot Jupiter' frequency is truly lower in this field. This deficiency will be overcome with the reduction of the rest of the data (see Section 7.3). It is also worth noting that the eclipse amplitudes of the variables found were all relatively high ($\geq 0\overset{m}{.}04$) compared with planetary transits (~few millimags to a few hundredths of a magnitude). The detection threshold was set deliberately high in order to avoid false alarms, and it is possible that this excluded transit events. In future a more sophisticated approach, perhaps based on comparing a star's χ^2_{red} with its $\Delta\chi^2_{tf}$, could reveal transit events in this data.

I would strongly recommend further study of the eclipsing stars identified by TRANSITFINDER before firm conclusions are drawn. The sparse sampling combined with the low amplitude events makes it very difficult to determine the nature of the event, or to

distinguish it from spuriously low datapoints. For this reason, I recommend that future transit studies use a higher sampling rate. More significantly, several of the objects in question appear to have very low mass companions which are worthy of further study in any case, as discussed below.

The results of this experiment have indicated two unforeseen sources of false transit candidates: stellar activity and blending. I found that a significant fraction ($\sim$ 9 percent) of the transit candidates found were actually caused by stellar activity. This is increasingly a problem towards later spectral types whereas the transit technique is better suited to smaller stars for which the transit amplitudes are greater. Blending was found to cause the vast majority ($\sim$ 75 percent) of false alarms however. In this work, I examined every candidate lightcurve manually in order to select the most promising events. While this method works, it is time consuming and clearly unworkable for larger datasets. Again, I found that plotting χ^2_{red} against $\Delta\chi^2_{tf}$ was a useful guide in isolating the true transit candidates. Alternatively, it may be that a different approach to transit detection, like those discussed in Borucki et al. (2001), Gilliland et al. (2000), Doyle et al. (2000) and Defaÿ, Deleuil & Barge (2001) for example, may not be as sensitive to these effects. In Section 7.3 I discuss the possibilities for future development in this area.

7.2 Variable Stars

A fortuitous side-product of searching for very low-amplitude variability of large numbers of stars is the excellent time-series photometry produced for an array of other variable types. Chapter 6 presents the photometry obtained for the 79 variables and suspected variables discovered in this survey.

The two most significant of these stars are the two possible M-dwarf binaries. While the colour of star 4305 ($B - V = 1.429$) confirms a late-type classification, the unequal eclipse depths indicate two different stellar types, given that the colour is derived from the combined light of the two stars. The colour information available for 8864 raises the possibility that the system could comprise of two earlier-type stars, but the object is too faint to be conclusive from the photometry alone. Eclipsing low-mass stellar binaries are crucial to our understanding of the field disc population as they provide a means to measure the physical dimensions of stars independently of theoretical models, thus helping

to constrain models of stellar properties (Anderson 1991). However, while there are many well studied F, G-type systems, the low luminosity of M-dwarfs means that few examples are known and only two (CM Dra and YY Gem) are well studied, with the result that stellar models are very poorly constrained at these masses. Further study of the possible M-dwarf binaries discovered in this work is therefore highly recommended. Although this study will be hampered by the faintness of the objects ($\sim$ 20 mag), well sampled two colour lightcurves could be obtained with AUX camera on WHT and orbital parameters could be determined spectroscopically using GMOS data from the Gemini telescopes, when available.

The discovery of three W UMa-type systems with distances similar to that of the cluster is particularly interesting. While this does not constitute conclusive proof of cluster membership, the distance estimates together with their small radial separations from the cluster centre and the position of the systems slightly above the main sequence on the colour-magnitude diagrams all point towards cluster membership. The paradigm of contact binary formation (refer to Kaluzny, Mazur & Krzemiński 1993 is that a pair of initially detached stars lose angular momentum via magnetic torques from the stellar wind and gradually spiral closer together. The stars eventually come into atmospheric contact and ultimately coalesce into a single object (a blue straggler), on a time-scale of a few Gyrs. Observations of open cluster W UMas, for which ages can be independently established, are therefore important in terms of confirming this theory and charting the progress of the evolution. As NGC 6819 is of intermediate ($\sim$ 2.5 Gyr) age, we would expect to see W UMas begining to form, and also a population of detached eclipsing binaries still evolving towards that state. This is consistent with my findings, although I have no membership indicators for the detached systems.

Kaluzny, Mazur & Krzemiński (1993) note that the position of the W UMas on the colour-magnitude diagram would help to identify the mechanism causing the angular momentum loss. They state that if the mechanism was due to nuclear evolution, the W UMas should be positioned close to the cluster turn off. Alternatively, a magnetic braking mechanism would place the stars well below the turn off. As the cluster turn off point is at a magnitude well saturated in the INT data, all the W UMas found are below the turn off point. While I therefore cannot comment on any possible brighter cluster binaries, this data does support the work of Kaluzny and others in that the mechanism cannot be solely due to nuclear evolution.

7.3 Future work

There are a number of ways in which I would like to improve and extend the current work:

- Improvements to the pipeline.

  The current self-calibration code (described in Chapter 4, Section 4.2.5) works by splitting each image into 500×500 pixel sectors. As I have shown this does a good job of removing the remaining position-dependent magnitude residuals from the data, but problems can occur at the sharp edges of the sectors, where there is a discontinuity. One solution to this problem would be to write self-calibration code which fits a smooth, two-dimensional function across the whole of each image.

  Fixed-position PSF photometry. Theoretically, fixing the star positions during the PSF fit removes two free parameters and should give improved photometry. I have only tentatively investigated this option so far.

  The major source of "noise" in the results of the planet-finding algorithm was found to be a large number of false alarms due to badly blended stars. Recent work by Mochejska et al. (2002) has found that image subtraction techniques can produce extremely precise time-series photometry of similar open cluster field. This technique could improve the photometry of the crowded cluster centre, and reduce the number of false alarms.

- Processing data from CCDs 1 and 3. It has been found that of the $\sim 18,000$ stars examined, approximately 2–3 would be expected to show transit events, assuming that 'hot Jupiter'-type planets are as common in these fields as in the Solar neighbourhood. Stronger conclusions about the presence or absence of planets could be drawn from a larger sample of stars. This is easily achieved by pipeline-processing the data from the remaining two CCDs on this cluster.

- Processing the NGC 6940 and NGC 7789 cluster data. Similarly, the data on clusters NGC 6940 and NGC 7789 must be reduced. As well as providing a larger sample of stars, the data on NGC 7789 from the 3rd observing run in 2000 has a higher sampling rate as only one cluster was observed. Furthermore, results from the three clusters can be mutually compared in terms of planets found and the cluster ages, densities, metallicities etc. It will also be interesting to assess the problems cause by blending in the other clusters. In the central regions of NGC 6819 the density of

saturated stars was so high that many fainter potential target stars were completely obscured. It may be that more widely disperse clusters, with fewer bright foreground stars, give better results.

- Comparison and development of transit finding algorithms. A number of authors have presented various transit-finding algorithms (see for example, Borucki et al. 2001, Gilliland et al. 2000, Doyle et al. 2000 and Defaÿ, Deleuil & Barge 2001). It would be instructive to compare the performance of the various methods both for detection efficiency and (assuming multiple algorithms are equivalent on this point) computational speed. The latter could become a important factor in many of the surveys, both ground and space-based, which are in the pipeline owing to the extremely large datasets involved. It would also be useful to compare how different algorithms handle the problems of blended and active stars. In the latter case, the algorithm needs to be able to successfully distinguish transits from the sinusoidal variations caused by star spots, which can have a larger amplitude. A seperate development would be to ensure that the algorithm is not drawn away from genuine transit events by larger amplitude scatter due to patches of cloud, poor seeing etc.

- Future observations.

  As I discussed in Chapter 2, there currently seem to be two main areas where transit-hunting efforts are being concentrated: very wide-field, bright star surveys and the (relatively) small-field, fainter star work such as that presented here. While the former search strategy is extremely promising, I will concentrate here only on the topic of my thesis. A couple of factors need to be considered when designing future observation strategies:

  Saturation in the central cluster. The photometry of NGC 6819 suffered noticeably in the central regions due to this problem and as a result many fainter central cluster stars were not measured. Clusters with a lower central density should be considered.

  Sampling rate. While I have shown that the ~ 2 images/hour sampling rate in the NGC 6819 observations is adequate to detect quick, very-low amplitude eclipses, a higher sampling rate would undoubtably improve the chances of detecting these events. The drop in $\Delta\chi^2_{tf}$ would be higher with better-sampled transits and the data could be binned to achieve greater precision.

More comprehensive colour data. Analysis of this dataset has shown that reliable colour information is extremely useful in estimating star radii and hence the expected depth of transit. This can in turn be used to identify suitable target populations.

Observations taken during 'dark time'. The RMS .vs. magnitude plots in Figure 5.2 show that the dominant source of noise for most of the stars is sky background noise. This could be reduced if the observations were made during dark time when the moonlight contamination is lower.

Detailed follow-up photometry and spectroscopy for the variable stars. Several of the variable stars discovered in this study, particularly the eclipsing stars found during the search for transits, and the possible M-dwarf binaries, are worthy of further study. Well-sampled, two-colour lightcurves plus classification spectra would allow full lightcurve solutions to be made, revealing the nature of the components.

With new instruments coming online, such as the 12-CCD mosaic camera on the CFHT for example, it is now possible to use a larger telescope to gather more light from cluster stars over a wider area than was previously available. These instruments are ideal for this type of survey if sufficient telescope time could be obtained. With sufficient numbers of stars, the technique should reveal the presence of perhaps hundreds of new planets. This work could then be extended to cover a range of clusters (perhaps working in concert with the very-wide-field surveys to cover bright clusters like the Pleiades) to investigate the effects of metallicity, density, age, even orbit around the Galaxy (in terms of cluster disruption by passage through the disc) on surviving planet population. In the process, huge numbers of field stars will also be surveyed, providing a comparison population both for the clusters and for the radial velocity results in the Solar neighbourhood.

These results fit into a wide range of transit-hunting work currently being carried out. Gilliland et al. (2000) were the first to report finding no planetary transits in their HST study of the globular cluster 47 Tuc. The large number of stars involved (> 34000) meant that they expected to find ~ 17 HD 209458-like transiting planets, and so they could conclude with some confidence that the stellar population of the cluster was significantly different from that of the Solar neighbourhood. Subsequently, a number of theoretical studies have explained this absence of planets as a result of stellar close encounters disrupting protoplanetary discs or ejecting planets after formation (for example,

Bonnell et al. 2001). This is thought to be less of a problem in open cluster environments, where the stellar density is lower. Concerns have also been raised about the stability of planet-forming discs to UV radiation from nearby stars (Scally & Clarke 2001). Finally, the radial velocity studies have indicated that planets are more common around high metallicity stars, whereas the 47 Tuc cluster contains mostly old, metal poor stars. These arguments appear to favour planet formation in open clusters. In addition to the search described here, Mochejska et al. (2002) recently published results of a similar survey of the open cluster NGC 6791. They found 62 variable stars, including many low amplitude variables.

There are currently a number of very-wide-field transit surveys of bright stars, such as VULCAN, STARE, BEST and WASP (see for example Borucki et al. 2001). While several of these have proved their ability to detect transits of HD 209458b, many are in fairly early stages of development and none have so far discovered a planet by this method.

Finally, the complementary technique of microlensing has been in use to survey dense Galactic star fields for some years now and although several hundred events have been found, no planets have been conclusively detected (Gaudi et al. 2001).

These results are in stark constrast to the outstanding success of the radial velocity technique in the Solar neighbourhood. Although it is too early in the development of these alternative techniques to make any firm statements about the presence or absence of planets in other environments, extensive study of them will reveal much about star and planet formation across the Galaxy. In the next few years the ground-based projects discussed here in addition to the planned space missions of the next decade should greatly increase our understanding, not only of 'hot Jupiters', but of terrestrial planets also. This will pave the way for the investigation of the nature of planets and the search for life beyond the Earth.

REFERENCES

Albrow M. D. et al., 2001, ApJ, 556, L113

Alekseev I. Y., 2000, SvA, 77, 784

Allen C. W., 1973, Astrophysical Quantities. Athlone Press, University of London

Anderson J., 1991, A&AR, 3, 91

Armitage P. J., Livio M., Lubow S. H., Pringle J. E., 2001, ApJ

Artmowicz P., 1993, ApJ, 419, 166

Auner G., 1974, A&AS, 13, 143

Barkhatova K. A., Vasilevsky A. V., 1967, Var. Star Bull., 16, 171

Barkhatova K. A., 1963, Astron. Circ. USSR, 233

Barnes T. G., Evans D. S., Moffett T. J., 1978, MNRAS, 183, 285

Beichman C., 1996, A Road Map for the Exploration of Neighbouring Planetary Systems (Ex-NPS). Jet Prop. Lab. Publ., Pasadena

Bennett D. P., Rhie S. H., 2000, in Garzón F., Eiroa C., de Winter D., Mahoney T. J., eds, Disks, Planetesimals and Planets: ASP conf. series. ASP, p. 542

Binney J., Merrifield M., 1998, Galactic Astronomy. Princeton Univ. Press, Princeton

Bonnell I. A., Smith K. W., Davies M. B., Horne K., 2001, MNRAS, 322, 859

Borucki W. J., Koch D. G., Dunham E. W., Jenkins J. M., 1997, in Soderblom D., ed, Planets Beyond the Solar System and The Next Generation of Space Missions: ASP conf. series. ASP, p. 153

Borucki W. J., Caldwell D., Koch D. G., Webster L. D., Jenkins J. M., Ninkov Z., Showen R., 2001, PASP, 113, 439

Borucki W. J., Scargle J. D., Hudson H. S., 1985, ApJ, 291, 852

Boss A. R., 1986, A&AS, 62, 519

Boss A. P., 1995, Sci, 267, 360

Boss A., 1998, Looking for Earths. John Wiley and Sons, Inc., New York

Bragaglia A. et al., 2001, AJ, 121, 327

Brown T. M., Charbonneau D., Gilliland R. L., Noyes R. W., Burrows A., 2001, ApJ, 552, 699

Burkhead M. S., 1971, AJ, 76, 251

Burrows A., Saumon D., Guillot T., Hubbard W. B., Lunine J. I., 1995, Nat, 375, 299

Burrows A. et al., 1998, in Rebolo R., Martin E., Zapatero Osorio M. R., eds, Brown Dwarfs and Extra-Solar Planets: ASP conf. series, vol. 134. ASP, p. 354

Burrows A., Guillot T., Hubbard W. B., Marley M. S., Saumon D., Lunine J. I., Sudarsky D., 2000, ApJ, 534, L97

Butler R. P., Marcy G. W., 1996, ApJ, 464, L153

Butler R. P., Marcy G. W., Williams E., Hauser H., Shirts P., 1997, ApJ, 474, L115

Butler R. P., Marcy G. W., Vogt S. S., Apps K., 1998, PASP, 110, 1389

Butler R. P., Marcy G. W., Fischer D. A., Brown T. M., Contos A. R., Korzennik S. G., Nisenson P., Noyes R. W., 1999, ApJ, 526, 916

Butler R. P., Vogt S. S., Marcy G. W., Fischer D. A., Henry G. W., Apps K., 2000, ApJ, 545, 504

Butler R. P., Marcy G. W., Fischer D. A., Vogt S. S., Tinney C. G., Jones H. R. A., Penny A. J., Apps K., 2001a, in Penny A., Artymowicz P., Lagrange A.-M., Russell S., eds, Planetary Systems in the Universe: Observation, Formation and Evolution: ASP conf. series. ASP

Butler R. P., Tinney C. G., Marcy G. W., Jones H. R. A., Penny A. J., Apps K., 2001b, ApJ, 555, 410

Cameron A. G. W., 1973, Icarus, 18, 407

Cameron A. G. W., 1978, Moon and Planets, 18, 5

Canterna R., Geisler D., Harris H. C., Olszewski E., Schommer R., 1986, AJ, 92, 79

Castellano T., Jenkins J., Trilling D. E., Doyle L., Koch D., 2000, ApJ, 532, L51

Charbonneau D., Noyes R. W., Korzennik S. G., Nisenson P., Jha S., Vogt S. S., Kibrick R. I., 1999, ApJ, 522, L145

Charbonneau D., Brown T. M., Latham D. W., Mayor M., 2000, ApJ, 529, L45

Claret A., Diaz-Cordoves J., Gimenez A., 1995, A&AS, 114, 247

Cochran W. D., Hatzes A. P., Butler R. P., Marcy G. W., 1997, ApJ, 483, 475

Collier Cameron A., Horne K., Penny A., James D., 1999, Nat, 402, 751

Currie M., Berry D., 1998, Starlink User Note 95.13, Rutherford Appleton Laboratory

Currie M. J., Privett G. J., Chipperfield A. J., Berry D. S., 2000, Starlink User Note 55.12, Rutherford Appleton Laboratory

Davies M. B., Sigurdsson S., 2001, MNRAS, 324, 612

de la Fuente Marcos C., de la Fuente Marcos R., 1997, A&A, 326, L21

de la Fuente Marcos R., de la Fuente Marcos C., 2001, A&A

de Laplace P. S., 1784, Théorie du Mouvement et de la figure elliptique des planetes. Impr. de P.D. Pierres, Paris

Deeg H. J., Garrido R., Claret A., 2001, New Astron., 6, 51

Defaÿ C., Deleuil M., Barge P., 2001, A&A, 365, 330

Defosse X., Forveille T., Mayor M., Perrier C., Naef D., Queloz D., 1998, A&A, 338, L67

Deleuil M., Barge P., Leger A., Schneider J., 1997, in Soderblom D., ed, Planets Beyond the Solar System and The Next Generation of Space Missions: ASP conf. series. ASP

Deliyannis C. P., Cunha K., King J. R., Boesgaard A. M., 2000, ApJ, 119, 2437

Descartes R., 1644, Principia Philosophiae

Diaz-Cordoves J., Claret A., Gimenez A., 1995, A&AS, 110, 329

Dick S., 1998, Life on Other Worlds: the 20th-century extraterrestrial life debate. CUP, University of Cambridge

Doyle L. R. et al., 2000, ApJ, 535, 338

Draper P., Eaton N., 1999, Starlink User Note 109.10, Rutherford Appleton Laboratory

Duquennoy A., Mayor M., 1991, A&A, 248, 485

Duquennoy A., Mayor M., Halbwachs J.-L., 1991, A&AS, 88, 281

Edgeworth K. E., 1949, MNRAS, 109, 600

Fischer D. A., Marcy G. W., Butler R. P., Vogt S. S., Apps K., 1999, PASP, 111, 50

Fischer D. A., Marcy G. W., Butler R. P., Vogt S. S., Frink S., Apps K., 2001, ApJ, 551, 1107

Fischer D. A., Marcy G. W., Butler R. P., Laughlin G., Vogt S. S., 2002, ApJ, 564, 1028

Friel E. D., Janes K. A., 1993, A&A, 267, 75

Fukugita M., Ichikawa T., Gunn J. E., Doi M., Shimasaku K., Schneider D. P., 1996, AJ, 111, 1748

Gatewood G. D., 1987, AJ, 94, 213

Gaudi B. S. et al., 2001, ApJ, 566

Gaudi B. S., 2001, ApJ

Gilliland R. L. et al., 2000, ApJ, 545, L47

Gizis J. E., Monet D. G., Reid I. N., Kirkpatrick J. D., Burgasser A. J., 2000, MNRAS, 311, 385

Gizis J. E., Kirkpatrick J. D., Burgasser A., Reid I. N., Monet D. G., 2001, ApJ, 551, L163

Glushkova E. V., Kulagin Y. V., Rastorguev A. S., 1993, Astron. Lett., 19, 232

Goldreich P., Tremaine S., 1980, ApJ, 241, 425

Goldreich P., Ward W. R., 1973, ApJ, 183, 1051

Gonzalez G., Laws C., 2000, AJ, 119, 390

Gonzalez G., Laws C., Sudhi T., Reddy B. E., 2001, AJ, 121, 432

Gray D. F., 1992, The observation and analysis of stellar photospheres, 2nd edition. CUP, University of Cambridge

Guillot T., Burrows A., Hubbard W. B., Lunine J. I., Saumon D., 1996, ApJ, 459, L35

Halbwachs J. L., Arenou F., Mayor M., Udry S., Queloz D., 2000, A&A, 355, 581

Harvey P. M., Wilking B. A., Joy M., 1984, Nat, 307, 441

Hatzes A. P. et al., 2000, ApJ, accepted

Heacox W. D., 1999, ApJ, 526, 928

Henry G. W., Marcy G. W., Butler R. P., Vogt S. S., 2000, ApJ, 529, L41

Hilditch R. W., 2001, An Introduction to Close Binary Stars. CUP, University of Cambridge

Holman M., Touma J., Tremaine S., 1997, Nat, 386, 254

Huygens C., 1698, Kosmotheoros, sive, de terris coelestibus earumque ornatu conjecturae

Israelian G., Santos N. C., Mayor M., Rebolo R., 2001, Nat, 411, 163

Janes K., Adler D., 1982, ApJS, 49, 425

Janes K., Phelps R. L., 1994, AJ, 108, 1773

Janes K., 1996, J. Geophys. Res., 101, 14853

Jha S., Charbonneau D., Garnavich P. M., Sullivan D. J., Sullivan T., Brown T. M., Tonry J. L., 2000, ApJ, 540, L45

Jiang I.-G., Ip W.-H., 2001, A&A, 367, 943

Jimenez A., Gonzalez Jorge H., Rabello-Soares M. C., 1998, A&AS, 129, 413

Jones H. R. A., Butler R. P., Tinney C. G., Marcy G. W., Penny A. J., McCarthy C., Carter B. D., Pourbaix D., 2001, MNRAS

Jorissen A., Mayor M., Udry S., 2001, A&A

Kalirai J. S. et al., 2001a, AJ, 122, 266

Kalirai J. S. et al., 2001b, AJ, 122, 257

Kalirai J. S. 2001. private communication

Kaluzny J., Ruciński S. M., 1993, MNRAS, 265, 34

Kaluzny J., Shara M. M., 1988, AJ, 95, 785

Kaluzny J., Krzemiński W., Mazur B., 1996, A&AS, 118, 303

Kaluzny J., Mazur B., Krzemiński W., 1993, MNRAS, 262, 49

Kant I., 1798, Allgemeine Naturgeschichte und Theorie des Himmels. Zeitz. Bei W. Webel

Kholopov P. N. et al., 1985, General Catalogue of Variable Stars, 4th Edition. Nauka, Moscow

Korzennik S., Brown T. M., Fischer D., Nisenson P., Noyes R., 2000, ApJ

Kürster M., Endl M., Els S., Hatzes A. P., Cochran W. D., Döbereiner S., Dennerl K., 2000, A&A, 353, L33

Labeyrie A., 1995, A&A, 298, 544

Latham D. W., Stefanik R. P., Mazeh T., Mayor M., Burki G., 1989, Nat, 339, 38

Laughlin G., 2000, ApJ, 545, 1064

Laws C., Gonzalez G., 2001, ApJ, 553, 405

Levison H. F., Lissauer J. J., Duncan M. J., 1998, ApJ, 116, 1998

Lin D. N. C., Papaloizou J., 1986, ApJ, 309, 846

Lin D. N. C., Bodenheimer P., Richardson D. C., 1996, Nat, 380, 606

Lindoff U., 1971, Inf. Bull. Variable Stars, 606

Lindoff U., 1972, A&AS, 7, 497

Lomb N. R., 1976, Ap&SS, 39, 447

Manteiga M., Martinez Roger C., Morales C., Sabau L., 1991, A&A, 251, 49

Marcy G., Butler R., 1996, ApJ, 464, L147

Marcy G. W., Butler R. P., 1997, ApJ, 464, L147

Marcy G., Butler R., 1998, ARA&A, 36, 57

Marcy G. W., Butler R. P., Vogt S. S., 2000, ApJ, 536, L43

Marcy G. W., Butler R. P., Vogt S. S., Fischer D., Liu M. C., 1999, ApJ, 520, 239

Marcy G. W., Butler R. P., Fischer D. A., Vogt S. S., Lissauer J. J., Rivera E. J., 2001a, ApJ, 556, 296

Marcy G. W. et al., 2001b, ApJ, 555, 418

Mayor M., Queloz D., 1995, Nat, 378, 355

Mayor M., Naef D., Pepe F., Queloz D., Santos N., Udry S., Burnet M., 2000, in Penny A., Artymowicz P., Lagrange A.-M., Russell S., eds, Planetary Systems in the Universe:

Observation, Formation and Evolution: ASP conf. series. ASP

Mazeh T., Goldberg D., Latham D. W., 1998, ApJ, 501, L199

Mazeh T., Krymolowski Y., Rosenfeld G., 1997, ApJ, 477, L103

Mizuno H., 1980, Prog. Th. Phys., 64, 544

Mochejska B. J., Stanek K. Z., Sasselov D. D., Szentgyorgyi A. H., 2002, ApJ

Morrison J. E., Röser S., McLean B., Bucciarelli B., Lasker B., 2001, AJ, 121, 1752

Moulton F. R., 1900, ApJ, 11, 103

Moulton F. R., 1905, ApJ, 22, 165

Moutou C., Coustenis A., Schneider J., Gilles R. S., Mayor M., Queloz D., Kaufer A., 2001, A&A, 371, 260

Murray N., Chaboyer B., 2001

Murray N., Hansen B., Holman M., Tremaine S., 1998, Sci, 279, 69

Naef D. et al., 2001a, A&A, in press

Naef D., Mayor M., Pepa F., Queloz D., Santos N. C., Udry S., Burnet M., 2001b, A&A, in press

Nelson R. P., Papaloizou J. C. B., Masset F., Kley W., 2000, MNRAS, 318, 18

Noyes R. W., Jha S., Korzennik S. G., Krockenberger M., Nisenson P., Brown T. M., Kennelly E. J., Horner S. D., 1997, ApJ, 483, L111

Penny A. J., Leger A., Mariotti J.-M., Schalinski C., Eiroa C., Laurance R. J., Fridlund M., 1998, in Reasenberg R. D., ed, SPIE vol. 3350: Astronomical Interferometry. SPIE, p. 666

Perryman M. A. C., 2000, Rep. Prog. Phys., 63, 1209

Podsiadlowski P., 1995, in Fruchter A. S., Tavani M., Backer D. C., eds, Millisecond Pulsars: A Decade of Surprise: ASP conf. series. ASP, p. 411

Purgathofer A., 1966, Mitt. Univ. Sternw. Wien, 13

Queloz D., Eggenberger A., Mayor M., Perrier C., Beuzit J. L., Naef D., Sivan J. P., Udry S., 2000a, A&A, 359, L13

Queloz D., Mayor M., Naef D., Pepe F., Santos N. C., Udry S., 2000b, in Penny A., Artymowicz P., Lagrange A.-M., Russell S., eds, Planetary Systems in the Universe: Observation, Formation and Evolution: ASP conf. series. ASP

Queloz D. et al., 2000c, A&A, 354, 99

Rasio F. A., Ford E. B., 1996, Sci, 274, 954

Reid I. N., Gizis J. E., 1997, AJ, 113, 2246

Reuyl D., Holmberg E., 1943, ApJ, 97, 41

Rivera E. J., Lissauer J. J., 2000, ApJ, 530, 454

Robichon N., Arenou F., 2000, A&A, 355, 295

Rosvick J. M., Vandenberg D. A., 1998, AJ, 115, 1516

Ruciński S. M., 1997, AJ, 113, 407

Russell H., 1935, The Solar System and its Origin. The Macmillan Company, New York

Ryan S. G., 2000, MNRAS, 316, L35

Sackett P., 1999, in Mariotti J.-M., Alloin D., eds, Planets outside the Solar System: theory and observations, NATO-ASI Series. Kluwer, Dordrecht, p. 189

Safronov V. S., 1969, Evolution of the Protoplanetary Cloud and Formation of the Earth and the Planets. Nauka, Moscow

Sahu K. C., Casertano S., Livio M., Gilliland R. L., Panagla N., Albrow M. D., Potter M., 2001, Nat, 411, 1022

Sanders W. L., 1972, A&A, 19, 155

Santos N. C., Israelian G., Mayor M., 2000, A&A, 363, 228

Santos N. C., Israelian G., Mayor M., 2001, A&A, 373, 1019

Santos N. C., Mayor M., Naef D., Pepe F., Queloz D., Udry S., Burnet M., 2001

Scally A., Clarke C., 2001, MNRAS, 325, 449

Seager S., Sasselov D. D., 1998, ApJ, 502, L157

Seager S., Whitney B. A., Sasselov D. D., 2000, ApJ, 540, 504

Shortridge K., Meyerdierks H., Currie M., Clayton M., Lockley J., Charles A., Davenhall C., Taylor M., 1998, Starlink User Note 86.16, Rutherford Appleton Laboratory

Sivan J.-P., Mayor M., Naef D., Queloz D., Udry S., Perrier-Bellet C., Beuzit J.-L., 2000, in Penny A., Artymowicz P., Lagrange A.-M., Russell S., eds, Planetary Systems in the Universe: Observation, Formation and Evolution: ASP conf. series. ASP

Smith B. A., Terrile R. J., 1984, Sci, 226, 1421

Snellgrove M. D., Papaloizou J. C. B., Nelson R. P., 2001, A&A, 374, 1092

Söderhjelm S., 1999, Inf. Bull. Variable Stars, 4816

Sozzetti A., Casertano S., Lattanzi M. G., Spagna A., 2001, A&A, 373, L21

Stauffer J. R., Caillault J.-P., Gagne M., Prosser C. F., Hartmann L. W., 1994, ApJS, 91, 625

Stepinski T. F., Black D. C., 2000, A&A, 356, 903

Stepinski T. F., Black D. C., 2001, A&A, 371, 250

Stetson P. B., 1987, PASP, 99, 191

Strand K. A., 1943, PASP, 55, 29

Strobel A., 1991, A&A, 247, 35

Sudarsky D., Burrows A., Pinto P., 2000, ApJ, 538, 885

Tabachnik S., Tremaine S., 2001, AJ

Thogersen E. N., Friel E. D., Fallon B. V., 1993, PASP, 105, 1253

Tinney C. G., Butler R. P., Marcy G. W., Jones H. R. A., Penny A. J., McCarthy C., Carter B. D., 2001a, ApJ

Tinney C. G., Butler R. P., Marcy G. W., Jones H. R. A., Penny A. J., Vogt S. S., Apps K., Henry G. W., 2001b, ApJ, 551, 507

Trilling D. E., Benz W., Guillot T., Lunine J. I., Hubbard W. B., Burrows A., 1998, ApJ, 500, 428

Trumpler R. J., 1930, Lick Obs. Bull., 14, 170

Udalski A., Olech A., Szymanski M., Kaluzny J., Kubiak M., Mateo M., Krzeminski W., 1995a,

Acta Astronomica, 45, 433

Udalski A., Szymanski M., Kaluzny J., Kubiak M., Mateo M., Krzeminski W., 1995b, Acta Astronomica, 45, 1

Udry S. et al., 2000, A&A, 356, 590

Unwin S. C., Turyshev S. G., Shao M., 1998, in Reasenberg R. D., ed, SPIE vol. 3350: Astronomical Interferometry. SPIE, p. 551

Vogt S. S., Marcy G. W., Butler R. P., Apps K., 2000, ApJ, 536, 902

Vogt S. S., Butler R. P., Marcy G. W., Fischer D. A., Pourbaix D., Apps K., Laughlin G., 2001

Wallace P. T., 1998, Starlink User Note 5.17, Rutherford Appleton Laboratory

Ward W. R., 1997, ApJ, 482, L221

Weidenschilling S. J., 1976, MNRAS, 180, 57

Williams D. M., Kasting J. F., Wade R. A., 1997, Nat, 385, 234

Wolszczan A., Frail D., 1992, Nat, 355, 145

Wolszczan A. et al., 2000, ApJ, 528, 907

Wolszczan A., 1999, in Arzoumanian Z., Van der Hooft F., van den Heuvel E. P. J., eds, Pulsar Timing, General Relativity and the Internal Structure of Neutron Stars. Koninklijke Nederlandse Akademie van Wetenschappen, p. 101

Woolf N., Angel J. R., 1998, ARA&A, 36, 507

Zucker S., Mazeh T., 2001, ApJ

Zucker S. et al., 2001, ApJ

APPENDIX A

Extra-Solar Planets Discovered to Date

Table A.1: Characteristics of all currently known extra-solar planets.

Star	M sin i (M_{jup})	a (AU)	Period (days)	e	Reference
PSR B1257+12	0.015 M_E	0.19	25.34	0.0	Wolszczan (1999)
	3.4 M_E	0.36	66.54	0.0182	Wolszczan & Frail (1992)
	2.8 M_E	0.47	98.22	0.0264	Wolszczan & Frail (1992)
	>0.05	>6	>12.4 yrs	0.0	Wolszczan et al. (2000)
HD 16141	0.22	0.35	75.8	0.28	Marcy et al. (2000)
HD 168746	0.24	0.066	6.409	0.00	ESO press release 07/01
HD 46375	0.25	0.041	3.024	0.04	Marcy et al. (2000)
HD 108147	0.34	0.098	10.881	0.558	ESO press release 07/01
HD 83443	0.35	0.038	2.9861	0.00	Mayor et al. (2000)
	0.16	0.174	29.83	0.42	Mayor et al. (2000)
HD 75289	0.46	0.047	3.508	0.014	Udry et al. (2000)
51 Peg	0.47	0.05	4.2293	0.00	Mayor & Queloz (1995)
BD -10°3166[2]	0.48	0.046	3.487	0.00	Butler et al. (2000)
HD 6434	0.48	0.15	22.09	0.30	Queloz et al. (2000b)
HD 187123	0.52	0.042	3.097	-	Butler et al. (1998)
HD 209458[1]	0.69 M_J	0.045	3.524738	0.00	Henry et al. (2000)
υ And	0.71	0.059	4.6170	0.034	Butler et al. (1997)
	2.11	0.83	241.2	0.18	Butler et al. (1999)
	4.61	2.50	1266.6	0.41	Butler et al. (1999)

continued on next page

continued from previous page

Star	M sin i (M_{jup})	a (AU)	Period (days)	e	Reference
HD 192263	0.78	0.15	24.36	0.22	Vogt et al. (2000)
HD 4208	0.81	1.69	829.0	0.04	Vogt et al. (2001)
55 Cnc[3]	0.84	0.11	14.648	0.015	Butler et al. (1997)
	>3.2	>5.5	>12 yrs	-	Fischer et al. (2001)
HD 82943	0.88	0.73	221.6	0.54	ESO press release 07/01
	1.63	1.16	444.6	0.41	ESO press release 07/01
HD 121504	0.89	0.32	64.6	0.13	Queloz et al. (2000b)
ϵ Eri[4]	0.86	3.3	2502.1	0.6	Hatzes et al. (2000)
HD 38529	0.77	0.13	14.3	0.27	Fischer et al. (2001)
HD 179949	0.84	0.045	3.093	0.05	Tinney et al. (2001b)
HD 114783	0.99	1.20	501.0	0.10	Vogt et al. (2001)
HD 37124	1.04	0.585	155.7	0.19	Vogt et al. (2000)
HD 130322	1.08	0.088	10.724	0.048	Udry et al. (2000)
ρ CrB	1.1	0.23	39.645	0.028	Noyes et al. (1997)
HD 52265	1.13	0.49	119.0	0.29	Butler et al. (2000)
PSR B1620-26	>1.2	>10	>61.8 yrs	>0.0	-
HD 177830	1.22	1.10	391.6	0.41	Vogt et al. (2000)
HD 210277	1.28	1.097	436.6	0.45	Marcy et al. (1999)
HD 217107	1.28	0.07	7.1260	0.14	Fischer et al. (1999)
HD 142	1.03	1.0	339.0	0.37	Tinney et al. (2001a)
HD 27442	1.43	1.18	415	0.058	Butler et al. (2001b)
16 Cyg B	1.5	1.70	804	0.67	Cochran et al. (1997)
HD 74156	1.56	0.276	51.61	0.649	ESO press release 07/01
	>7.5	4.47	2300.0	0.395	ESO press release 07/01
HD 134987	1.63	0.82	264.6	0.37	Butler et al. (2001b)
HD 4203	1.64	1.09	406.0	0.53	Vogt et al. (2001)
HD 68988	1.90	0.071	6.276	0.14	Vogt et al. (2001)
HD 160691	1.97	1.65	743	0.62	Butler et al. (2001b)
Gliese 876[5]	1.98–2.1	0.21	61.02	0.27	Defosse et al. (1998)

continued on next page

continued from previous page

Star	M sin i (M_{jup})	a (AU)	Period (days)	e	Reference
	0.56	0.13	30.1	0.12	Marcy et al. (2001a)
HD 19994	2.0	1.3	454	0.2	Queloz et al. (2000b)
HD 17051	2.13	0.91	312	0.15	Butler et al. (2001b)
HD 8574	2.23	0.76	228.8	0.40	ESO press release 07/01
ι Hor	2.26	0.925	320.1	0.161	Kürster et al. (2000)
47 UMa	2.54	2.09	3.0 yrs	0.06	Fischer et al. (2002)
	0.76	3.73	7.3 yrs	0.005	Fischer et al. (2002)
HD 23079	2.5	1.5	626.0	0.02	Tinney et al. (2001a)
HD 12661	2.79	0.79	252.7	0.23	Fischer et al. (2001)
HD 169830	2.94	0.82	229.9	0.35	Naef et al. (2001b)
14 Her	3.3	2.5	1619	0.354	-
GJ 3021	3.37	0.49	133.71	0.511	Naef et al. (2001b)
HD 80606	3.90	0.469	111.81	0.927	Naef et al. (2001a)
HD 195019	3.43	0.14	18.3	0.05	Fischer et al. (1999)
HD 213240	4.5	2.03	951	0.45	Santos et al. (2001)
HD 92788	3.34	0.95	326.7	0.30	Fischer et al. (2001)
τ Boo	3.87	0.0462	3.3128	0.018	Butler et al. (1997)
Gl 86	4	0.11	15.78	0.046	Queloz et al. (2000c)
HD 13445	4.04	0.114	15.764	0.046	Butler et al. (2001b)
HD 50554	4.9	2.38	1279.0	0.42	ESO press release 07/01
HD 190228	4.99	2.31	1127	0.43	Sivan et al. (2000)
HD 168443	7.7	0.29	58	0.53	Marcy et al. (2001b)
	17.2	2.9	1753.2	0.20	Marcy et al. (2001b)
HD 222582	5.4	1.35	575.9	0.71	Vogt et al. (2000)
HD 28185	5.7	1.03	383	0.07	Santos et al. (2001)
HD 178911B	6.29	0.32	71.49	0.124	Zucker et al. (2001)
HD 10697	6.35	2.12	1072.3	0.12	Vogt et al. (2000)
70 Vir	6.6	0.43	116.6	0.4	Marcy & Butler (1997)
HD 106252	6.81	2.61	1500.0	0.54	ESO press release 07/01

continued on next page

continued from previous page

Star	M sin i (M_{jup})	a (AU)	Period (days)	e	Reference
HD 89744	7.2	0.88	256	0.7	Korzennik et al. (2000)
HD 33636	7.71	2.62	1553.0	0.39	Vogt et al. (2001)
ι Dra	8.7	1.34	1.5 yrs	0.71	U.C.S.D. press release
HD 141937	9.7	1.49	658.8	0.40	ESO press release 07/01
HD 39091	10.3	3.34	2083	0.62	Jones et al. (2001)
HD 114762	11	0.3	84.03	0.334	Latham et al. (1989)
HD 202206	14.7	554	259	-	-
HD 110833	16.8	-	271.165	0.784	Halbwachs et al. (2000)
HD 184860	32	1.44	693.0	0.67	Vogt et al. (2001)
HD 112758	33.5	-	103.258	0.139	Halbwachs et al. (2000)
HD 127506	36	891	2599	-	Halbwachs et al. (2000)
HD 29587	40.8	-	1474.9	0.356	Halbwachs et al. (2000)
HD 18445	44.0	-	554.58	0.558	Halbwachs et al. (2000)
HD 140913	46.1	-	147.956	0.608	Halbwachs et al. (2000)
HIP 19832	47.1	-	716.68	0.074	Halbwachs et al. (2000)
HD 283750	50.3	-	1.787992	0.002	Halbwachs et al. (2000)
HD 89707	57.6	-	297.708	0.952	Halbwachs et al. (2000)
HD 217580	67.0	-	454.66	0.520	Halbwachs et al. (2000)

[1] $R_p = 1.54\ R_{jup}$, $i = 85.2°$, [2] $i < 84.3°$, [3] $i \sim 23°$, [4] $i = 46°$, [5] $i = 37°$.

Table A.2: Characteristics of all stars currently known to host extra-solar planets.

Star	m_V (mag)	(B-V) (mag)	Sp. Type	[Fe/H]	d (pc)	RA	Dec
PSRB1257+12	-	-	Pulsar	-	300.0	13 00 01	+12 40 00
HD 16141	6.78	0.71	G5 IV	0.15	35.9	02 35 20	-03 33 38
HD 168746	7.95	0.69	G5	-0.06	43.12	18 21 50	-11 55 22
HD 46375	7.94	0.76	K1 IV	0.21	33.4	06 33 13	+05 27 47
HD 108147	6.99	0.51	F8/G0 V	0.20	38.57	12 25 46	-64 01 20

continued on next page

continued from previous page

Star	m_V (mag)	(B-V) (mag)	Sp. Type	[Fe/H]	d (pc)	RA	Dec
HD 83443	8.23	0.80	K0V	0.39	43.54	09 37 12	-43 16 20
HD 75289	6.35	0.59	G0 V	0.28	28.94	08 47 40	-41 44 13
51 Peg	5.5	0.66	G2 IV	0.21	14.7	22 57 27	+20 46 05
BD -10 3166	10.0	0.9	G4 V	-	-	10 58 29	-10 46 13
HD 6434	7.72	0.60	G3 IV	-0.55	40.32	01 04 40	-39 29 18
HD 187123	7.86	0.61	G5	0.16	50.0	19 46 58	+34 25 16
HD 209458	7.65	0.53	G0 V	0.04	47.0	22 03 11	+18 53 04
υ And	4.09	0.54	F7 V	0.12	16.5	01 36 49	+41 24 39
HD 192263	8.1	0.4	K2 V	-0.03	19.9	20 14 00	-00 52 01
HD 4208	7.79	0.67	G5 V	-0.24	-	00 44 27	-26 30 56
55 Cnc	5.95	0.87	G8 V	0.45	13.4	08 52 38	+28 20 03
HD 82943	6.539	0.591	G0	0.33	27.46	09 34 51	-12 07 46
HD 121504	7.54	0.76	G2 V	0.17	44.37	13 57 17	-56 02 24
ϵ Eri	3.73	0.88	K2 V	-0.07	3.2	03 32 56	-09 27 30
HD 38529	5.938	0.746	G4	0.39	42.43	05 46 35	+01 10 06
HD 179949	6.254	0.503	F8 V	-	27.0	19 15 33	-24 10 46
HD 114783	7.57	0.91	K0	0.33	-	13 12 44	-02 15 54
HD 37124	7.68	0.67	G4 IV-V	-0.41	33.0	05 37 03	+20 43 51
HD 130322	8.05	0.75	K0 V	0.05	30.0	14 47 33	-00 16 53
ρ CrB	5.40	0.61	G0/2 V	-0.29	16.7	16 01 03	+33 18 52
HD 52265	6.301	0.536	G0 V	0.24	28.0	07 00 18	-05 22 02
PSRB1620-26	21.3	-	Pulsar	-	3800.0	16 20 34	-26 24 59
HD 177830	7.175	1.092	K0	0.36	59.0	19 05 21	+25 55 14
HD 210277	6.63	0.71	G0	0.23	22.0	22 09 30	-07 32 33
HD 217107	6.180	0.720	G8 IV	1.01	37.0	22 58 16	-02 23 42
HD 142	5.70	0.52	G1 IV	-0.04	-	00 06 19	-49 04 31
HD 27442	4.442	1.075	K2 IVa	-	18.1	04 16 29	-59 18 08
16 Cyg B	6.20	0.66	G2.5 V	0.07	21.4	19 41 52	+50 31 03
HD 74156	7.62	0.54	G0	-	64.56	08 42 25	+04 34 41

continued on next page

continued from previous page

Star	m_V (mag)	(B-V) (mag)	Sp. Type	[Fe/H]	d (pc)	RA	Dec
HD 134987	6.45	0.70	G5 V	0.32	25.0	15 13 29	-25 18 34
HD 4203	8.68	0.73	G5	0.22	-	00 44 41	+20 26 56
HD 68988	8.21	0.62	G0	0.24	-	08 18 22	+61 27 39
HD 160691	5.15	0.70	G3 IV-V	-	15.2	17 44 09	-51 50 03
Gliese 876	10.17	1.60	M4 V	-	4.72	22 53 13	-14 15 13
HD 19994	5.07	0.56	F8 V	0.26	22.38	03 12 46	-01 11 46
HD 17051	5.40	0.57	G0 V	-	-	02 42 34	-50 48 01
HD 8574	7.8	-0.2	F8	-	44.15	01 25 13	+28 34 00
HR 810	5.40	0.57	G0 Vp	0.25	15.5	02 42 32	-50 48 12
. 47 UMa	5.03	0.56	G0 V	0.01	13.3	10 59 29	+40 25 46
HD 23079	7.1	0.5	F8/G0 V	-	-	03 39 43	-52 54 57
HD 12661	7.44	0.72	G6	0.35	37.16	02 04 34	+25 24 52
HD 169830	5.911	0.475	F8 V	0.22	36.32	18 27 50	-29 49 01
14 Her	6.67	0.90	K0 V	0.50	17.0	16 10 24	+43 49 18
GJ 3021	6.59	0.61	G6 V	0.11	17.62	00 16 13	-79 51 04
HD 80606	8.93	0.72	G5	0.43	58.38	09 22 38	+50 36 13
HD 195019	6.91	0.64	G3 IV-V	-	20.0	20 28 17	+18 46 13
HD 213240	6.81	0.603	G4 IV	0.16	40.74	22 31 00	-49 26 00
HD 92788	7.31	0.29	G5	0.31	32.82	10 42 49	-02 11 02
τ Boo	4.50	0.48	F7 V	0.32	15.0	13 47 17	+17 27 22
Gliese 86	6.17	0.77	K1 V	-0.20	12.0	02 10 14	-50 50 01
HD 50554	6.860	0.532	F8	-	31.03	06 54 43	+24 14 44
HD 190228	7.307	0.757	G5 IV	-0.24	66.11	20 03 01	+28 18 25
HD 168443	6.92	0.70	G5	0.10	33.0	18 20 04	-09 35 35
HD 222582	7.70	0.60	G5	0.02	42.0	23 41 52	-05 59 09
HD 28185	7.80	0.750	G5 V	0.24	39.6	04 26 26	-10 33 03
HD 178911B	7.98	0.73	G8 V	0.28	46.73	19 09 03	+34 36 00
HD 10697	6.292	0.665	G5 IV	0.16	30.0	01 44 56	+20 04 59
70 Vir	5.0	0.69	G4 V	-0.03	22.0	13 28 27	+13 47 12

continued on next page

continued from previous page

Star	m_V (mag)	(B-V) (mag)	Sp. Type	[Fe/H]	d (pc)	RA	Dec
HD 106252	7.36	0.64	G0	-	37.44	12 13 30	+10 02 30
HD 89744	5.741	0.491	F7 V	0.30	40.0	10 22 11	+41 13 46
HD 33636	7.06	0.58	G0	-0.13	-	05 11 47	+04 24 13
ι Dra	3.310	1.183	K2 III	+0.03	31	15 24 56	+58 57 58
HD 141937	7.25	0.60	G2/3 V	-	33.46	15 52 18	-18 26 10
HD 39091	5.65	0.58	G1 V	0.09	18.2	05 37 10	-80 28 09
HD 114762	7.30	0.55	F9 V	-0.60	28.0	13 12 22	+17 31 01
HD 202206	8.08	0.69	G6 V	+0.36	-	21 14 58	-20 47 21
HD 110833	7.04	0.94	K3 V	-	-	12 44 15	+51 45 34
HD 184860	8.40	1.01	K2 V	-0.13	-	19 36 46	-10 26 36
HD 112758	7.56	0.78	K0 V	-	-	12 59 02	-09 50 03
HD 127506	8.70	1.05	K3 V	-	-	14 30 45	+35 27 14
HD 29587	7.29	0.64	G2 V	-	-	04 41 36	+42 07 07
HD 18445	7.78	0.94	K2 V	-	-	02 57 13	-24 58 30
HD 140913	8.069	0.572	G0 V	-	-	15 45 08	+28 28 12
HIP 19832	9.39	1.17	K5 V	-	-	04 15 10	-04 25 06
HD 283750	8.42	1.12	K2	-	-	04 36 48	+27 07 56
HD 89707	7.19	0.55	G1 V	-	-	10 20 50	-15 28 48
HD 217580	7.46	0.95	K4 V	-	-	23 01 52	-03 50 55

APPENDIX B

Variables in the field of NGC 6819

B.1 Variable star details and finder charts

Table B.1: Details of the variable stars of CCD 2 numerically ordered by star number. The classification categories are: W Ursae Majoris type eclipsing binary (EW), Algol-type eclipsing binary (EA), β Lyrae type eclipsing binary (EB), RS Canum Venaticorum stars (RS CVn), BY Draconis star (BY Dra), Cepheid and unclassified (Unclass). Suspected variables are labelled with ^{S}. The error on the last decimal place is given in brackets.

Star	RA (J2000.0)	Dec (J2000.0)	V mag	Type	Comments
50	19 40 15.78	+40 16 28.9	19.18(6)	Unclass	
56	19 40 10.58	+40 16 28.0	18.63(6)	BY Dra	Blended
90	19 39 23.46	+40 16 19.3	18.26(9)	BY Dra	Bright comp.
145	19 39 47.55	+40 16 12.4	16.64(6)	-	
324	19 39 24.15	+40 15 46.3	21.2(2)	EW	
681	19 39 52.73	+40 14 56.4	19.11(6)	BY Dra	
863	19 39 19.93	+40 14 26.7	16.94(6)	BY Dra	
935	19 40 05.30	+40 14 17.7	18.90(7)	EA	
946	19 39 59.49	+40 14 15.8	19.60(8)	EW	Blended
1220	19 40 05.96	+40 13 40.2	17.27(6)	-	
1283	19 39 54.68	+40 13 30.3	21.3(1)	EW	
2155	19 40 03.22	+40 11 25.4	17.0(2)	EW	Blended

continued on next page

continued from previous page

Star	RA (J2000.0)	Dec (J2000.0)	V mag	Type	Comments
2160	19 39 29.60	+40 11 23.6	20.4(1)	EW	
2422	19 39 56.13	+40 10 48.0	18.92(6)	-	
2435	19 39 50.25	+40 10 46.3	18.52(6)	Unclass	
2848	19 40 01.55	+40 09 50.4	18.45(6)	BY Dra	
2876	19 39 20.19	+40 09 45.3	20.27(8)	EW	
3240	19 40 05.63	+40 08 56.7	17.20(6)	-	Blended
3450	19 39 36.68	+40 08 26.4	17.785(3)	BY Dra	
3590	19 40 07.59	+40 08 07.2	16.68(7)	EW	
4305	19 39 41.89	+40 06 28.8	20.420(3)	EA	
4690	19 39 50.03	+40 05 36.2	17.025(1)	-	Pair with 4694
4694	19 39 49.67	+40 05 35.9	19.058(1)	Unclass	Pair with 4690
4698	19 39 27.86	+40 05 35.4	16.548(2)	BY Dra	
4843	19 39 30.42	+40 05 13.4	18.755(1)	BY Dra	RS CVn?
4977	19 39 24.14	+40 04 54.2	19.34(8)	BY Dra	
5132	19 39 32.37	+40 04 30.5	16.745(2)	-	
5137	19 40 05.26	+40 04 29.4	19.08(6)	-	
5171	19 39 21.49	+40 04 26.1	16.92(6)	-	
5291	19 39 36.85	+40 04 09.4	17.526(3)	EW	
5362	19 39 24.34	+40 03 58.3	17.08(6)	EW	Blended
5567	19 40 00.84	+40 03 26.9	18.513(1)	Unclass	Bright comp.
5786	19 40 01.22	+40 02 57.3	20.212(3)	BY Dra	
6142	19 39 32.55	+40 02 04.9	18.884(1)	BY Dra	
6336	19 39 48.84	+40 01 34.9	16.447(2)	-	
6694	19 39 39.81	+40 00 45.5	18.157(1)	BY Dra	
7090	19 39 37.69	+39 59 45.0	16.384(2)	-	
7298	19 39 43.38	+39 59 15.7	16.915(2)	EW	
7662	19 39 25.15	+39 58 25.6	19.19(6)	BY Dra	
7767	19 39 35.75	+39 58 12.4	19.48(6)	-	
8124	19 39 20.76	+39 57 22.9	17.3(2)	EW	

Table B.2: Details of the variable stars of CCD 4 numerically ordered by star number. The classification categories are: W Ursae Majoris type eclipsing binary (EW), Algol-type eclipsing binary (EA), β Lyrae type eclipsing binary (EB), RS Canum Venaticorum stars (RS CVn), BY Draconis star (BY Dra), Cepheid and unclassified (Unclass). Suspected variables are labelled with ^{S}. The error on the last decimal place is given in brackets.

Star	RA (J2000.0)	Dec (J2000.0)	V mag	Type	Comments
224	19 42 11.66	+40 06 48.7	17.611(1)	Unclass	
1753	19 41 52.26	+40 12 23.8	20.078(3)	EW	
1815	19 41 51.38	+40 12 33.6	19.400(2)	EW	
2031^S	19 41 48.92	+40 14 12.3	18.334(1)	-	
2393	19 41 44.46	+40 14 23.8	18.765(1)	BY Dra	
2501^S	19 41 42.74	+40 08 40.2	19.427(2)	-	
2576	19 41 41.61	+40 07 03.1	18.833(1)	EW	
2605	19 41 41.69	+40 11 41.5	18.474(1)	Unclass	Near diffraction spike
2825^S	19 41 39.15	+40 13 26.8	19.693(2)	-	
3126	19 41 36.05	+40 16 19.9	19.939(2)	BY Dra	Close companion
3127	19 41 35.88	+40 13 53.3	19.758(2)	BY Dra	
3236^S	19 41 34.26	+40 06 34.9	17.027(1)	-	
3856	19 41 28.58	+40 16 24.8	17.246(1)	EW	
3878^S	19 41 28.16	+40 12 32.9	17.269(1)	-	
4003	19 41 26.77	+40 10 49.5	18.2(4)	BY Dra	
4339^S	19 41 23.67	+40 11 52.2	17.0(4)	-	
4441^S	19 41 22.91	+40 14 39.5	18.275(1)	EW	Sits on dead column
4448^S	19 41 22.61	+40 11 07.1	17.494(1)	EW	Close to bright star
4484	19 41 22.18	+40 10 11.4	19.1(4)	BY Dra	
5302	19 41 15.27	+40 12 31.8	18.106(1)	EA	Crowded field
5371^S	19 41 14.72	+40 12 14.2	18.247(1)	-	
5590^S	19 41 12.60	+40 12 06.5	18.7(4)	-	
5660	19 41 11.73	+40 06 39.8	18.172(1)	EW	

continued on next page

continued from previous page

Star	RA (J2000.0)	Dec (J2000.0)	V mag	Type	Comments
5834^S	19 41 10.33	+40 15 18.3	16.610(2)	EW	Blended, dead column
5861	19 41 09.75	+40 10 38.1	19.120(2)	BY Dra	
6230	19 41 05.84	+40 12 54.3	20.724(4)	EW?	
6728	19 40 59.64	+40 08 25.0	19.811(2)	EW	
7333	19 40 53.05	+40 11 17.5	20.056(2)	EA/RS CVn	
7711	19 40 48.43	+40 16 19.3	20.677(4)	BY Dra	
7916	19 40 44.83	+40 09 23.0	17.359(3)	EA/RS CVn	
8080	19 40 42.71	+40 13 25.9	20.374(3)	EB	
8132	19 40 41.60	+40 07 46.9	19.2(5)	Cepheid?	
8152^S	19 40 41.72	+40 13 37.7	19.499(2)	-	
8741^S	19 40 33.50	+40 15 57.6	18.520(1)	-	
8830	19 40 32.00	+40 10 40.3	18.402(1)	Unclass	
8864	19 40 31.55	+40 12 51.8	20.5(5)	EA	
8943	19 40 30.48	+40 16 24.1	19.559(2)	EB	
9440	19 40 21.82	+40 12 08.5	20.6(5)	EW	

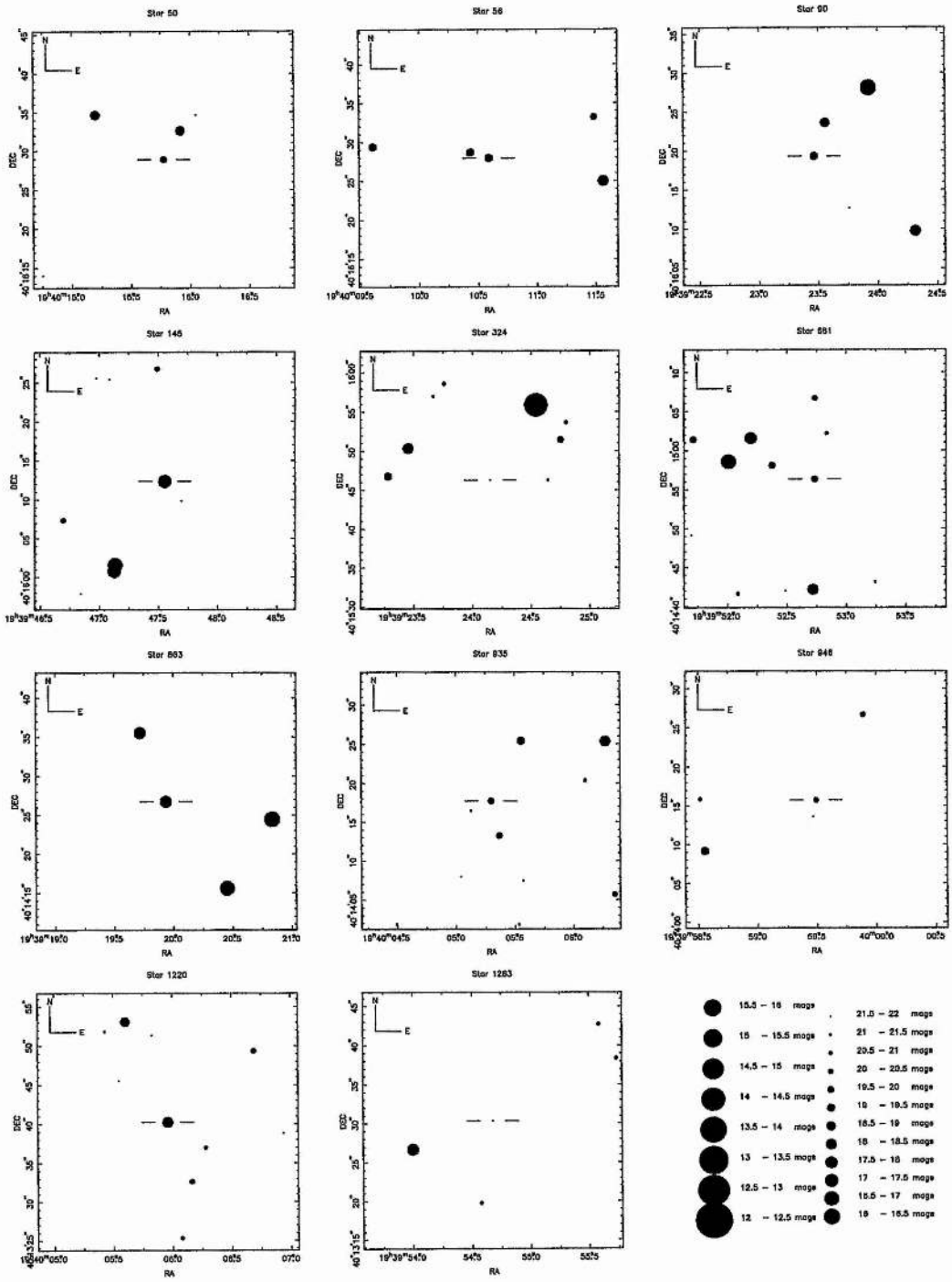

Figure B.1: Finder charts for the CCD 2 variable stars 50–1283.

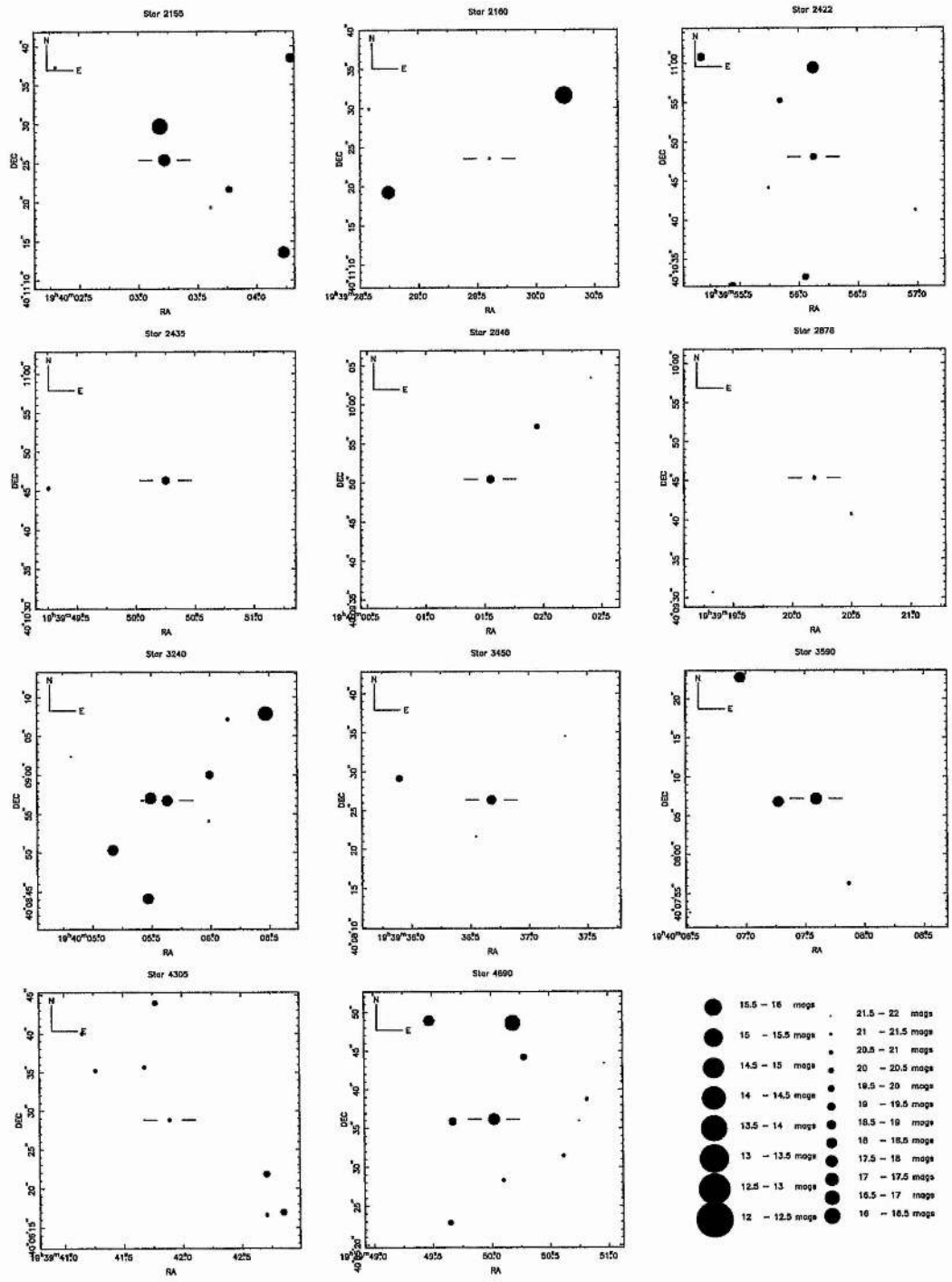

Figure B.2: Finder charts for the CCD 2 variable stars 2155–4690.

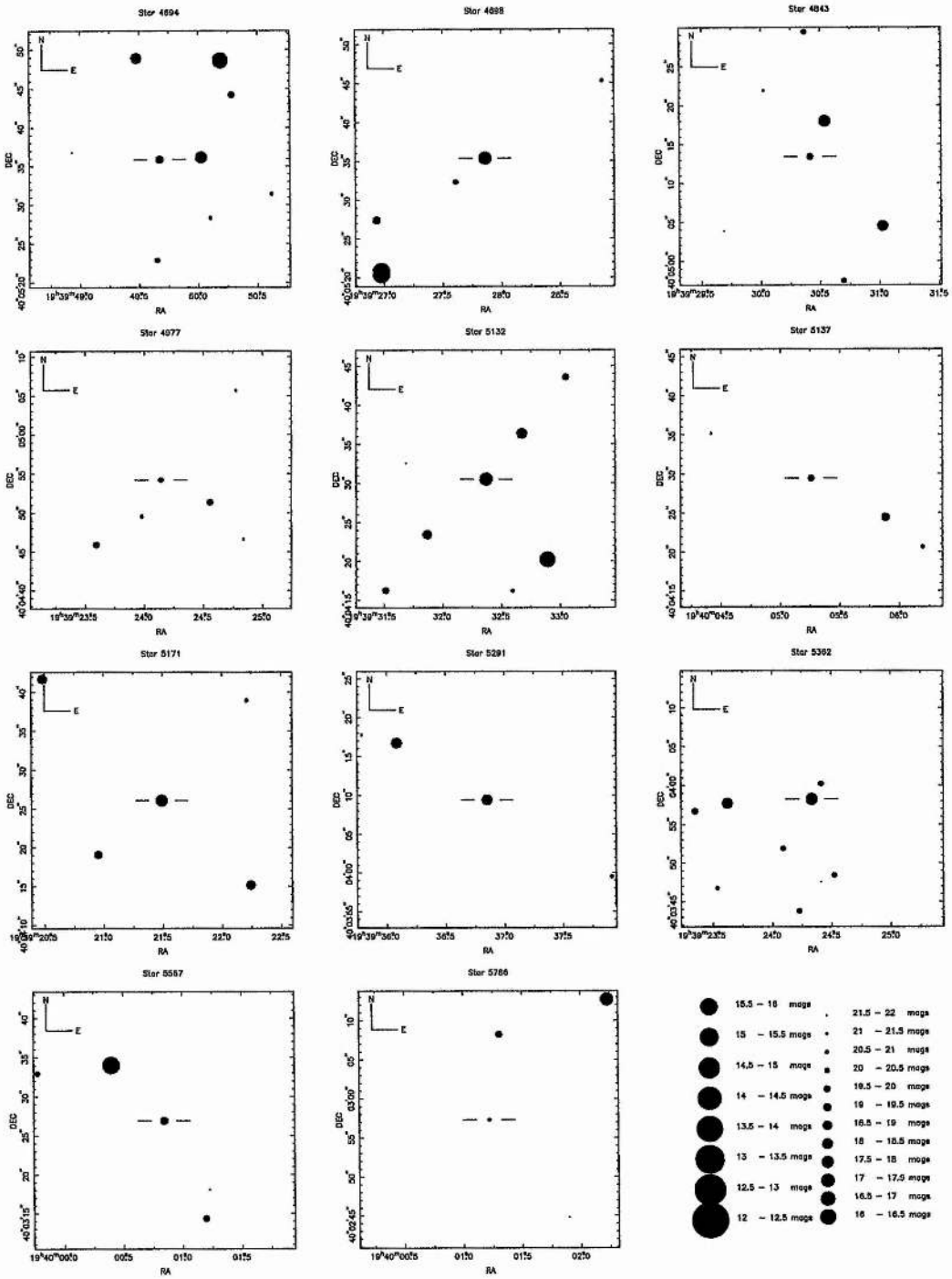

Figure B.3: Finder charts for the CCD 2 variable stars 4694–5786.

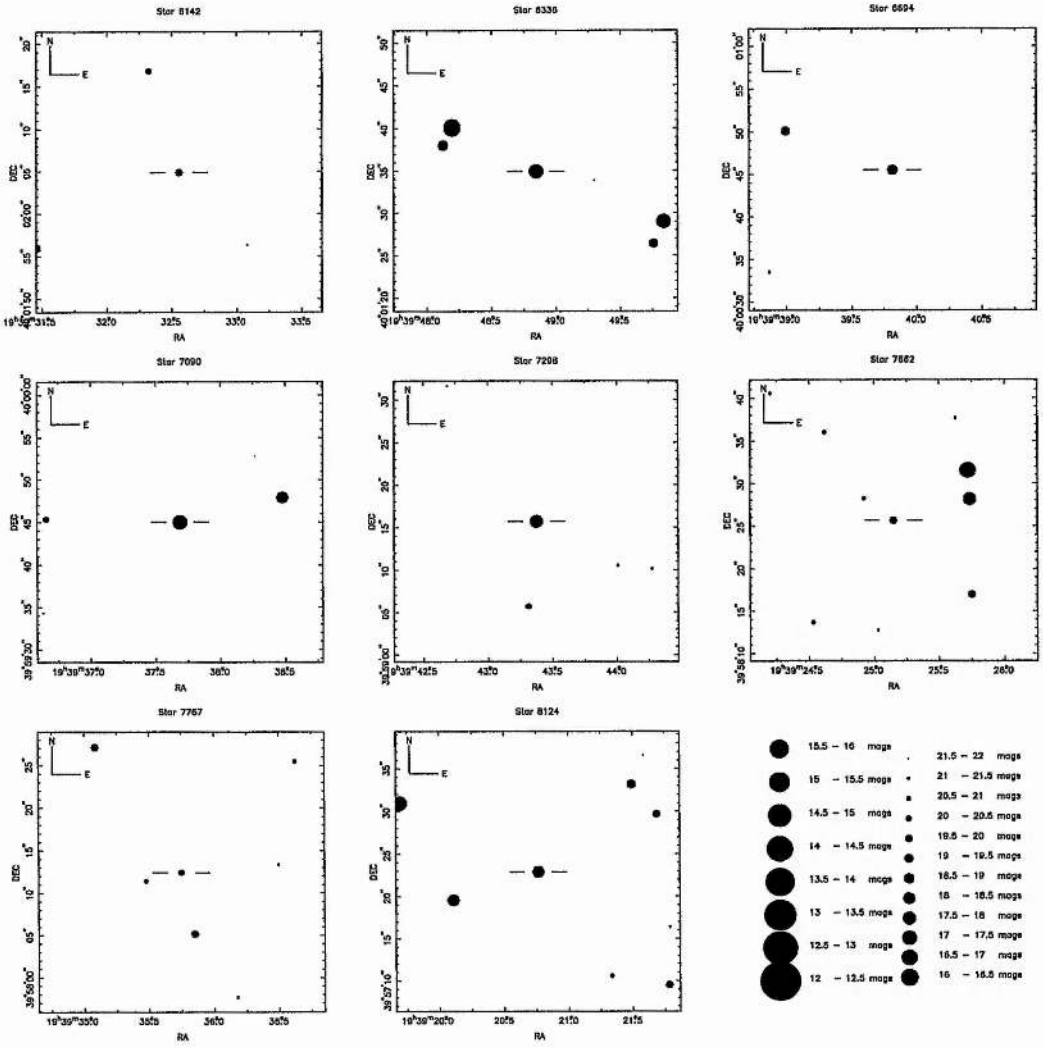

Figure B.4: Finder charts for the CCD 2 variable stars 6142–8124.

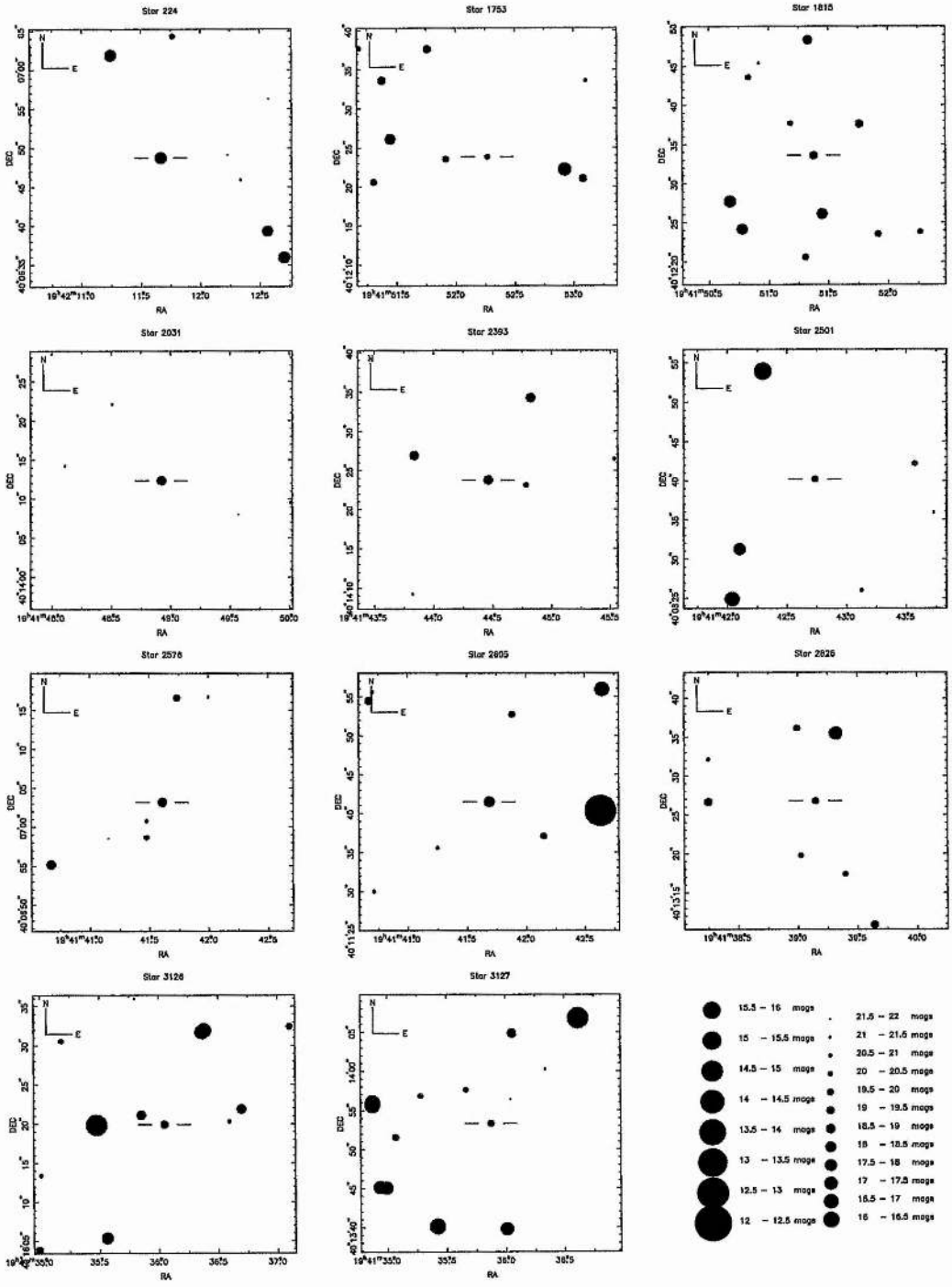

Figure B.5: Finder charts for the CCD 4 variable stars 224–3127.

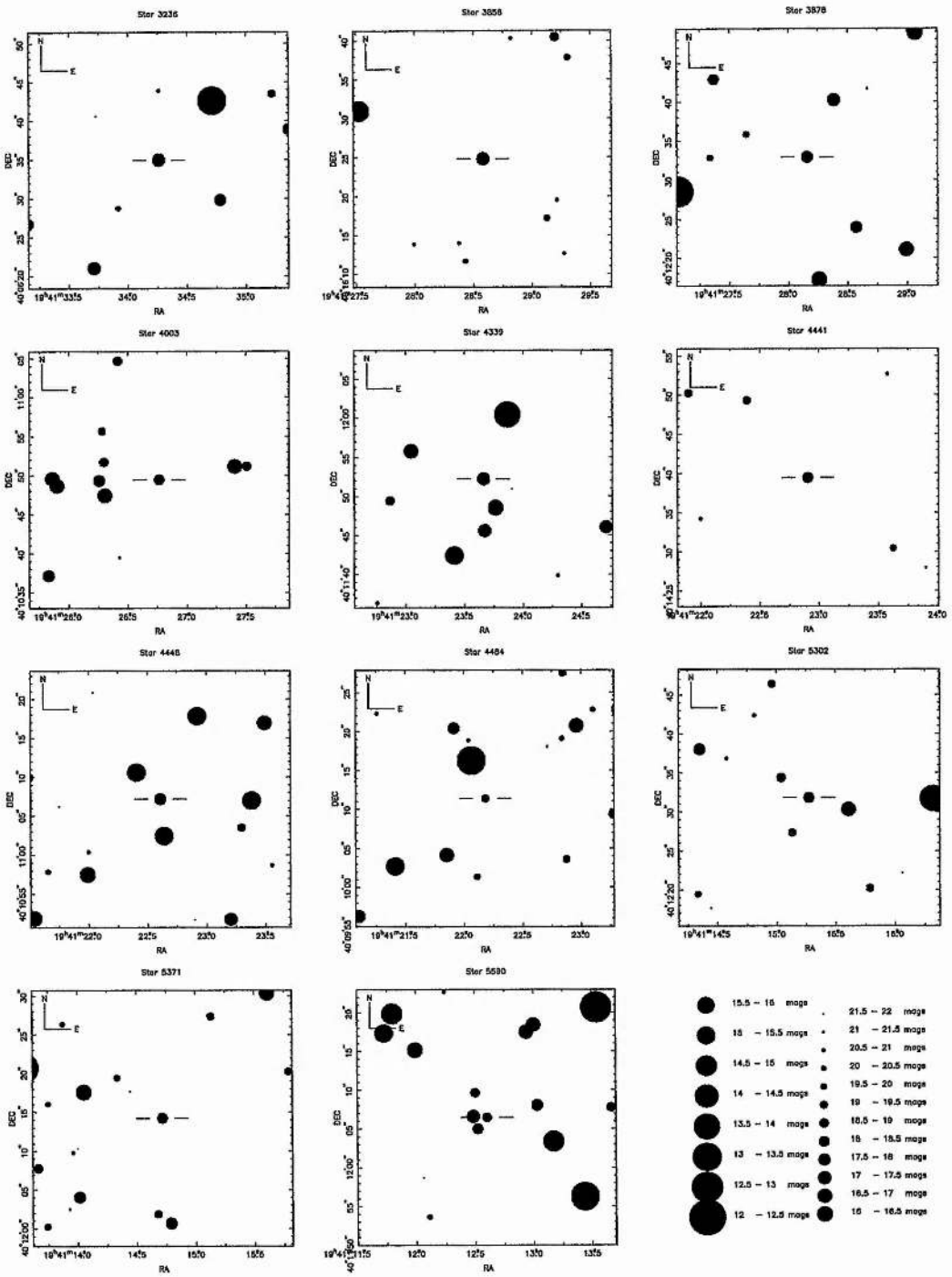

Figure B.6: Finder charts for the CCD 4 variable stars 3236–5590.

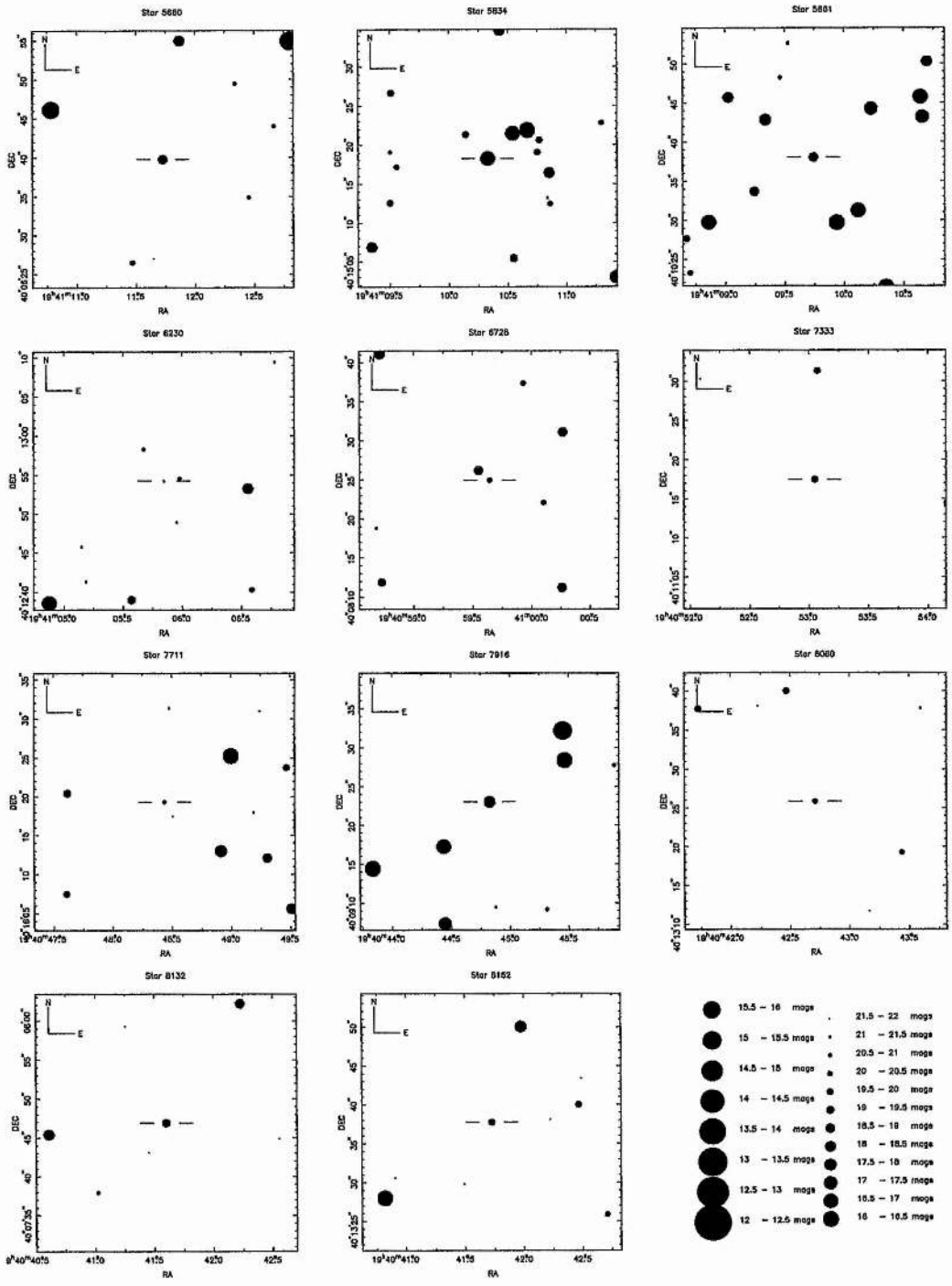

Figure B.7: Finder charts for the CCD 4 variable stars 5660–8152.

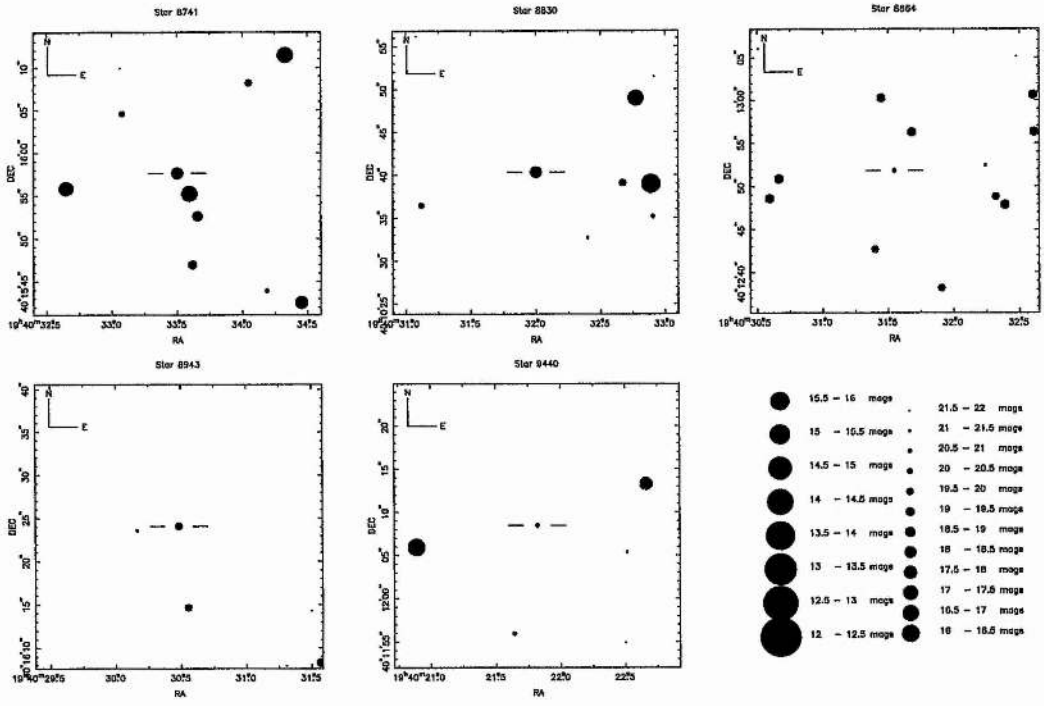

Figure B.8: Finder charts for the CCD 4 variable stars 8741–9440.